Westerduinweg 3
1755 LE Petten
P.O. Box 15
1755 ZG Petten
The Netherlands

www.tno.nl

T +31 88 866 50 65

TNO report

TNO 2019 R11389

Validation of BEM and Vortex-wake models with numerical tunnel data

TKI WoZ VortexLoads WP2

Date	September 2019
Author(s)	K. Boorsma, F. Wenz†, M. Aman‡, C. Lindenburg∓, M. Kloosterman∓ † USTUTT-IAG ‡ DNV-GL ∓ LM Windpower
Copy no	
No. of copies	
Number of pages	238 (incl. appendices)
Number of appendices	3
Sponsor	TKI WoZ
Project name	TKI WoZ VortexLoads
Project number	060.33833

Acknowledgement

This project has been executed within the framework of TKI Wind op Zee.

Summary

Within the framework of the TKI WoZ VortexLoads project, CFD simulations were carried out to verify the earlier observed differences in dynamic loading and the resultant fatigue equivalents between BEM and vortex wake codes in turbulent inflow. Hereto a 'numerical' wind tunnel was set-up subjecting a rigid (or non-flexible) version of the AVATAR 10MW wind turbine model, which can be considered as a reference for the present turbine size. Firstly comparisons in uniform, constant inflow conditions provided a good agreement between all code types, which is a prerequisite for a consistent comparison in more challenging inflow conditions. Sheared inflow conditions demonstrated a difference in the cyclic loading amplitude between BEM and vortex / CFD models. A parameter variation study revealed this difference to scale with the magnitude of the axial induction factor. Turbulent inflow simulations were carried out to verify the influence of turbulence length scale, turbulence intensity and thrust coefficient on the observed differences between the codes.

Concluding it can be stated that a variety of CFD simulations have confirmed the hypothesis that conventional BEM models overpredict fatigue loading for wind turbine design load calculations up to 20% depending on the load case considered. On the other hand the unsteady loading characteristics from lifting line free vortex wake models were shown to agree well with the CFD simulations. The mentioned over prediction was shown to be partly related to the shed vorticity modeling. However, both for the shear and turbulent inflow cases a difference between BEM on the one hand and vortex models on the other hand remains after including a shed vorticity model in BEM. Poor tracking of induced velocities with apparent wind speed variations as experienced by the blade was shown to be the underlying cause for the differences between the models, becoming increasingly important for higher thrust coefficients. It is recommended to have a further look into the cause for this difference. In addition to that it is recommended to perform a validation in a real rather than a 'numerical' wind tunnel, featuring a rotor in representative inflow conditions.

Contents

1 Introduction

The TKI WoZ VortexLoads project [1] considers the application of vortex wake models to design load calculations and its potential added value against traditional BEM methods. Within Work Package 2 of the project, 'numerical wind tunnel data' from CFD simulations is used to validate earlier observed differences in dynamic loading and the resultant fatigue equivalents between BEM and vortex wake codes in turbulent inflow conditions [2]. Hereto several comparison rounds were executed amongst the participants, i.e. ECN.TNO, DNV-GL and LM. These participants have a variety of BEM and free vortex wake models which are validated with the CFD code from US-TUTT. Chapter 2 describes the codes used by the participants. Firstly a comparison is made in uniform, constant wind conditions as reported in chapter 3. Chapter 4 and 5 give the results in respectively sheared and turbulent inflow conditions, followed by conclusions in chapter 6.

2 Code descriptions

2.1 DNV-GL

Bladed is the industry standard integrated software package for the design and certification of onshore and offshore turbines. It provides users with a design tool that has been extensively validated against measured data from a wide range of turbines and enables them to conduct the full range of performance and loading calculations. Bladed offers a Windows-based user interface and supports calculations of combined wind and wave loading, with full aeroelastic and hydroelastic modelling. It has been validated for the calculation of wind turbine loads for design and certification. DNV GL's approach to the calculation of wind turbine performance and loading has been constantly evolving since 1984. The ongoing software development has maintained DNV GL's reputation for delivering robust and reliable tools for use in the design and certification of wind turbines.

2.1.1 Bladed 4.8-BEM

The results provided by DNV GL are based on the BEM code of Bladed 4.8. The BEM code in Bladed 4.8 is completely rewritten and replaces the code used in Bladed 4.7 and lower. Recent public validation work is presented in references [3] and [4]. The model is based on classical BEM theory where the axial and tangential Glauert momentum equations are expressed in dimensional form instead of non-dimensional factors. Further the dynamic submodels (dynamic wake, dynamic stall, skew wake correction) are fully expressed in state-space form allowing combined direct integration of structural and aerodynamic states. The aerodynamic and structural states are integrated with a 4th order variable step Runge-Kutta integrator. The following engineering correction models are available in the Bladed 4.8 BEM code:

- Option between an Øye and Pitt&Peters dynamic wake model.
- Compressible and Incompressible Beddoes-Leishman dynamic stall model in state-space format.
- Glauert skew wake correction method.
- Prandtl tip correction and Glauert corrections for highly loaded rotors.
- Option to include or exclude the drag in the induction calculations. By default, the drag is included.
- Option to apply the dynamic wake on element or on annulus level. By default, the dynamic wake is applied on element level.
- An option to exclude the out of plane rotation of the blade elements in the inflow calculations. By default, all structural rotations are included in the calculation of the inflow angles.
- Potential flow model for tower shadow, in case of upwind turbines. In case of downwind turbines an empirical model can be selected.

Details of the Bladed BEM theory can be found in the Bladed 4.8 theory manual which is available by contacting DNV GL at Bladed@dnvgl.com.

2.1.2 Bladed 4.8-VL

Next to the classical BEM model, Bladed 4.8 and higher features a fully coupled free wake lifting line model. At present this code is used for internal purposes only and is not yet commercially released. The theory of the lifting line code is described in [5]. Recent work published with the code is found in [4] and [6]. The implementation in Bladed is however fully coupled to the Bladed multibody model and allows for aeroelastic load simulations. The following submodels are applied in the vortex line code:

- Beddoes Leishman dynamic stall model, equivalent to the one in the BEM code. The attached flow terms due to shed vorticity are however excluded as this follows from the free wake solution directly.
- Corrections for viscous core growth using the Ramasamy-Leishman core growth models.
- Vortex core size is subsequently corrected for vortex stretching effects.
- Option to run the calculation in prescribed wake mode in which case the wake pitch is decided based on the average induction at 70% blade length.
- Option to control the amount of free wake points to speed up the simulation while retaining solution accuracy.
- By default the shed vorticity is excluded from the wake deformation calculations.
- Parallel computing on a CPU.

2.1.3 Simulation settings

BEM The blade discretization as provided to all consortium partners is directly used in Bladed. Also, the aerofoil information and distribution along the blade is identical to all consortium partners. For the steady calculations, the following options are used:

- Dynamic submodels are turned off
- Drag is included in induction calculations
- No additional 3D models are included
- Tip losses included, hub losses excluded

Vortex Line The identical blade discretization is used as for the BEM calculations. However, inflow parameters are computed at the midpoint between blade stations. The aerofoil properties are therefore interpolated. The following computational settings are used:

- Dynamic submodels are turned off
- 200s of simulation time to get converged steady state solutions
- After 200m downstream the wake nodes are frozen and convected with the last computed induced velocity.
- After 1000m downstream the wake is truncated.
- A time step for the vortex wake of 0.167s is used.

For dynamic simulations, the sub models mentioned in section 2.1.1 and 2.1.2 were applied. The Øye dynamic wake model and Glauert skew wake corrections were applied in BEM simulations. The incompressible Beddoes-Leishman dynamic stall model [7] was applied for both BEM and vortex wake simulations. For all other sub-models, default settings were applied. A vortex wake time step of 0.167s was also used for the steady and shear inflow test cases. For the turbulent inflow test cases, a smaller time step of 0.02425s was applied, which is approximately equivalent to 1 step per degree of revolution.

2.2 ECN part of TNO

The ECN Aero Module [8, 9] is used as aerodynamic solver for the current investigation. The two aerodynamic models included are the Blade Element Momentum (BEM) method similar to the implementation in Phatas [10] and a free vortex wake code in the form of AWSM [11]. Both models are lifting line codes, i.e. they make use of aerodynamic look-up tables to evaluate airfoil performance. Several dynamic stall models, 3D correction models, wind modeling options and a module for calculating tower effects are included. The set-up allows to easily switch between the two aerodynamic models whilst keeping the external input the same, which is a prerequisite for a good comparison between them. Although the package can be coupled to simulation software that solves the structural dynamics of a wind turbine (FOCUS [12], SIMPACK [13]), the stand-alone option is used simulating a rigid turbine with prescribed operational conditions.

2.2.1 AWSM

The Aerodynamic Wind turbine Simulation Module (AWSM) has been developed at the Energy research Centre of the Netherlands (ECN) by Van Garrel [11]. The main scope was to keep the advantages of BEM codes in terms of calculation time and ease of use, but to obtain a superior quality, especially concerning wake and time dependent wake-related phenomena. The code is based on generalized lifting line theory in combination with a free vortex wake method. The main assumption in this theory is that the extension of the geometry in spanwise direction is predominant compared to the ones in chordwise and thickness direction. Because of this, the real geometry is represented by a line passing through the quarter chord point of each cross section. Hence the total flow field in chord-wise direction is concentrated in this point (Figure 2.1(a)).

In AWSM, the effects of viscosity are taken into account through the user-supplied nonlinear relationship between angle of attack and local lift, drag and pitching moment coefficients. Along the lifting line, the generated elementary force can be determined by using the three-dimensional form of the Kutta-Jukowsky theorem. The two dimensional aerodynamic characteristics of the sections are known; this means that the elementary force can be calculated also from the sectional properties. By matching these two formulations, the lift along the blade can be obtained.

As in the continuous flowfield representation, the vorticity is shed from the trailing edge of the configuration surface and convected downstream in the AWSM flow model as time advances. The blade geometry consists of one or more strips that carry a vortex ring whose bound vortices are located at the quarter chord position and at the trailing edge. The vortex strengths Γ of these vortex rings are to be determined. Each timestep Δt new vortex rings with these strengths are shed from the trailing edge and joined with the older vortex rings. These vortex rings together will form a vortex lattice. A sketch of the wake geometry for three strips after four timesteps is shown in Figure 2.1(b). The position of the first shed free spanwise vortex behind the trailing edge (TE) lies at some fraction between the current TE position and the wind-convected TE position from the previous timestep. Upstream of this position the vortex rings have

a strength equal to the corresponding vortex ring at the configuration. The position of the downstream part of the wake is determined each timestep by convection of the wake vortex-lattice nodes.

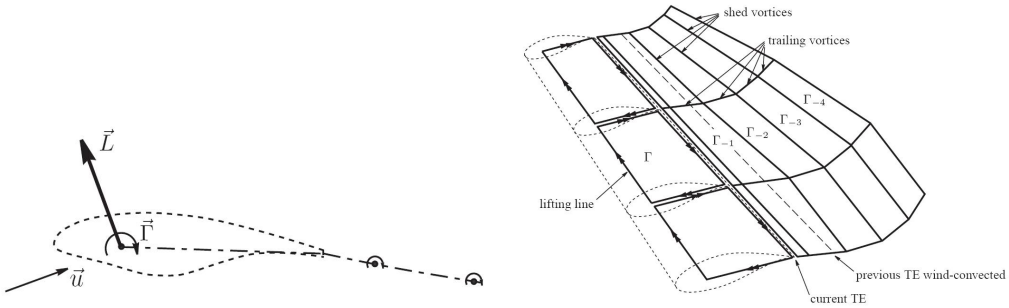

(a) Flowfield model (b) Wake geometry

Figure 2.1: Visualization of AWSM model

To reduce the simulation time of the tool, the Biot-Savart calculation for induced velocities over the free wake has been parallelized using OpenMP. In addition to that it is possible to prescribe part of the wake [9]. The current prescription determines convection based on the induced velocity at the blade extrapolated using axial momentum theory. Alternatively it is possible to specify the near wake free and prescribe the far wake convection. Another possibility to reduce the computational burden is the option to remove shed vorticity lines in the far wake [14], also called 'wake reduction'.

2.2.2 BEM

Many different options exist for implementing a BEM formulation, and this especially holds with regard to the various engineering extensions. Within the ECN Aero Module it is possible to switch off or vary many of these options, or use the default settings. The most important options are briefly highlighted below.

In order not to average out the effect of inflow variations (e.g. shear, turbulence) on local induction, an unsteady BEM formulation is implemented. Here the momentum equation is evaluated locally for each blade instead of balancing the aggregate of all blade element forces within the annulus with the momentum of a full annulus. The ECN dynamic inflow model [15] has been implemented, adding another term to the axial momentum equation to account for the aerodynamic rotor 'inertia' in the case of pitch action, rotational speed variation or wind speed variation. The term is proportional to the time derivative of the annulus averaged axial rotor induction and has a dependency on the radial position.

To account for the azimuthal variation of axial induction in oblique inflow, the model as defined by Schepers [16, 17] is employed by default. A skew function is determined for each element as a function of effective yaw angle, azimuth angle and radial location. This skew function then relates the local induction at each element to the annulus averaged axial induction. The skew function from the yaw model was originally developed from the correlation between annulus averaged and local induction velocities for an annulus by means of wind tunnel measurements. The Glauert correction for yaw [18] is also implemented. The main difference with the Schepers model lies in the refinement between inboard and outboard sections through inclusion of the effects of the root vortex.

To account for the finite number of blades, the Prandtl correction [19] (optionally for both root and tip) is calculated for each element. In its current implementation, axial

wind speed, root- or tip vortex location and annulus averaged axial and tangential induction at the root or tip are necessary input for the evaluation of this function. The calculated Prandtl factor is incorporated in the iterative convergence procedure to relate the annulus averaged axial and tangential induction to the local induction at each element.

For heavily loaded rotors, BEM theory predicts flow reversal in the wake, whilst in reality the wake transforms into a turbulent state by sucking in air from outside the streamtube. To account for this effect the momentum equation is replaced by a turbulent wake state (TWS) equation if the annulus averaged axial induction coefficient exceeds a user specified value. The default value for this parameter is 0.38. The quadratic relationship between axial force and induction in the momentum equation is then replaced by a linear relationship tangent to the original quadratic line at the specified induction value.

By default, drag is excluded in the calculation of induction.

2.2.3 Simulation settings

For most of the cases both the BEM and AWSM aerodynamic solvers have been used. Default options have been used unless mentioned otherwise. The Snel dynamic stall model [20] was applied to all simulations (unless stated explicitly otherwise) and rotational corrections were disabled. For the free vortex wake simulation, the number of wake points was chosen to make sure that the wake length was developed over at least 3 rotor diameters downstream of the rotor plane. The wake convection was free for the first part of the wake, depending on the load case type. For the remaining wake length, the blade averaged induction at the free to fixed wake transition is applied to all wake points. For both aerodynamic solvers approximately 20 elements in spanwise direction were used. The spanwise discretization in AWSM features a cosine distribution, whereas this is linear for BEM featuring half the spacing at the tip.

For the uniform inflow cases, the time step was kept at the approximate equivalent of 5° azimuth for both the BEM and AWSM simulations at a simulation length of 350 s. The wake convection was free for approximately 2 rotor diameters downstream. Output values were taken from the last time step.

For the turbulent inflow calculations, the time step was kept at the approximate equivalent of 1° azimuth for both the BEM and AWSM simulations at a simulation length of 400s (200s for the 16 m/s case) plus about 100s initialization for the AWSM simulation. Wake reduction was applied after a full revolution skipping 9 shed vortices to end up with an effective distance of 10° azimuth between the shed vortices in the remaining part of the wake. The AWSM simulations took about 7h to 50h on a 40 node cluster, depending on the case. The upper limit is for the high thrust case which required many wake points to fulfill the wake length requirement. The lower limit is for the 16 m/s case which features a low induction (and consequently fewer wake points needed) plus half the duration of the other cases.

2.3 LM Wind Power

The computer program Phatas, ”Program for Horizontal Axis wind Turbine Analysis and Simulation”, is developed for the time-domain calculation of the dynamic response and the corresponding loads on a Horizontal Axis wind Turbine, HAT. The program Phatas is available as tool in the integrated wind turbine design package FOCUS6. The program Phatas has its own ”internal” BEM based aerodynamic model but is also available in a configuration ’phatAERO’ that uses the aerodynamics from an external module such as ECN-aeromodule.

This section gives a description of the modelling of the aerodynamic loads on the rotor blades. This model is based on the engineering BEM theory which is computationally fast, but which does not provide as much detail on the velocity distributions as is given by vortex wake descriptions.

The program Phatas has initially been developed at ECN. Since 2014 the maintenance and further development was taken over by WMC and subsequently LM Wind Power. The program Phatas is used by various designers of rotor blades and wind turbines worldwide.

2.3.1 Aerodynamic modelling

The aerodynamic modelling in the program Phatas uses a BEM based description for the rotor wake aerodynamics. Basic elements of the Phatas model for rotor blade aerodynamics are:

- Use of tables with dimensionless coefficients for the lift, drag, and moment coefficient for the airfoil sections.
- Optional engineering models for modelling the dynamic stall behaviour. These models have been developed in 1997 by H. Snel [20].
- Optional model to add a correction on the lift coefficient to account for the effects of rotation. This model was developed in 1994 by H. Snel [21]. For the modelling of wind turbine response this model was extended with a factor $\lambda^2/(1+\lambda^2)$ where λ is the local speed ratio of the cross section that is considered. If the increaded lift correction for the effects of rotation is "switched ON" then this correction is applied up to 80% of the rotor radius.
- A semi-empirical reduction of the lift coefficients that accounts for the 'pressure equalisation' of the airfoils near the blade tip. This 'pressure equalisation' describes the fact that the flow around the tip section differs from the flow around a 2D airfoil.

The model for the rotor wake aerodynamics contain the following sub-models:

- A tip-loss factor that accounts for the finite distance between the trailing vortex sheets. In the program Phatas the Prandtl factor is used for the tip loss. Phatas has an optional model for root loss, which is also based on the Prandtl factor.
- For large relative values of the rotor loading ($a > 0.5$) the momentum equations would predict a reversed flow downstream of the rotor disk. For large rotor disk loading the flow downstream of the rotor becomes turbulent, also known as 'Turbulent Wake State'. For modelling the turbulent wake state Phatas uses the correction model of Wilson.
- For the inflow stagnation from the presence of the tower, Phatas uses the potential flow solution of a semi-empirical dipole model.
- For unsteady rotor disk loading the wake downstream of the rotor is not in direct equilibrium with the rotor loads but take some 'settling time' that is based on the inertia of the air in the rotor wake. This time-lagging effect of the wake influence is modelled in Phatas with the dynamic inflow model of Schepers and Snel [15].
- The inflow of a rotor that operates in yawed condition has a wake influence that is stronger at the "downstream yawed rotor half" compared to the "upstream yawed rotor half". This asymmetry in the rotor wake influence is described with

the empirical skewed inflow model of Schepers and Vermeer [16]. This model has been derived on basis of measured load distributions of a scaled rotor in the wind tunnel of TU-Delft.

2.3.2 Settings used for the constant wind validations

The calculations for the comparisons in WP2 of the TKI Wind op Zee project VortexLoads are done with the AVATAR rotor model provided by ECN part of TNO with tables of aerodynamic coefficients that are derived from CFD simulations by the university of Stuttgart. Consequently the optional correction in Phatas for the effects of rotation was set 'OFF'. Because of the relatively low rotor disk loading the dynamic stall model was not used.

The table with geometric blade properties as provided by ECN part of TNO was reduced to a table with 31 records. This was done because in the calculations with the AWSM model in ECN-Aeromodule uses the records of this table for the modelling of the blade vortex segments. For the calculations with Phatas the same table with geometric input properties was used. For the calculations with Phatas the blade was modelled with 30 elements of equal spanwise size. Here it should be noted that the aerodynamic loading on the outer (30-th) elements are calculated with 2 BEM solutions for the half-span elements. In practice this means that the blade aerodynamics are calculated with 31 BEM solutions for each blade.

The rotor speed was set constant. The turbine geometry was modelled as rigid while the blades were modelled straight (without pre-bend). The rotor shaft tilt angle and also the rotor blade cone angle were set to zero. The tower diameter was set to zero so that there is no stagnation of the inflow at the rotor plane.

2.3.3 Settings used for the sheared and turbulent wind validations

The calculations for the sheared and turbulent wind comparisons were done with the model of the AVATAR rotor of which the cone angle, tilt angle, and pre-bend blade axis shape were set to zero. It was chosen to use the programs phatas and phatAERO + ECN-Aeromodule with the same structural algorithms as used in the practise of dynamic load calculations for design and certifications. This means that the calculations were performed including bending of the rotor blades, while the bending stiffnesses were multiplied with a factor 1000 such that the deformations of the blades were less than 0.01m at the tip. For the time increment used, also the dynamic blade bending motions have a strong numerical damping and as a result they are insignificant.

2.3.3.1 Aerodynamic modelling

The aerodynamic properties of the blade were modelled with the Cl-Cd-Cm tables derived from the CFD calculations of the University of Stuttgart. The options for correction of the lift coefficient for the effects or rotation ('3D effects') was not used. There was no model for dynamic stall used. The blades were modelled with 31 elements over the span, where 29 elements have equal length and the 2 elements close to the tip have half that length. The aerodynamic stagnation from the tower was not included.

2.3.3.2 Calculations for a fixed rotor speed

For the calculations with sheared inflow and with 8 m/s turbulent wind the rotor speed and the pitch angle was fixed. The time increment was set to 0.02424666s which equals the time increment in the turbulent wind files that were provided. For the 6.418697rpm rotor speed at 8 m/s wind this time increment gives a 1° increment in rotor azimuth.

2.3.3.3 Settings for the 8 m/s turbulent wind with large length scale

The calculations with 8 m/s turbulent wind with large turbulent length scale were done for a fixed blade pitch angle of 0 °, and for a rotor speed that was read from a file. For reading this rotor speed, the program Phatas was modified such that at each time in the simulations the rotor speed was represented as 'steady rotor speed' which means that inertia loads from rotor acceleration / deceleration are practically zero. The time increment for the 8 m/s wind with large length scale was set to 0.04849331s which is twice the increment in the wind file.

2.3.3.4 Settings for ECN-Aeromodule-AWSM

The calculations with the 8m/s turbulent wind with the normal and with the large length scale were performed for twice the 410.2538s length of the turbulent wind field. The first wind period of 410.2538s was then subtracted and the second wind period was processed for comparisons within WP2, where it may be trivial that the time variable starts at 0.0. This skipping of the first 410.2538s was done such that the calculations with phatAERO + ECN-Aeromodule-AWSM can develop its vortex structure of the wake. The input settings of ECN-Aeromodule-AWSM are for a 6 diameter total wake length of which 2 diameters are for a free-geometry wake length. The calculations with phatAERO + ECN-Aeromodule-AWSM were done with the option 'skip_odd_aero_calls' which reduces the number of Aerodynamic evaluations and likewise reduce the CPU needed.

2.3.3.5 Settings for phatasBSV

The calculations with phatas were done for the conventional modelling without the Blade Shed Vorticity, and with the contribution of the Blade Shed Vorticity from 20 shed vortices.

2.4 University of Stuttgart

This study was conducted based on the process chain for the simulation of wind turbines, which was developed at the Institute of Aerodynamics and Gas Dynamics (IAG, USTUTT) in the last years, i.e. [22]. The main part of the chain is the CFD code FLOWer, which is complemented by different pre- and post-processing tools. The CFD code FLOWer was developed by the German Aerospace Center (DLR) within the MEGAFLOW project [23] in the late 1990s. It is a compressible code and solves the three dimensional, Navier-Stokes equations in an integral form with several turbulence models. The numerical scheme is based on a finite-volume formulation for block-structured grids. For the spatial discretization, a second order central discretization with artificial damping, Jameson-Schmidt-Turkel (JST) [24] method, and the 5th order weighted essentially non-oscillatory scheme WENO [25] are available. Time integration is accomplished by an explicit multi-stage scheme. Time accurate simulations use the dual time stepping method as implicit scheme. The pseudo time iterations can be accelerated with the same methods as steady computations.

To close the Navier-Stokes equation several RANS and hybrid RANS/LES turbulence models, were implemented in FLOWer. The turbulence model equations are solved separately from the main flow equations using a full implicit time integration method. The ROT module allows body motions in translating/rotating reference frames for unsteady wind turbine simulations. FLOWer is optimized for parallel computing and uses Message-Passing Interface (MPI).

2.4.1 Mesh

The blade geometry of the 10MW AVATAR research wind turbine is used. The radius of the blade is 102.88m and since only the rotor is simulated without nacelle

and tower, the three blades are simply connected in the root region (Figure 2.2b) with a connector. All structures are treated as rigid in all cases. To resolve ambient turbulence, block structured meshes were generated separately for the blade and background, and they were combined without sacrificing the quality of the meshes by using the Chimera overlapping grid technique [26] as shown in Figure 2.2a. A blade mesh convergence test was performed in a previous study [27]. Three different resolutions of the blade mesh were examined. The values of power and thrust for the medium and the fine grids are very close with extrapolated relative errors of less than 0.5%. Considering the computational cost and the solution accuracy, the medium grid was chosen and used in all the simulations presented in this paper. The blade mesh is a C-type mesh with $[280 \times 128 \times 192]$ grid cells in the chord, wall-normal and span-wise directions [27]. The first wall-off cell size is less than 3×10^{-6}m, which satisfies the condition $y_1^+ < 1$. Compared to the AVATAR project a new background mesh was created in VortexLoads. A uniform mesh was applied with 1m resolution at which ambient turbulence needs to be resolved [28]. The 1m resolution extends up to 512m downstream from the rotor, see Figure 2.3. A coarsening of the mesh towards the domain boundaries was applied to reduce the mesh size ($\sim$88.8 million cells). The domain size was set to $[3584 \times 1792 \times 1792]$ m^3 in the stream-wise (x) and two crossflow (y, z) directions. The rotating axis was aligned with the x axis and located at the origin, which was at a distance of 1536m from the inlet boundary. The total number of cells for simulations with the rotor were 123.5×10^6.

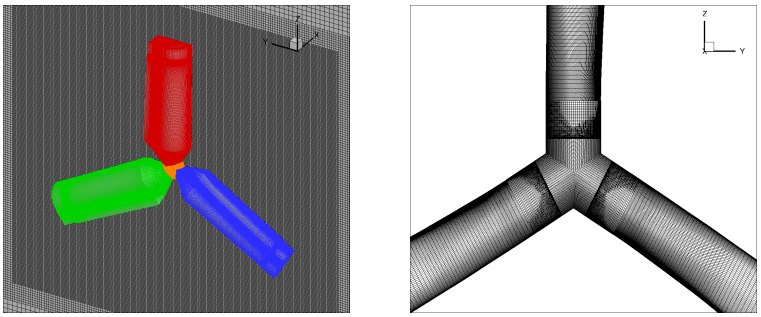

(a) Chimera meshes (b) Connector shape

Figure 2.2: Mesh topology of a) Chimera meshes of blades and connector and b) shape of connection in blade root region.

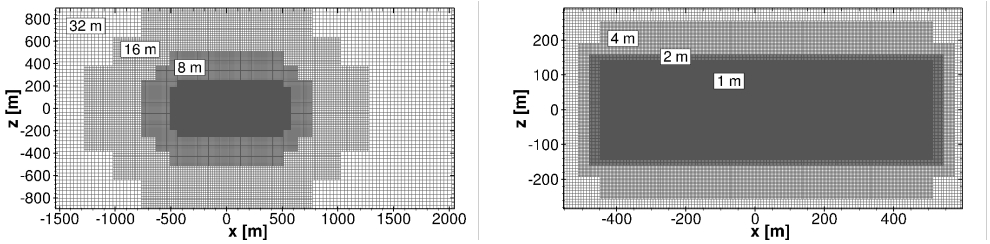

(a) Overall domain (slice at $y = 0$) (b) Refinement (slice at $y = 0$)

Figure 2.3: Mesh topology of a) background mesh for overall view and b) local refinement for turbulence propagation.

2.4.2 CFD setup

A no-slip wall condition was used on the blade surface without any wall function and a far field condition was applied in the cross flow directions, i.e. y, z. A uniform

velocity and constant pressure were set at the inlet and outlet boundaries respectively. For the current task the Menter SST $k-\omega$ [29] based IDDES model [30] was adopted, and no transition model was considered, i.e. fully turbulent simulations were conducted. A second order dual time stepping method was adopted for the time discretisation and a five-stage Runge-Kutta scheme was used for every inner-iteration. The JST scheme was adopted for the blade meshes, and 5th order WENO scheme was adopted for the background mesh. The freestream air properties are density $\rho = 1.225\,\mathrm{kgm}^{-3}$, pressure $p = 101.3\,\mathrm{kNm}^{-2}$, temperature $T = 288.15\,\mathrm{K}$ and dynamic viscosity $\mu = 1.7879\mathrm{E}{-5}\,\mathrm{kgm}^{-1}\mathrm{s}^{-1}$.

In CFD an initialisation simulation is necessary for each case to propagate the turbulence from the injecting position at $x = -400\mathrm{m}$ to the rotor position. These simulations were conducted with a constant mean rotor speed $\omega_{initialisation}$ in [rpm] and pitch angle $\beta_{initialisation}$ (even for cases with controller). To also cover the wake and allow the induction effect to evolve properly, the simulation length of the initialisation T_{ini} varies slightly between the cases. It was ensured Blade 1 always pointed upwards at the end of the initialisation. Hence, T_{ini} was a multiple of $60/\omega_{initialisation}$ for each case.

For the initialisation simulation the time step is $\Delta t \approx 2^\circ$ with 45 inner iterations according to the AVATAR baseline setting [31]. A detailed analyses of a case with $u_\infty = 10.5\mathrm{m/s}$ (AVATAR case *10.5LOW* [31]) revealed that more inner iterations or a smaller time step slightly alter the results, exemplarily depicted for thrust F_x in Figure 2.4a. Especially the time offset visible at the peaks is important with regard to the objective of a time alignment to BEM. Figure 2.4b shows the residuals which emphasis the better converged results with a smaller time step.

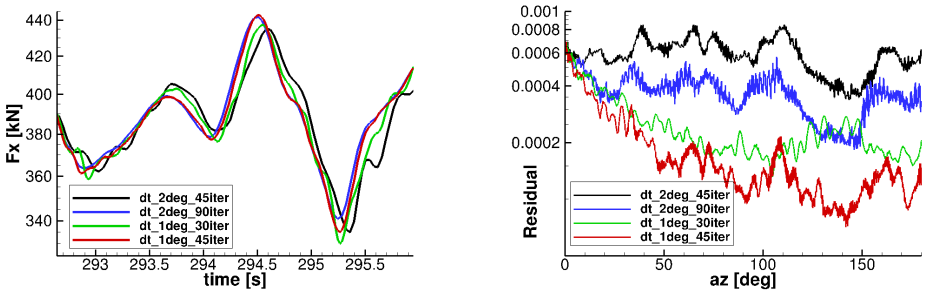

(a) Thrust F_x (b) Residual

Figure 2.4: Influence of number of inner iterations and time step on results.

Therefore, after the initialisation the time step was halved to be approximately 1° azimuthal variation of the blades per time step for the actual simulation and recording of the loads. The reference rotation speed to quantify the time step is taken from the controller for an uniform inflow with the desired mean inflow velocity u_{avg}. The loads according to the sensor list in appendix A were recorded for a duration of T_{sim}.

3 Comparison in uniform constant inflow

Before a comparison in turbulent inflow condition is made, a benchmark is made by comparing CFD against lifting line simulations in uniform, constant axial inflow conditions. This will allow for cross checking of the absolute value of the load level predictions between the codes and to streamline the input (rotor definition) and output (comparison variables). For this purpose, CFD simulations from University of Stuttgart from the EU AVATAR project have been used. First a description of the cases is given, after which the results are presented.

3.1 Case description

The 205.76 m diameter AVATAR rotor was used for the comparison round, which is described in more detail within the EU AVATAR project [32]. Essentially this is a low-induction rotor, featuring an axial induction factor of around 0.2 in normal operational conditions. The version of the rotor taken for this comparison features no tilt, no cone (pure axial inflow) and no consideration of tower effects. The rotor is assumed to be rigid. The blade planform for the lifting line simulations was deduced from the 3D CAD model. To be consistent with the CFD simulations from University of Stuttgart, the airfoil data prescribed for the lifting line simulations is deduced from post-processing 3D rotating CFD simulations (from University of Stuttgart as well) using the inverse BEM method. As such the use of 3D rotational augmentation models was precluded for the lifting line simulations. Since the inverse BEM method contains a correction to account for the finite number of blades (Prandtl effect), which is implicitly modeled in vortex codes, 2D CFD simulations were used to obtain lift and drag polars for the outboard sections (r/R>0.65).

Four cases were simulated following part of the power curve, as summarized in Table 3.1. A more detailed description of the conditions and the data format and variable definition can be found in appendix A. All variables are displayed as supplied. An exception lies in the axial force and torque which are post-processed to thrust and power coefficients Cd_{ax} and Cp using

$$Cd_{ax} = \frac{\text{Fax}}{0.5\rho {U_\infty}^2 \pi R^2}, \quad Cp = \frac{\text{Torque} \quad \omega}{0.5\rho {U_\infty}^3 \pi R^2}, \quad \text{with}$$

Cd_{ax}	[-]	Axial force coefficient
Cp	[-]	Power coefficient
Fax	[N]	Rotor axial force
Torque	[Nm]	Rotor torque
ω	[rad/s]	Rotor speed
ρ	[kg/m^3]	Air density
U_∞	[m/s]	Wind speed
R	[m]	Rotor radius

The legend of each graph refers to the parties and their codes that were used to perform the simulations. The model description corresponding to the legends can be found in chapter 2.

3.2 Results

The resulting load comparison is given in Figures 3.1 and 3.2 for normal and tangential force distributions respectively, plus the deduced integral aerodynamic variables axial

Table 3.1: Uniform inflow comparison cases

Wind speed U_∞ [m/s]	Pitch angle [°]	Rot. speed [rpm]	Tip speed ratio λ [-]	Angle of attack $\alpha^\dagger$@80%R [°]	Axial ind. factor a†@80%R [-]
4.0	0.0	6.0000	16.2	-1.0	0.28
5.0	0.0	6.0000	12.9	-0.1	0.25
6.0	0.0	6.0000	10.8	0.9	0.23
8.0	0.0	6.8738	9.3	1.9	0.21

† estimate

force, flapwise bending moment and torque. It is observed that generally speaking a good agreement is found between lifting line and CFD simulations. Also we can see that, although the differences are small in absolute sense, the treatment of the transition section of the blade (r<20 m) is not uniform between the codes resulting in scatter of the tangential force plots. However, the implication of these differences is small for the (fatigue) load application, which is the main subject of the current project.

It should be mentioned that the plots shown here are the result of a number of iterations between the participants, which featured some lessons learned in the light of guidelines for the usage of vortex wake codes in design (WP5). Here one can think of the number of specified wake points, radial spacing, but also airfoil data interpolation in spanwise direction.

To facilitate observations between different code types (BEM and vortex wake models), the supplied results have been averaged over the participants per code type. For BEM, the results of Bladed4.8-BEM, ECNAero-BEM and WMC-Phatas are used. For the vortex wake code only the free wake codes are taken, i.e. Bladed4.8-VL and ECNAero-AWSM. To obtain the loading averages, first the normal and tangential force are determined at 12 specified spanwise positions (r/R=0.1, 0.2, 0.3, 0.4, 0.5, 0.6, 0.7, 0.8, 0.9, 0.925, 0.95, 0.975) using linear interpolation from the supplied radial distributions. A simple average $\overline{x}$ is determined using

$$\overline{x} = \frac{1}{n}\sum_{i=1}^{n}(x_i) \quad .$$

In addition to that, to give an indication of the variability between the results, a partly transparent band is plotted around the average of each code type illustrating the standard error x_{err} between the supplied results of a code type

$$x_{err} = \sqrt{\sum_{i=1}^{n}\frac{(x_i - \overline{x})^2}{n(n-1)}}.$$

The resulting graphs are shown in Figures 3.3 and 3.4. For the uniform inflow cases under consideration, the differences between BEM and vortex wake model are very limited. For high tip speed ratios, vortex codes seem to predict a slightly higher normal force in the outboard part of the blade. It is unclear at this point whether this is due to a shortage of specified wake points in the vortex codes, or the fact that these code account for wake expansion (which is not modeled in BEM). In agreement with Figure 3.2, Figure 3.4 shows high variability within a code type for the inboard tangential force prediction.

Concluding it can be stated that generally speaking a good agreement is found between lifting line and CFD simulations, which is a prerequisite for a successful comparison of unsteady aerodynamics in turbulent inflow conditions.

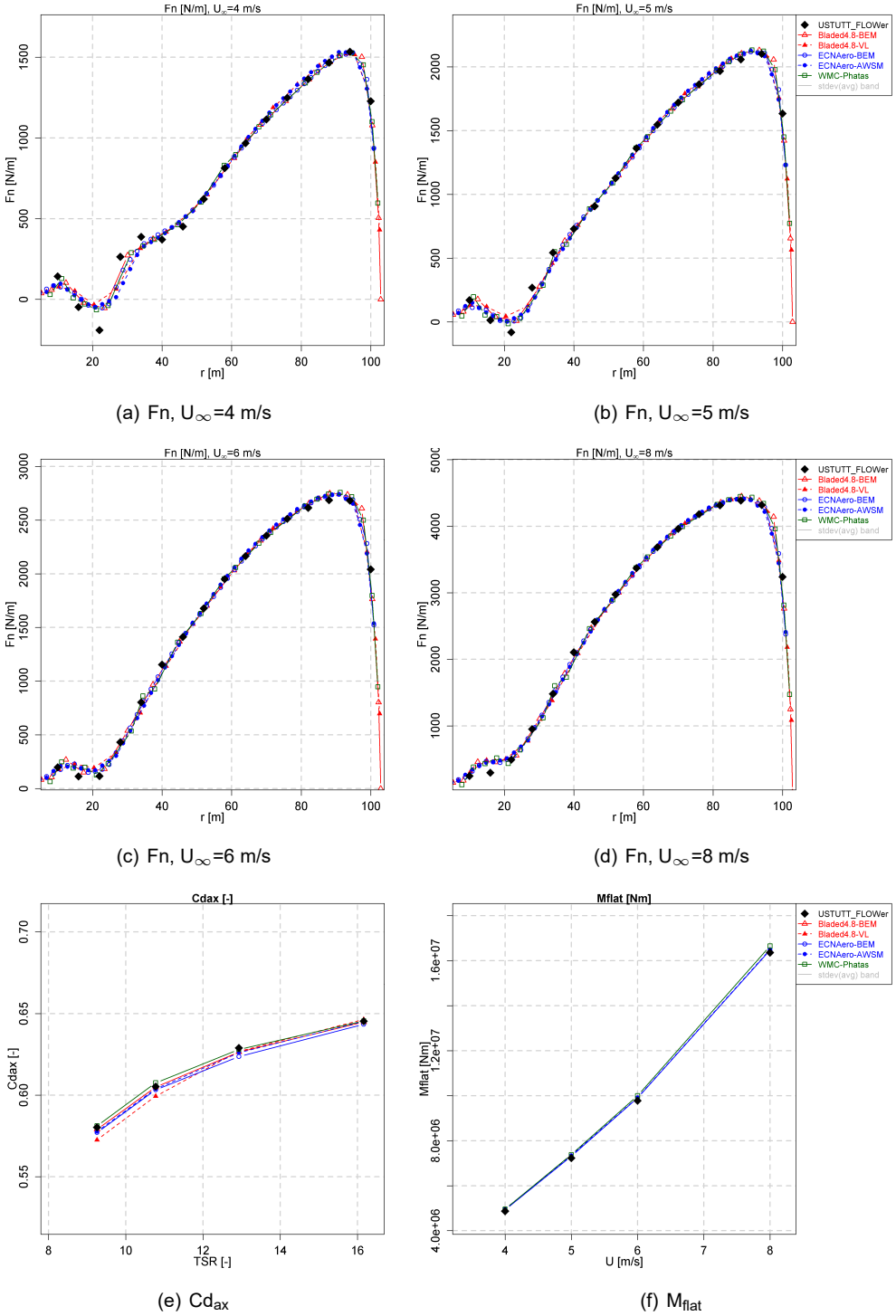

(a) Fn, U_∞=4 m/s

(b) Fn, U_∞=5 m/s

(c) Fn, U_∞=6 m/s

(d) Fn, U_∞=8 m/s

(e) Cd_{ax}

(f) M_{flat}

Figure 3.1: Load comparison in uniform inflow (1)

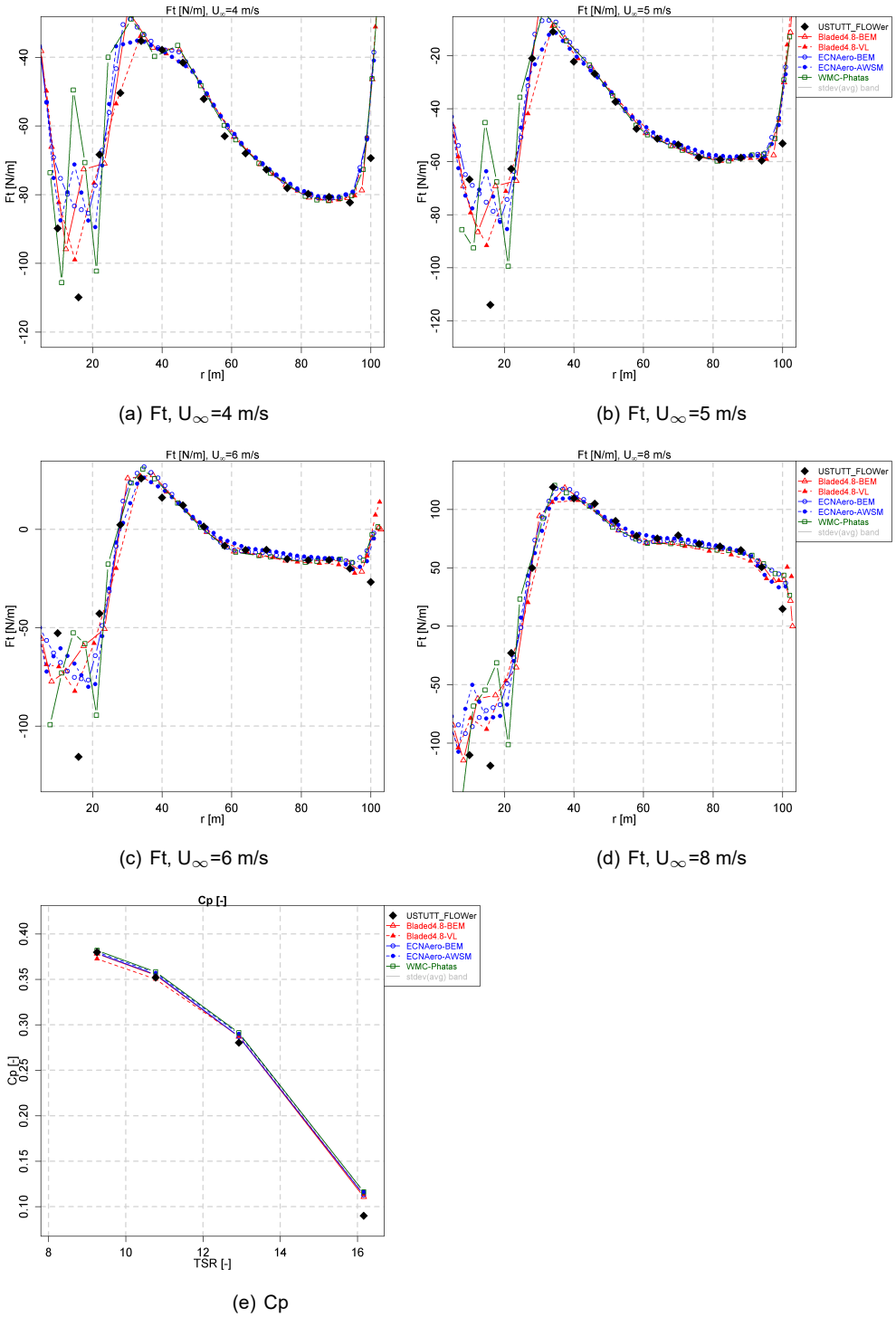

(a) Ft, U_∞=4 m/s

(b) Ft, U_∞=5 m/s

(c) Ft, U_∞=6 m/s

(d) Ft, U_∞=8 m/s

(e) Cp

Figure 3.2: Load comparison in uniform inflow (2)

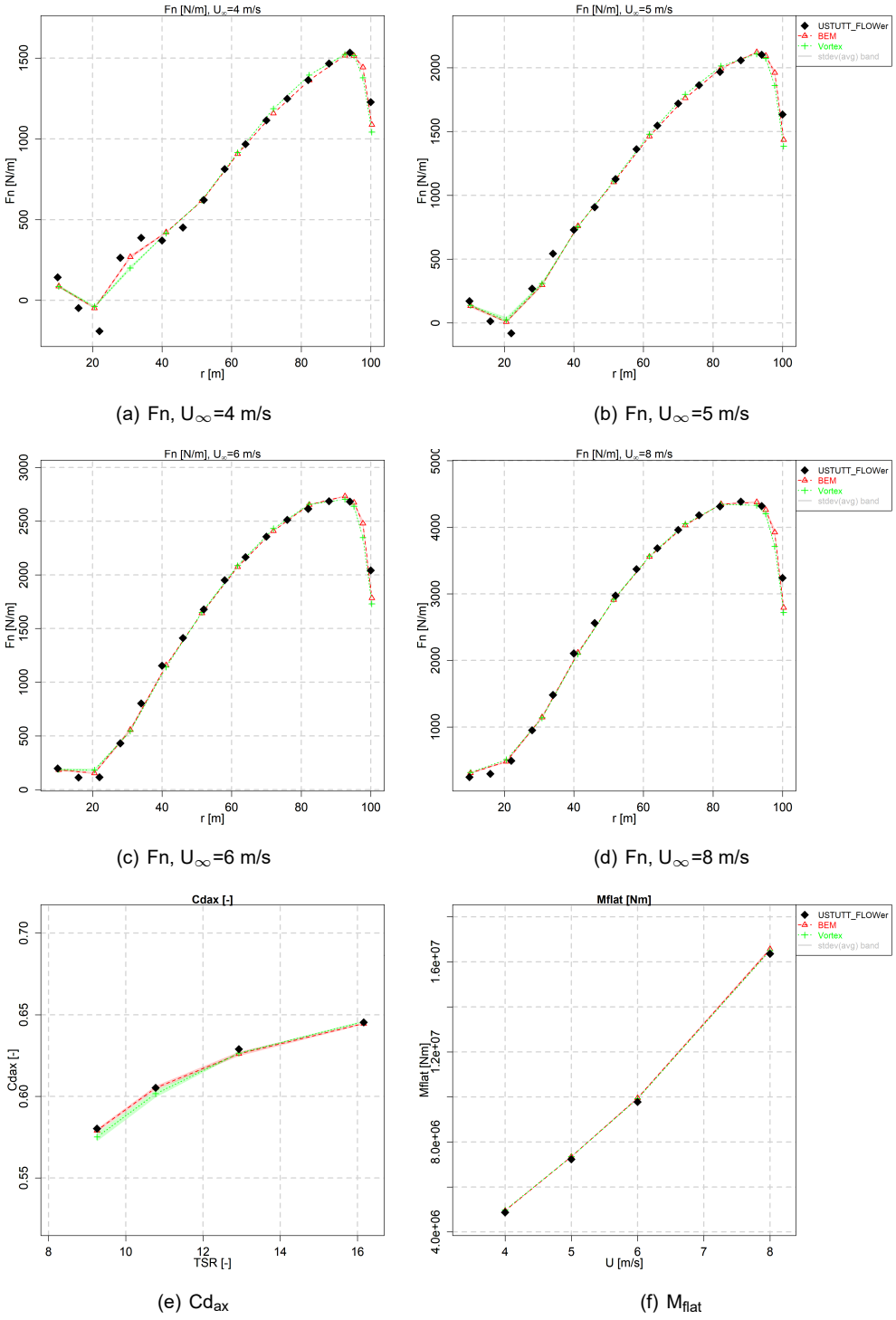

(a) Fn, U_∞=4 m/s

(b) Fn, U_∞=5 m/s

(c) Fn, U_∞=6 m/s

(d) Fn, U_∞=8 m/s

(e) Cd_{ax}

(f) M_{flat}

Figure 3.3: Load comparison per code type in uniform inflow (1)

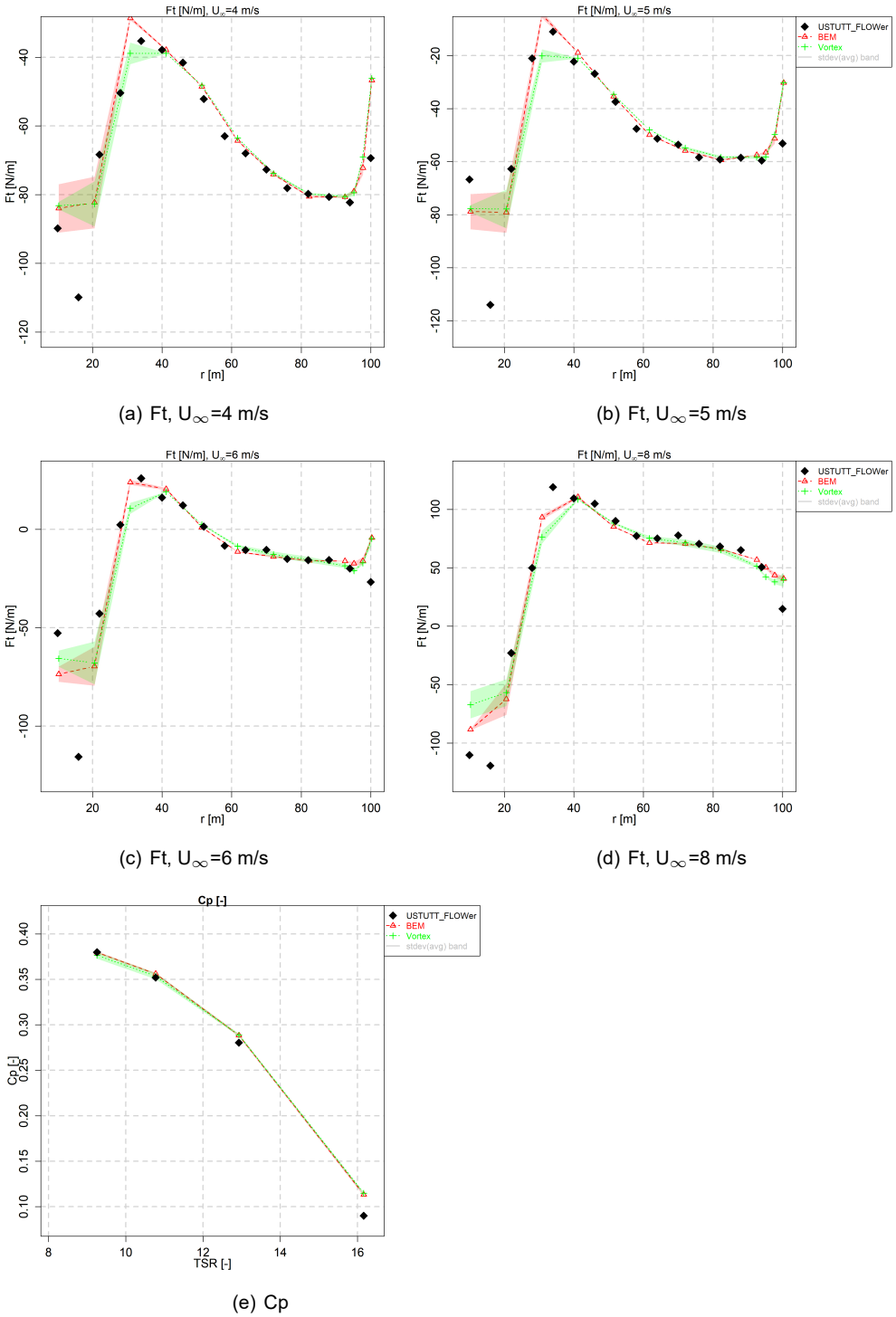

(a) Ft, U_∞=4 m/s

(b) Ft, U_∞=5 m/s

(c) Ft, U_∞=6 m/s

(d) Ft, U_∞=8 m/s

(e) Cp

Figure 3.4: Load comparison per code type in uniform inflow (2)

4 Comparison in sheared inflow

As an intermediate step to increased complexity it was decided to include a comparison round in sheared inflow. A sheared case features non-uniform inflow across the rotorplane like turbulent inflow, albeit in a deterministic way. In fact, sheared inflow can be thought of as a large turbulent 'eddy' through which the blades slice periodically. Thus this case allows to study the dynamic response to non-uniform inflow conditions in a more controlled way. For this purpose, CFD simulations from University of Stuttgart from the EU AVATAR project have been used. First a description of the cases is given, after which the results are presented.

4.1 Case description

The same turbine definition is used as for the uniform inflow case. Two cases were simulated, as summarized in Table 4.1. As we are comparing the variation of rotor aerodynamic variables along the rotor revolution, a different file format was used with various variables stored in columns as a function of time. A more detailed description of the data format and variable definition can be found in appendix A.

Table 4.1: Sheared inflow comparison cases

Wind speed U_∞ [m/s]	Pitch angle [°]	Rot. speed [rpm]	Shear expon. [-]	Tip speed ratio λ [-]	Angle of attack $\alpha^\dagger$@80%R [°]	Axial ind. factor a†@80%R [-]
10.5	0.00	9.0218	0.2	9.26	1.7	0.20
14.0	6.06	9.6000	0.2	7.39	-1.4	0.04

† estimate of average over rotor revolution

4.2 Results

For the 10.5 m/s case, Figure 4.1(a) and 4.1(b) show the azimuthal variation of the encountered wind at 30%R and 95%R of the blade respectively due to the shear. The agreement between the codes indicates that the wind shear definition has been consistent between the codes. Looking at the flapwise blade root moment variation in Figure 4.1(c) we can observe differences between the predicted amplitudes of the codes. These differences grow larger for the chord normal and tangential forces in Figure 4.2, and even larger for the underlying axial induced velocities in Figure 4.3 where the scatter is enormous for the tangential induced velocities in the same Figure. For the latter, the vortex type codes seem to predict a rather different trend opposed to the BEM type codes. Here it is noted that 'lifting line variables' such as angle of attack and induced velocities are not available for the CFD results and hence are not displayed.

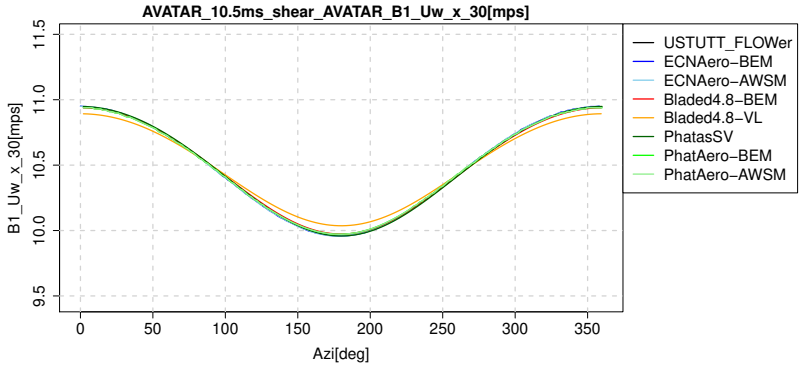

(a) Uw$_x$, 30%R

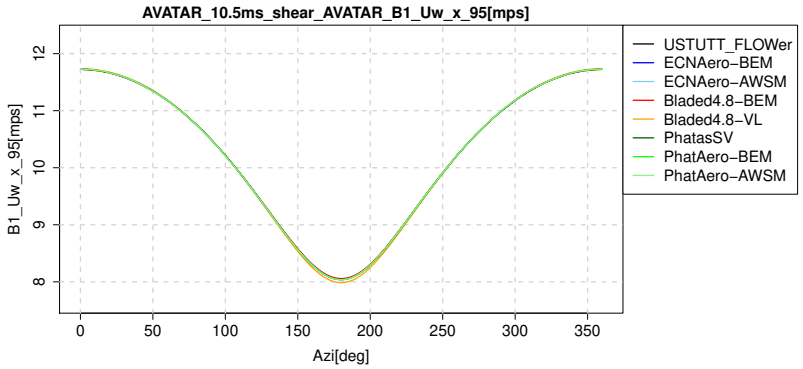

(b) Uw$_x$, 95%R

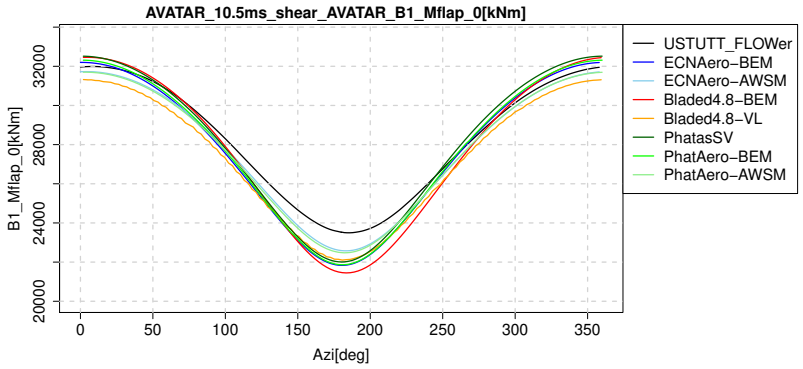

(c) Mflap

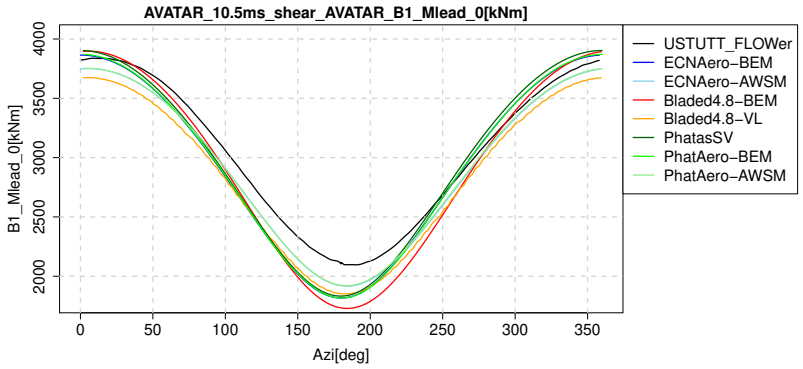

(d) Mlead

Figure 4.1: Azimuthal variation in shear of wind speed and blade root moments, U$_\infty$=10.5 m/s

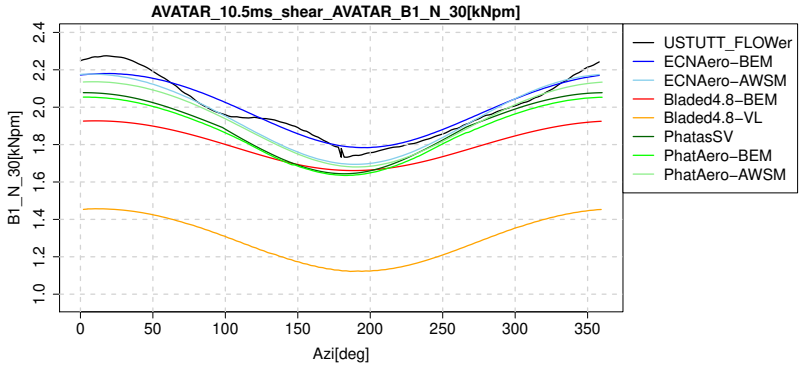

(a) N, 30%R

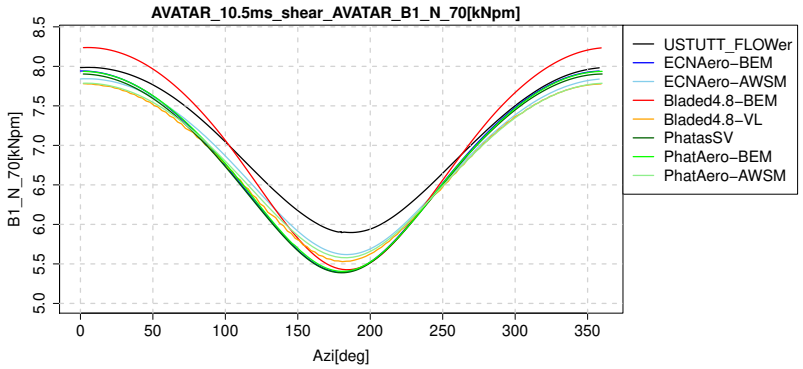

(b) N, 70%R

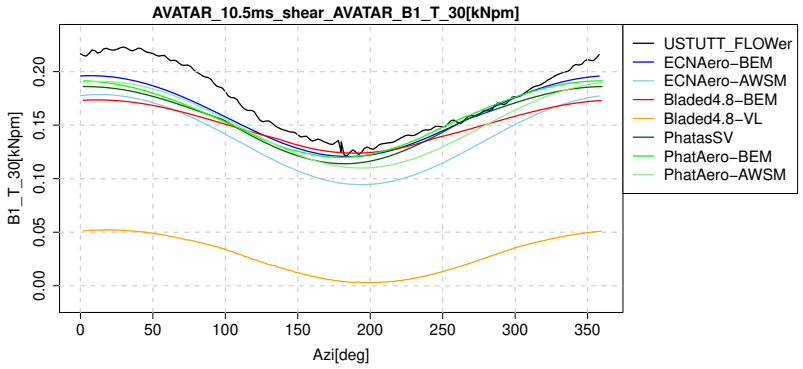

(c) T, 30%R

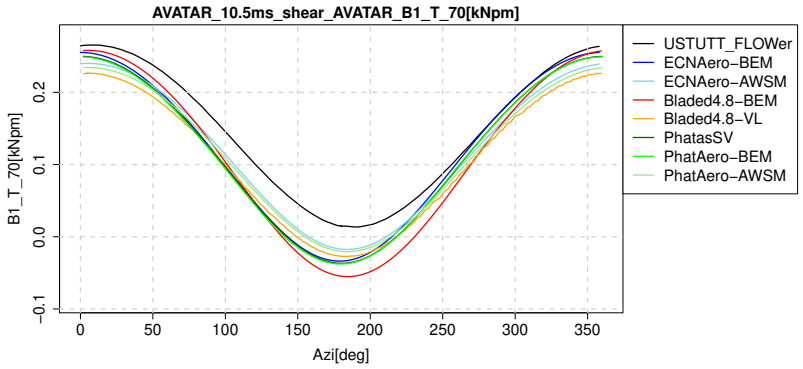

(d) T, 70%R

Figure 4.2: Azimuthal variation in shear of distributed loads, U_∞=10.5 m/s

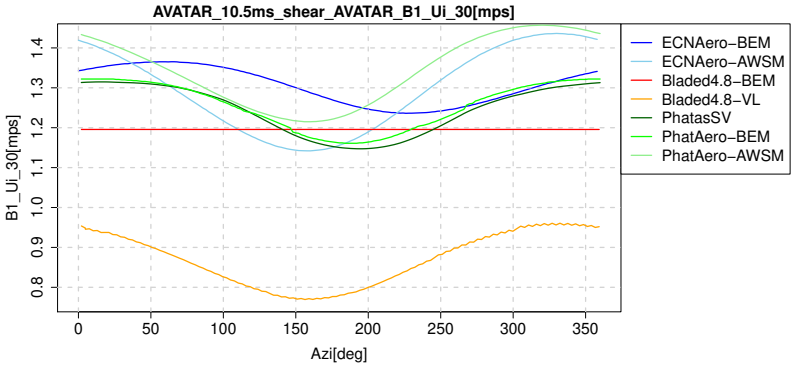

(a) Ui, 30%R

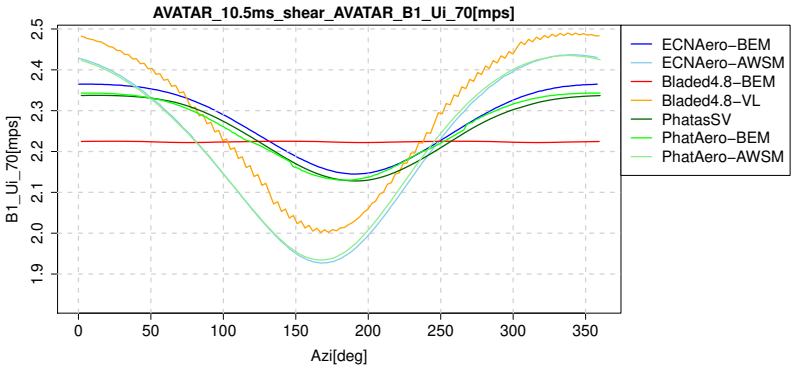

(b) Ui, 70%R

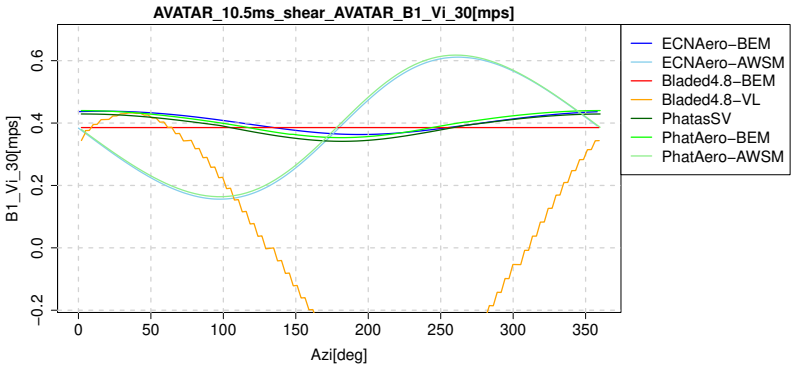

(c) Vi, 30%R

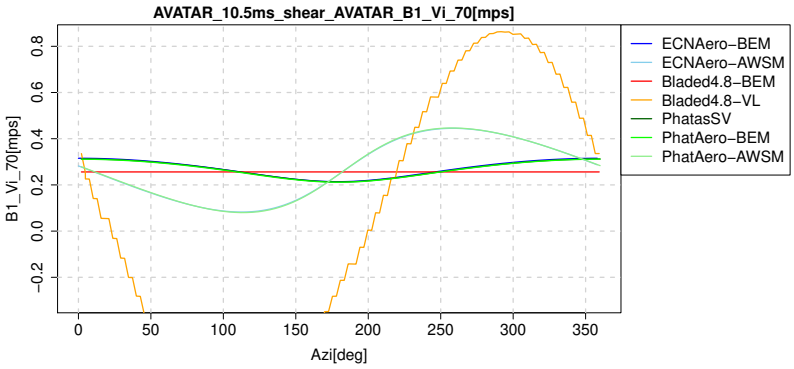

(d) Vi, 70%R

Figure 4.3: Azimuthal variation in shear of rotor induced velocities, U_∞=10.5 m/s

To better observe the differences the simulation results are post-processed to average values and amplitudes (by evaluating the difference between maximum and minimum values) of the fluctuation along a rotor revolution. The results in Figure 4.4 show that generally speaking the codes are in good agreement with respect to their mean values, albeit not as a good as the agreement for the uniform constant inflow comparison from chapter 3. On top of the colored bars, the grey dotted lines indicate the maximum and minimum value, where the black lines are an indicator for the standard deviation of the underlying time series. Figure 4.5 shows the results of the amplitude comparison and here we do observe a striking difference between vortex and BEM type codes. The BEM type codes systematically over predict the amplitudes of the flapwise blade root moment in comparison to the CFD and vortex wake results (that are in relatively good agreement). Zooming in on the normal force distribution (Figure 4.4(b)), which is the driving contribution to this moment, this difference is consistent along the blade span except for the most inboard station at 30%R. The difference can be traced back to the angle of attack and the underlying axial induced velocity variation, which can be considered as the 'heart' of lifting line models. For the vortex codes, the axial induced velocity follows more extremely the inflow velocity variations as the blades rotate through the sheared velocity field. Between the BEM codes it can also be observed that where some of them predict a substantial azimuthal variation of axial induced velocity, there are also BEM results where this azimuthal variation along a rotor revolution is almost negligible. It is known that a wide variety of BEM implementations exist, e.g. solving the momentum equations for a whole annulus or per element, not to mention the interaction with a dynamic wake or dynamic inflow model. This example illustrates the effect these implementation differences can have. For the cases under consideration it was verified that for the Aero Module results switching off the dynamic inflow model had a negligible effect on the predicted load amplitudes.

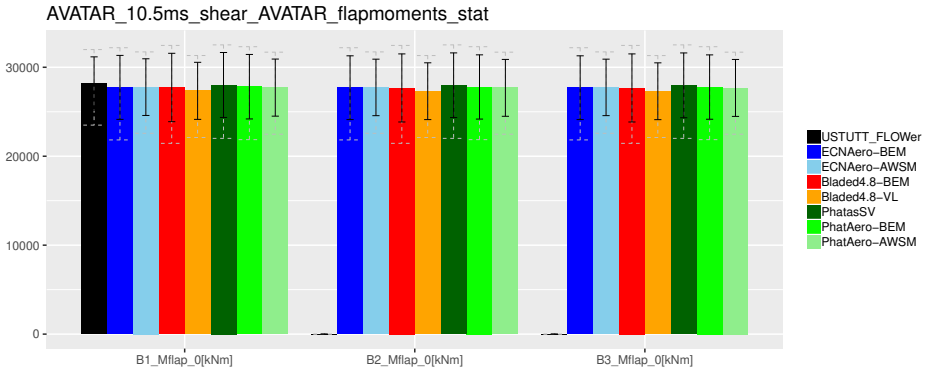

(a) Mflap

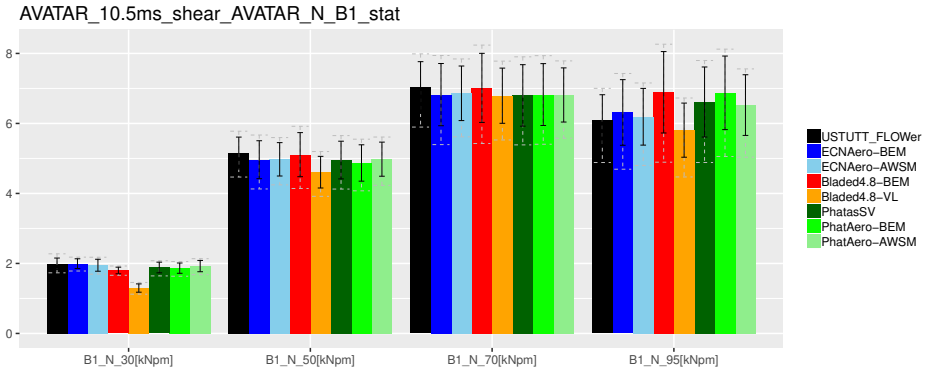

(b) N

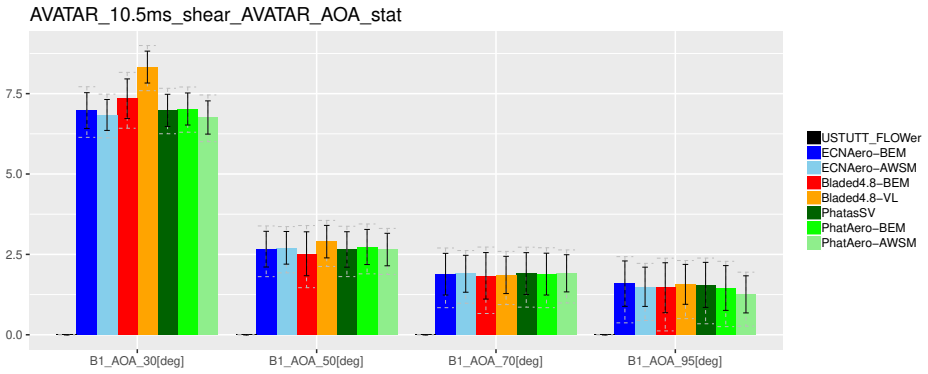

(c) AOA

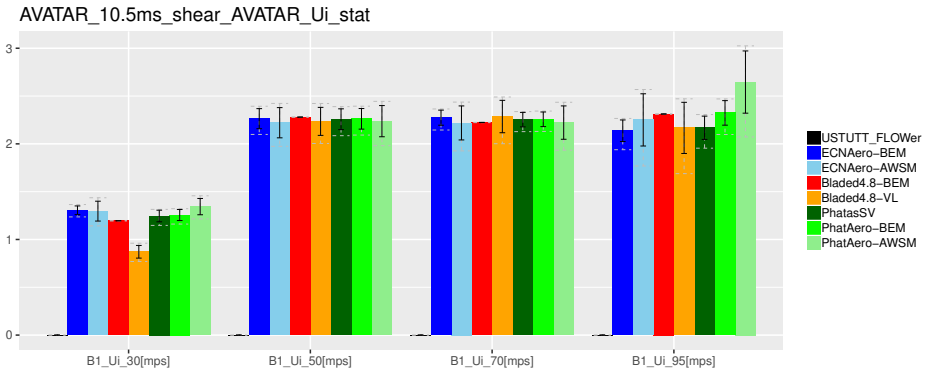

(d) Ui

Figure 4.4: Average values in shear, U_∞=10.5 m/s

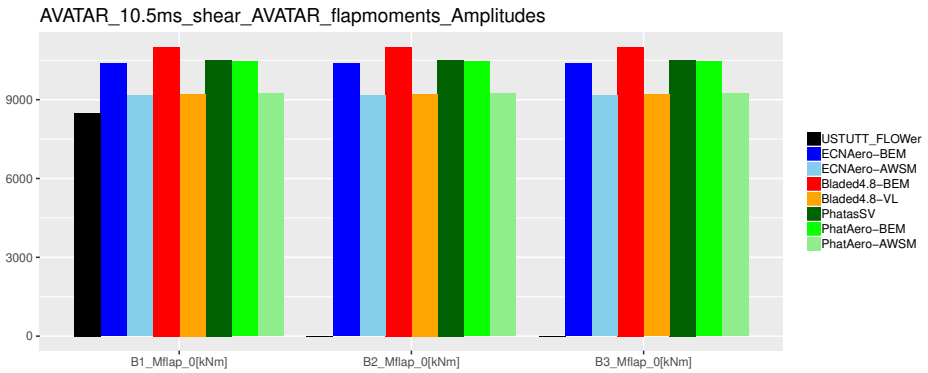

(a) Mflap

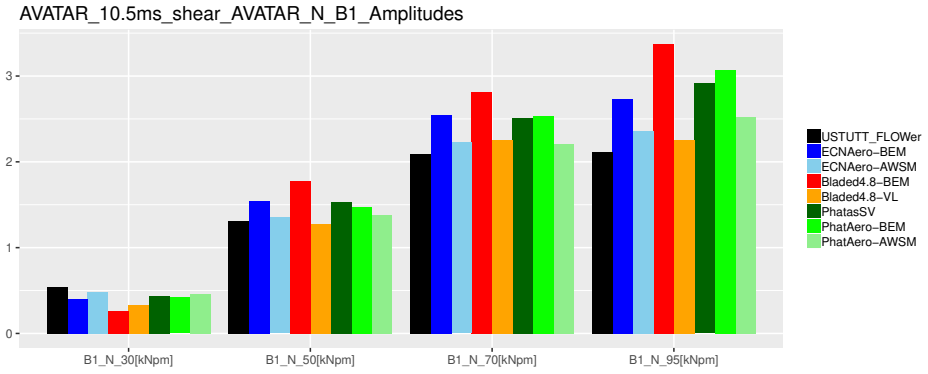

(b) N

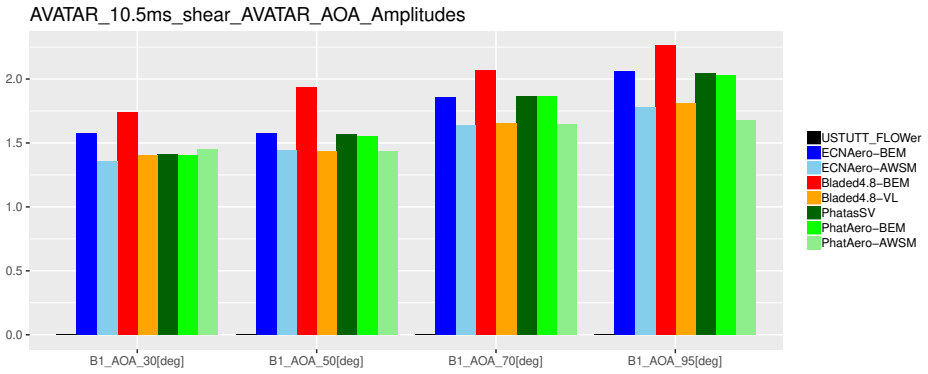

(c) AOA

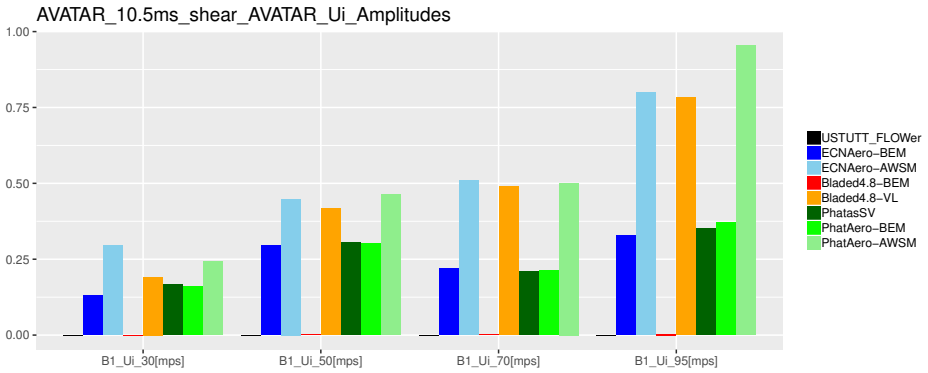

(d) Ui

Figure 4.5: Apmlitudes in shear, U_∞=10.5 m/s

The corresponding 14 m/s results are shown in Figure 4.6 and 4.7. As indicated in Table 4.1, the angle of attack and axial induced velocity factor are significantly lower for this case which can also be observed in the averaged value plot. As such it is noted that this is a full load case featuring a relatively low thrust coefficient. Similar to the 10.5 m/s case the averaged values are largely in agreement between the BEM, vortex and CFD codes. For the amplitudes, also here a systematic difference between BEM and vortex type codes can be observed, where this difference is relatively smaller in comparison to the 10.5 m/s case.

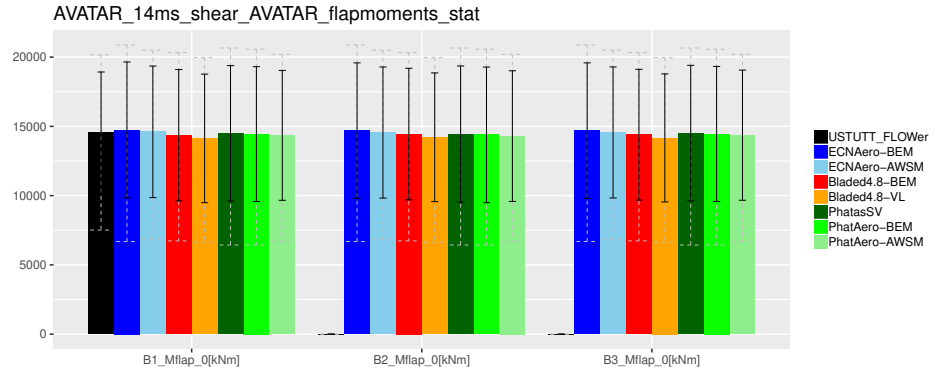

(a) Mflap

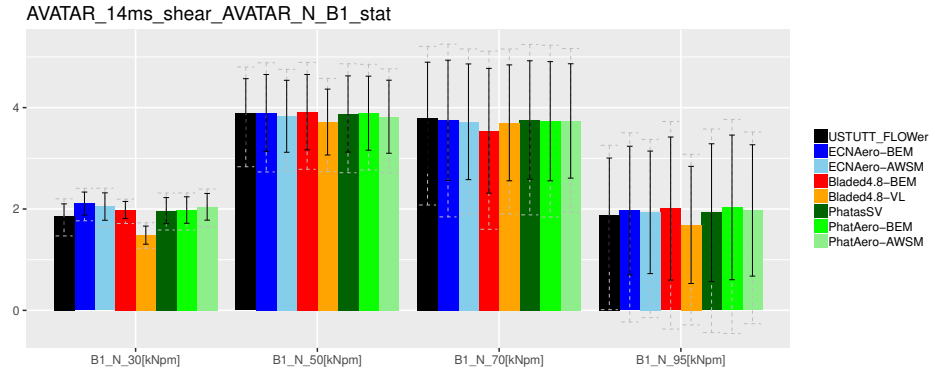

(b) N

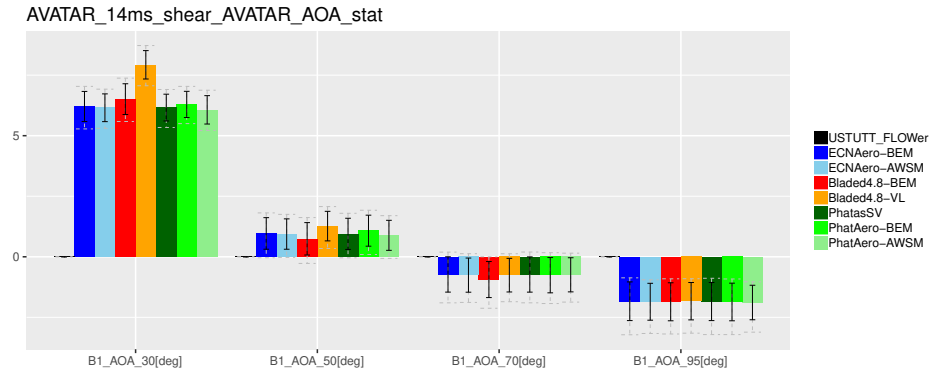

(c) AOA

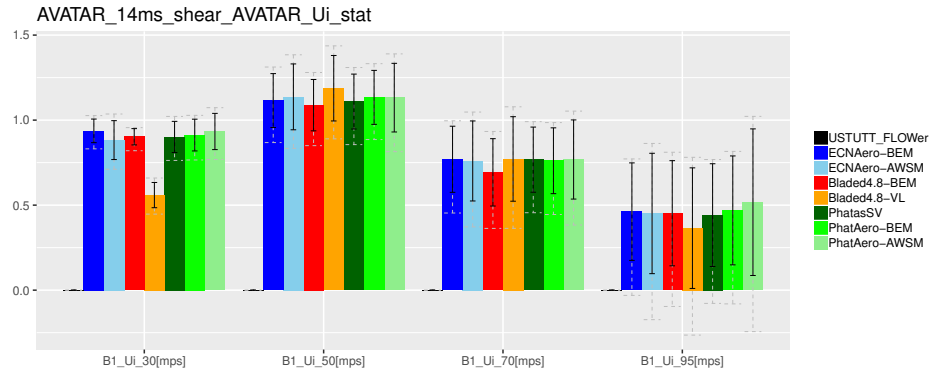

(d) Ui

Figure 4.6: Average values in shear, U_∞=14 m/s

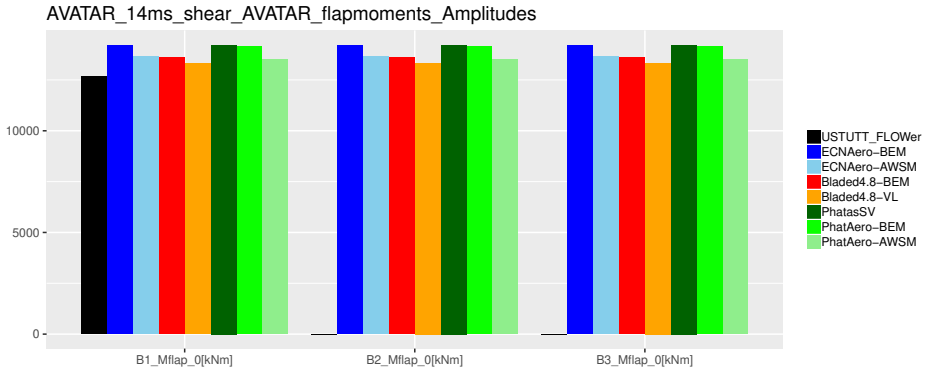

(a) Mflap

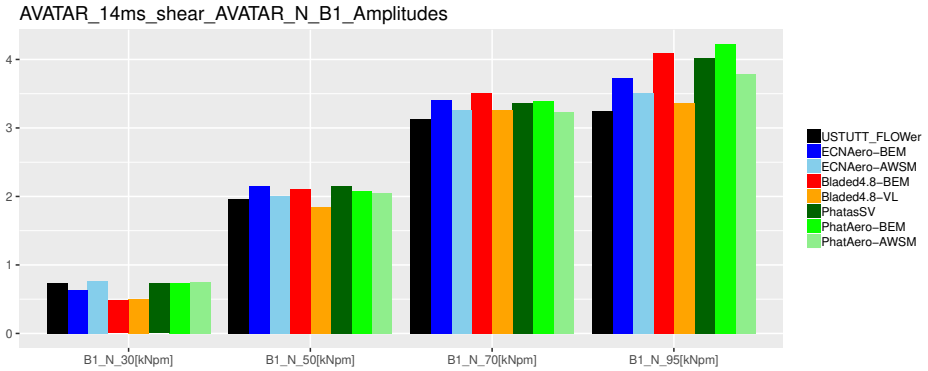

(b) N

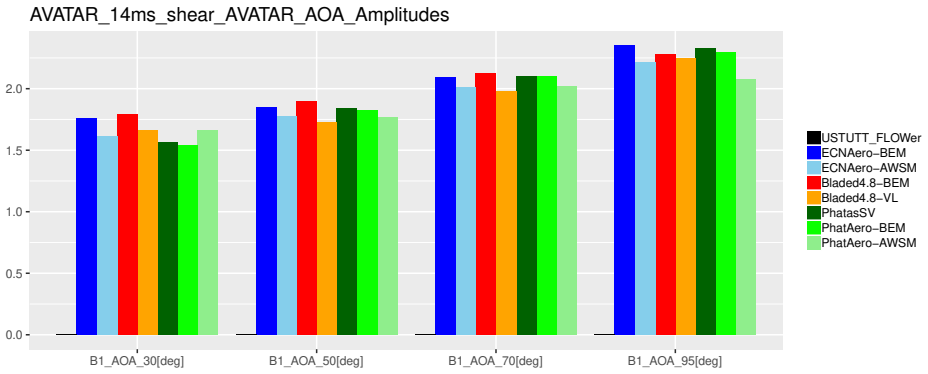

(c) AOA

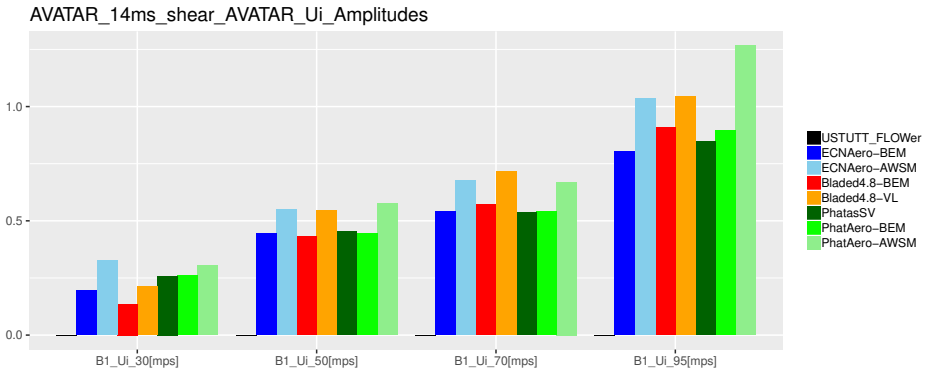

(d) Ui

Figure 4.7: Apmlitudes in shear, U_∞=14 m/s

4.3 Parametric investigation of observed difference

The above results for vertical shear showed that calculations with BEM type codes show stronger periodic load variations than calculations with vortex wake codes. In search of a fundamental reason for this different behaviour, calculations were done for various conditions with the Phatas and PhatAero code. These conditions also include 2-bladed and 4-bladed versions of the AVATAR rotor. For the 2-bladed rotor models the chord distribution is simply 1.5 times larger compared to the chord distribution of the 3-bladed rotor. The 4-bladed rotor model has 75% of the chord distribution compared to the 3-bladed rotor. This ”scaling” gives a similar rotor disk loading except near the blade tip. For all configurations the solidity of the rotor is 0.0408. Table 4.2 shows that for all operational conditions the 1P variation of the blade root flap moment from the BEM based calculations is larger than from the AWSM calculations. This seems to be related with the axial induction factor, see also Figure 4.8, in which results from several extra high induction cases are added. Although the values of the axial induction factor are not distributed homogeneously, a nearly linear trend follows of the ratio between blade root flapwise bending moment variation from BEM simulations compared to the vortex wake (AWSM) simulations. The ratio between root moment variations shows to be quite insensitive to the number of rotor blades, c.q. the distance between the vortex sheets of the blades. The relative ’over estimation’ of the BEM based calculations is a bit larger for the program Phatas, in particular for the sub-rated wind velocity of 8.0 m/s (at induction factor of 0.17).

Table 4.2: Summary of parametric shear investigation

Hub wind speed [ms]	Nr of rotor blades [-]	Rotor speed [-]	Pitch angle [°]	Tip speed ratio [-]	Axial induct factor [-]	Blade vortex dist [m]	Δ Mflap PhatAero AWSM [kNm]	Δ Mflap PhatAero BEM [kNm] [%]†	Δ Mflap Phatas [kNm] [%]†
6.0	2	6.0000	0.00	10.8	0.18	24.7	5040	5776 +14.6%	5805 +15.2%
6.0	3	6.0000	0.00	10.8	0.18	16.4	3446	3932 +14.1%	3956.3 +14.8%
6.0	4	6.0000	0.00	10.8	0.18	12.3	2621	2973 +13.4%	2988.5 +14.0%
8.0	2	6.8738	0.00	9.3	0.17	29.0	7836	8952 +14.2%	9210 +17.5%
8.0	3	6.8738	0.00	9.3	0.17	19.3	5374	6083 +13.2%	6228 +15.9%
8.0	4	6.8738	0.00	9.3	0.17	14.5	4062	4574 +12.6%	4708 +15.9%
10.5	3	9.6000	0.00	9.9	0.17	18.1	9757	11087 +13.6%	11214 +14.9%
10.5	2	9.0218	0.00	9.3	0.17	29.0	13477	15385 +14.2%	15497 +15.0%
10.5	3	9.0218	0.00	9.3	0.17	19.3	9223	10443 +13.2%	10545 +14.3%
10.5	4	9.0218	0.00	9.3	0.17	14.5	7021	7898 +12.5%	7973 +13.6%
10.5	3	9.0218	4.70	9.3	0.05	22.1	9267	9667 +4.3%	9771 +5.4%
12.0	3	9.6000	1.50	8.6	0.13	21.8	11363	12413 +9.2%	12525 +10.2%
14.0	2	9.6000	6.06	7.4	0.05	41.6	20081	21110 +5.1%	21172 +5.4%
14.0	3	9.6000	6.06	7.4	0.05	27.7	13756	14363 +4.4%	14471 +5.2%
14.0	4	9.6000	6.06	7.4	0.05	20.8	10421	10768 +3.3%	10864 +4.3%
16.0	3	9.6000	7.20	6.5	0.05	31.8	15971	16660 +4.3%	16761 +4.9%
18.0	3	9.6000	6.06	5.7	0.06	35.1	17786	18720 +5.3%	18834 +5.9%
18.0	3	9.6000	9.40	5.7	0.03	36.3	18343	18999 +3.6%	19069 +4.0%

† relative difference w.r.t. PhatAero-AWSM

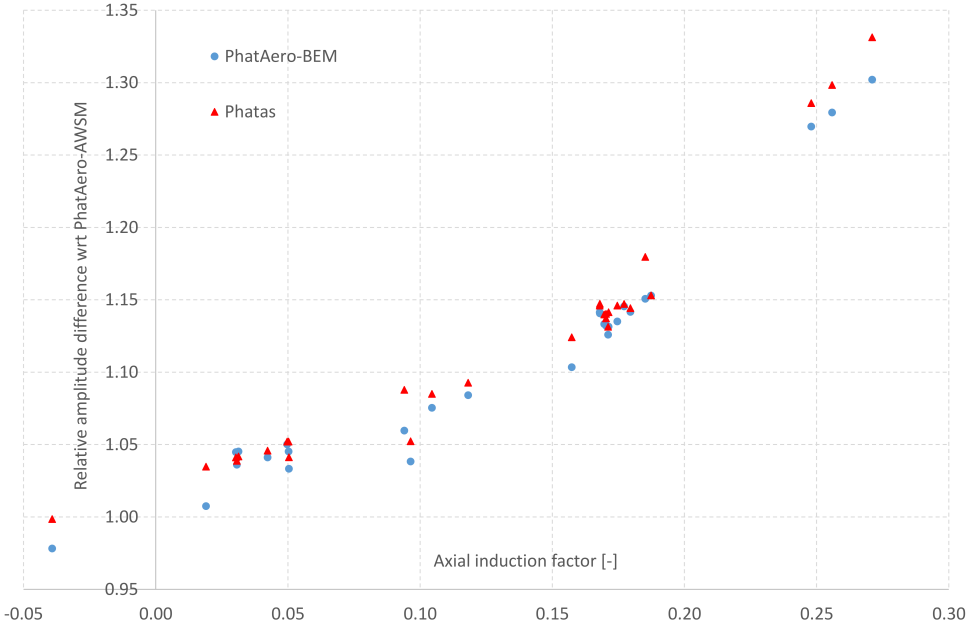

Figure 4.8: Relative difference of Mflap amplitudes in shear w.r.t. PhatAero-AWSM as a function of axial induction factor

5 Comparison in turbulent inflow

After exposing the differences between the codes in sheared inflow, the next step is a comparison in turbulent inflow. For this purpose dedicated CFD simulations from University of Stuttgart have been performed, see also the WP1 report of TKI WoZ VortexLoads [33]. First a description of the cases is given, after which the results are presented.

5.1 Case description

The same turbine definition is used as for the uniform and sheared inflow cases. Six cases were simulated, as summarized in Table 5.1. The same comparison format was used as for the sheared flow comparison, with various variables stored in columns as a function of time. A more detailed description of the data format and variable definition can be found in appendix A. To ensure everybody reads the turbulent wind

Table 5.1: Turbulent inflow comparison cases

Nr [-]	Case	Hub wind [m/s]	Turb. intensity [%]	Length scale [m]	Rot. speed [rpm]	Pitch angle [deg]	Wind seed [-]	Duration [s]
1	8ms_fixed	8	~23	33.6	6.87	0.0	205	400
2	8ms_prscrbd	8	~23	33.6	prscrbd	0.0	205	400
3	16ms_prscrbd	16	~17	33.6	prscrbd	prscrbd	205+offset	200
4	8msTI10_prscrbd	8	~10	33.6	prscrbd	0.0	205+scale	400
5	8msCt_prscrbd	8	~23	33.6	prscrbd+1.5	-1.5	205	400
6	8msL_prscrbd	8	~23	134.4	prscrbd	0.0	208	400

file in the same way and signal processing is in agreement amongst the partners, first an alignment study was performed using a 150 s simulation from the EU AVATAR project [31], which featured a constant pitch and rotational speed at an average hub height wind speed of 10.5 m/s. The cases summarized in Table 5.1 are defined in agreement with IEC Class 1A, where wind shear was excluded from the comparison. The first case featured a constant rotational speed and pitch angle at 8 m/s hub height wind speed. For the AVATAR turbine the class 1A specification leads to a rather high turbulence intensity of 23% and a length scale of 33.6 m. Seed selection and wind field duration follow from the specific studies reported in WP1 [33]. For the second case, a BEM simulation with the AVATAR controller activated was performed with the wind seed under investigation. The resulting rotational speed and pitch angle variations were recorded and fed to the CFD simulation. The same procedure was adopted for the other cases as well. Since the wind speed was below rated, the resulting pitch angle remained constant for this case at 0°. For the third case the same wind seed was used but the offset was increased to result in an average of 16 m/s hub height wind speed. Acknowledging that a wind seed turbulence box has a constant length, doubling the wind speed effectively means that the simulation duration is halved to 200s. In agreement with IEC Class 1A specifications, the wind speed fluctuations were scaled to match an average turbulence intensity of roughly 17%. For the fourth case, the influence of varying the turbulence intensity was investigated by scaling the amplitude of fluctuations for the same seed to approximately 10%. For the fifth case, the influence of an increased thrust coefficient or axial induction factor was

investigated. To this means an offset was applied to the rotational speed and pitch angle variation of the second case. This way the operating angle of attack was not significantly different from the second case and the spanwise variation of the averaged axial induction remained relatively constant. Finally for case six, the influence of a different length scale was investigated by increasing this parameter with a factor of four. The idea behind this case is to mimic the effect of rotor size by changing the turbulence length scale. It is anticipated that the rotational sampling will be different between small and larger rotors, influencing the coherence of the encountered wind gusts. For more info on the case description, please consult the dedicated Work Package 1 report from University of Stuttgart [33].

5.2 Results

The results of the various cases are discussed below. All of the underlying plots are given in appendix B. This appendix shows per case:

- Temporal variation, zoomed in around the time span featuring the largest load fluctuations to check alignment and behavior.
- Temporal variation, overview of the full time serie.
- Statistics (min / max / avg / std) over the full time serie.
- 1Hz Equivalent loading based on rainflow counting procedure, using a slope of m=11.
- Staircase plots obtained from rainflow counting.
- Power spectral density plot dividing the time series into 5 blocks (without overlap and window function) and a moving average function to smoothen the spectra.

5.2.1 Alignment

From the temporal variation of the virtual wind probes it can be observed that the alignment of wind conditions between CFD and lifting line codes as devised in WP1 [33] generally works quite well. Here it should be noted that the CFD probes are located a chord ahead of the leading edge and include local flow perturbation and bound vortex induced velocities, which are not present for the BEM and vortex results. The effect of these is mostly visible in the lateral and vertical directions. The offset observed in the hub height wind velocity is caused by the blockage included in the CFD simulation and a phase shift due to the fact that the CFD values are taken 7.1m upstream of the rotor center.

The time series of blade root moments and integral forces also indicate that the turbulence structures from empty box and rotor CFD are highly alike, providing similar fluctuations due to the rotational sampling. The forces at the local stations and in particular the fluctuations due to the smaller eddies feature more discrepancies, which could (in addition to the difference between the subjected aerodynamic models) very well be attributed to small differences in the resulting turbulence box with respect to the rotor CFD. Where we employ a single blockage correction for the full rotor plane and time series (to correct the empty box sampled wind speeds for the time delay due to the velocity in front of the rotor, see also the WP1 report [33]), in reality the blockage is time and space dependent. It should be realized that although the method as outlined in WP1 comes close, definition of identical inflow conditions between CFD and lifting line codes is impossible and the current approach is an approximation based on an engineering method.

The 8 m/s fixed case allows to study the alignment between the lifting line codes, as results from all partners are available. Although the wind probe values show similar large scale fluctuations, there still seem to be small differences in the way selected codes read in the turbulent wind files. Unfortunately the project timing prevented a deeper dive to resolve these observed differences, although discrepancies in wind field interpolation and turbine blade geometry definition and its rotation are likely causes for it. Despite the small differences in inflow definition, a comparison of aerodynamic loads between the codes is still judged to be meaningful.

5.2.2 Model differences

Despite the small differences in inflow definition, the 8 m/s fixed case allows to draw some interesting conclusions with respect to the effects of modeling differences.

- Vortex models versus BEM
  In agreement with results from the AVATAR project and the sheared inflow comparison, the induced velocity variation of vortex wake models follows more directly the underlying inflow variations than the BEM results. The vortex wake model from Bladed features the same behavior as the previously studied vortex wake models. As a result, the fluctuations in angle of attack and consequently aerodynamic loads are smaller. This is clearly affecting the equivalent sectional load levels at all radial stations (inboard at 30%R often excepted) and hence also the blade root moments.

- Comparison to CFD
  The comparison to CFD indicates that generally speaking the vortex codes agree better with CFD than BEM judging by the magnitude of load fluctuations and resulting equivalent load levels. However Figure B.16(a) shows this image is not always consistent between the different blades, as for blade 1 the equivalent flapwise blade root moment levels from CFD seem to agree better with BEM. The figures below show the underlying spanwise distribution, which indicates that although the 30%R, 50%R and 70%R stations show a better agreement between CFD and vortex type codes, this is not the case for the 95%R station that drives the flapwise moment for a large part.

  A deeper dive into this matter leads us to Figure B.1(c), which shows the axial wind velocity as encountered by the blade at this station (see also the sensor list definition from appendix A.2), zoomed in at the largest flapwise moment fluctuation over the time series around t=50 s. As the CFD value is taken from a probe a chord ahead of the leading edge, and the lifting line values are taken directly from the wind field without induction and bound vorticity, differences in level can be expected. Indeed, on average the CFD probe gives a somewhat higher axial velocity than the lifting line value. But the magnitude of fluctuations, especially on a larger time scale are generally very similar. The peak around t=50s at 95%R is an exception, and opposite to the encountered apparent axial wind speed variation at 70%R, the fluctuation from CFD is significantly larger. It is hypothesized that discrepancies in inflow definition between CFD and lifting line codes are the cause, resulting in a larger normal force fluctuation at 95%R (Figure B.3(e)) and consequently the flapwise moment (Figure B.3(a)). As such this could explain the unexpected disagreement in predicted fatigue loads between CFD and vortex codes for blade 1.

  Since the equivalent load level over a time series is heavily dominated by the largest fluctuation occurring over the time serie, it is believed that a better criterium is needed to judge the differences between the codes. Especially bearing in mind that small differences in inflow definitions between lifting line and CFD codes exist as discussed previously. Therefore it is decided to study the staircase plots resulting from the rainflow counting, which are an intermediate result

showing the range of fluctuations versus the number of occurrences or counts. Instead of focusing on the equivalent load level determined by the largest ranges with very few occurrences, statistically it makes more sense to study the ranges with a large number of counts. Figure B.17(a) shows indeed that for the ranges featuring more than 10 counts, CFD and vortex models tend to agree well. To pursue a more qualitative statement than the given staircase plots, these plots are integrated (keeping the logarithmic distribution for the number of counts), above a threshold value of 10 counts. The resulting image given in Figure 5.1 indeed shows the inconsistency between the three blades to disappear. It should be noted that this quantity does not represent equivalent loading and gives a different weighting to small scale fluctuation (in addition to ruling out the ranges below the threshold) in comparison to the conventional equivalent load determination.

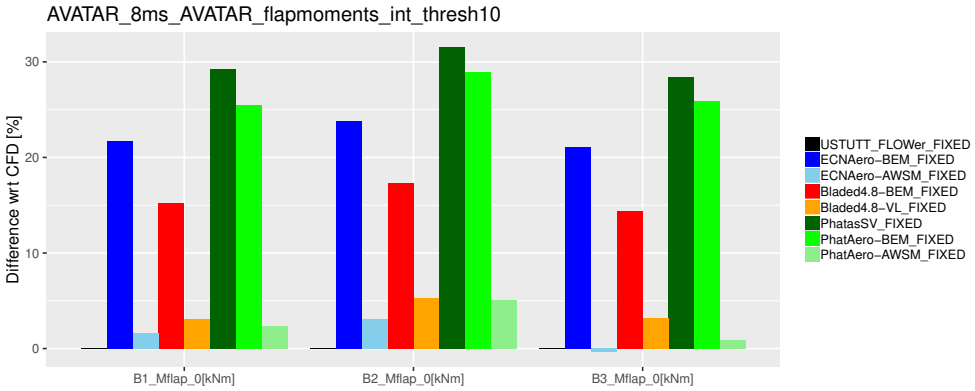

Figure 5.1: Relative comparison of integrated staircase plot values for the flapwise blade root moment, starting at a threshold of 10 counts

The underlying spectra in Figure B.20 show that the 1P fluctuations (~0.1 Hz) dominate the spectra resulting from the blade slicing through the turbulent eddies. The higher frequencies, in agreement with the staircase plots, show the lowest energy levels predicted by CFD and vortex type codes. The 1P variation is less dominant at the 30%R station, which is attributed to the fact that the relative velocity is small in comparison to the outboard stations and temporal variations (or variations in axial direction) of the wind are gaining importance relative to the spatial variations (in the rotorplane). As a result the non-uniformity of the wind speeds and its corresponding gradients encountered by a blade section over a revolution can be argued to be less.

- Effect of shed vorticity
  From previous work [2] it was hypothesized that part of the observed difference between BEM and vortex type codes can be explained by the shed vorticity modeling which is implicitly included for vortex wake models but not in BEM. A dedicated model to simulate the effect of shed vorticity changes has been developed within the framework of WP4 [34]. It is also noted that the indical method from Beddoes & Leishman [35, 36] for modeling unsteady sectional aerodynamics includes a part dedicated to modeling shed vorticity effects based on Theodorsen's theory [37]. It was studied to what extent the Beddoes Leishman model as extension to the BEM method, following the implementation in the Aero Module outlined in [38] as alternative to Snel's dynamic stall model, can confirm the hypothesis mentioned above. It is noted that the DNV-GL Bladed results feature the Beddoes Leishman model by default as reported in chapter 2. The 8 m/s fixed case is recalculated varying the dynamic stall model and

the resulting plots are given in appendix C, where the results with the Beddoes Leishman model are given in orange.

As the Beddoes Leishman model acts on the airfoil coefficients rather than induced velocities, it can be observed that the effect on the axial and tangential induced velocities is limited in comparison to the BEM results featuring the default Snel dynamic stall model (Figures C.7, C.8, C.20 and C.21). However the lift and especially the drag coefficient fluctuations show differences in Figures C.4 and C.5. For the lift coefficient it can clearly be observed that shed vorticity modeling slightly tops off the fluctuation amplitudes, resulting in a lower standard deviation of the normal force time series consequently bringing the flapwise fatigue equivalent moment better in line with the vortex wake model (Figure C.15). The drag coefficient can be observed to fluctuate vigorously due to the activation of the Beddoes Leishman model. This is however not directly carried through to the tangential force time series (Figure C.3) as also the lift coefficient is an important driver to this variable depending on the angle of attack decomposition. Where for the normal force and flapwise moment the BEM Beddoes Leishman results are somewhere in between conventional BEM and vortex wake results in terms of equivalent moments, the corresponding tangential force and leadwise moment from the BEM Beddoes Leishman simulation are almost similar to the vortex wake results. Following this results it seems that part of the difference (30%-50% for the difference in flapwise moment eql) between conventional BEM and vortex wake can be attributed to shed vorticity effects. Although not shown here, it was verified that the earlier observed differences in sheared flow can not be attributed to this effect. It is anticipated that shed vorticity effects are present in more abrupt changes in inflow condition rather than gradual inflow changes as encountered in vertical shear. So it remains important to further clarify the origin of the remaining differences, for which a hypothesis will be given in the work package 4 report [34]. In addition to that it is noted that the Beddoes Leishman model accounts for shed vorticity on a two-dimensional level, whereas the a vortex wake model models the shed vortices including the effect of rotation.

- BEM implementation
  Studying the axial induced velocity variations in Figure B.8 reveals not only large differences between BEM and vortex type codes, but also between the different BEM codes. Where the red line shows a nearly constant level, the other BEM codes feature more variation with inflow velocity as can also be observed by the standard deviation over the time serie in Figure B.15(b). This was also observed in the sheared inflow comparison. It is known that a wide variety of BEM implementations exist, e.g. solving the momentum equations for a whole annulus or per element, not to mention the interaction with a dynamic wake or dynamic inflow model. This example illustrates the effect these implementation differences can have. Within work package 4 a deeper look into the effect of several implementations and a possible improvement is given [34].

5.2.3 Effect of load case variations

To compare the results between the codes over the simulated load cases, the staircase plots of the flapwise blade root moments were integrated (starting at a threshold of 10 counts) as discussed above, similar to the results shown in Figure 5.1. A summary of the results is given in Table 5.2. In agreement with the results of the 8m/s fixed case, the vortex wake results tend to agree well with CFD also for the other cases. Drawing conclusion on variations between the load cases is complicated because observed differences between the cases can potentially be caused by the difference in specific turbulence boxes and the way the rotor blades slice through them. It seems that similar to the shear case, a higher thrust coefficient value results in larger differences between BEM on the one hand and vortex / CFD models on the other hand.

Table 5.2: Relative difference of integrated flapwise blade root moment staircase plot results† against CFD results

Nr [-]	Case	ECNAero-BEM [%]	ECNAero-BEM-BL [%]	ECNAero-AWSM [%]
1	8ms_fixed	22.2	10.0	1.4
2	8ms_prscrbd	29.6	11.2	5.6
3	16ms_prscrbd	31.6	9.2	12.6
4	8msTI10_prscrbd	26.1	8.5	2.8
5	8msCt_prscrbd	34.8	13.4	0.8
6	8msL_prscrbd	30.1	11.4	6.4

† Averaged over 3 blades, staircase plots integrated from a threshold value of 10 counts.

The 16 m/s result features a very low thrust (axial induction factor around 0.06), which makes the BEM with shed vorticity modeling come very close to the vortex model, although a rather high unexplained difference remains with CFD. Simulating a higher length scale (mimicking a 4 times smaller turbine) unexpectedly seems to have hardly any impact on the magnitude of the differences between the models.

Although comparison of equivalent loads between CFD and lifting line codes is hindered by small differences in inflow conditions, a comparison between lifting line codes (BEM and vortex) in terms of fatigue loading is deemed useful in Table 5.3. It is clear that the low turbulence intensity case features the smallest fatigue loads,

Table 5.3: Relative difference of damage equivalent flapwise blade root moments against ECNAero-AWSM results

Nr [-]	Case	ECNAero-AWSM [Nm]	ECNAero-BEM [%]	ECNAero-BEM-BL [%]
1	8ms_fixed	16979	13.8	8.9
2	8ms_prscrbd	20509	12.5	5.4
3	16ms_prscrbd	26750	8.5	-1.6
4	8msTI10_prscrbd	8884	14.0	8.0
5	8msCt_prscrbd	24383	19.4	11.0
6	8msL_prscrbd	22830	14.9	7.5

where the 16 m/s wind speed shows the highest fatigue. These numbers also confirm that the shed vorticity modeling in BEM for this 16 m/s case make these results come very close to the vortex wake results. And this difference to be at maximum for the high thrust case. It can also be observed that, although the absolute level of the flapwise fatigue load clearly decreases with a lower turbulence intensity, the relative difference between BEM and vortex code type results remains similar.

6 Conclusions and recommendations

Within the framework of the TKI WoZ VortexLoads project, CFD simulations were carried out to verify the earlier observed differences in dynamic loading and the resultant fatigue equivalents between BEM and vortex wake codes. Hereto a 'numerical' wind tunnel was set-up subjecting a rigid (or non-flexible) version of the AVATAR 10MW wind turbine model. Firstly comparisons in uniform, constant inflow conditions provided a good agreement between all code types, which is a prerequisite for a consistent comparison in more challenging inflow conditions. Sheared inflow conditions demonstrated a difference in the cyclic loading amplitude between BEM and vortex / CFD models. A parameter variation study revealed this difference to scale with the magnitude of the axial induction factor. Turbulent inflow simulations were carried out to verify the influence of turbulence length scale, turbulence intensity and thrust coefficient on the observed differences between the codes.

Concluding it can be stated that a variety of CFD simulations have confirmed the hypothesis that conventional BEM models overpredict fatigue loading for wind turbine design load calculations. The differences were shown to be partly related to the shed vorticity modeling. However, both for the shear and turbulent inflow cases a difference between BEM with shed vorticity model on the one hand and vortex wake models on the other hand remains. Poor tracking of induced velocities with apparent wind speed variations as experienced by the blade was shown to be the underlying cause for the differences between the models, becoming increasingly important for higher thrust coefficients. It is recommended to have a further look into the cause for this difference. In addition to that it is recommended to perform a validation in a real rather than a 'numerical' wind tunnel, featuring a rotor in representative inflow conditions.

7 References

[1] K. Boorsma and F. Wenz and M. Aman and C. Lindenburg and M. Kloosterman. TKI WoZ VortexLoads Final report. Technical Report TNO 2019 R11388, TNO, September 2019. http://publications.tno.nl/publication/34634923/tbIASC/TNO-2019-R11388.pdf.

[2] K. Boorsma, P. Chasapogiannis, D. Manolas, M. Stettner, and M. Reijerkerk. Avatar deliverable d4.6: Comparison of aerodynamic models for calculation of fatigue loads in turbulent inflow, 2016. http://www.eera-avatar.eu/fileadmin/avatar/user/avatard4.6_v8.pdf.

[3] W. Collier and J. Milan Sanz. Comparison of linear and non-linear blade model predictions in bladed to measurement data from ge 6mw wind turbine. *Journal of Physics*, 2016.

[4] J.G. Schepers and K. Boorsma et al. Final report of IEA Task 29, Mexnext (Phase 2). Ecn-e-14-060, Energy Research Center of the Netherlands, December 2014.

[5] M.H.M. Kloosterman. Development of the free wake behind a horizontal axis wind turbine. Master's thesis, Delft University of Technology, Delft, the Netherlands, 2009.

[6] M. Harrison, M. Kloosterman, and R. Buils Urbano. Aerodynamic modelling of wind turbine blade loads during extreme deflection events. *Journal of Physics: Conference Series*, 1037(6):062022, 2018.

[7] M.H. Hansen, M. Gauna, and H.A. Madsen. A Beddoes-Leishman type dynamic stall model in state-space and indicial formulations . Risø-r-1354(en), Risoe, June 2004.

[8] K. Boorsma, F. Grasso, and J.G. Holierhoek. Enhanced approach for simulation of rotor aerodynamic loads. Technical Report ECN-M–12-003, ECN, presented at EWEA Offshore 2011, Amsterdam, 29 November 2011 - 1 December 2011, 2011.

[9] K. Boorsma, M. Hartvelt, and L.M. Orsi. Application of the lifting line vortex wake method to dynamic load case simulations. *Journal of Physics: Conference Series*, 753(2):022030, 2016.

[10] C. Lindenburg and J.G. Schepers. Phatas-iv aeroelastic modelling, release "dec-1999" and "nov-2000". Technical Report ECN-CX–00-027, ECN, 2000.

[11] A. Van Garrel. Development of a wind turbine aerodynamics simulation module. Technical Report ECN-C–03-079, ECN, 2003.

[12] http://www.wmc.eu/focus6.php. 2016.

[13] https://www.3ds.com/products-services/simulia/products/simpack/. 2018.

[14] K. Boorsma, L. Greco, and G. Bedon. Rotor wake engineering models for aeroelastic applications. *Journal of Physics: Conference Series*, 1037(6):062013, 2018.

[15] H. Snel and J.G. Schepers. Joule1: Joint investigation of dynamic inflow effects and implementation of an engineering model. Technical Report ECN-C–94-107, ECN, 1994.

[16] J.G. Schepers and Vermeer L.J. Een engineering model voor scheefstand op basis van windtunnelmetingen. Technical Report ECN-CX–98-070, ECN, 1998.

[17] J.G. Schepers. An engineering model for yawed conditions, developed on basis of wind tunnel measurements. Technical Report AIAA-1999-0039, AIAA, 1999.

[18] H. Glauert. A General Theory of the Autogyro. Technical Report ARC R&M No.1111, ARC R&M, 1926.

[19] L. Prandtl and A. Betz. *Vier Abhandlungen zur hydrodynamik und aerodynamik*. Göttingen, Germany, 1927.

[20] H. Snel. Heuristic modelling of dynamic stall characteristics. In *Conference proceedings European Wind Energy Conference*, pages 429–433, Dublin, Ireland, October 1997.

[21] H. Snel, R. Houwink, J. Bosschers, W.J. Piers, G.J.W. Van Bussel, and A. Bruining. Sectional prediction of 3-d effects for stalled flow on rotating blades and comparison with measurements. In *Conference proceedings European Wind Energy Conference*, Lübeck-Travemünde, Germany, March 1993.

[22] Christoph Schulz, Annette Fischer, Pascal Weihing, Thorsten Lutz, and Ewald Krämer. Evaluation and control of loads on wind turbines under different operating conditions by means of cfd. In *High Performance Computing in Science and Engineering´ 15*, pages 463–478. Springer, 2016.

[23] Norbert Kroll, Cord-Christian Rossow, Klaus Becker, and Frank Thiele. The megaflow project. *Aerospace Science and Technology*, 4:223–237, 2000.

[24] Antony Jameson, Wolfgang Schmidt, and Eli Turkel. Numerical solution of the euler equations by finite volume methods using runge kutta time stepping schemes. In *14th fluid and plasma dynamics conference*, 1981.

[25] Guang-Shan Jiang and Chi-Wang Shu. Efficient implementation of weighted eno schemes. *Journal of computational physics*, 126:202–228, 1996.

[26] G Chesshire and William D Henshaw. Composite overlapping meshes for the solution of partial differential equations. *Journal of Computational Physics*, 90:1–64, 1990.

[27] Galih Bangga, Thorsten Lutz, Eva Jost, and Ewald Krämer. Cfd studies on rotational augmentation at the inboard sections of a 10 mw wind turbine rotor. *Journal of Renewable and Sustainable Energy*, 9(2):023304, 2017.

[28] Yusik Kim, Pascal Weihing, Christoph Schulz, and Thorsten Lutz. Do turbulence models deteriorate solutions using a non-oscillatory scheme? *Journal of Wind Engineering and Industrial Aerodynamics*, 156:41–49, 2016.

[29] Florian R Menter. Two-equation eddy-viscosity turbulence models for engineering applications. *AIAA journal*, 32:1598–1605, 1994.

[30] Mikhail L Shur, Philippe R Spalart, Mikhail Kh Strelets, and Andrey K Travin. A hybrid rans-les approach with delayed-des and wall-modelled les capabilities. *International Journal of Heat and Fluid Flow*, 29:1638–1649, 2008.

[31] Y. Kim, Th. Lutz, E. Jost, S. Gomez-Iradi, A. Munoz, B. Mendez, N. Lampropoulos, Stefanatos N., N.N. Sørensen, H. Madsen, P. van der Laan, H. Heißelmann, S. Voutsinas, and G. Papadakis. Avatar deliverable d2.5: Effects of inflow turbulence on large wind turbines, 2016. `http://www.eera-avatar.eu/fileadmin/avatar/user/avatar_D2p5_revised_20161231.pdf`.

[32] `https://www.eera-avatar.eu/`, Password protected environment for exchange of AVATAR data. ECN, 2016.

[33] F. Wenz and K. Boorsma and G. Bangga and Y. Kim and T. Lutz. CFD Modelling and Results of VortexLoads WP1. Technical report, University of Stuttgart, Institute for Aerodynamics and Gasdynamics, September 2019.

[34] K. Boorsma and M. Aman and C. Lindenburg. Improvement of BEM and vortex-wake models, TKI WoZ Vortexloads WP4. Technical Report TNO 2019 R11391, TNO, September 2019. http://publications.tno.nl/publication/34634926/xeUGvL/TNO-2019-R11391.pdf.

[35] J.G. Leishman and T.K. Beddoes. A generalized method for unsteady airfol behaviour and dynamic stall using the indicial method. In *42nd Annual Forum*, Washington D.C., June 1986. American Helicopter Society.

[36] J.G. Leishman and T.K. Beddoes. A semi-empirical model for dynamic stall. *Journal of the American Helicopter Society*, 34:3–17, 1989.

[37] T. Theodorsen. General theory of aerodynamic instability and the mechanism of flutter. Technical Report NACA Report 496, NACA, 1935.

[38] M.A. Khan. Dynamic stall modeling for wind turbines. Master's thesis, Delft University of Technology, Delft, the Netherlands, 2018.

A Data format and test cases

A.1 Uniform, constant inflow

TKI VortexLoads: Definition of first round of calculations (uniform constant inflow)

K. Boorsma
13 July 2018

1. Description of the rotor

The AVATAR rotor is simulated for a number of test cases, of which the USTUTT CFD results are readily available from the EU AVATAR project. The AVATAR rotor is described on the teamsite of VortexLoads:
https://vortexloads.ecn.nl/do/document?id=901-646f63756d656e74

The rotor taken for this comparison features no tilt, cone (pure axial inflow) and the tower effect should be disabled. The rotor is assumed to be rigid.
The airfoil data that needs to be used is deduced from post-processing USTUTT CFD simulations and also supplied in the same excel sheet on the teamsite.

Please disable the usage of 3d rotational effects, since they are already contained within the prescribed airfoil data set.

2. Description of cases.

- Pitch angle: 0.0 degrees (see also Figure 1 for definition)
- Air density 1.225 kg/m^3
- Yaw angle: 0 degrees

WIND SPEED [m/s]	RPM	PITCH
4	6.00000	0.00000
5	6.00000	0.00000
6	6.00000	0.00000
8	6.87380	0.00000

3. Results to be supplied:

- Requested data and units:
  - F_{ax} : Rotor axial force on the rotor [N].
  - Torque: Aerodynamic torque of the rotor [Nm].
  - Mflap: Flapwise blade root moment [Nm] (r=2.8m from rotor center, My_B from Figure 1d)
  - For a minimum of 10 (preferably more) radial locations:
    - F_{normal} (i.e. the force normal to the local chord, positive pointing in downwind direction) [N/m]
    - $F_{tangential}$ (i.e. the force parallel to the local chord, positive pointing from trailing to leading edge) [N/m].

Files to be supplied:
  - Please supply the data in one ASCII file which should contain the data for all wind speeds. Please upload the file to the teamsite.

- Format: Each row contains 9 columns with data. Separate the columns by tabs or blanks. The first row gives the identification of data. The second row gives the axial force for the four wind speeds. Please duplicate the values for F_{ax} since 2 columns are available for each wind speed. The next rows give the data at the three wind speeds for the chosen radial locations (a total of n), increasing from root to tip. The variable r is defined to start at the rotor center (r=0m) increasing towards the blade tip (r=102.88m). Hence, the format is as follows

r	F_{n4}	F_{t4}	F_{n5}	F_{t5}			-	F_{n8}	F_{t8}
F_{ax}	--	--	--	--			-	--	--
Torque	--	--	--	--			-	--	--
r_1	--	--	--	--			-	--	--
|	|	|	|	|	|	|	-	--	--
|	|	|	|	|	|	|	-	--	--
r_n	--	--	--	--	--	--	-	--	--

Note that this makes the total number of rows to be n + 3
(1 (header) + 1 (axial force) + 1 (torque) + n radial locations)

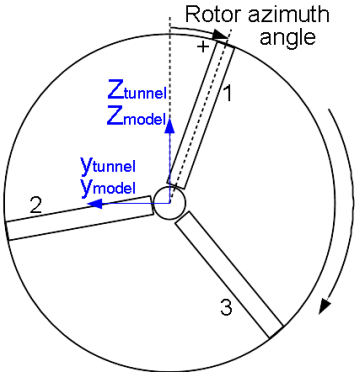

(a) Front view

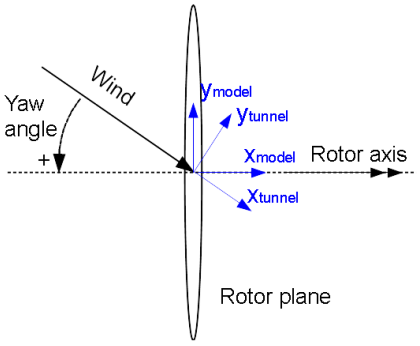

(b) Top view

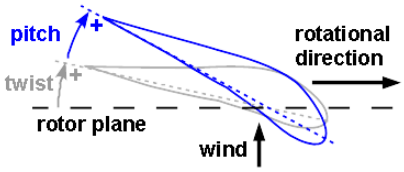

(c) Sectional view: Pitch angle

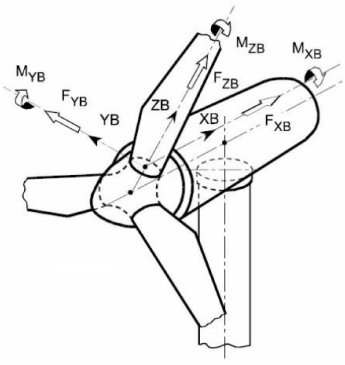

(d) Blade coordinate system (co-rotating with pitch and azimuth angle)

Figure 1: Definitions and conventions

A.2 Sheared and turbulent inflow

Description of work

TKI WoZ Vortex Loads WP2: Comparison between CFD and lifting line codes in turbulent inflow

K. Boorsma (TNO), version 7, 26th February 2019

1 Introduction

The description of work aims at providing a frame of reference for WP2. The aim of this task is to compare aerodynamic models for the purpose of fatigue load analysis of the AVATAR RWT. CFD simulations will be performed as a reference to compare to.

The analysis will be done using BEM (WMC, TNO, DNV-GL, GE?) and Vortex methods (TNO, DNV-GL, GE?). The CFD simulation will be performed by USTUTT.

2 Reference wind turbine

The AVATAR reference turbine will be simulated in this task. The relevant information to model the turbine is available on the Vortex Loads project website at (.\WP2 Validation of BEM and Vortex-wake models with numerical tunnel data\1st Comparison round Axial uniform constant inflow\AVATAR10MWReferenceWindTurbine-VortexLoads_1stround_v09May2018.xls)

https://365tno.sharepoint.com/:x:/r/teams/P060.33833/Extranet/WP2%20Validation%20of%20BEM%20and%20Vortex-wake%20models%20with%20numerical%20tunnel%20data/1st%20Comparison%20round%20Axial%20uniform%20constant%20inflow/AVATAR10MWReferenceWindTurbine-VortexLoads_1stround_v09May2018.xls?d=w5d992aff9d11472bab8b4965fa605ef2&csf=1&e=dekIoP

Furthermore:

-A rigid turbine will be used to compare between CFD and lifting line codes. A comparison including flexibility could be performed amongst lifting line codes.

-Cone and tilt angle are set to zero degree

-Only the rotor will be simulated. Tower and nacelle are excluded

-Airfoil data is supplied by USTUTT as deduced from 3D rotating simulations

3 Wind

The wind excitation is to be supplied by USTUTT after recording the wind field distribution from their CFD simulation. USTUTT will inject a MANN wind field into the computational domain about a kilometer upstream of the rotor.

3.1 MANN wind field

To reduce the computational effort and still allow to obtain statistics a 400s wind field duration is proposed for most of the turbulent cases. Periodic wind fields (which is for the case of MANN wind fields) shorter than the simulation duration will be used to match statistics in case of long settling times of CFD and Vortex simulations.
It is not possible to perform simulations for all seeds as is common in IEC load set calculation. A set of 12 400s simulations is carried out using BEM. Because the resulting wind field needs to be used for CFD, the domain needs to be multiple D high and wide around the rotor center (fairly large). The damage equivalent load of representative load sensors (Blade My) is computed for each of the seeds. Then a single seed is selected which gives DEL closest to the mean DEL of the 12 seeds. In this way we ensure selection of a "statistically representative" wind seed. Particular attention will be paid to gusts resulting in large load variations that dominate the fatigue loads.

3.2 USTUTT sampled wind field

The resulting wind supplied by USTUTT should contain equidistant spacing on a rectangular grid with about 25 points in vertical and lateral direction. Temporal spacing preferably about 0.01s but this will obviously depend on the time step taken for the CFD simulations.

4 Simulation settings

4.1 Simulation length

As indicated in section 3.1, wind files with a length of 400 s (6.7 min) are provided. Because CFD and vortex wake codes need time to initialize the wake (settling time), only the results after settling of the simulation will be used for the comparison. Therefore the total simulation length has to be set to approximately 500 s. It is realized that this time span (in combination with number of seeds) is not sufficient to determine representative fatigue loads. However the emphasis lies on the comparison between models, both in the time domain as well as the resulting statistics.

4.2 Time step size

Torsional and edgewise vibrations are amongst the highest frequencies to be resolved, but because we are simulating a rigid rotor, time step requirements are less strict. Therefore it is expected we can suffice with a 2deg azimuth time step. However based on the convergence of CFD simulations in relation to the number of subiterations the time step is reduced to 1deg azimuth. Because rotational speed will vary as function of time (see below), the time averaged rotational speed can be used to set this parameter.

4.3 Controller settings

To match better the operational conditions of a real wind turbine and get a representative simulation it is proposed to include RPM and pitch angle variations as a function of time in the CFD simulation. These will be pre-determined from a BEM simulation with controller subjected to the same wind field excitation. For

the comparison between CFD and lifting line codes everybody will stick to the prescribed rpm and pitch angle variation as a function of time.

4.4 Airfoil data

The prescribed airfoil data from the VortexLoads teamsite should be used for the comparison cases. Because these are deduced from 3D rotating CFD simulations, a 3D correction model on the airfoil data should not be performed. For BEM simulations, the tip loss model (e.g. Prandtl) should be activated.

4.5 Test matrix

A test matrix is given in section 5. A first iteration at 10.5 m/s wind (AVATAR WP2.5 simulation) has been performed by TNO and USTUTT to check the approach for aligning wind fields between CFD and lifting line codes. Also a comparison round using quasi steady CFD simulations in uniform constant wind (rotating) has been performed already. A comparison round in sheared inflow is also performed using the same sensor list and result file as for the turbulent inflow comparison.

5 Test matrix

		No cone ,tilt, tower , nacelle, rotor only												
nr	**Rank**	**Name**	**U_avg[m**	**shear**	**Wind type**	**TI[%]**	**L [m]**	**rpm**	**pitch[deg**	**rigid/flex**	**n_wind**	**T_wind[s]**	**dt[deg]**	**Comments**
1	high	turb	8	n	turb	~23 (IEC 1A)	33.6 (IEC)	CONSTAN	CONSTAN	rigid	1	400	1	
2	high	turb	8	n	turb	~23 (IEC 1A)	33.6 (IEC)	prscrbd	prscrbd	rigid	1	400	1	
3	medium	turb+highwind	16	n	turb	~17 (IEC 1A)	33.6 (IEC)	prscrbd	prscrbd	rigid	1+offset	200	1	Same wind field, different offset (hence shorter simulation duration)
4	medium	turb+lowTI	8	n	turb	~10	33.6 (IEC)	prscrbd	prscrbd	rigid	1+scale	400	1	Same wind field, different scaling
5	medium	turb+highCt	8	n	turb	~23 (IEC 1A)	33.6 (IEC)	prscrbd+1	prscrbd-1	rigid	1	400	1	
6	medium	turb+L (small rotor)	8	n	turb	~23 (IEC 1A)	x4 (134.4)	prscrbd	prscrbd	rigid	2	400	1	
7	low	turb+flex	8	n	turb	~23 (IEC 1A)	33.6 (IEC)	prscrbd	prscrbd	flex	1	400	1	Only between BEM/Vortex?
8	low	turb+shear	8	y	turb	~23 (IEC 1A)	33.6 (IEC)	prscrbd	prscrbd	rigid	1+shear	400	1	Only between BEM/Vortex?

6 Output signal definition

Coordinate systems for the data output

6.1 Hub coordinate system

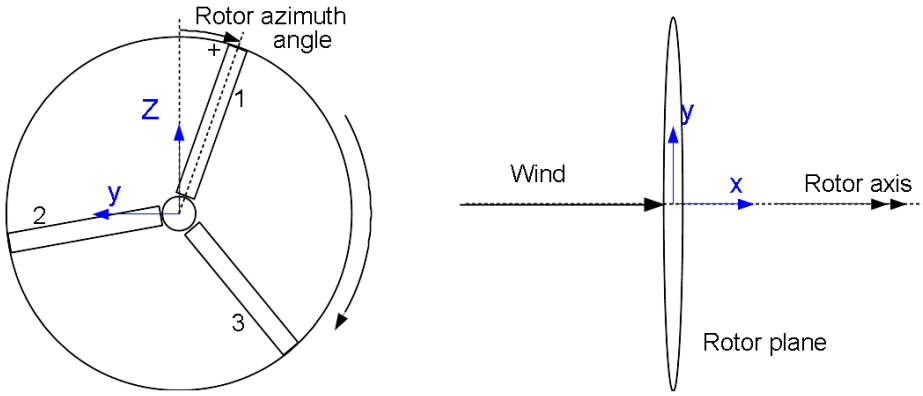

Figure 1: Definition of the hub coordinate system (left: front view, right: top view)

Axial force, torque and power are defined in this coordinate system as well as wind and induced velocities. Blade numbering and azimuth angle are also defined here. The coordinate system can be considered as an inertial coordinate system and hence is fixed in space.

6.2 Blade coordinate system

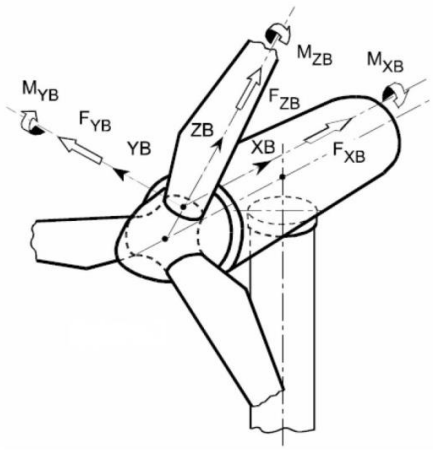

Figure 2: Definition of the blade coordinate system

The blade coordinate system originates in the blade root and co-rotates with pitch and azimuth angle. Flapwise (M_{YB}) and edgewise (M_{XB}) moments are defined in this coordinate system.

6.3 Element coordinate system

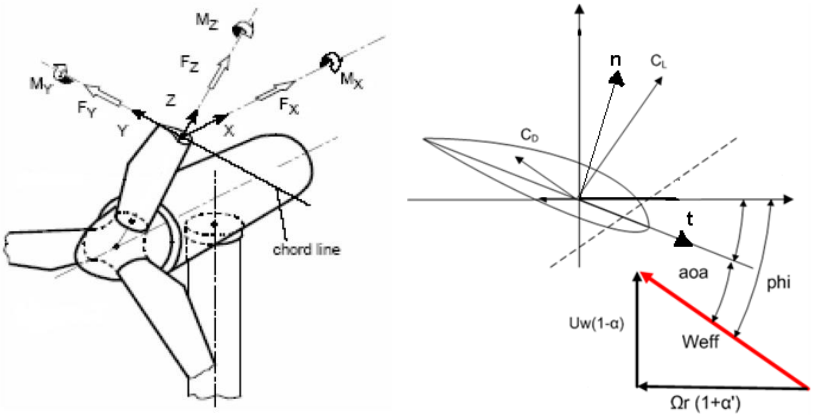

Figure 3: Definition of Element coordinate system

Sensor list and format of the result text file

Each partner should deliver one text file which contains all the sensors in different columns. Each name of the record field/column is listed below. The columns of the text file should be separated with the blanks (or TAB). The units of each sensor are also listed together with the name of each column. The post processing into azimuth averaged data, min-mean-max will be done when making the final plots.

1 time [s] (time should be in accordance with time setting of wind file, i.e. please donot apply a shift e.g. due to initialization)

2 azimuth of blade 1 [deg] (zero angle is with blade 1 pointing **upwards**)

3 pitch angle [deg]

4 rotor speed [rpm]

5 hub height total wind speed [m/s]

6 rotor aerodyanmic axial force [kN]

7 rotor aerodynamic torque [kNm]

8 rotor aerodynamic power [kW]

9 blade 1 flapwise aerodynamic root moment Mflap [kNm] (defined in blade coordinate system around yB)

10 blade 1 edgewise aerodynamic root moment Medge [kNm] (defined in blade coordinate system around xB)

11 blade 2 flapwise aerodynamic root moment Mflap [kNm]

12 blade 2 edgewise aerodynamic root moment Medge [kNm]

13 blade 3 flapwise aerodynamic root moment Mflap [kNm]

14 blade 3 edgewise aerodynamic root moment Medge [kNm]

15 axial wind speed u @ 30%R blade 1 as read in from wind file# (x direction of Fig. 1) [m/s]*

16 axial wind speed u @ 50%R blade 1 as read in from wind file# (x direction of Fig. 1) [m/s]*

17 axial wind speed u @ 70%R blade 1 as read in from wind file# (x direction of Fig. 1) [m/s]*

18 axial wind speed u @ 95%R blade 1 as read in from wind file# (x direction of Fig. 1) [m/s]*

19 lateral wind speed v @ 30%R blade 1 as read in from wind file# (y direction of Fig. 1) [m/s]

20 lateral wind speed v @ 50%R blade 1 as read in from wind file# (y direction of Fig. 1) [m/s]

21 lateral wind speed v @ 70%R blade 1 as read in from wind file# (y direction of Fig. 1) [m/s]

22 lateral wind speed v @ 95%R blade 1 as read in from wind file# (y direction of Fig. 1) [m/s]

23 vertical wind speed w @ 30%R blade 1 as read in from wind file# (z direction of Fig. 1) [m/s]

24 vertical wind speed w @ 50%R blade 1 as read in from wind file# (z direction of Fig. 1) [m/s]

25 vertical wind speed w @ 70%R blade 1 as read in from wind file# (z direction of Fig. 1) [m/s]

26 vertical wind speed w @ 95%R blade 1 as read in from wind file# (z direction of Fig. 1) [m/s]

27 chord normal aerodynamic force @ 30%R blade 1 (positive downwind) [kN/m]**

28 chord normal aerodynamic force @ 50%R blade 1 (positive downwind) [kN/m]

29 chord normal aerodynamic force @ 70%R blade 1 (positive downwind) [kN/m]

30 chord normal aerodynamic force @ 95%R blade 1 (positive downwind) [kN/m]

31 chord tangential aerodynamic force @ 30%R blade 1 (positive towards LE) [kN/m]**

32 chord tangential aerodynamic force @ 50%R blade 1 (positive towards LE) [kN/m]

33 chord tangential aerodynamic force @ 70%R blade 1 (positive towards LE) [kN/m]

34 chord tangential aerodynamic force @ 95%R blade 1 (positive towards LE) [kN/m]

35 axial wind speed u @ 30%R blade 2 as read in from wind file# (x direction of Fig. 1) [m/s]*

36 axial wind speed u @ 50%R blade 2 as read in from wind file# (x direction of Fig. 1) [m/s]*

37 axial wind speed u @ 70%R blade 2 as read in from wind file# (x direction of Fig. 1) [m/s]*

38 axial wind speed u @ 95%R blade 2 as read in from wind file# (x direction of Fig. 1) [m/s]*

39 lateral wind speed v @ 30%R blade 2 as read in from wind file# (y direction of Fig. 1) [m/s]

40 lateral wind speed v @ 50%R blade 2 as read in from wind file# (y direction of Fig. 1) [m/s]

41 lateral wind speed v @ 70%R blade 2 as read in from wind file# (y direction of Fig. 1) [m/s]

42 lateral wind speed v @ 95%R blade 2 as read in from wind file# (y direction of Fig. 1) [m/s]
43 vertical wind speed w @ 30%R blade 2 as read in from wind file# (z direction of Fig. 1) [m/s]
44 vertical wind speed w @ 50%R blade 2 as read in from wind file# (z direction of Fig. 1) [m/s]
45 vertical wind speed w @ 70%R blade 2 as read in from wind file# (z direction of Fig. 1) [m/s]
46 vertical wind speed w @ 95%R blade 2 as read in from wind file# (z direction of Fig. 1) [m/s]
47 chord normal aerodynamic force @ 30%R blade 2 (positive downwind) [kN/m]**
48 chord normal aerodynamic force @ 50%R blade 2 (positive downwind) [kN/m]
49 chord normal aerodynamic force @ 70%R blade 2 (positive downwind) [kN/m]
50 chord normal aerodynamic force @ 95%R blade 2 (positive downwind) [kN/m]
51 chord tangential aerodynamic force @ 30%R blade 2 (positive towards LE) [kN/m]**
52 chord tangential aerodynamic force @ 50%R blade 2 (positive towards LE) [kN/m]
53 chord tangential aerodynamic force @ 70%R blade 2 (positive towards LE) [kN/m]
54 chord tangential aerodynamic force @ 95%R blade 2 (positive towards LE) [kN/m]
55 axial wind speed u @ 30%R blade 3 as read in from wind file# (x direction of Fig. 1) [m/s]*
56 axial wind speed u @ 50%R blade 3 as read in from wind file# (x direction of Fig. 1) [m/s]*
57 axial wind speed u @ 70%R blade 3 as read in from wind file# (x direction of Fig. 1) [m/s]*
58 axial wind speed u @ 95%R blade 3 as read in from wind file# (x direction of Fig. 1) [m/s]*
59 lateral wind speed v @ 30%R blade 3 as read in from wind file# (y direction of Fig. 1) [m/s]
60 lateral wind speed v @ 50%R blade 3 as read in from wind file# (y direction of Fig. 1) [m/s]
61 lateral wind speed v @ 70%R blade 3 as read in from wind file# (y direction of Fig. 1) [m/s]
62 lateral wind speed v @ 95%R blade 3 as read in from wind file# (y direction of Fig. 1) [m/s]
63 vertical wind speed w @ 30%R blade 3 as read in from wind file# (z direction of Fig. 1) [m/s]
64 vertical wind speed w @ 50%R blade 3 as read in from wind file# (z direction of Fig. 1) [m/s]
65 vertical wind speed w @ 70%R blade 3 as read in from wind file# (z direction of Fig. 1) [m/s]
66 vertical wind speed w @ 95%R blade 3 as read in from wind file# (z direction of Fig. 1) [m/s]
67 chord normal aerodynamic force @ 30%R blade 3 (positive downwind) [kN/m]**
68 chord normal aerodynamic force @ 50%R blade 3 (positive downwind) [kN/m]
69 chord normal aerodynamic force @ 70%R blade 3 (positive downwind) [kN/m]
70 chord normal aerodynamic force @ 95%R blade 3 (positive downwind) [kN/m]
71 chord tangential aerodynamic force @ 30%R blade 3 (positive towards LE) [kN/m]**
72 chord tangential aerodynamic force @ 50%R blade 3 (positive towards LE) [kN/m]
73 chord tangential aerodynamic force @ 70%R blade 3 (positive towards LE) [kN/m]
74 chord tangential aerodynamic force @ 95%R blade 3 (positive towards LE) [kN/m]

Following signals are for lifting line codes only (please include zeros for CFD)

75 Blade 1 r=30%R, AOA [deg]

76 Blade 1 r=50%R, AOA [deg]

77 Blade 1 r=70%R, AOA [deg]

78 Blade 1 r=95%R, AOA [deg]

79 Blade 1 r=30%R, induction_axial (positive pointing upwind) [m/s]

80 Blade 1 r=50%R, induction_axial (positive pointing upwind) [m/s]

81 Blade 1 r=70%R, induction_axial (positive pointing upwind) [m/s]

82 Blade 1 r=95%R, induction_axial (positive pointing upwind) [m/s]

83 Blade 1 r=30%R, induction_tangential (positive opposite to direction of rotation) [m/s]

84 Blade 1 r=50%R, induction_tangential (positive opposite to direction of rotation) [m/s]

85 Blade 1 r=70%R, induction_tangential (positive opposite to direction of rotation) [m/s]

86 Blade 1 r=95%R, induction_tangential (positive opposite to direction of rotation) [m/s]

87 Blade 1 r=30%R, Cl [-]

88 Blade 1 r=50%R, Cl [-]

89 Blade 1 r =70%R, Cl [-]

90 Blade 1 r=95%R, Cl [-]

91 Blade 1 r=30%R, Cd [-]

92 Blade 1 r=50%R, Cd [-]

93 Blade 1 r=70%R, Cd [-]

94 Blade 1 r=95%R, Cd [-]

[#]For CFD please supply the velocity from a probe 1 chord ahead of the leading edge (extrapolated along the local chordline)

*Radial locations are expressed as a percentage of the rotor radius, starting at the rotor center. Hence 0%R is the rotor center and 100%R is the blade tip.

**Chord normal or tangential force means the force perpendicular or parallel to the local chord direction (see n and t in Figure 3)

B Plot results for the turbulent cases

B.1 8 m/s fixed case

B.1.1 Time (zoomed)

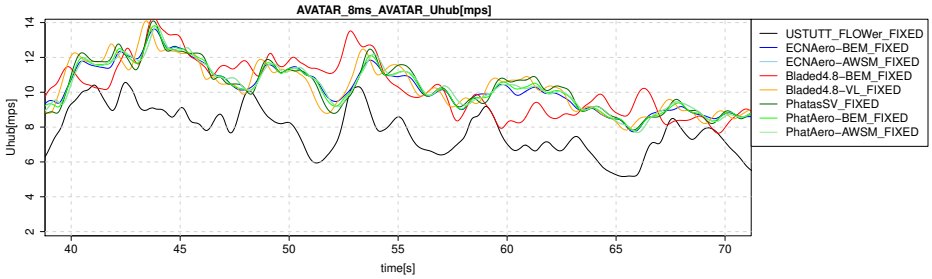

(a) Hub height wind speed

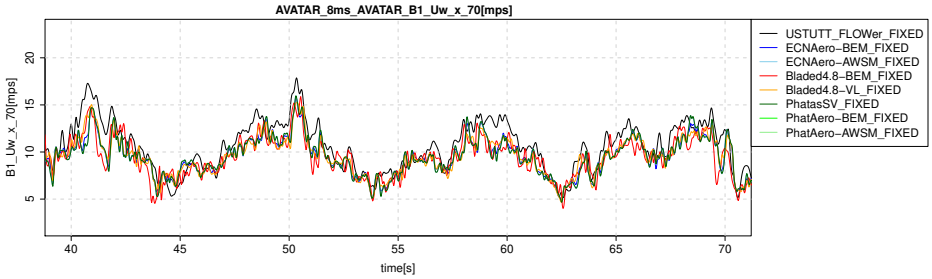

(b) Wind probe axial velocity at 70%R

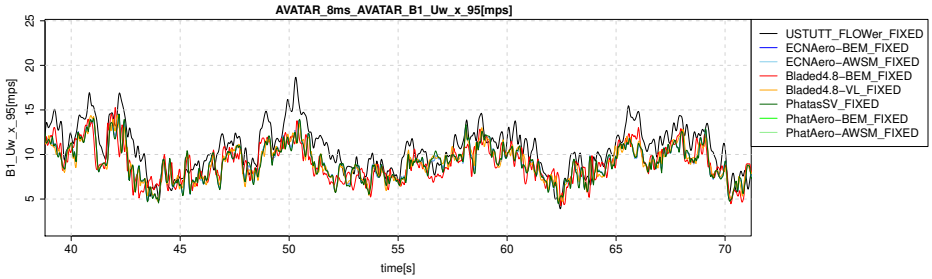

(c) Wind probe axial velocity at 95%R

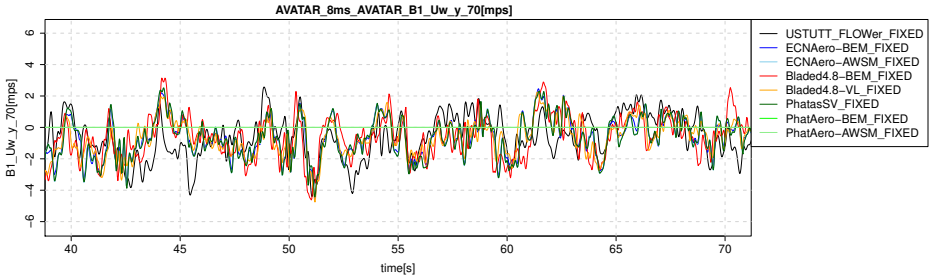

(d) Wind probe lateral velocity at 70%R

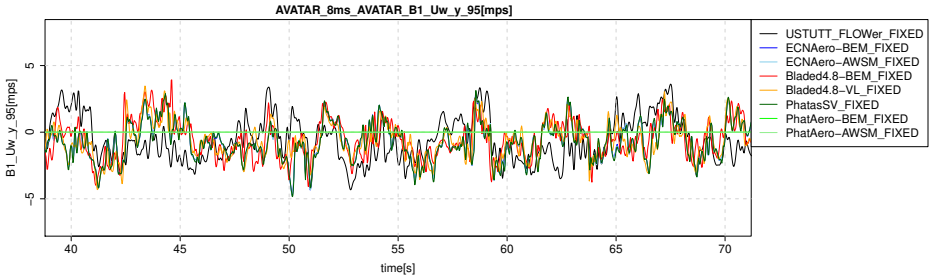

(e) Wind probe lateral velocity at 95%R

Figure B.1: Wind speed alignment check

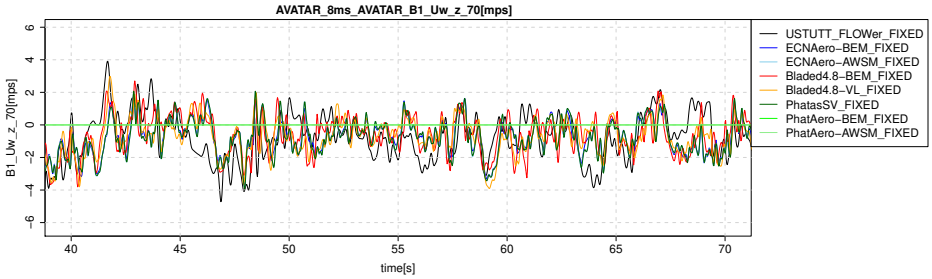

(a) Wind probe vertical velocity at 70%R

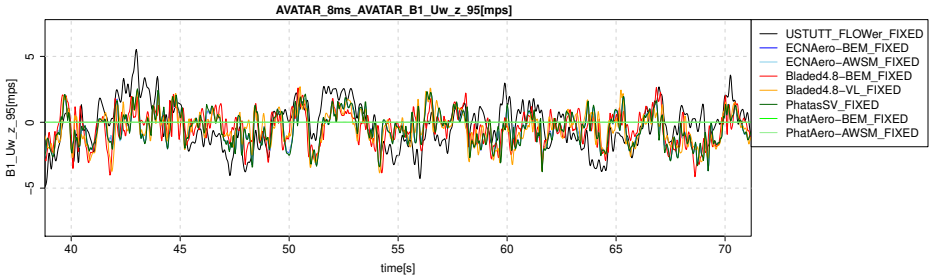

(b) Wind probe vertical velocity at 95%R

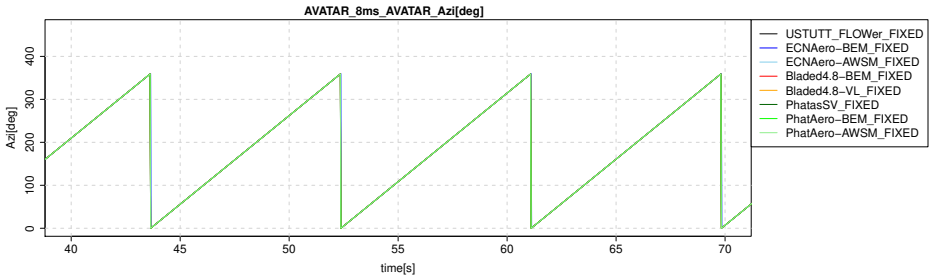

(c) Rotor azimuth angle

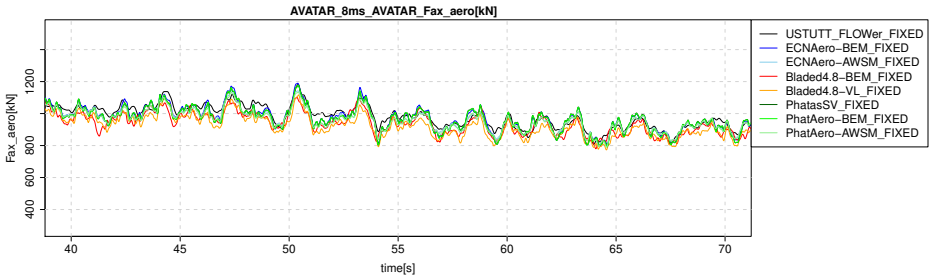

(d) Rotor axial force

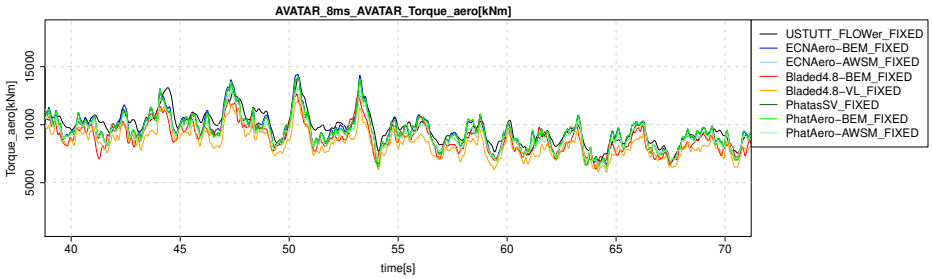

(e) Rotor torque

Figure B.2: Alignment check

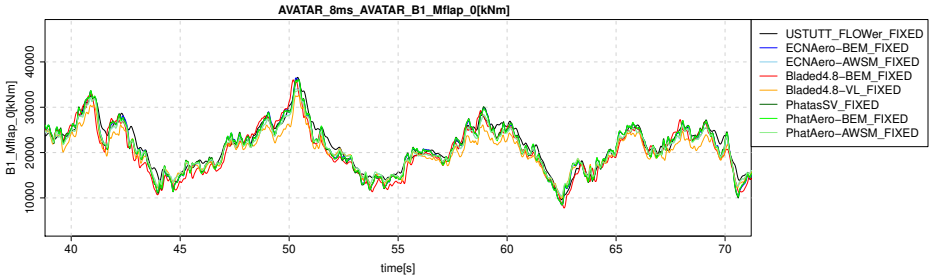

(a) Flapwise blade root moment

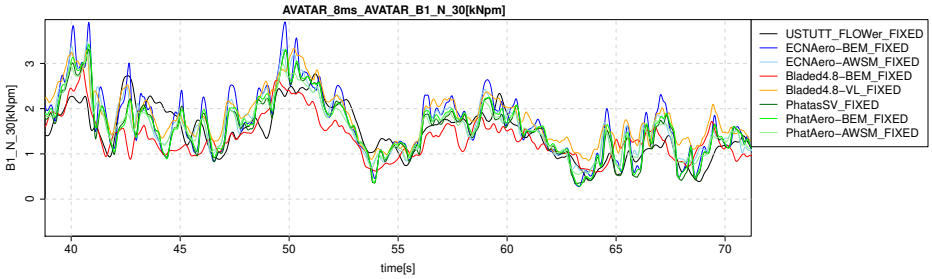

(b) Chord normal force at 30%R

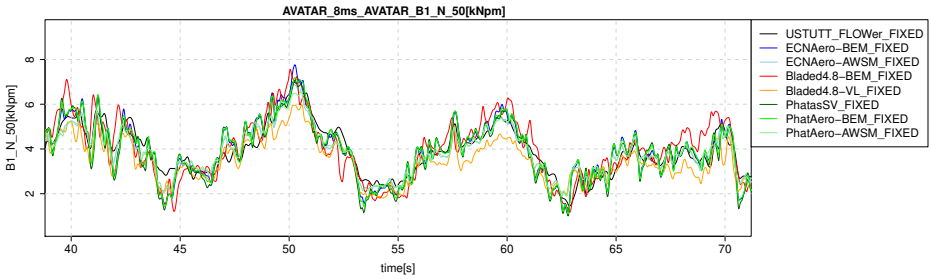

(c) Chord normal force at 50%R

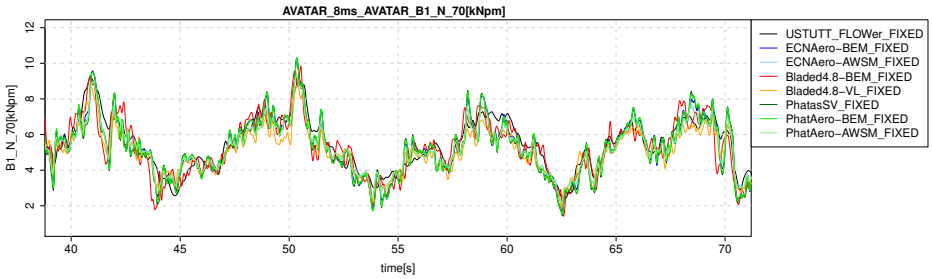

(d) Chord normal force at 70%R

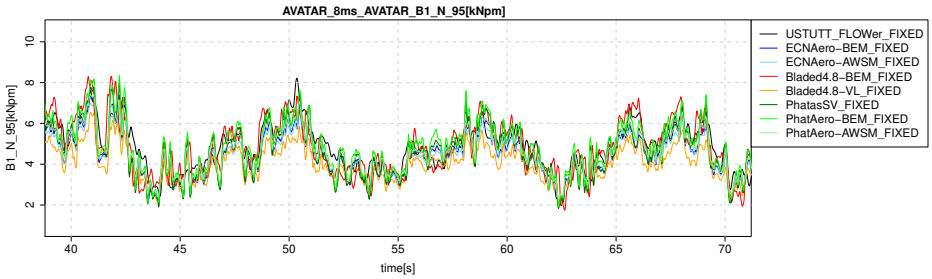

(e) Chord normal force at 95%R

Figure B.3: Flapwise moment and normal force

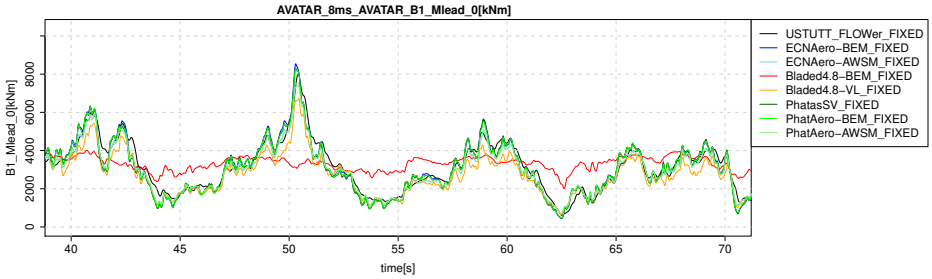

(a) Leadwise blade root moment

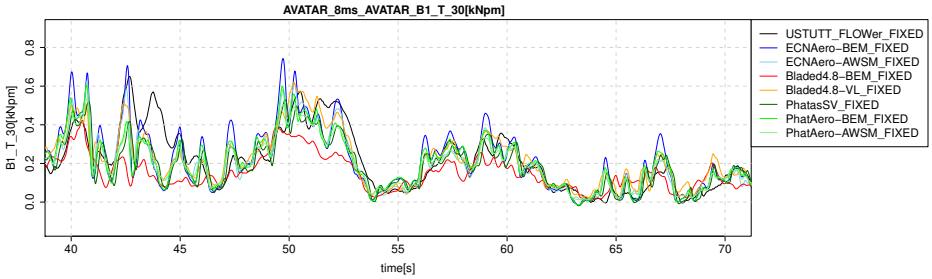

(b) Chord tangential force at 30%R

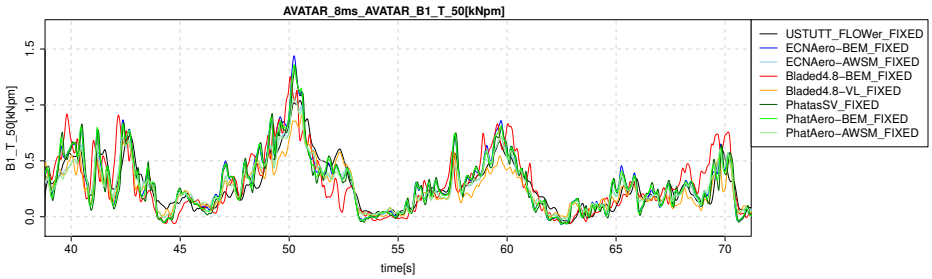

(c) Chord tangential force at 50%R

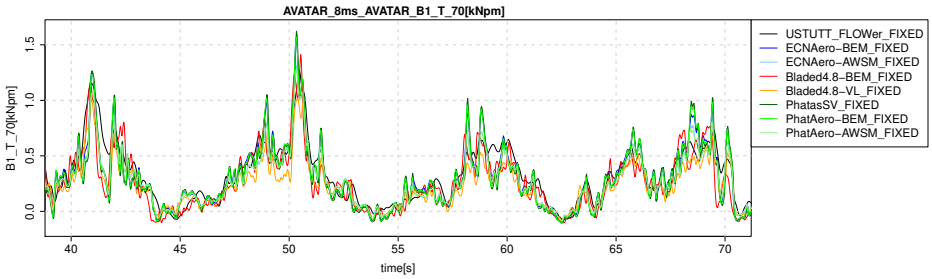

(d) Chord tangential force at 70%R

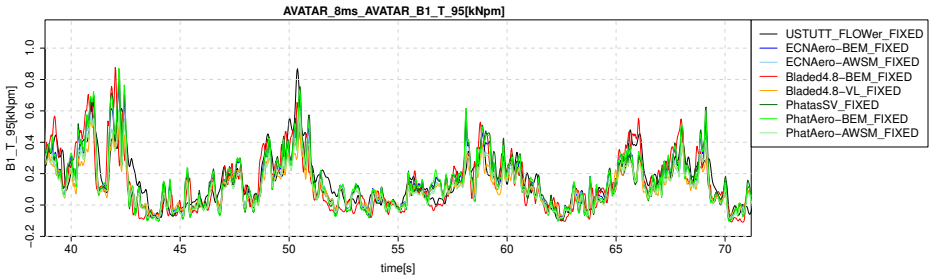

(e) Chord tangential force at 95%R

Figure B.4: Leadwise moment and tangential force

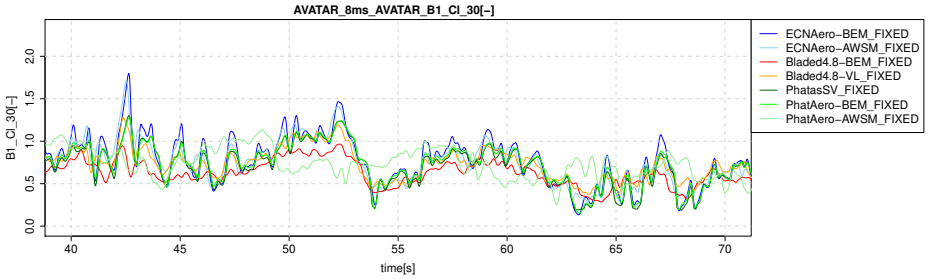

(a) Lift coefficient at 30%R

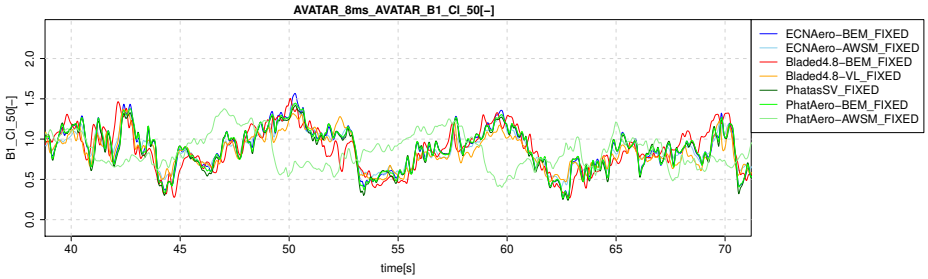

(b) Lift coefficient at 50%R

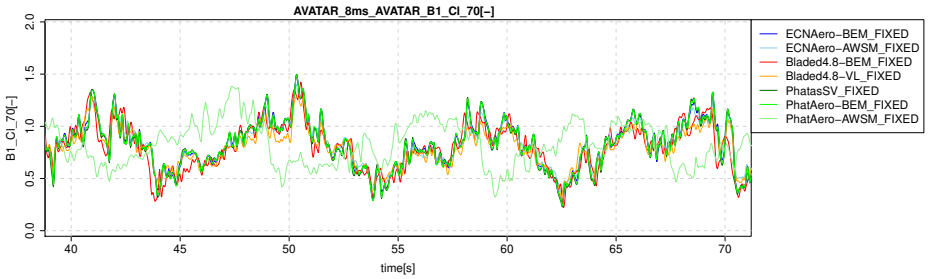

(c) Lift coefficient at 70%R

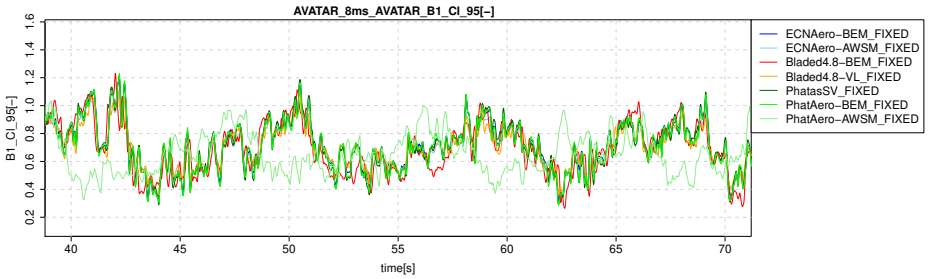

(d) Lift coefficient at 95%R

Figure B.5: Lift coefficients

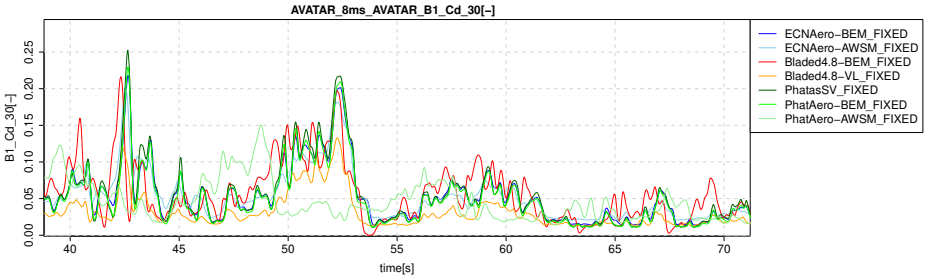

(a) Drag coefficient at 30%R

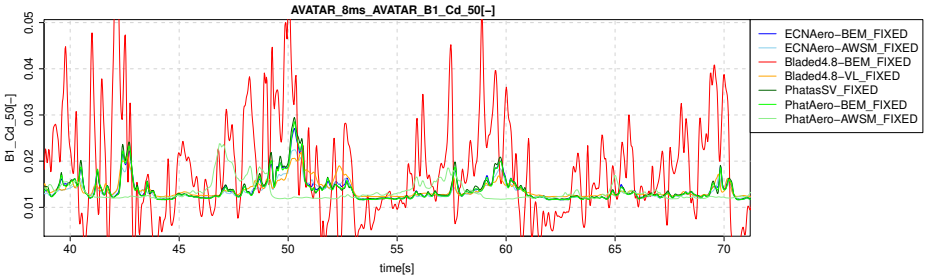

(b) Drag coefficient at 50%R

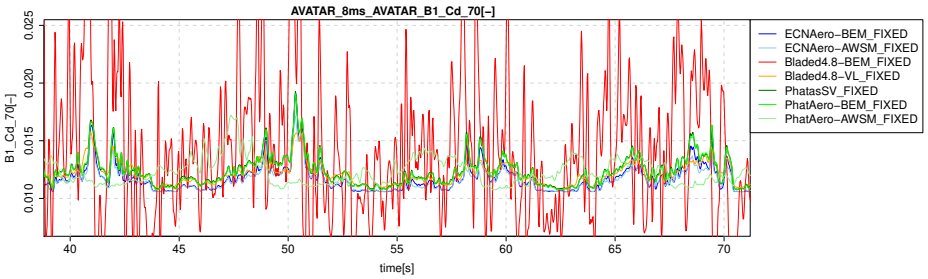

(c) Drag coefficient at 70%R

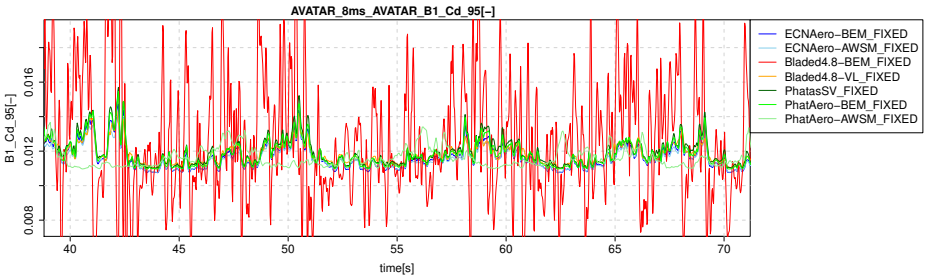

(d) Drag coefficient at 95%R

Figure B.6: Drag coefficients

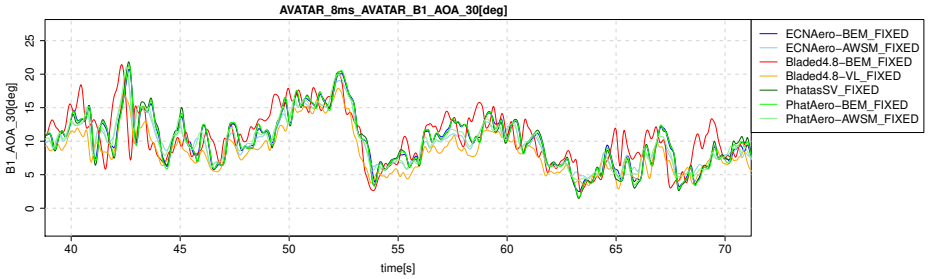

(a) Angle of attack at 30%R

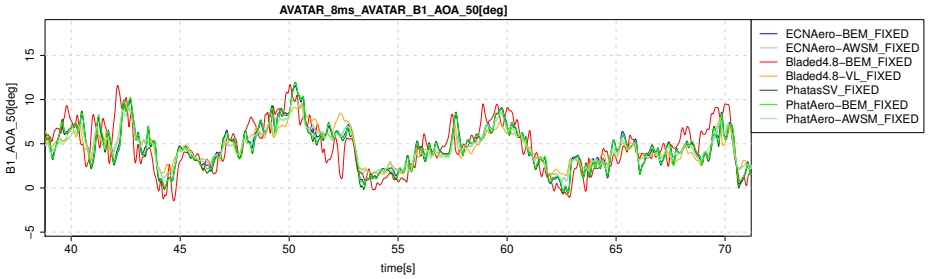

(b) Angle of attack at 50%R

(c) Angle of attack at 70%R

(d) Angle of attack at 95%R

Figure B.7: Angles of attack

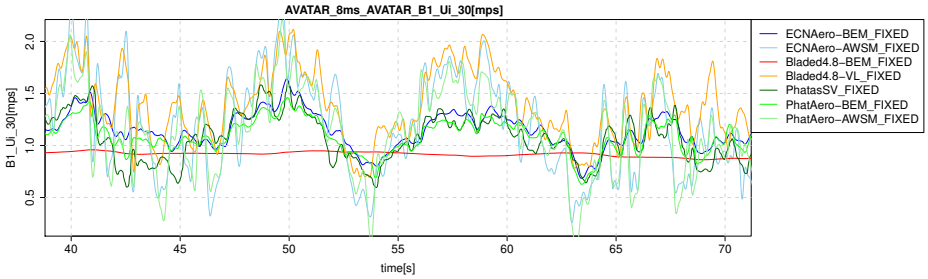

(a) Axial induced velocity at 30%R

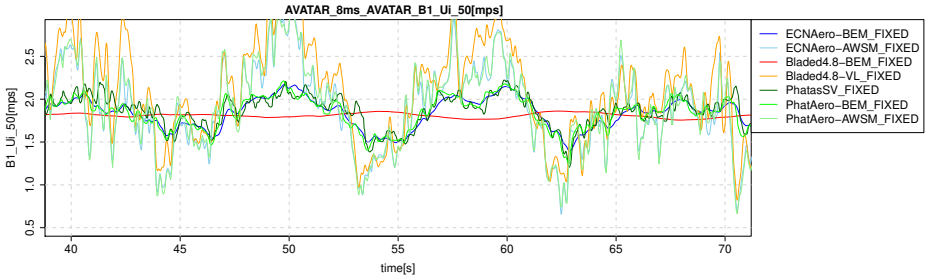

(b) Axial induced velocity at 50%R

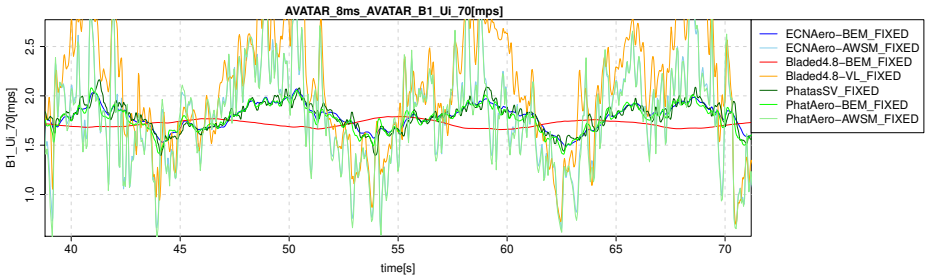

(c) Axial induced velocity at 70%R

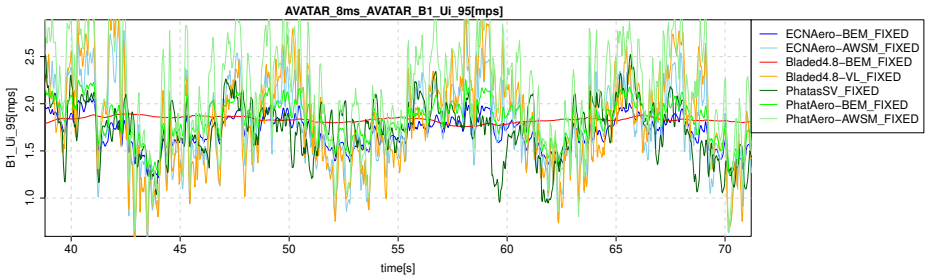

(d) Axial induced velocity at 95%R

Figure B.8: Axial induced velocities

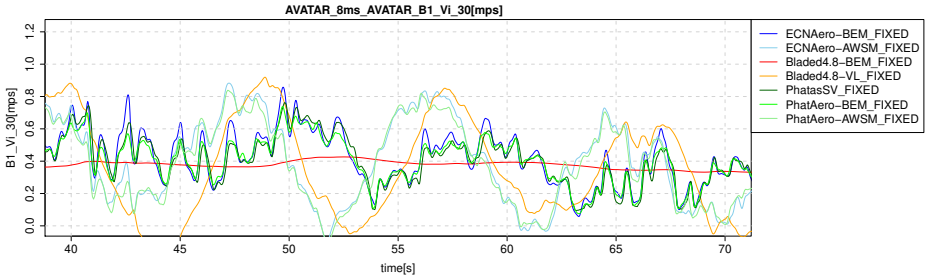

(a) Tangential induced velocity at 30%R

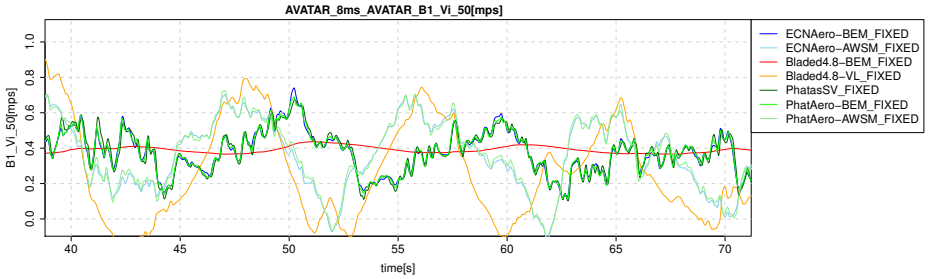

(b) Tangential induced velocity at 50%R

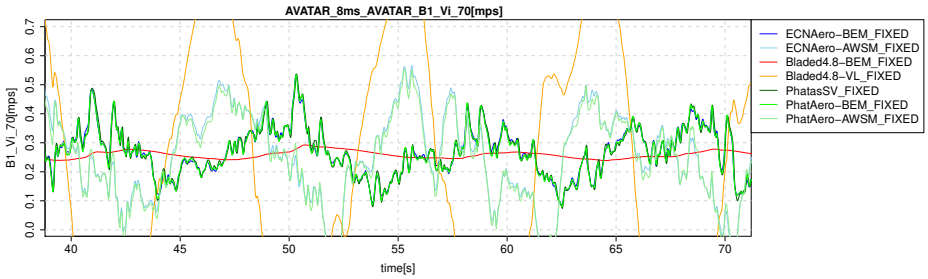

(c) Tangential induced velocity at 70%R

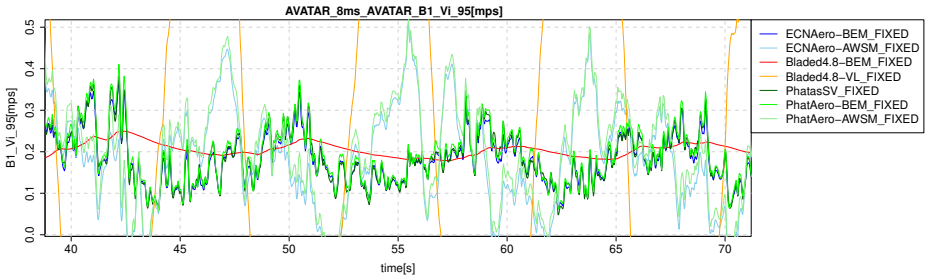

(d) Tangential induced velocity at 95%R

Figure B.9: Tangential induced velocities

B.1.2 Time

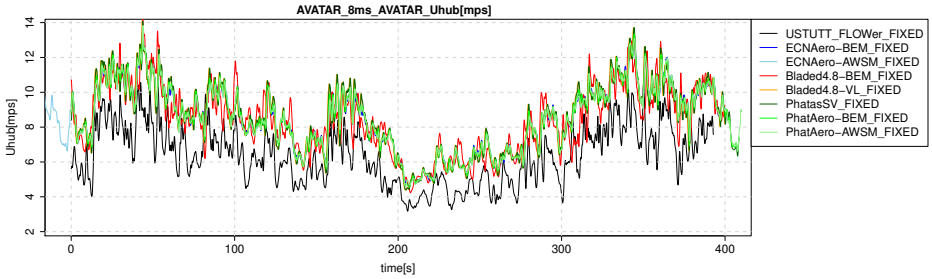

(a) Hub height wind speed

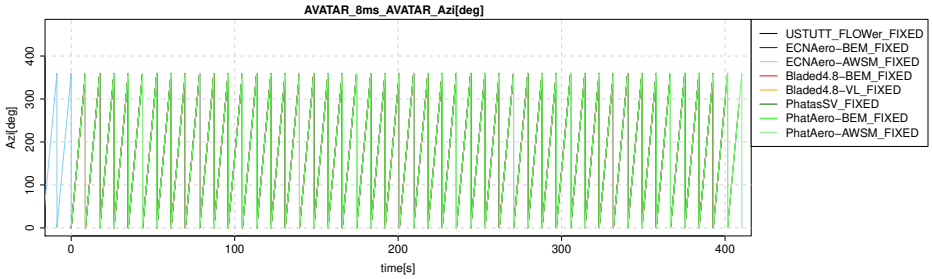

(b) Rotor azimuth

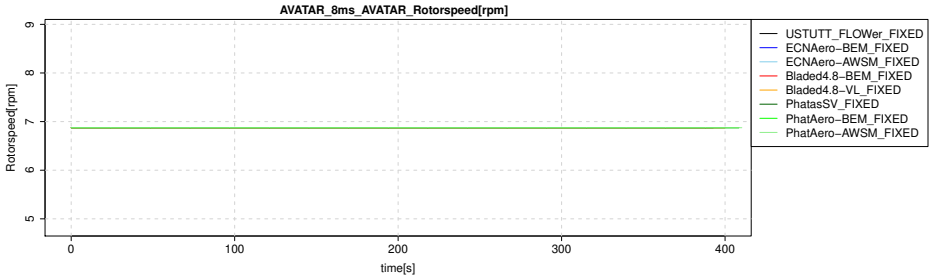

(c) Rotor speed

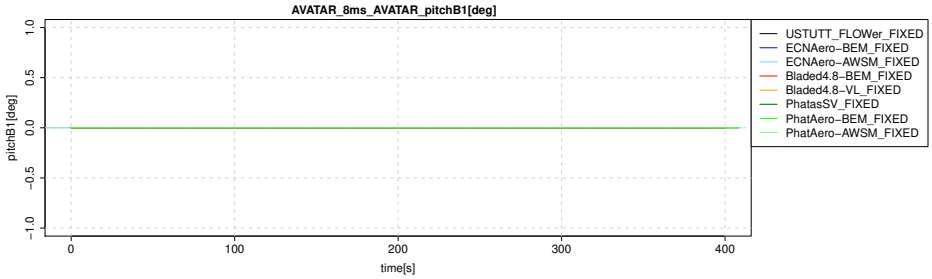

(d) Pitch angle

Figure B.10: Wind and control parameters

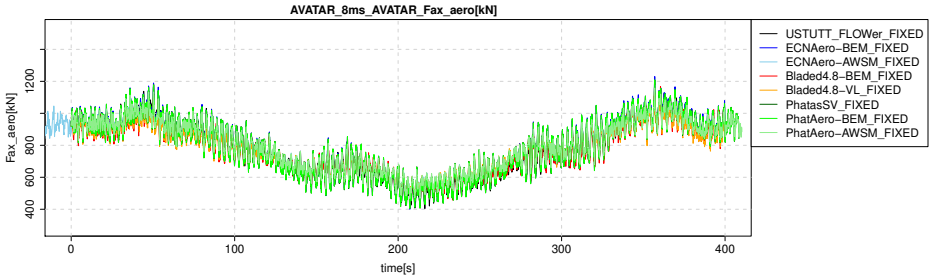

(a) Rotor axial force

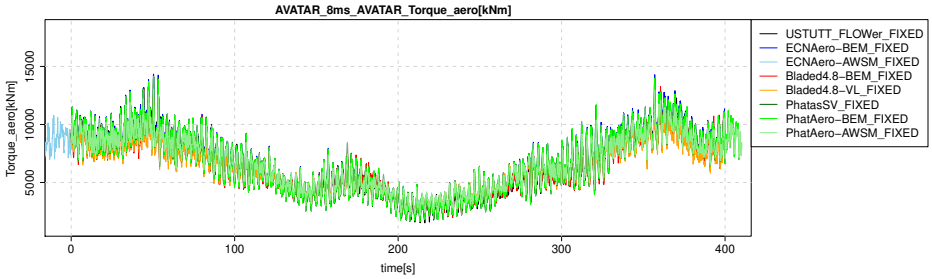

(b) Rotor torque

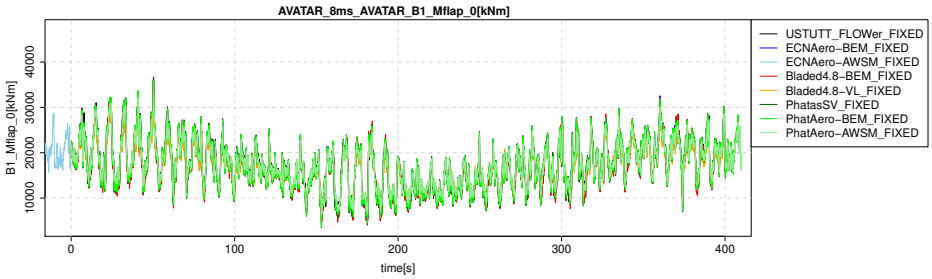

(c) Flapwise blade root moment

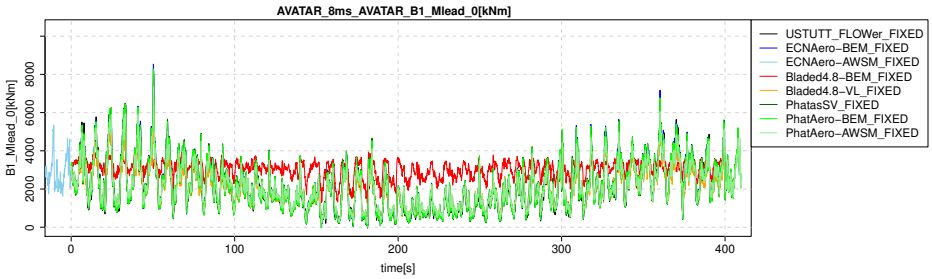

(d) Leadwise blade root moment

Figure B.11: Rotor and blade forces and moments

B.1.3 Statistics

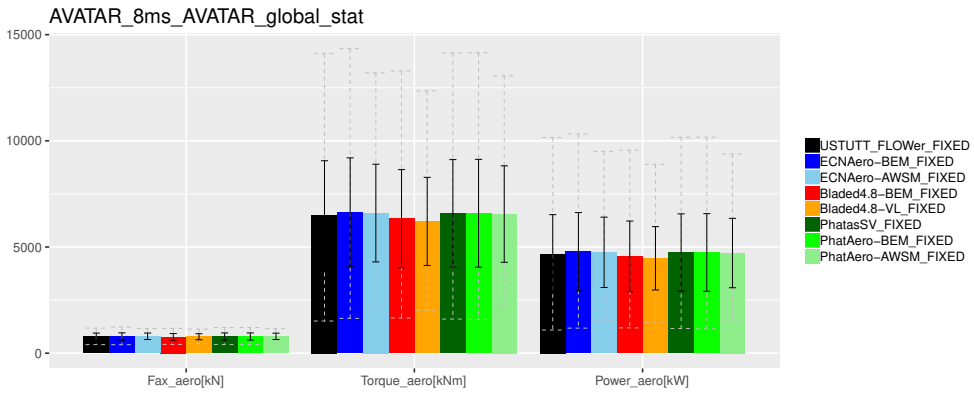

(a) Global performance

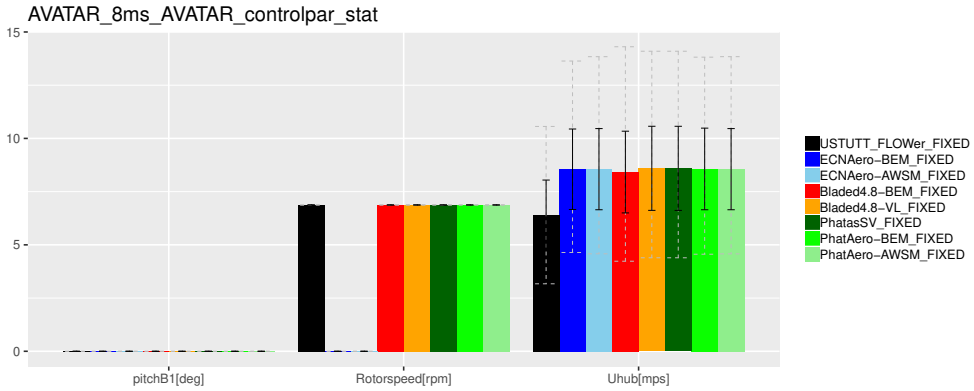

(b) Control parameters

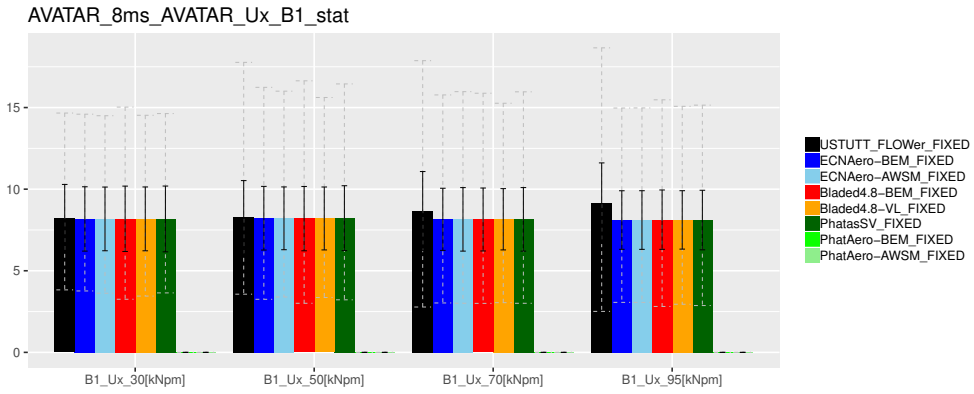

(c) Wind probes, axial

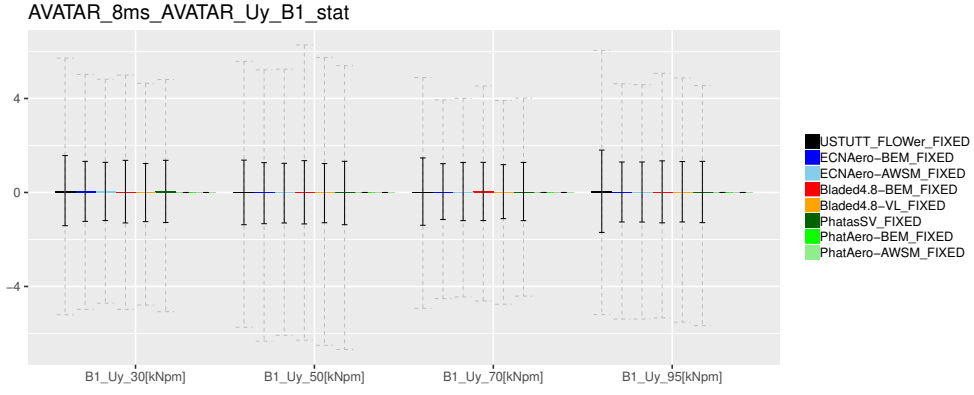

(d) Wind probes, lateral

Figure B.12: Global performance, wind and control parameters

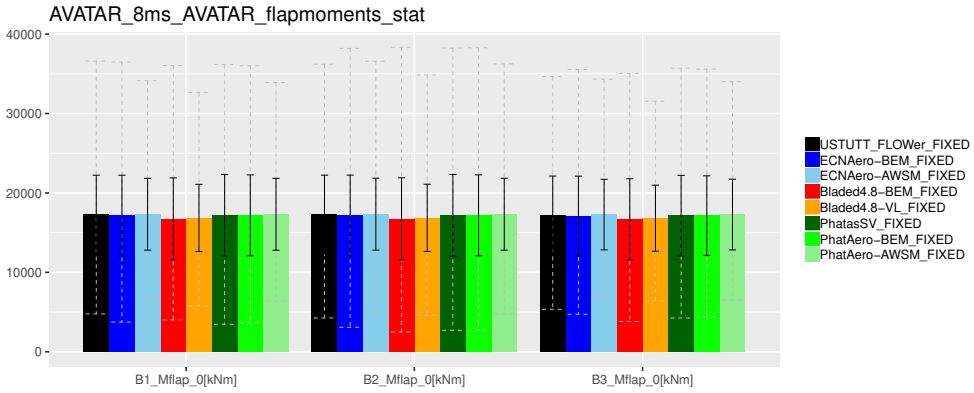

(a) Flapwise moments

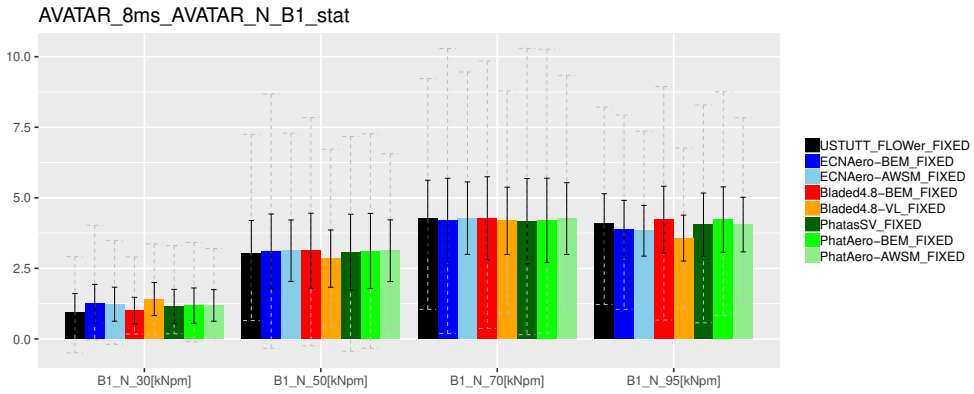

(b) Chord normal force

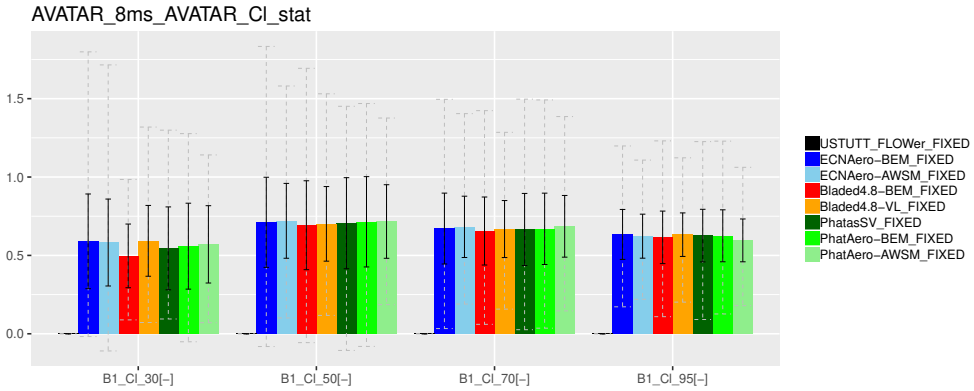

(c) Lift coefficient

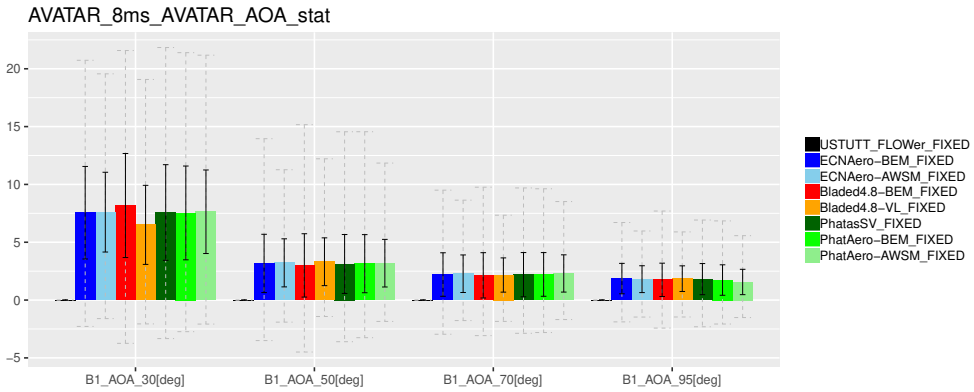

(d) Angle of attack

Figure B.13: Force decompostion in axial direction

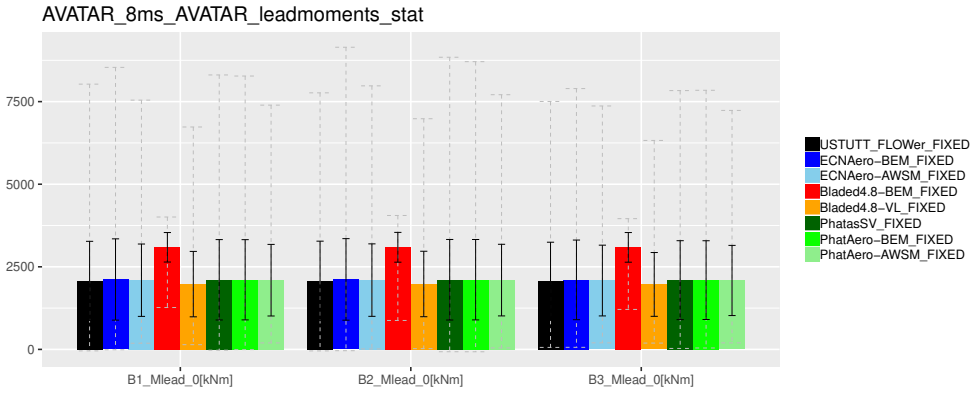

(a) Leadwise moments

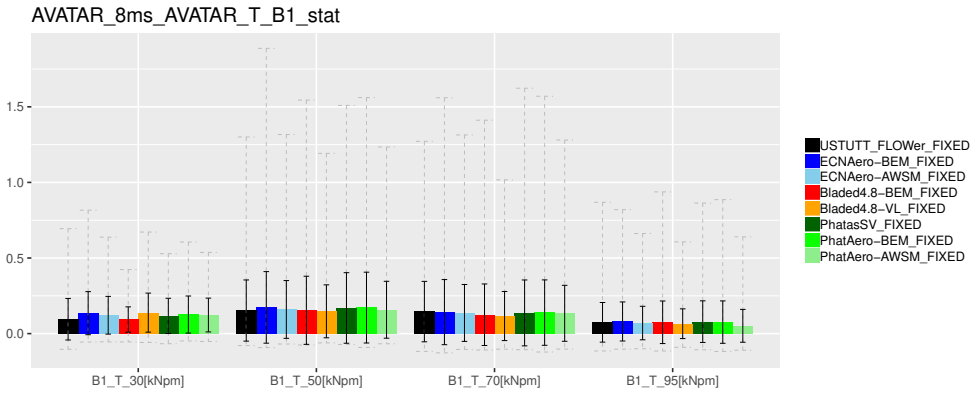

(b) Chord tangential force

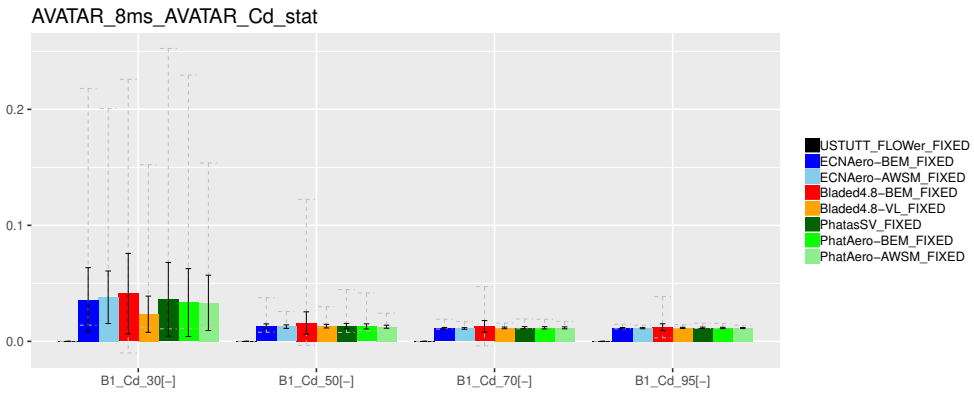

(c) Drag coefficient

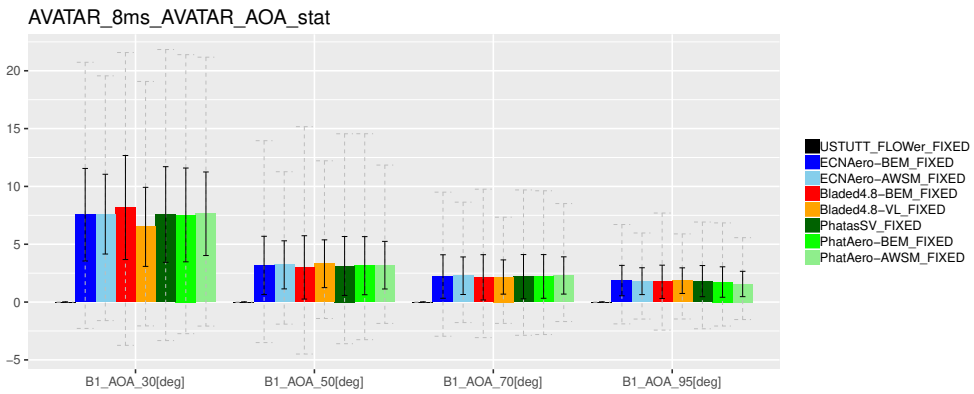

(d) Angle of attack

Figure B.14: Force decompostion in tangential direction

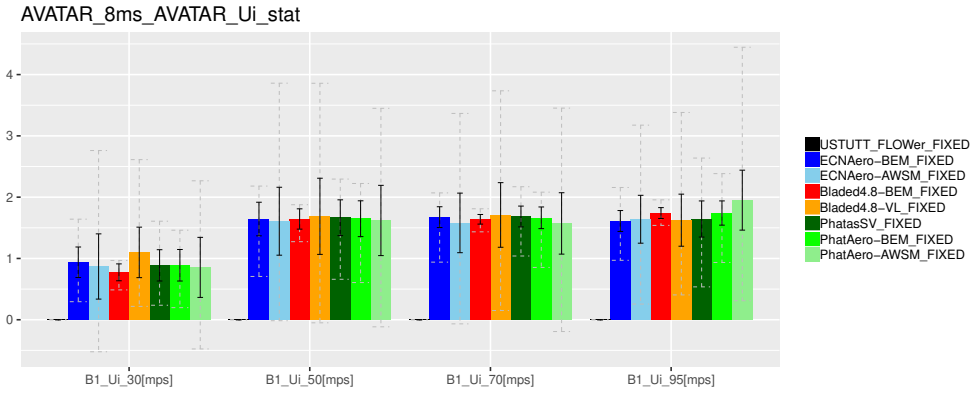

(a) Axial induced velocity

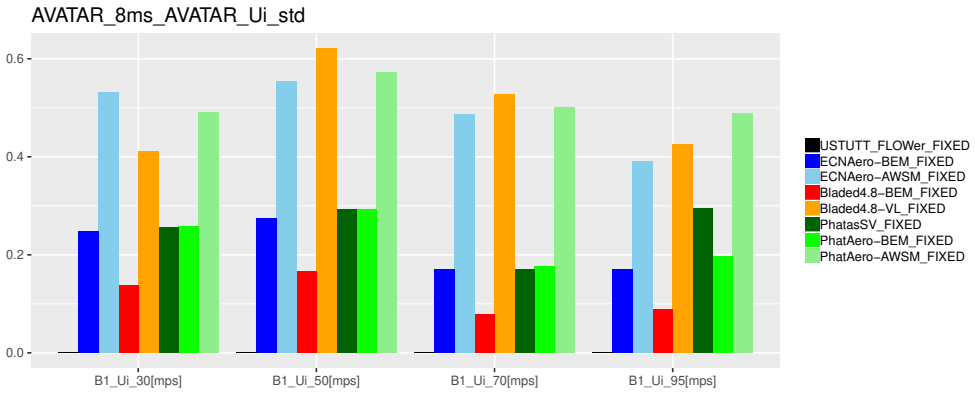

(b) Axial induced velocity (standard deviation)

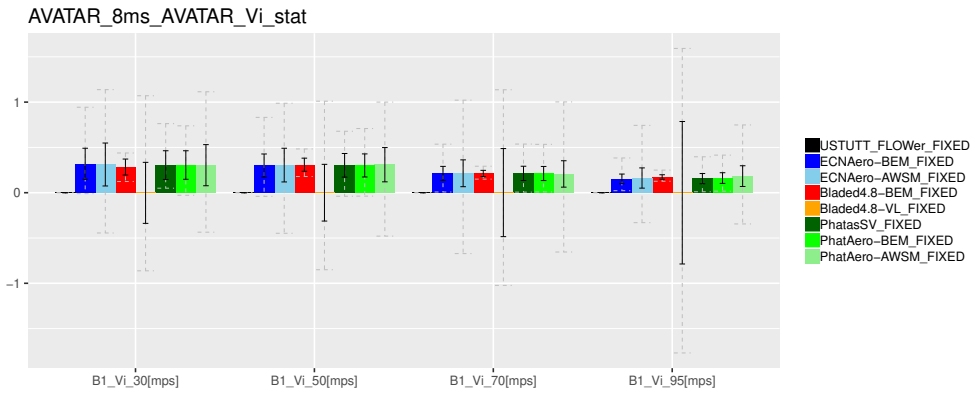

(c) Tangential induced velocity

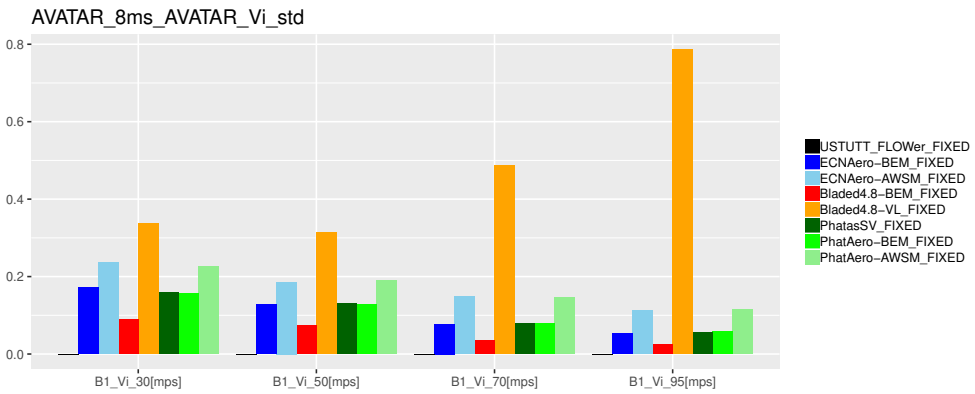

(d) Tangential induced velocity (standard deviation)

Figure B.15: Induced velocities

B.1.4 Equivalent load levels

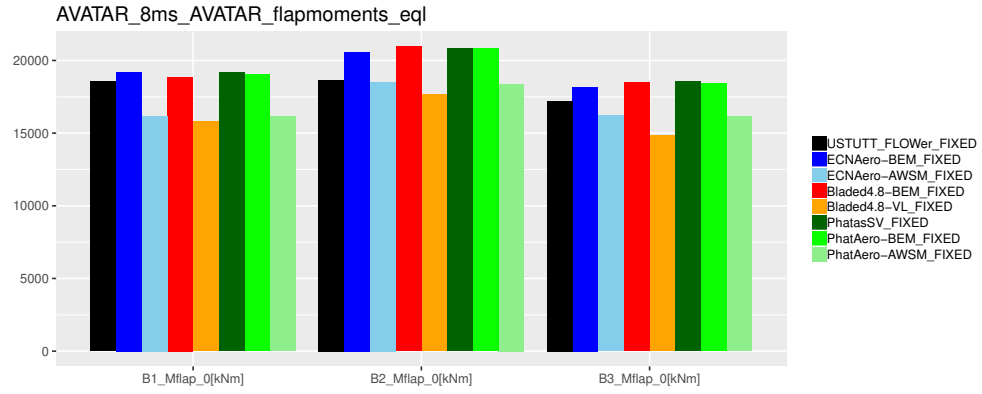

(a) Flapwise moments

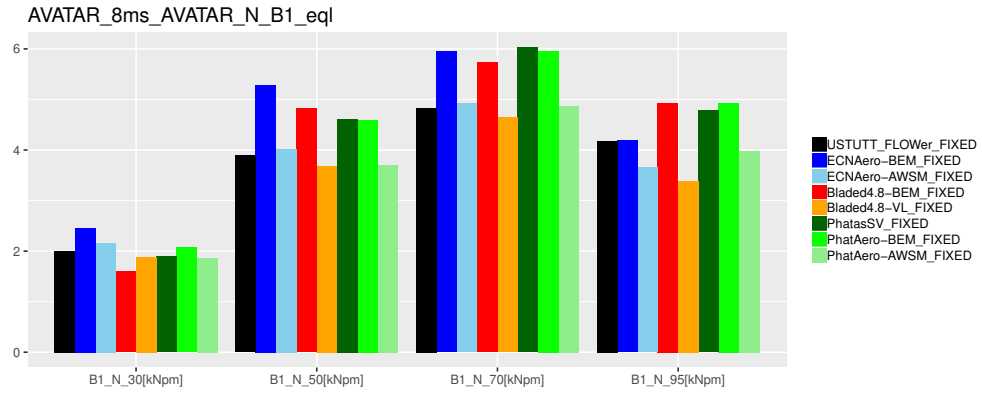

(b) Normal force

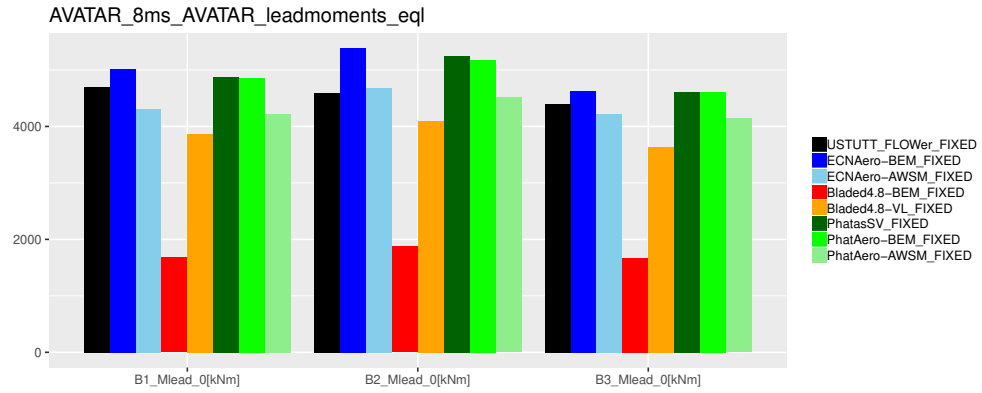

(c) Leadwise moments

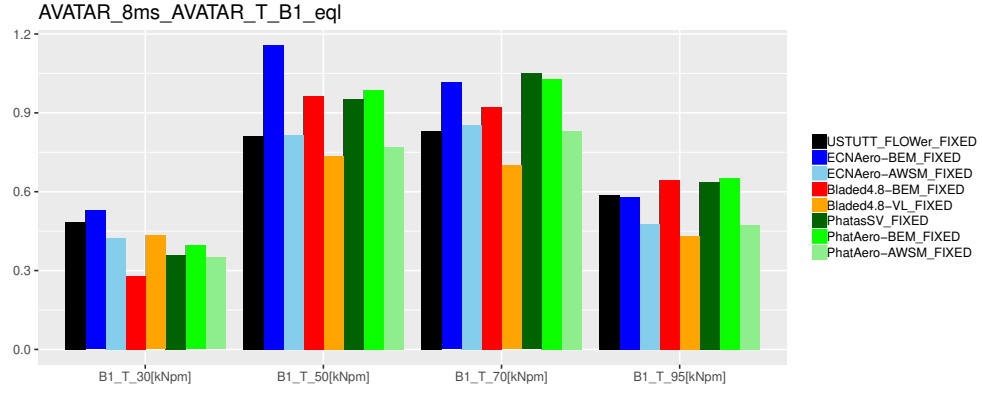

(d) Tangential force

Figure B.16: Forces and moments

B.1.5 Staircase plots

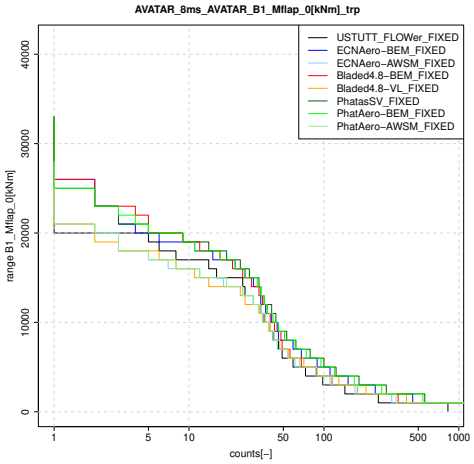

(a) Flapwise blade root moment

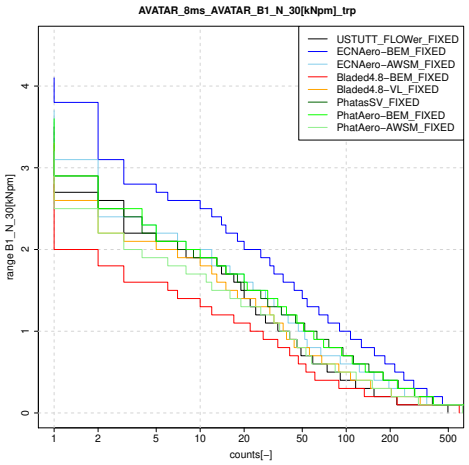

(b) Normal force, 30%R

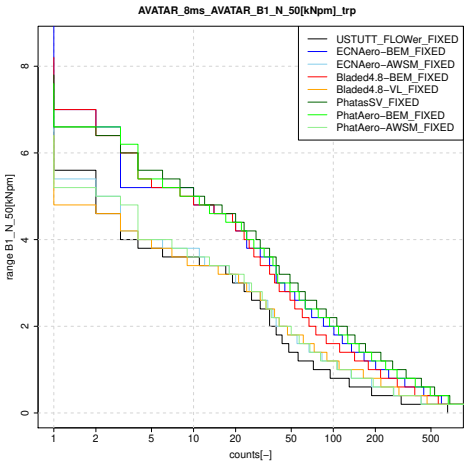

(c) Normal force, 50%R

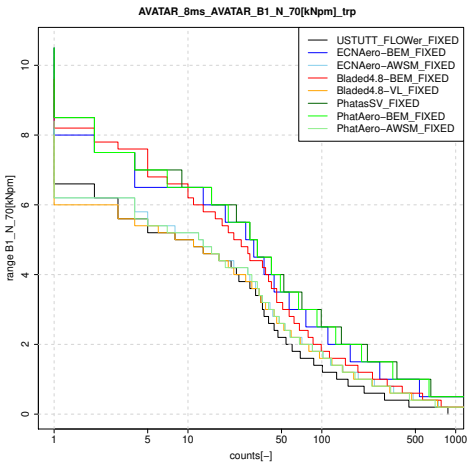

(d) Normal force, 70%R

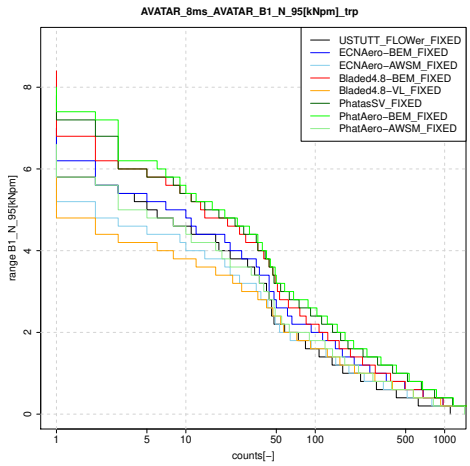

(e) Normal force, 95%R

Figure B.17: Flapwise moment and normal forces

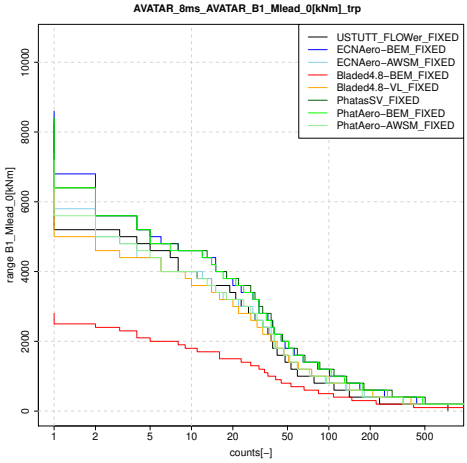

(a) Leadwise blade root moment

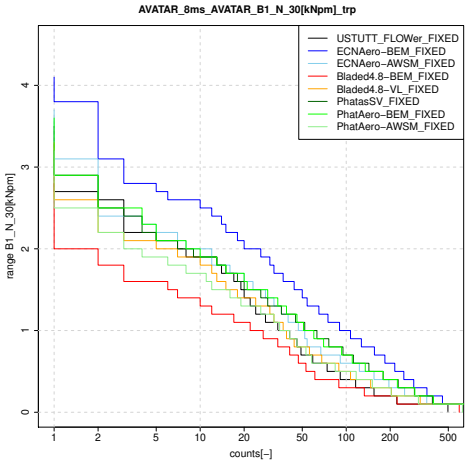

(b) Tangential force, 30%R

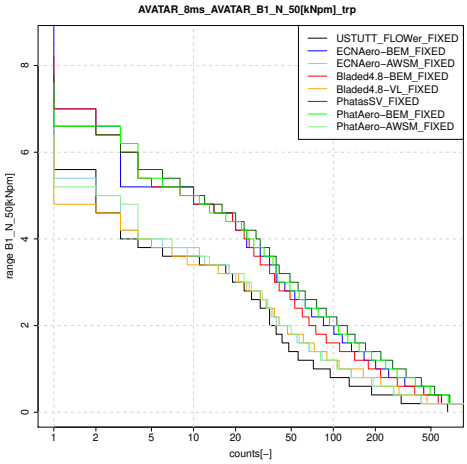

(c) Tangential force, 50%R

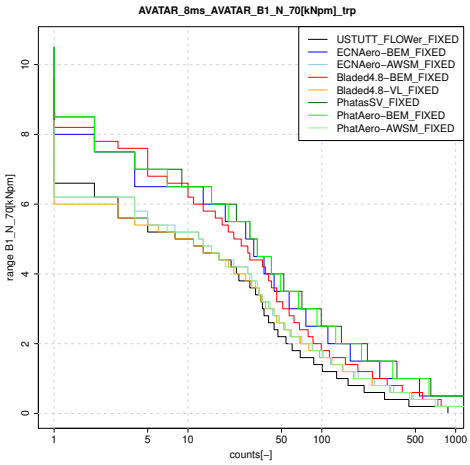

(d) Tangential force, 70%R

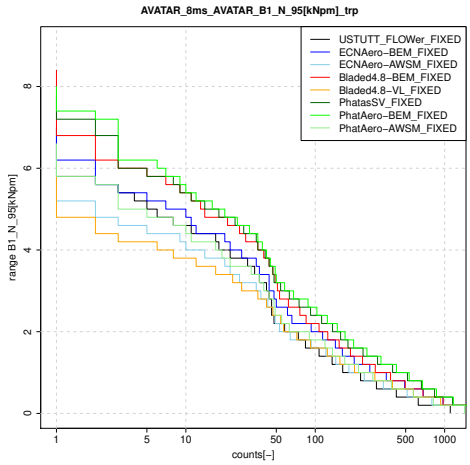

(e) Tangential force, 95%R

Figure B.18: Leadwise moment and tangential forces

B.1.6 PSD

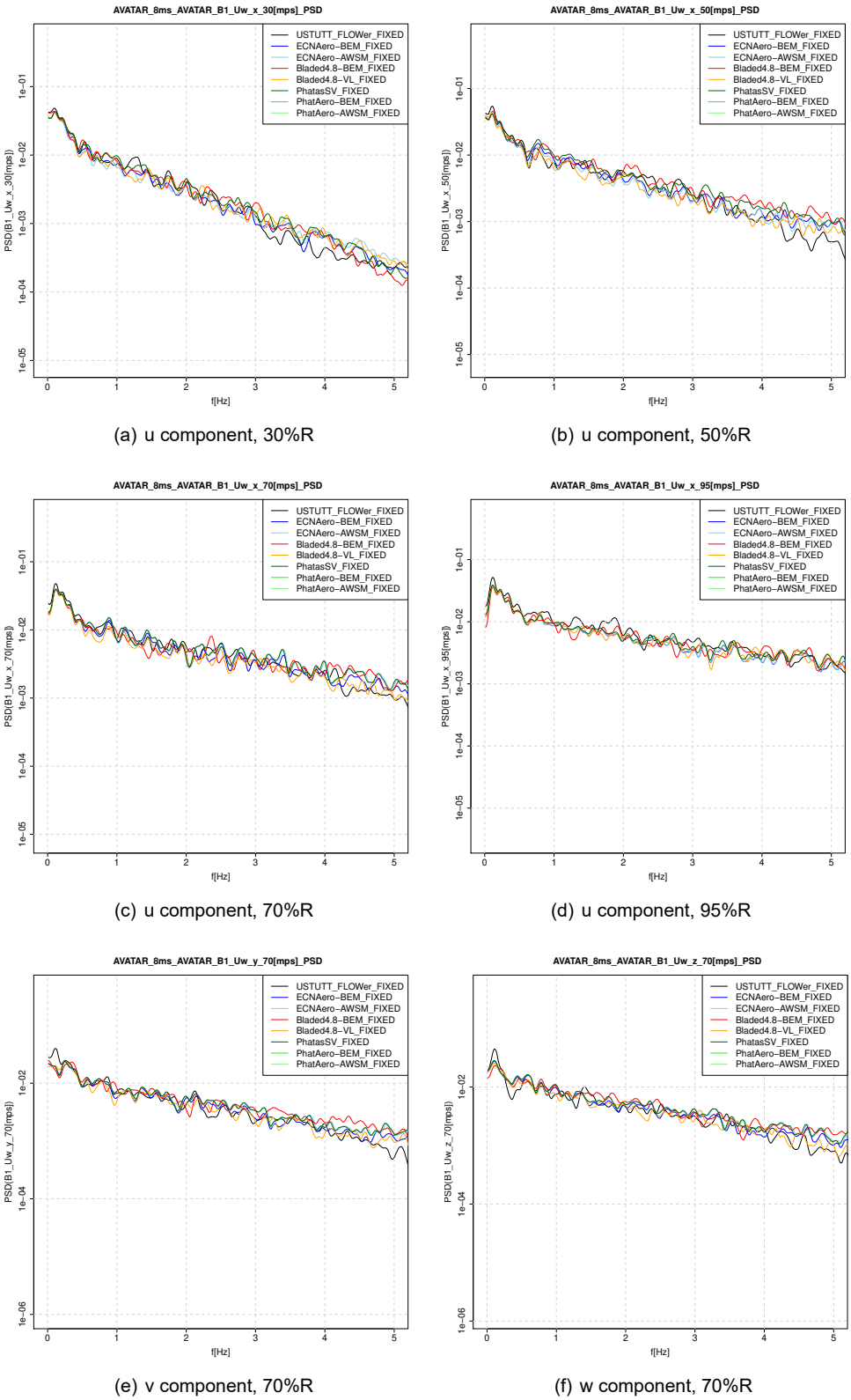

(a) u component, 30%R

(b) u component, 50%R

(c) u component, 70%R

(d) u component, 95%R

(e) v component, 70%R

(f) w component, 70%R

Figure B.19: Wind probes at blade 1

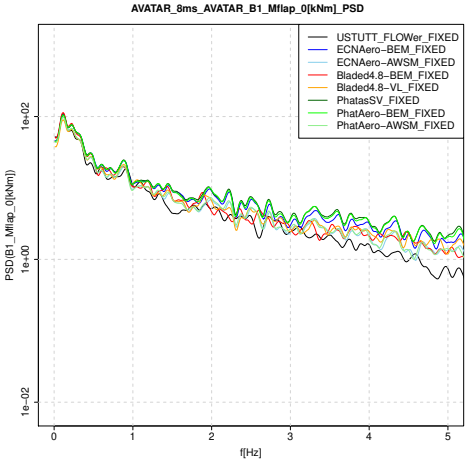

(a) Flapwise blade root moment

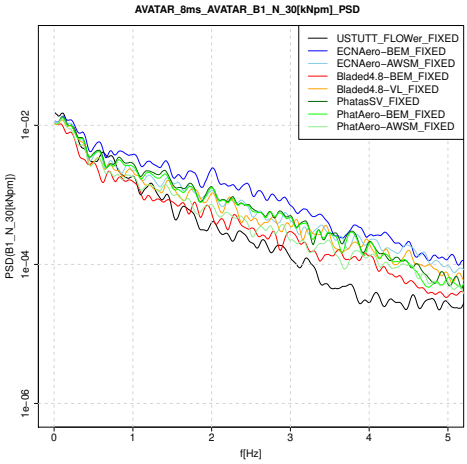

(b) Normal force, 30%R

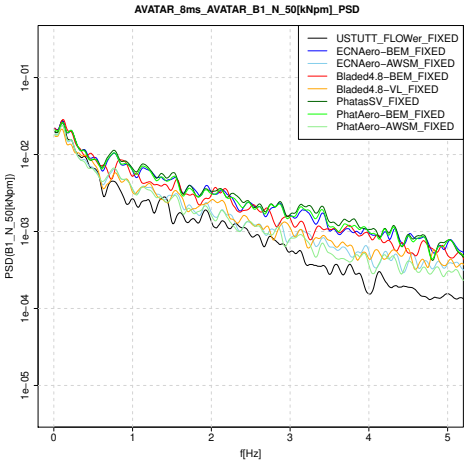

(c) Normal force, 50%R

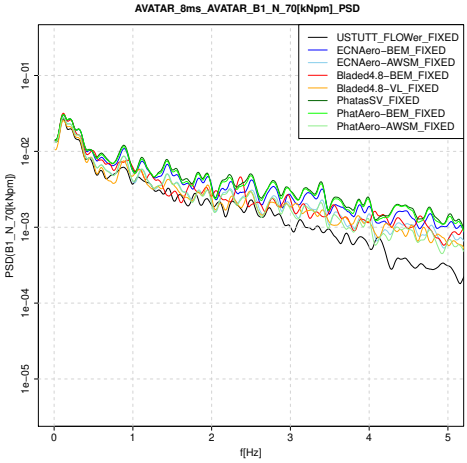

(d) Normal force, 70%R

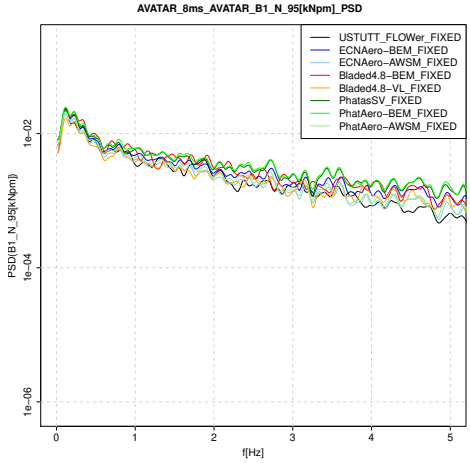

(e) Normal force, 95%R

Figure B.20: Flapwise moment and normal forces

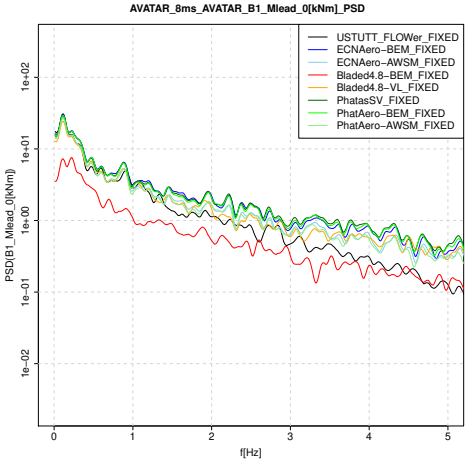

(a) Leadwise blade root moment

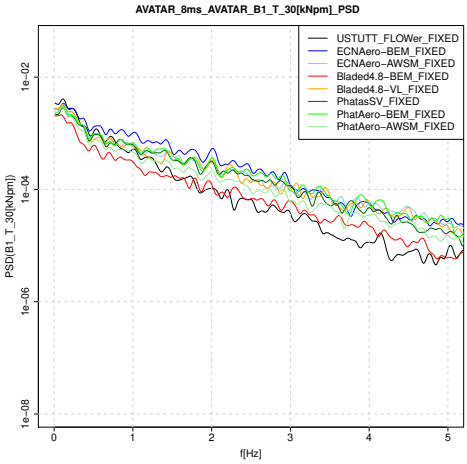

(b) Tangential force, 30%R

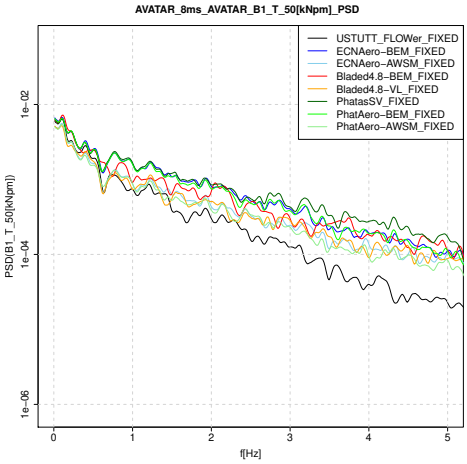

(c) Tangential force, 50%R

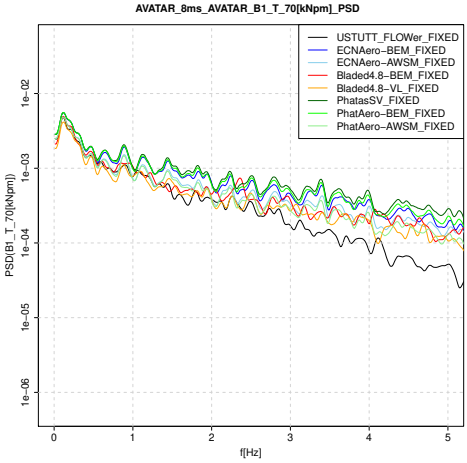

(d) Tangential force, 70%R

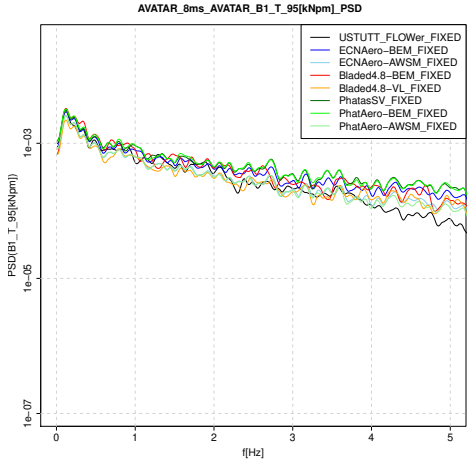

(e) Tangential force, 95%R

Figure B.21: Leadwise moment and tangential forces

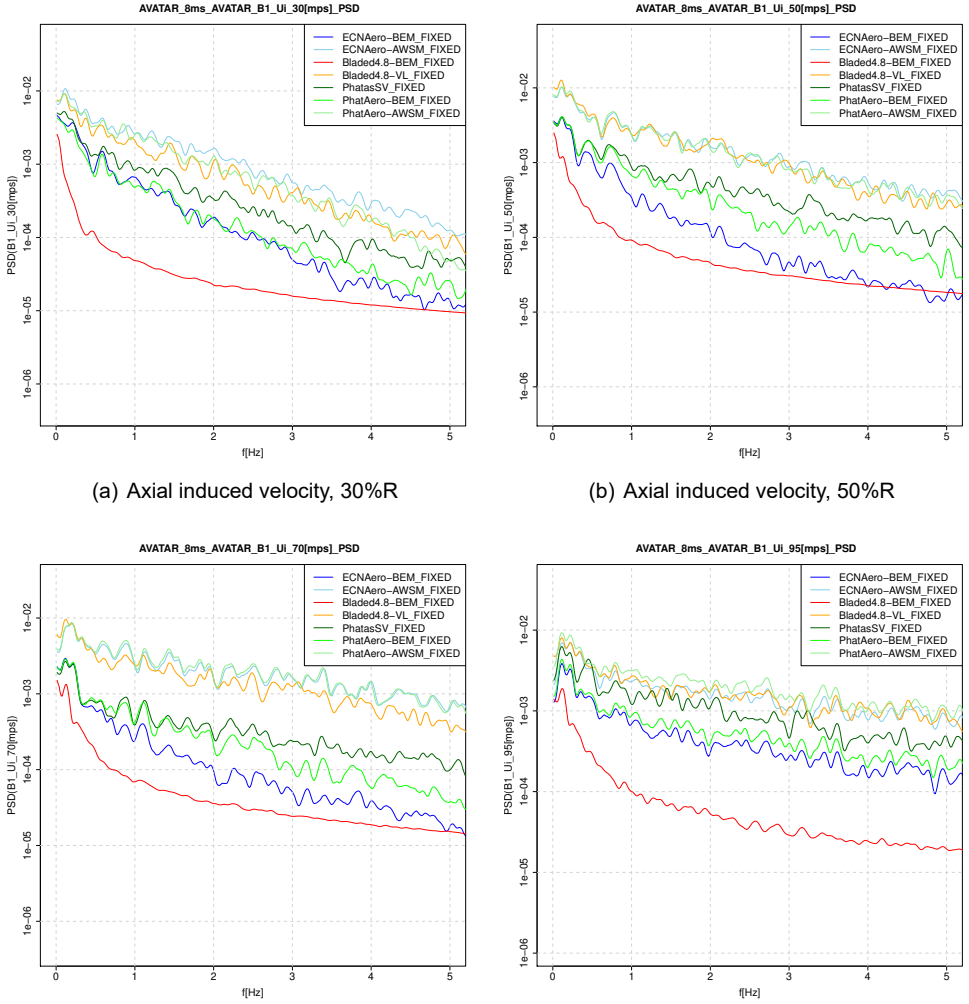

(a) Axial induced velocity, 30%R

(b) Axial induced velocity, 50%R

(c) Axial induced velocity, 70%R

(d) Axial induced velocity, 95%R

Figure B.22: Axial induced velocities

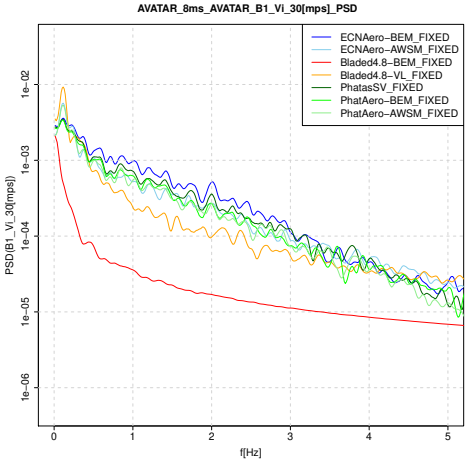

(a) Tangential induced velocity, 30%R

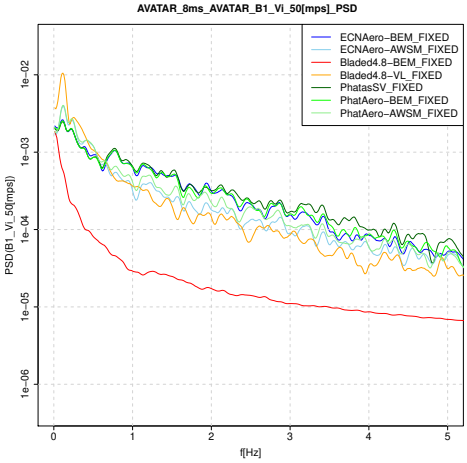

(b) Tangential induced velocity, 50%R

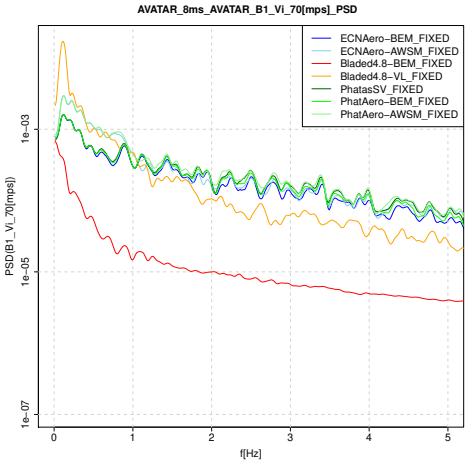

(c) Tangential induced velocity, 70%R

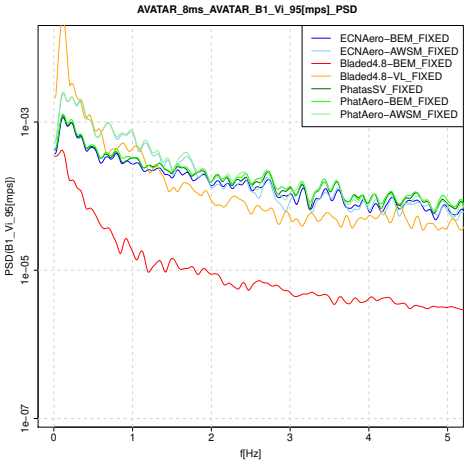

(d) Tangential induced velocity, 95%R

Figure B.23: Tangential induced velocities

B.2 8 m/s prescribed case

B.2.1 Time (zoomed)

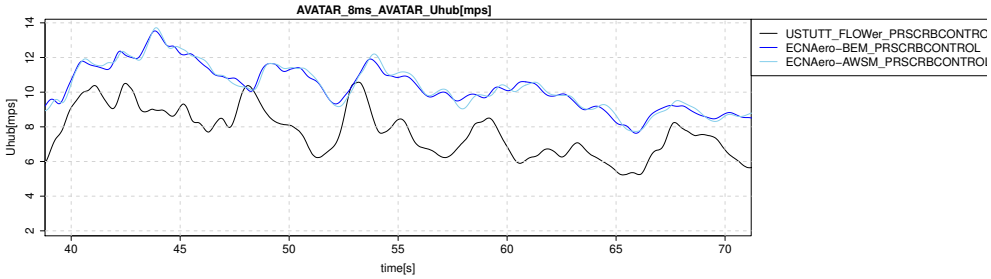

(a) Hub height wind speed

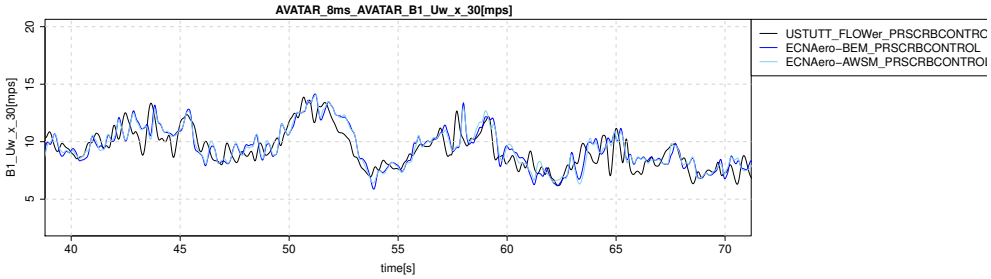

(b) Wind probe axial velocity at 30%R

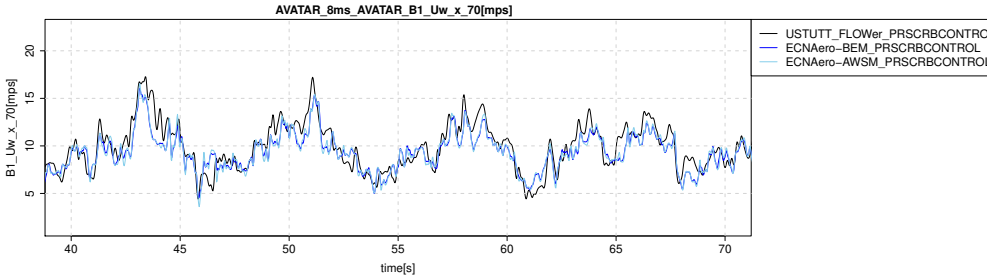

(c) Wind probe axial velocity at 70%R

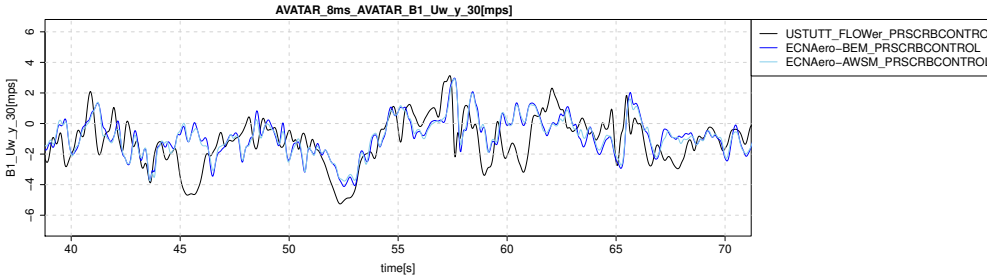

(d) Wind probe lateral velocity at 30%R

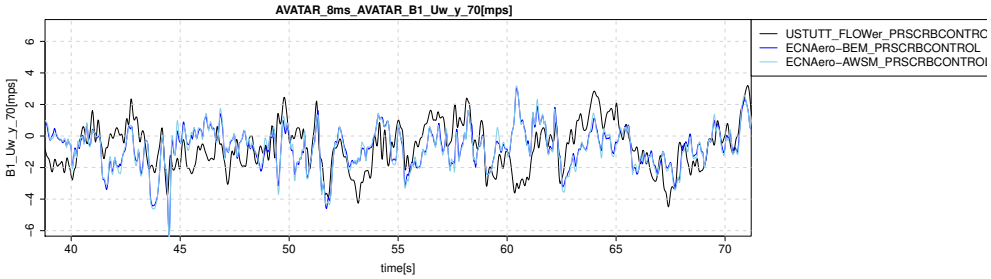

(e) Wind probe lateral velocity at 70%R

Figure B.24: Wind speed alignment check

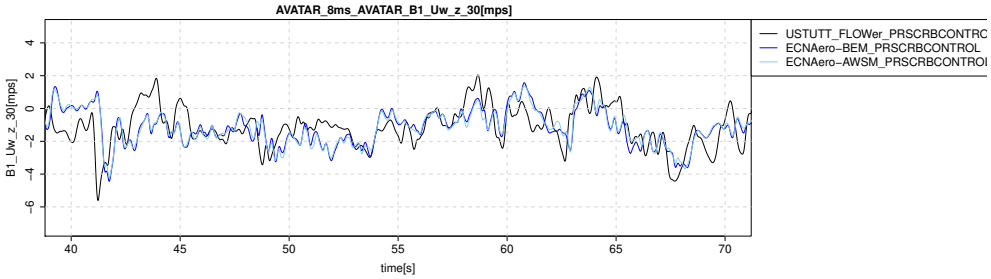

(a) Wind probe vertical velocity at 30%R

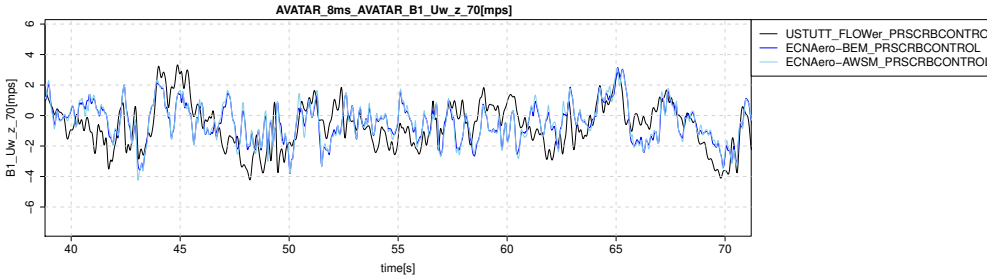

(b) Wind probe vertical velocity at 70%R

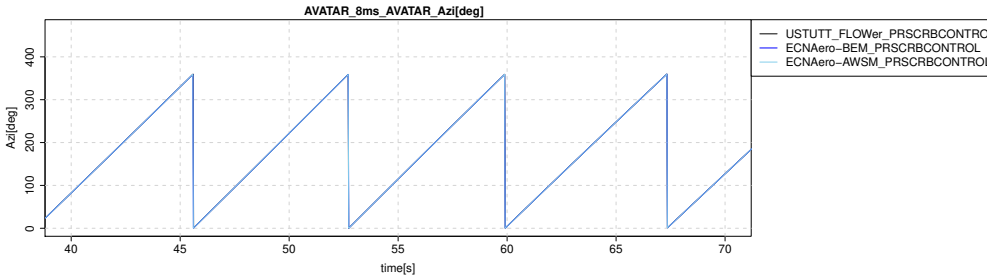

(c) Rotor azimuth angle

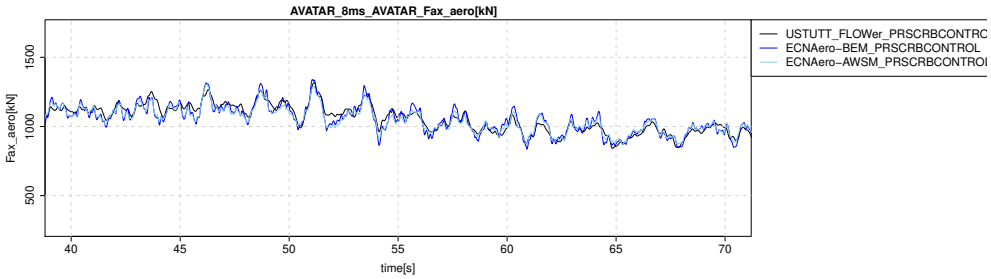

(d) Rotor axial force

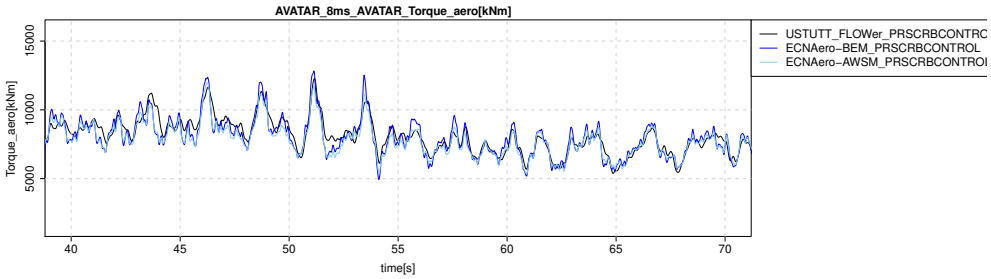

(e) Rotor torque

Figure B.25: Alignment check

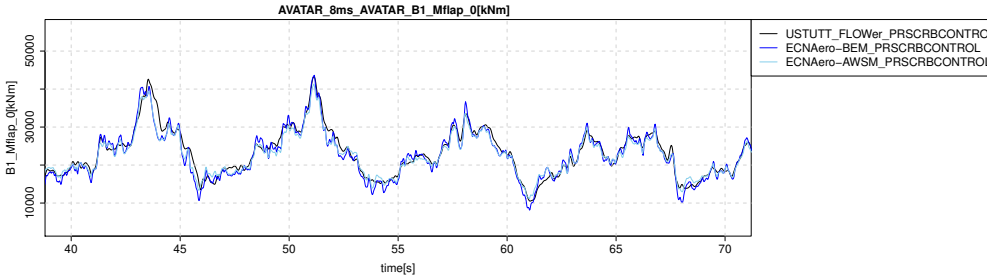

(a) Flapwise blade root moment

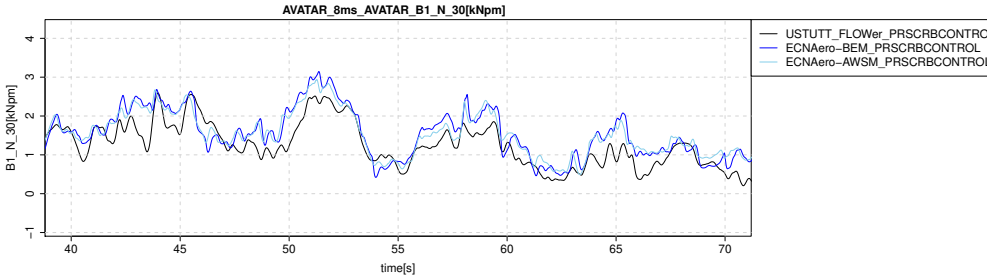

(b) Chord normal force at 30%R

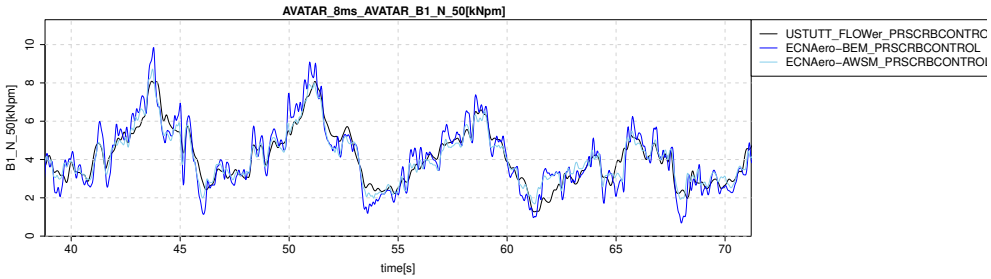

(c) Chord normal force at 50%R

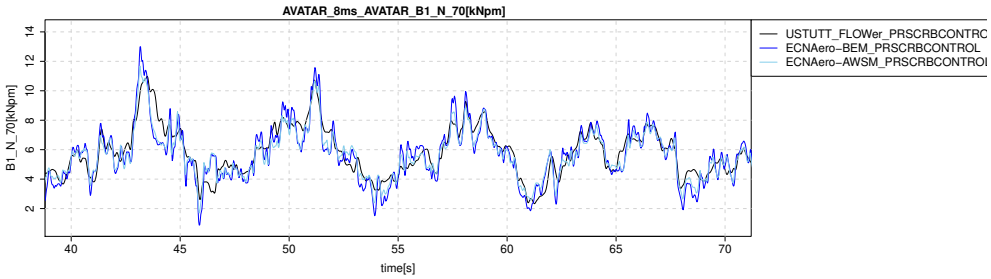

(d) Chord normal force at 70%R

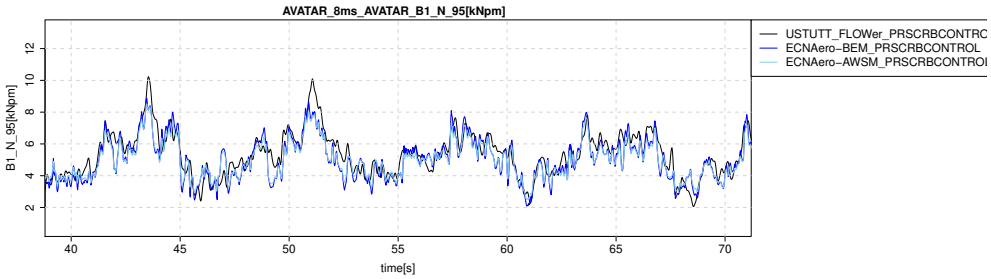

(e) Chord normal force at 95%R

Figure B.26: Flapwise moment and normal force

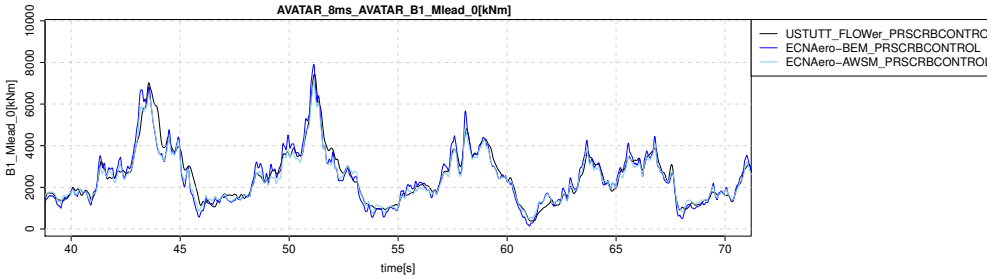

(a) Leadwise blade root moment

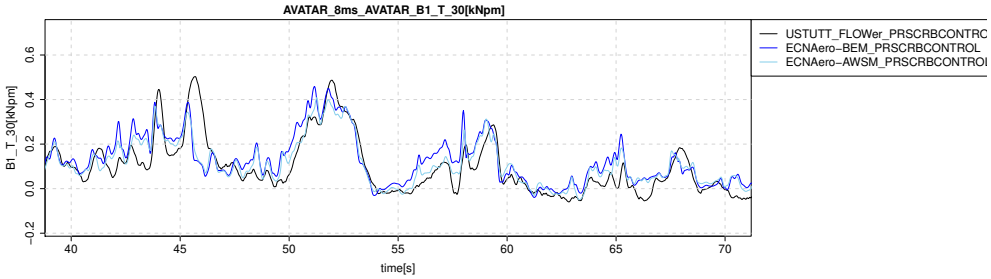

(b) Chord tangential force at 30%R

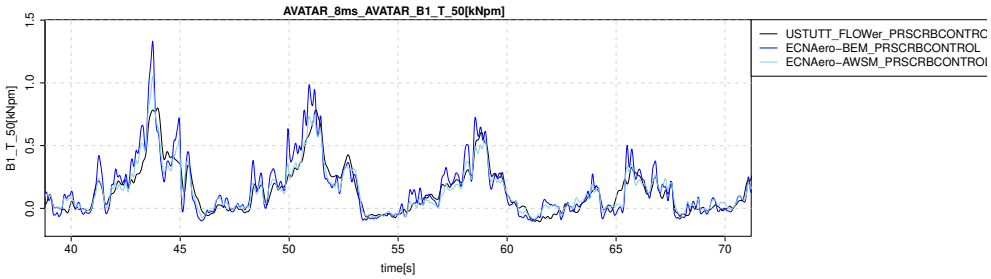

(c) Chord tangential force at 50%R

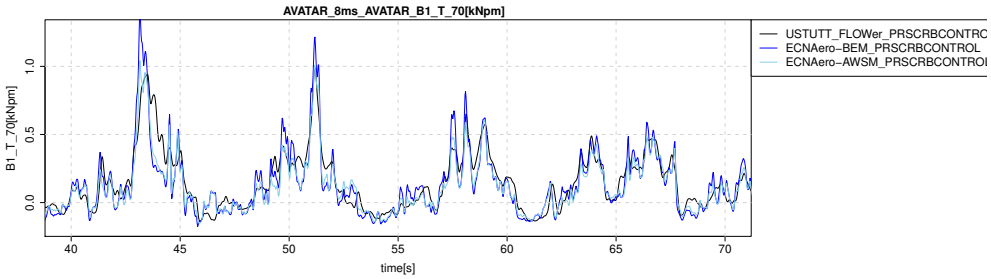

(d) Chord tangential force at 70%R

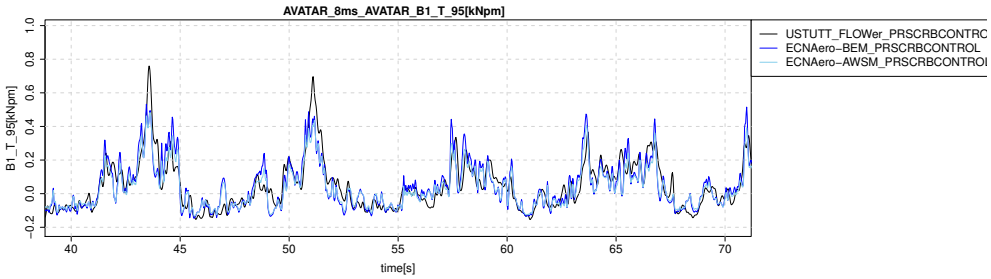

(e) Chord tangential force at 95%R

Figure B.27: Leadwise moment and tangential force

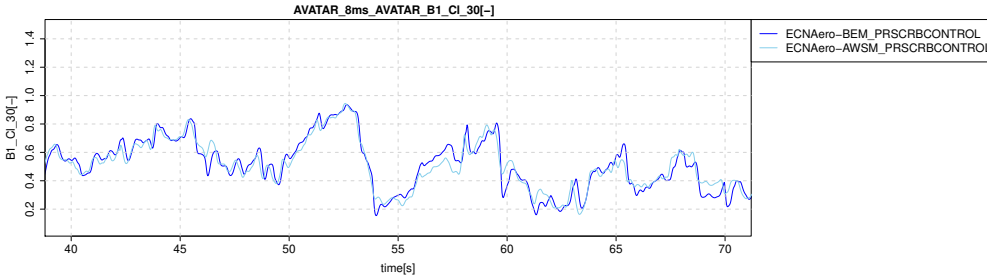

(a) Lift coefficient at 30%R

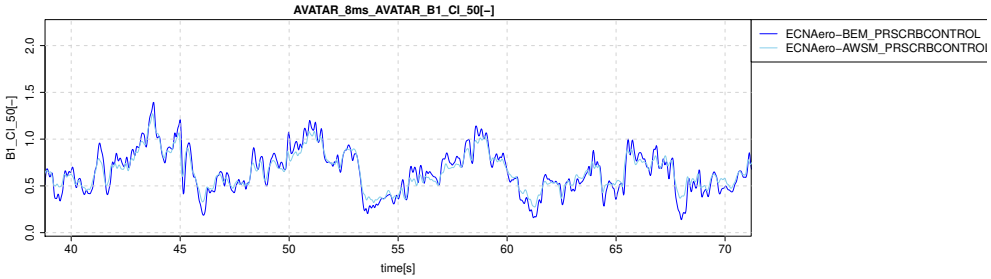

(b) Lift coefficient at 50%R

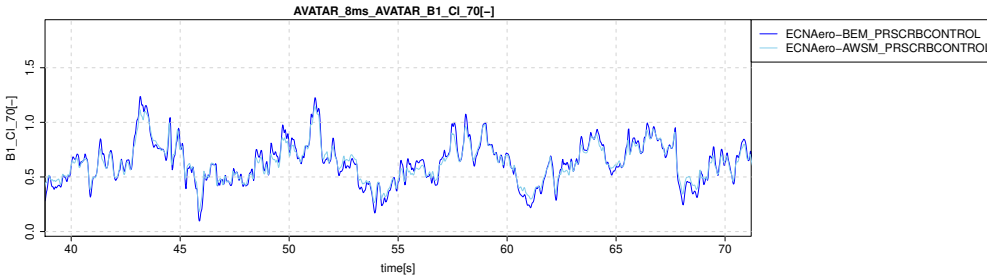

(c) Lift coefficient at 70%R

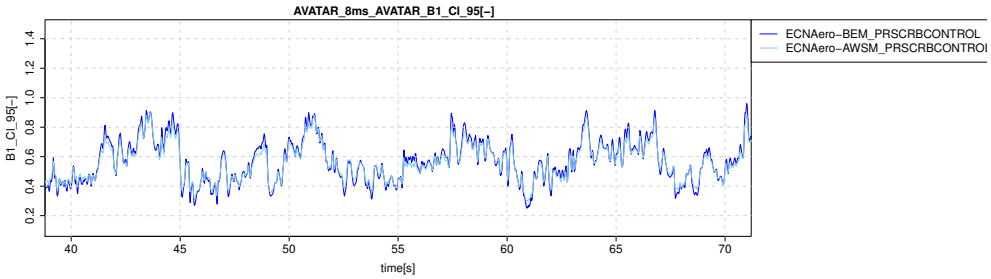

(d) Lift coefficient at 95%R

Figure B.28: Lift coefficients

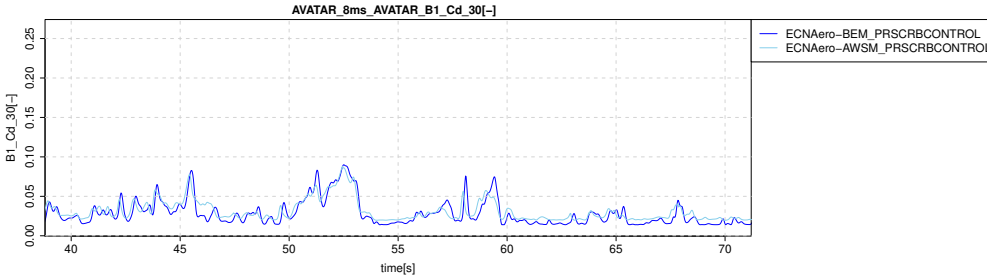

(a) Drag coefficient at 30%R

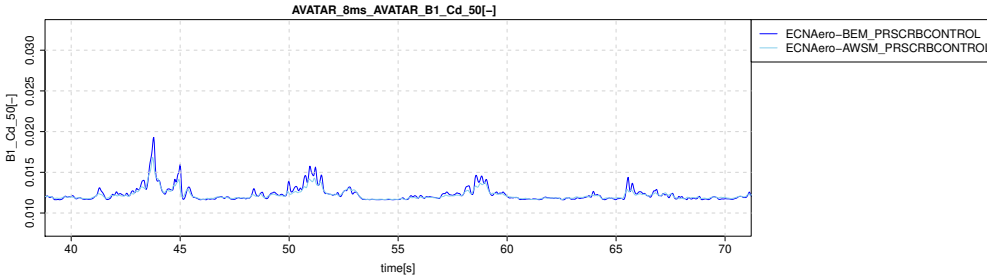

(b) Drag coefficient at 50%R

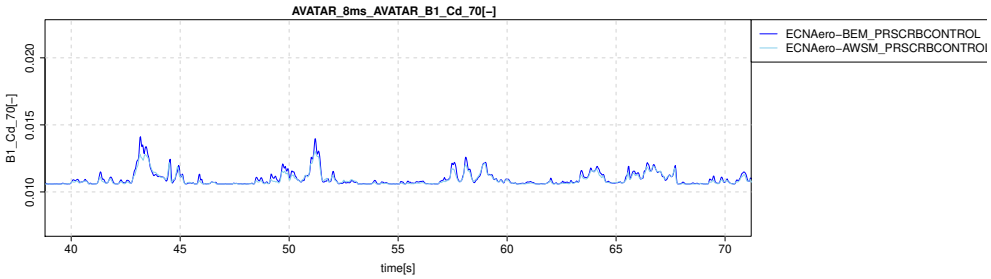

(c) Drag coefficient at 70%R

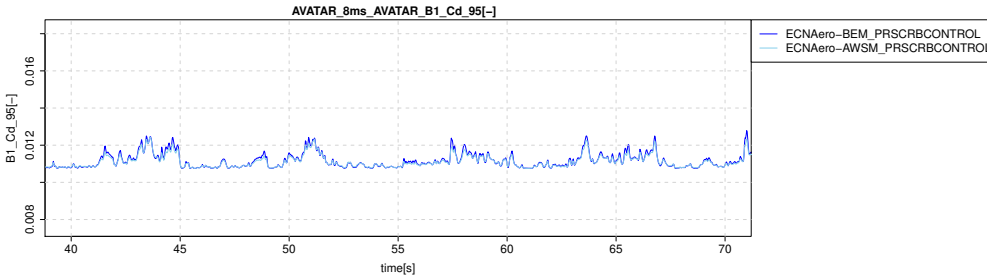

(d) Drag coefficient at 95%R

Figure B.29: Drag coefficients

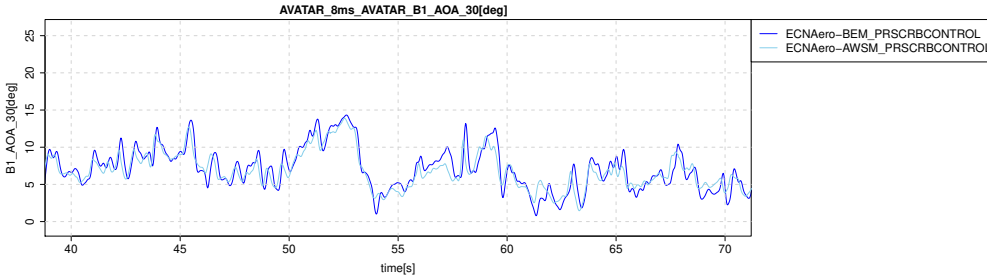

(a) Angle of attack at 30%R

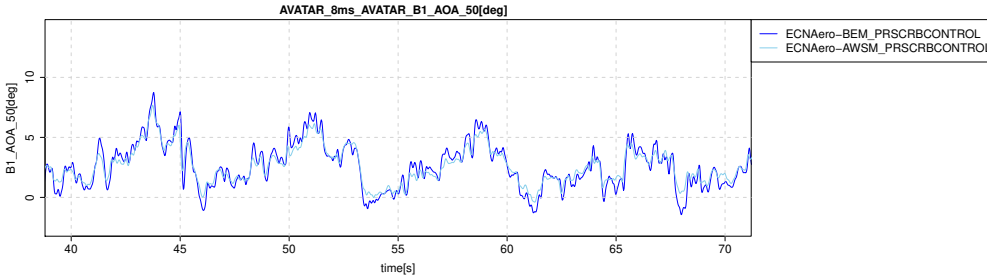

(b) Angle of attack at 50%R

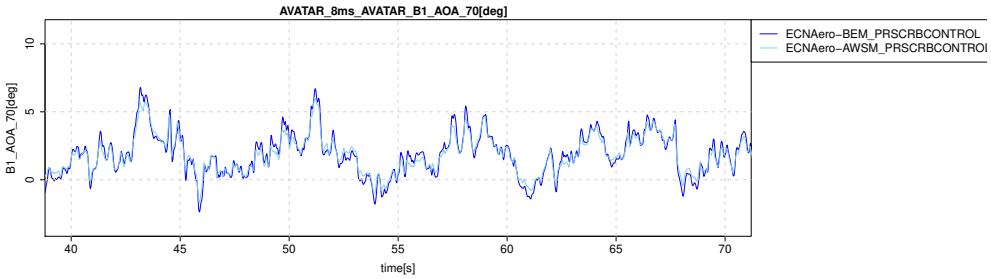

(c) Angle of attack at 70%R

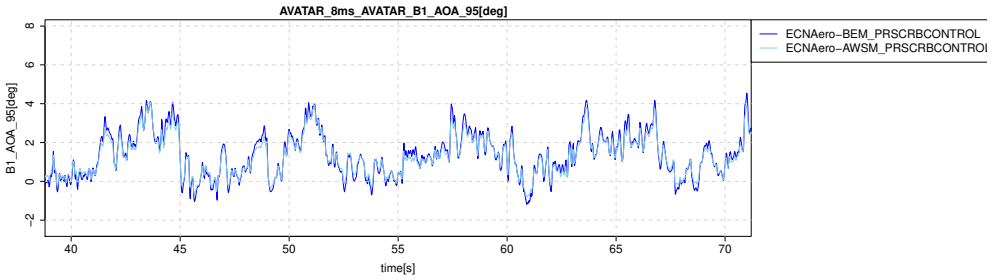

(d) Angle of attack at 95%R

Figure B.30: Angles of attack

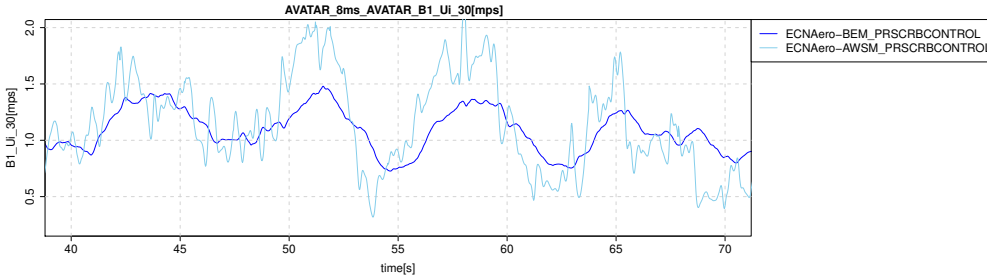

(a) Axial induced velocity at 30%R

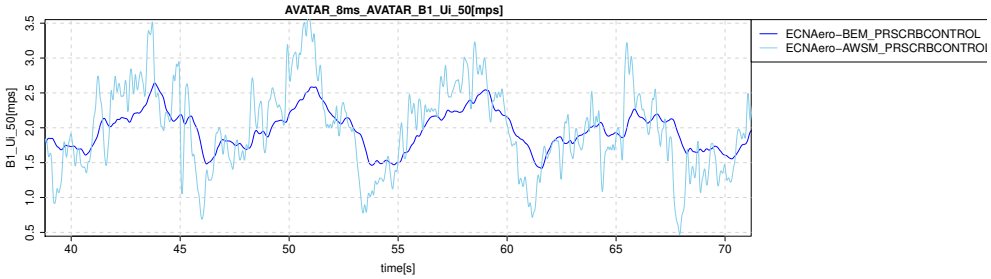

(b) Axial induced velocity at 50%R

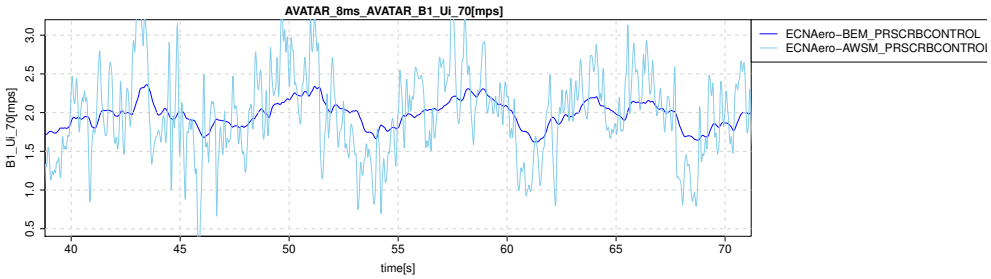

(c) Axial induced velocity at 70%R

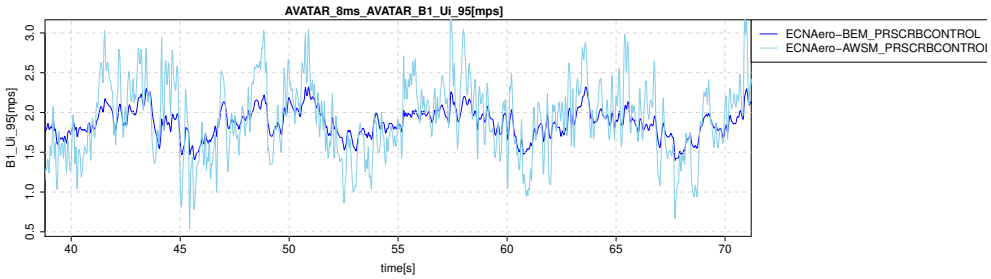

(d) Axial induced velocity at 95%R

Figure B.31: Axial induced velocities

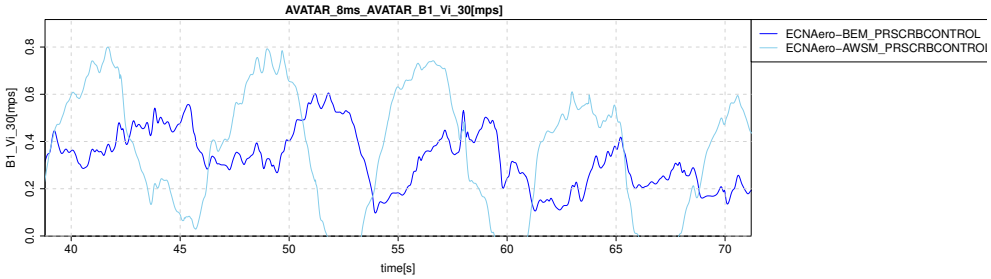

(a) Tangential induced velocity at 30%R

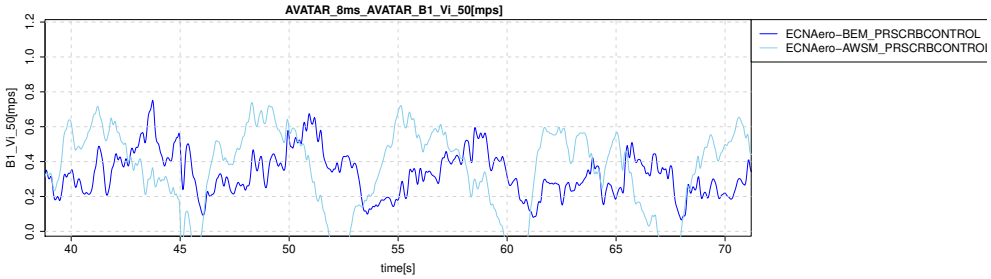

(b) Tangential induced velocity at 50%R

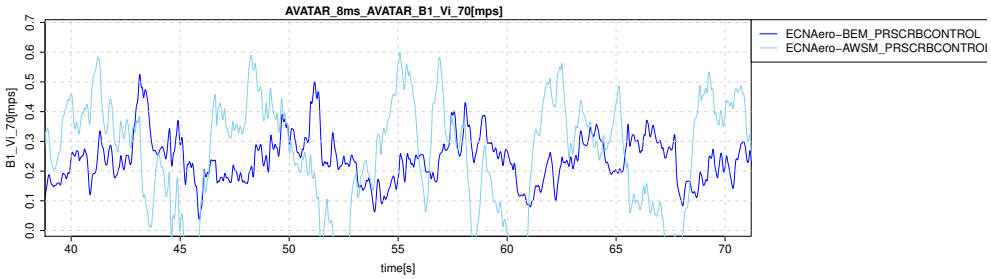

(c) Tangential induced velocity at 70%R

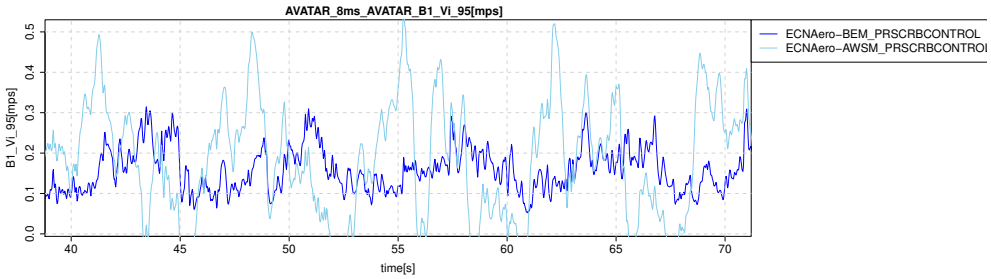

(d) Tangential induced velocity at 95%R

Figure B.32: Tangential induced velocities

B.2.2 Time

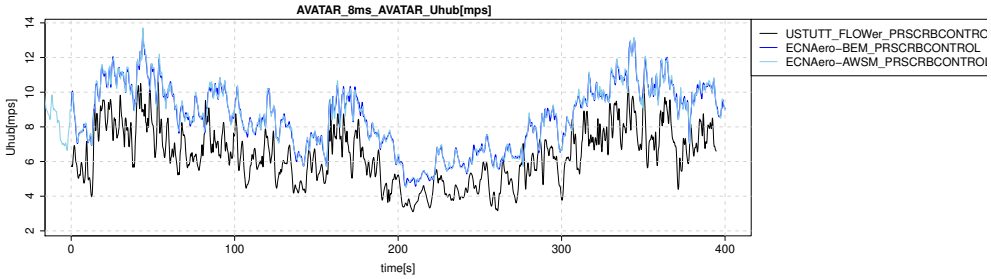

(a) Hub height wind speed

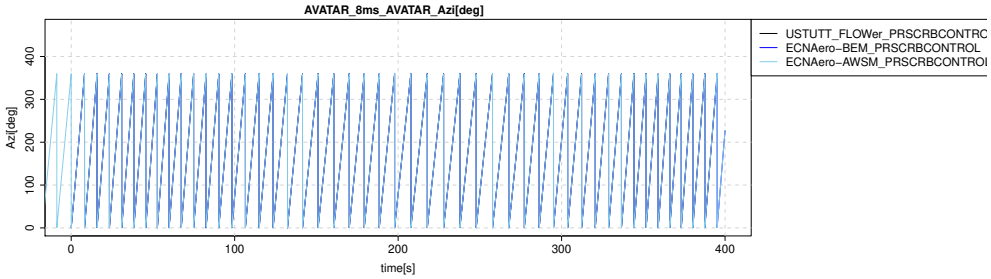

(b) Rotor azimuth

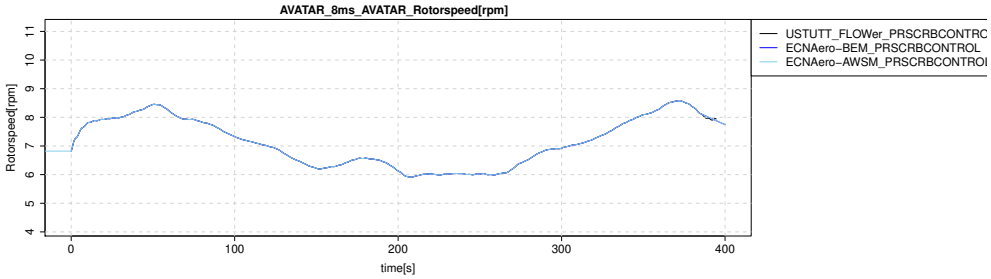

(c) Rotor speed

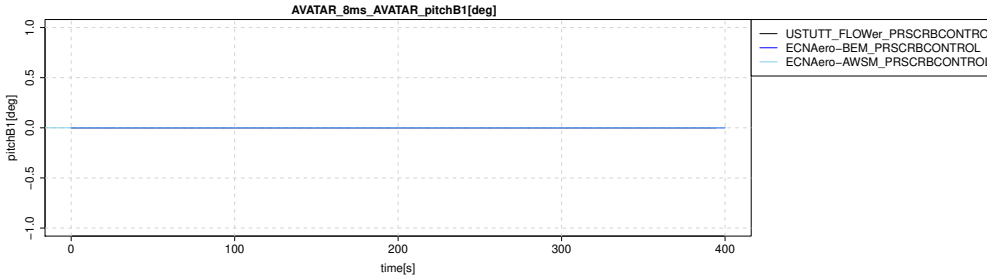

(d) Pitch angle

Figure B.33: Wind and control parameters

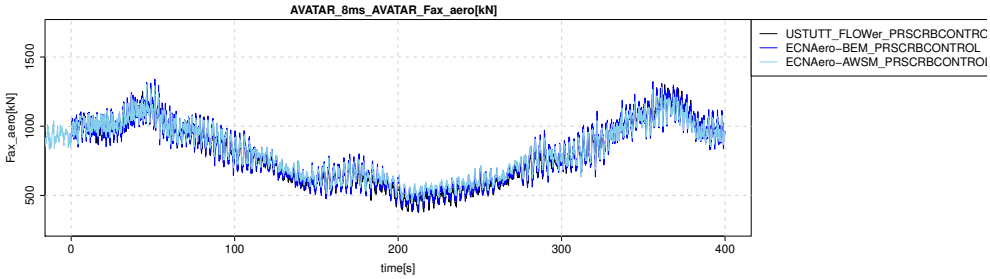

(a) Rotor axial force

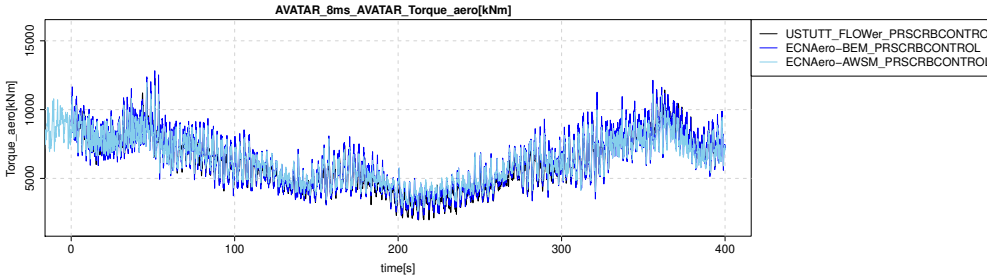

(b) Rotor torque

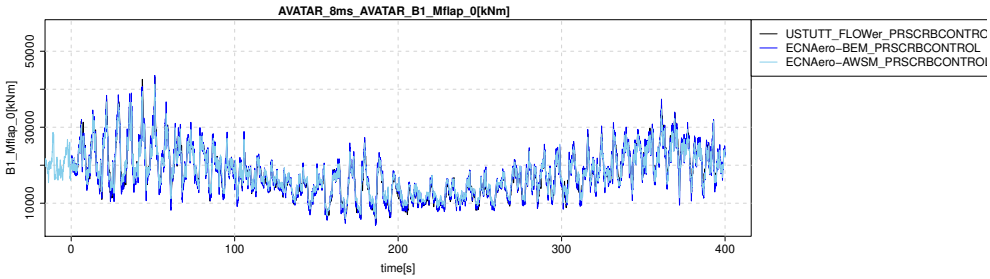

(c) Flapwise blade root moment

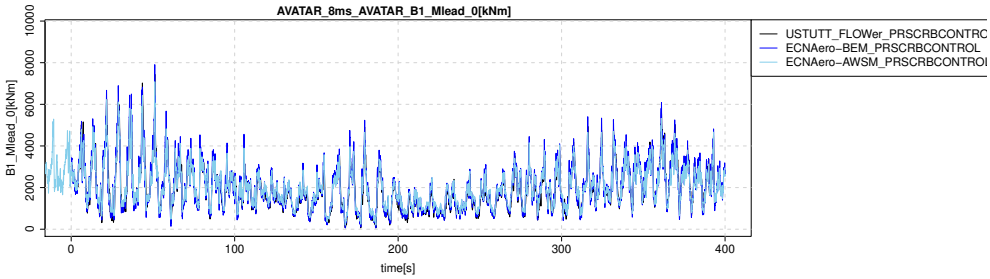

(d) Leadwise blade root moment

Figure B.34: Rotor and blade forces and moments

B.2.3 Statistics

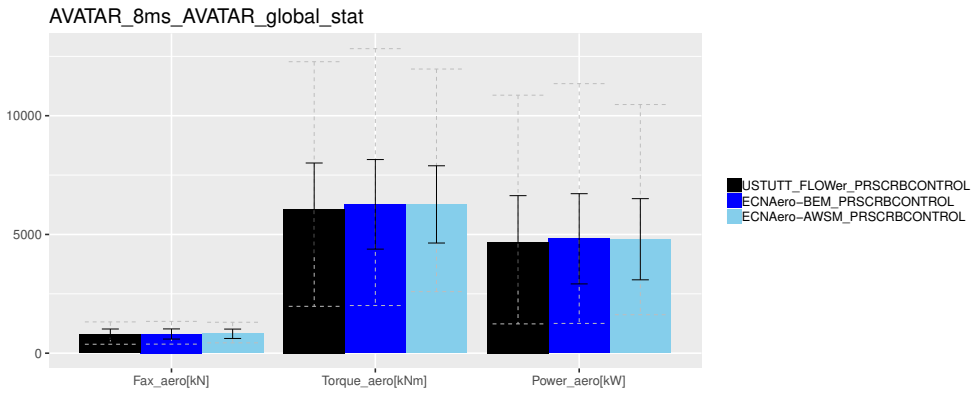

(a) Global performance

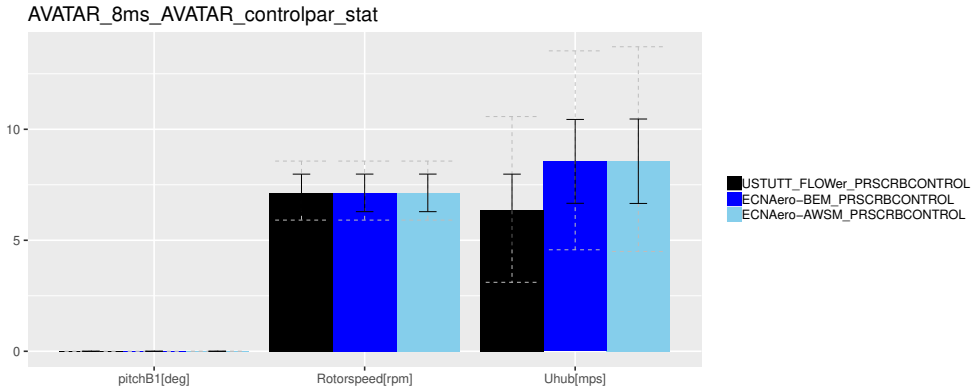

(b) Control parameters

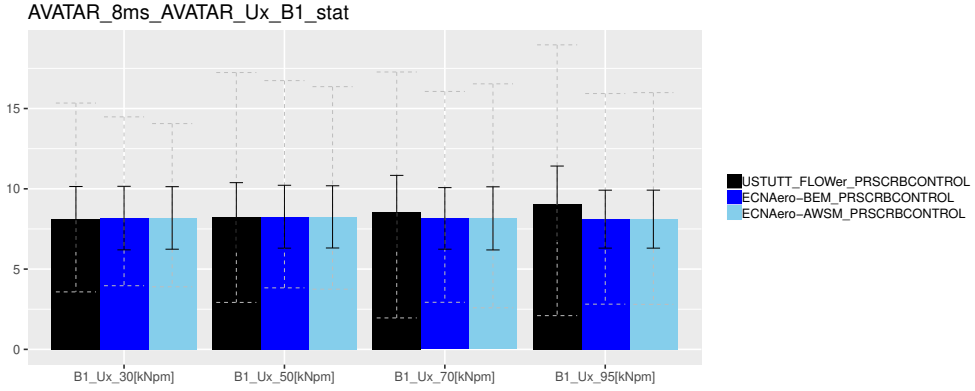

(c) Wind probes, axial

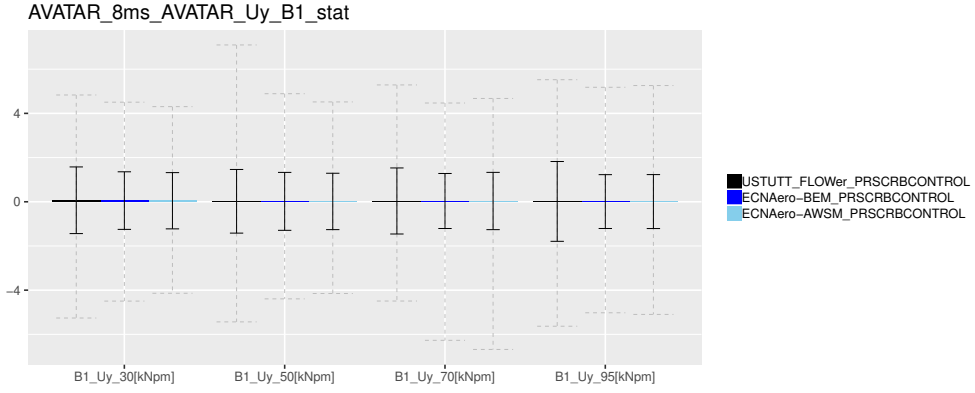

(d) Wind probes, lateral

Figure B.35: Global performance, wind and control parameters

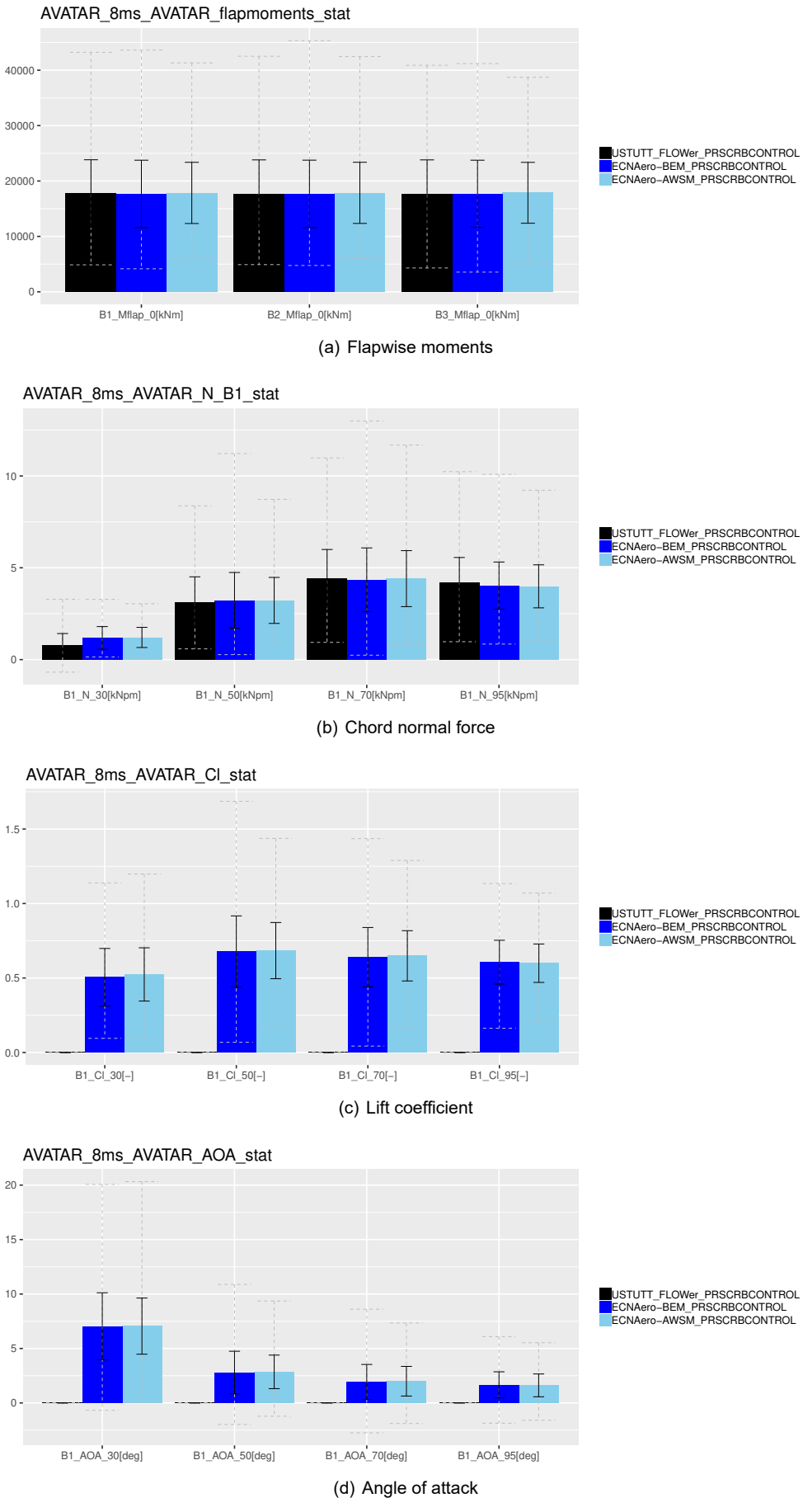

Figure B.36: Force decompostion in axial direction

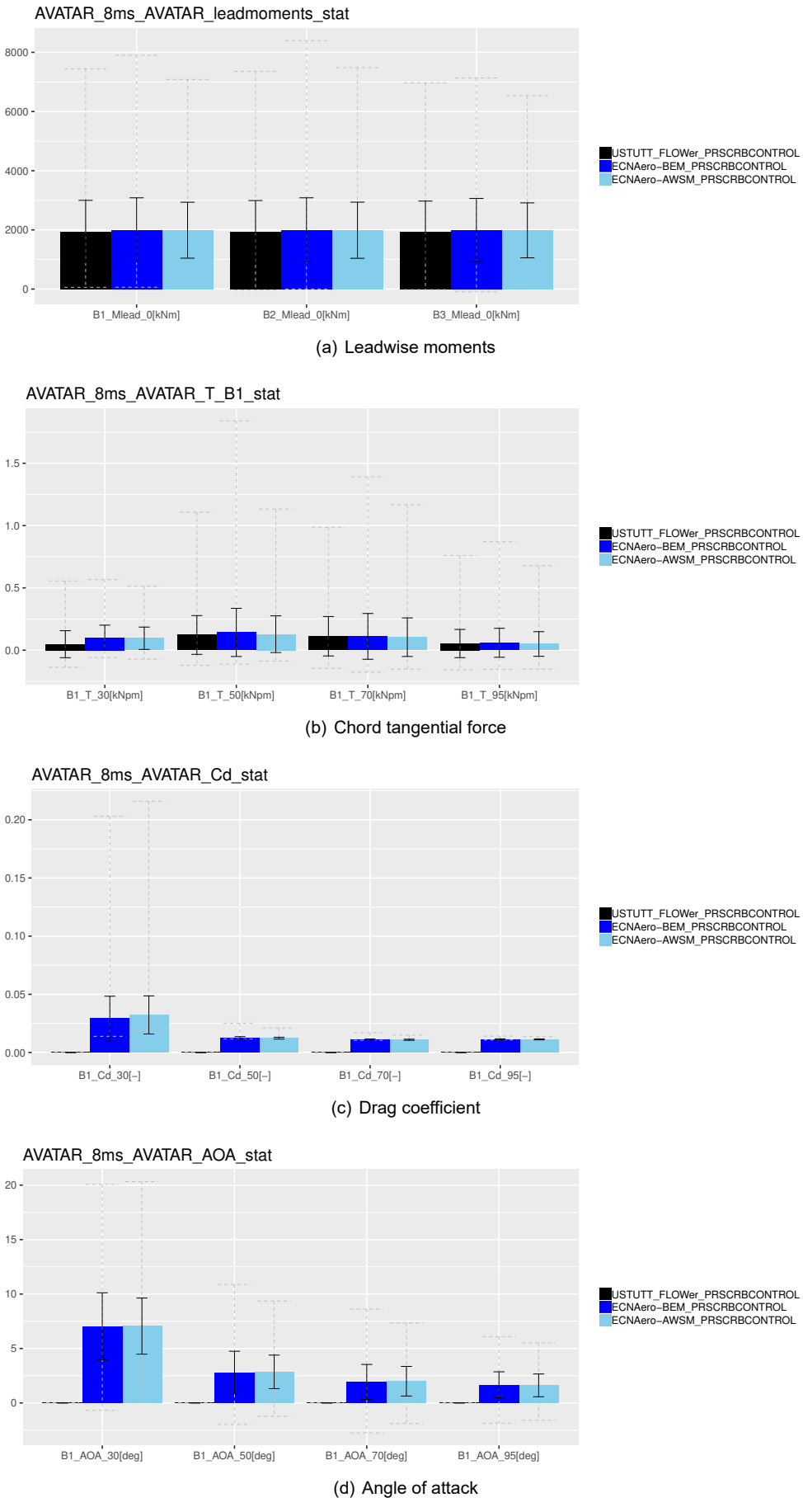

Figure B.37: Force decompostion in tangential direction

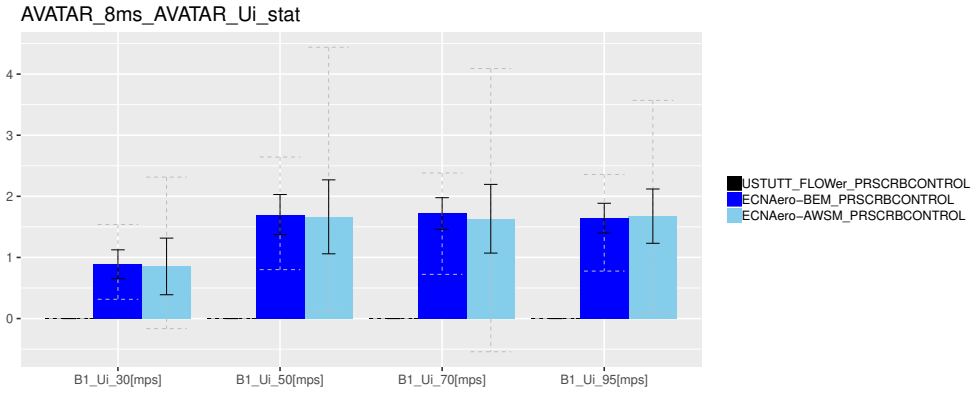

(a) Axial induced velocity

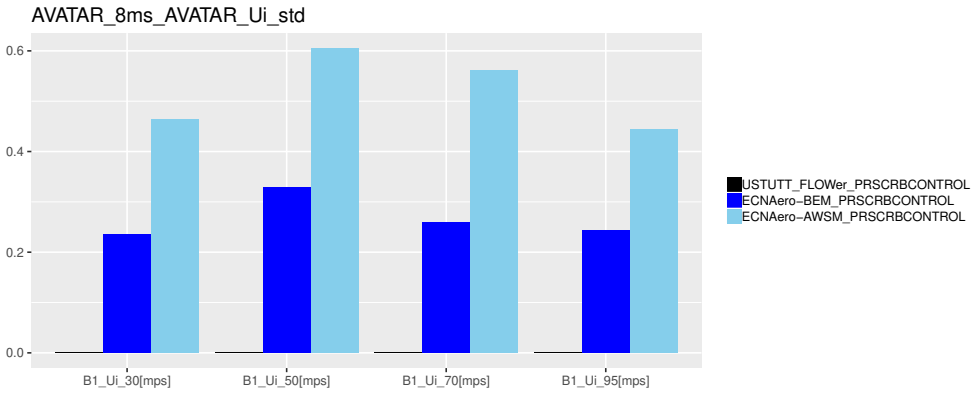

(b) Axial induced velocity (standard deviation)

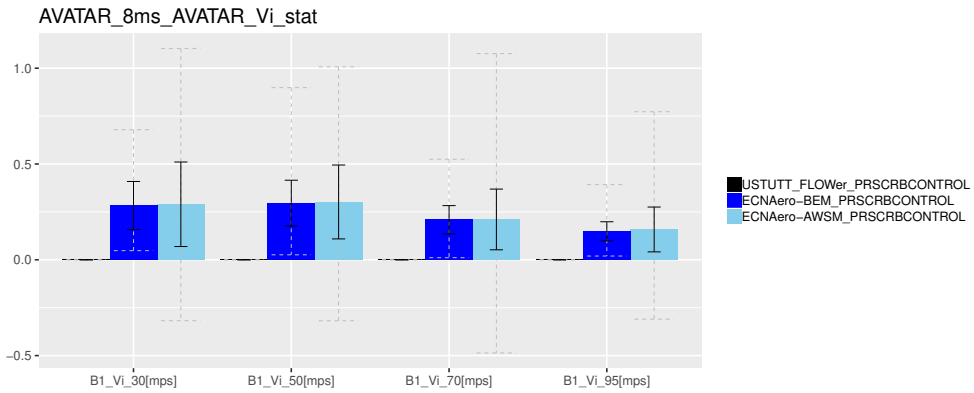

(c) Tangential induced velocity

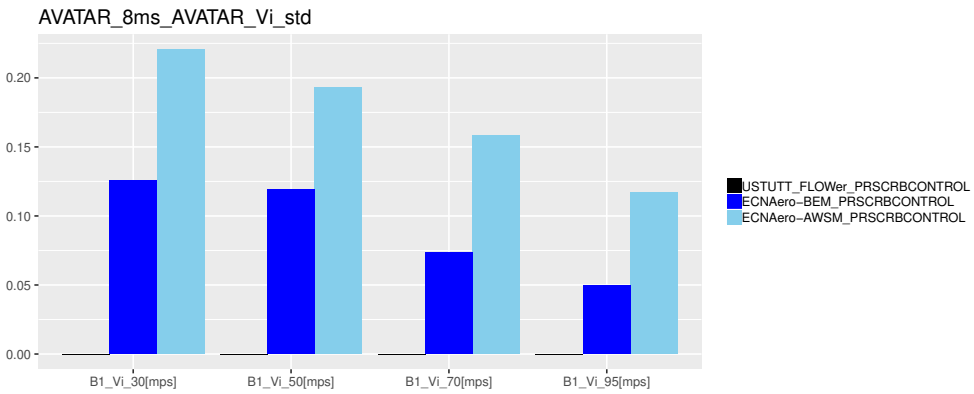

(d) Tangential induced velocity (standard deviation)

Figure B.38: Induced velocities

B.2.4 Equivalent load levels

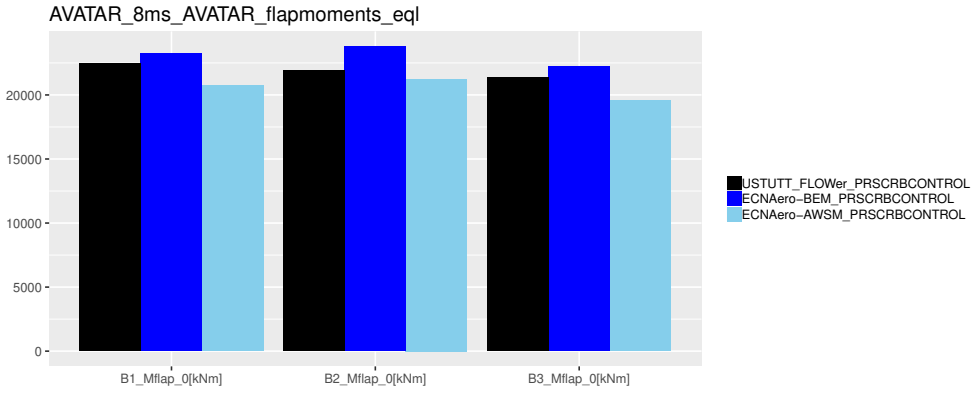

(a) Flapwise moments

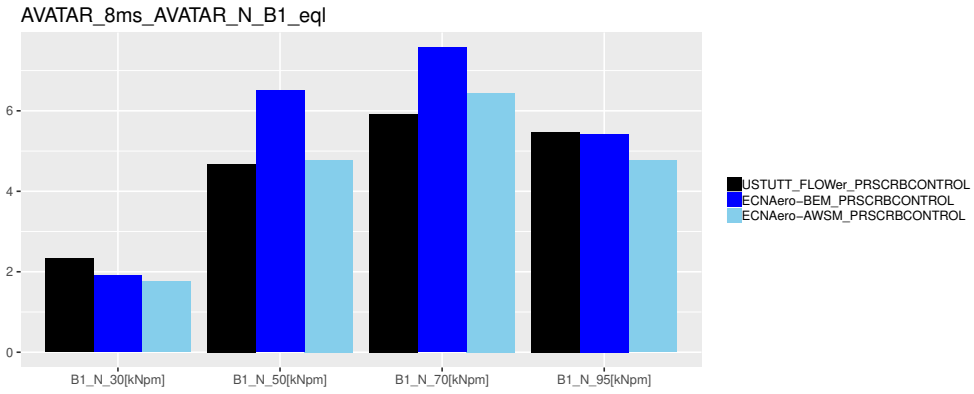

(b) Normal force

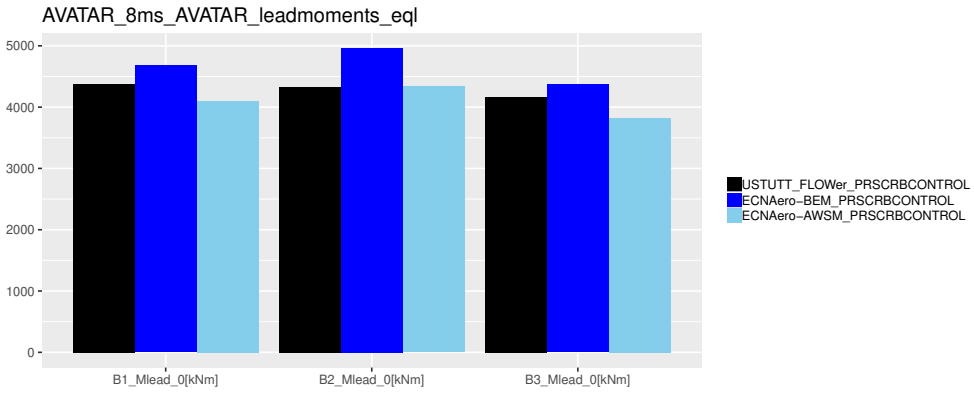

(c) Leadwise moments

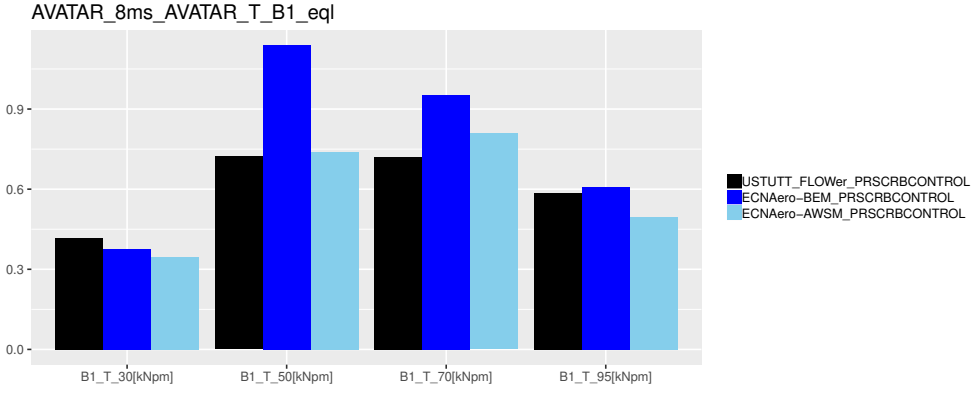

(d) Tangential force

Figure B.39: Forces and moments

B.2.5 Staircase plots

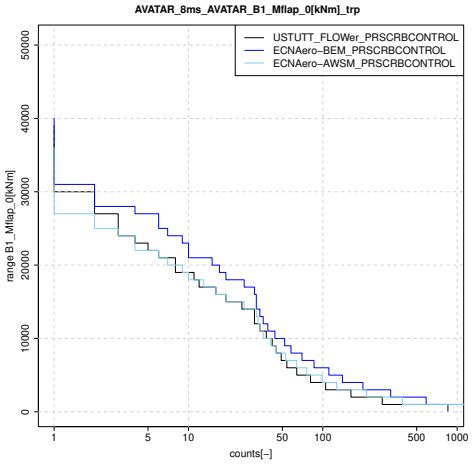

(a) Flapwise blade root moment

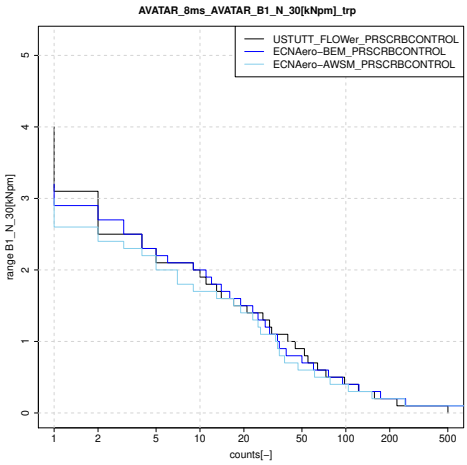

(b) Normal force, 30%R

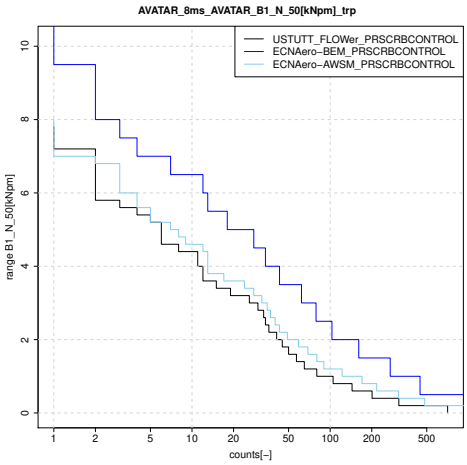

(c) Normal force, 50%R

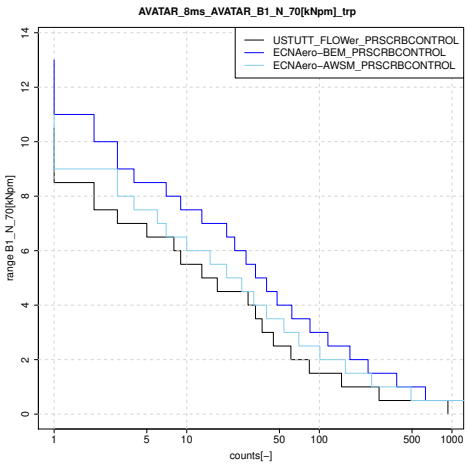

(d) Normal force, 70%R

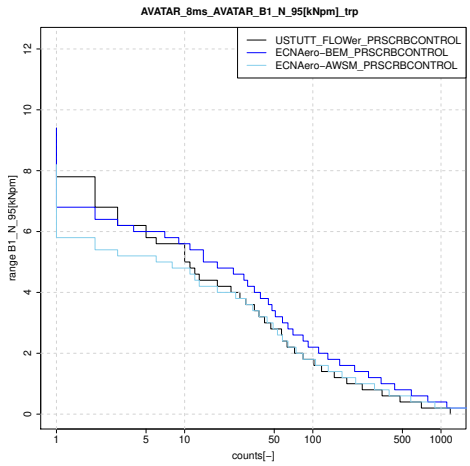

(e) Normal force, 95%R

Figure B.40: Flapwise moment and normal forces

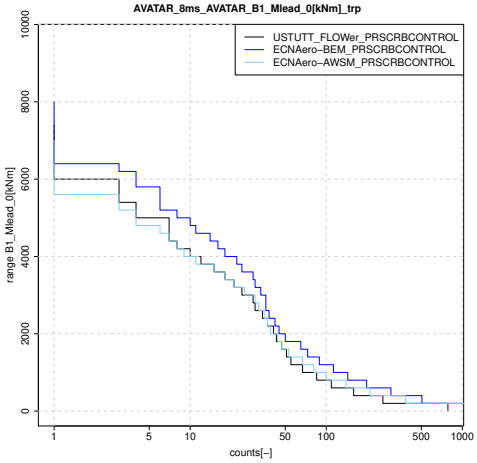

(a) Leadwise blade root moment

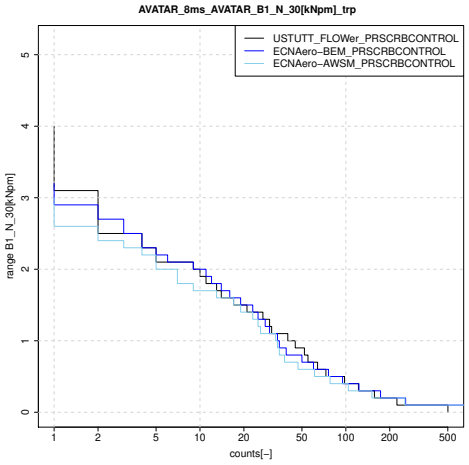

(b) Tangential force, 30%R

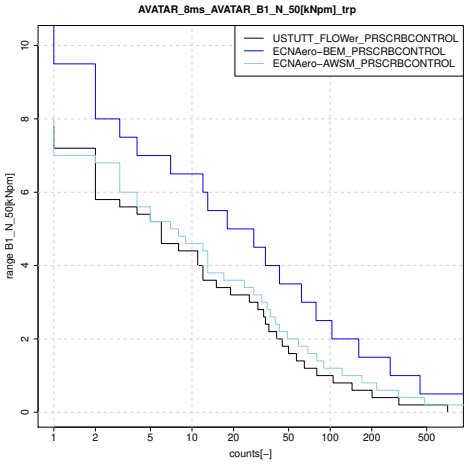

(c) Tangential force, 50%R

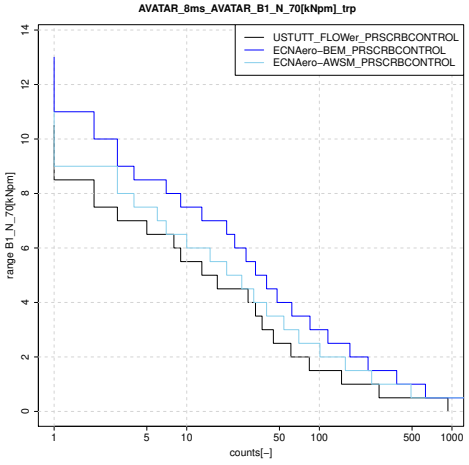

(d) Tangential force, 70%R

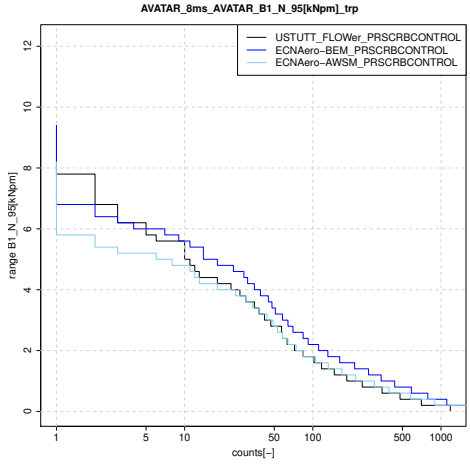

(e) Tangential force, 95%R

Figure B.41: Leadwise moment and tangential forces

B.2.6 PSD

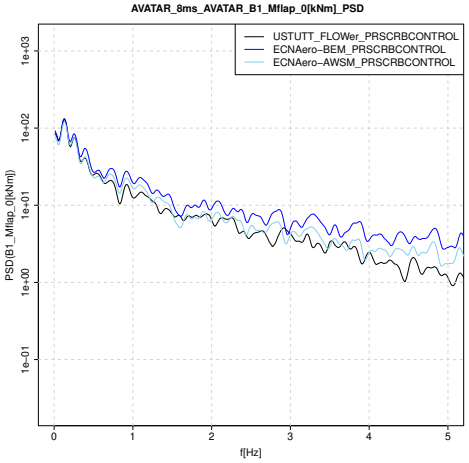

(a) Flapwise blade root moment

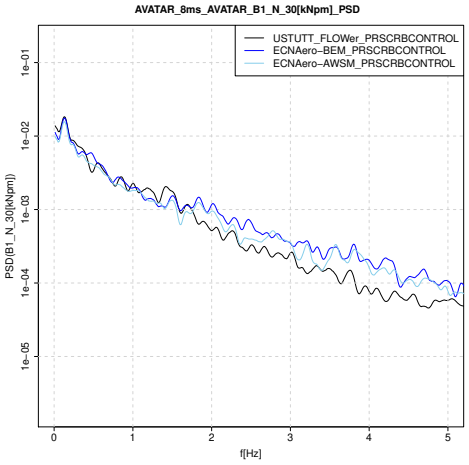

(b) Normal force, 30%R

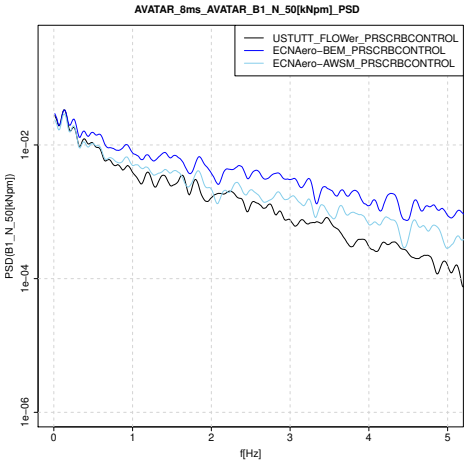

(c) Normal force, 50%R

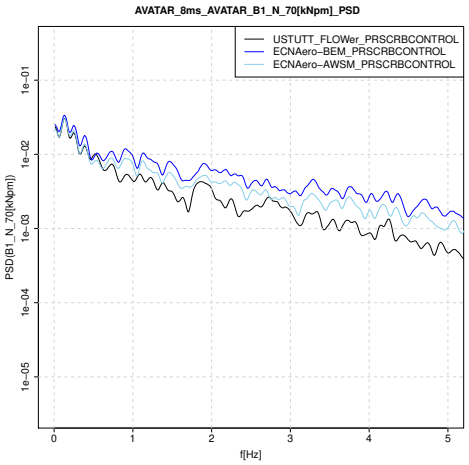

(d) Normal force, 70%R

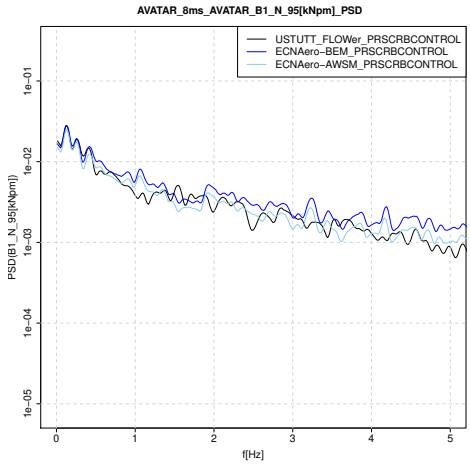

(e) Normal force, 95%R

Figure B.42: Flapwise moment and normal forces

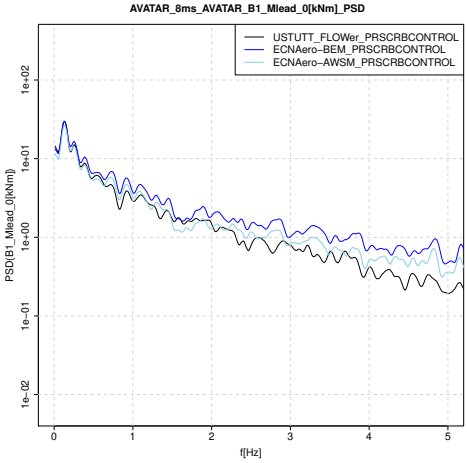

(a) Leadwise blade root moment

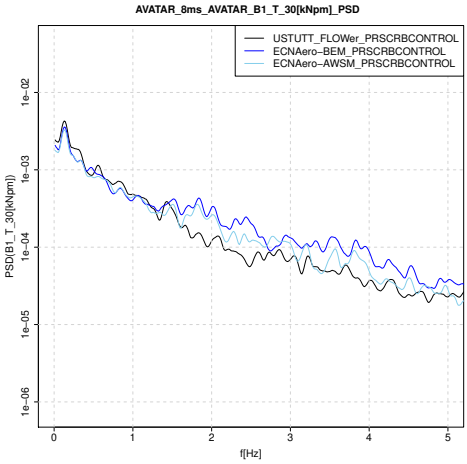

(b) Tangential force, 30%R

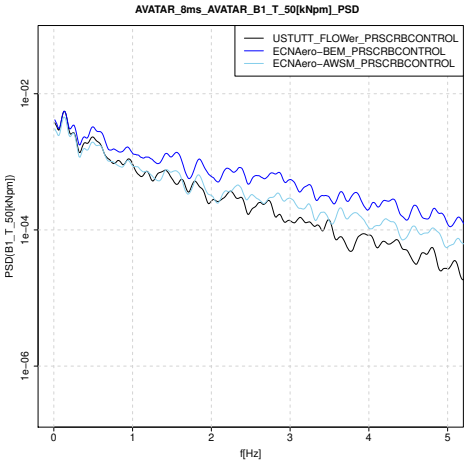

(c) Tangential force, 50%R

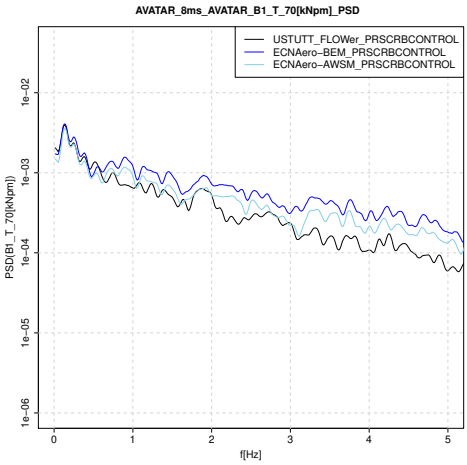

(d) Tangential force, 70%R

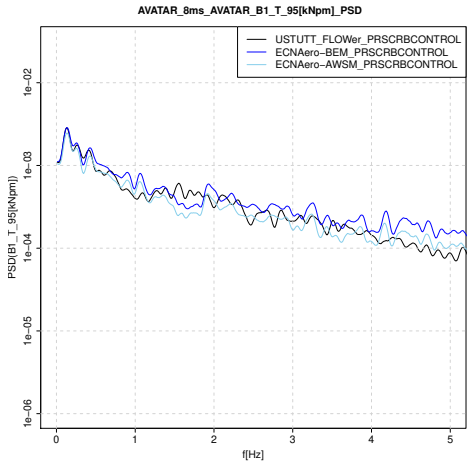

(e) Tangential force, 95%R

Figure B.43: Leadwise moment and tangential forces

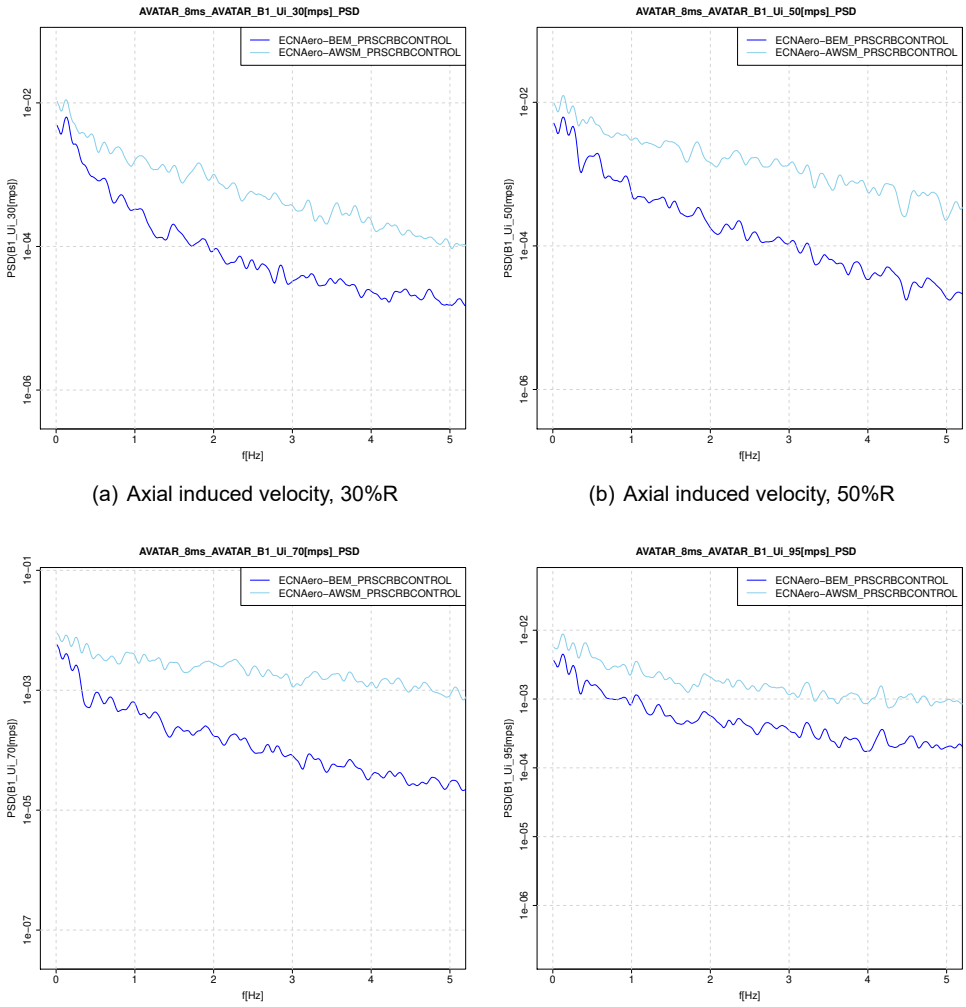

(a) Axial induced velocity, 30%R

(b) Axial induced velocity, 50%R

(c) Axial induced velocity, 70%R

(d) Axial induced velocity, 95%R

Figure B.44: Axial induced velocities

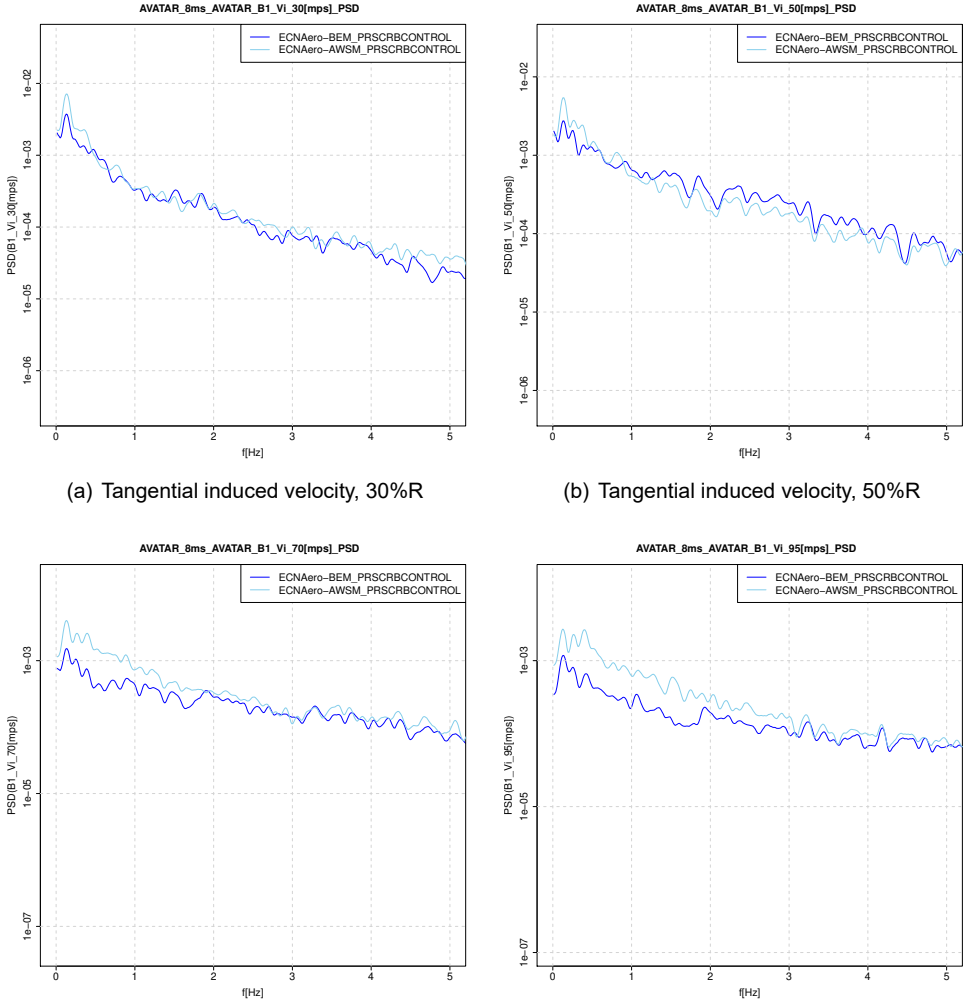

(a) Tangential induced velocity, 30%R

(b) Tangential induced velocity, 50%R

(c) Tangential induced velocity, 70%R

(d) Tangential induced velocity, 95%R

Figure B.45: Tangential induced velocities

B.3 16 m/s case

B.3.1 Time (zoomed)

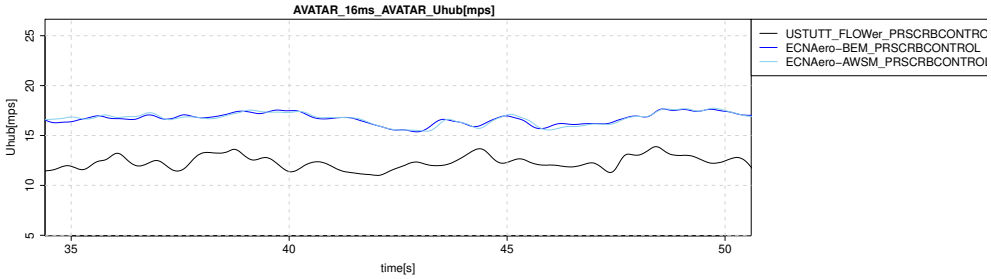

(a) Hub height wind speed

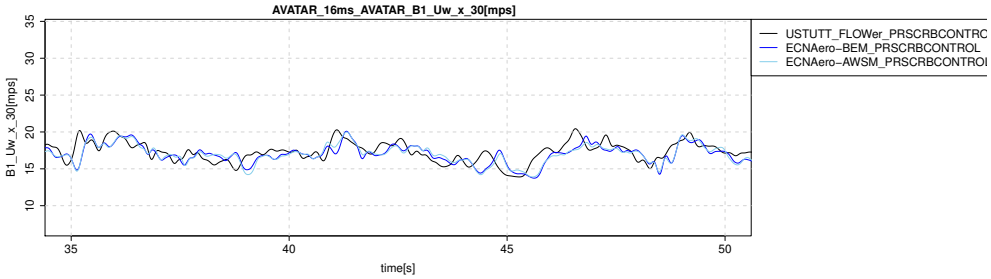

(b) Wind probe axial velocity at 30%R

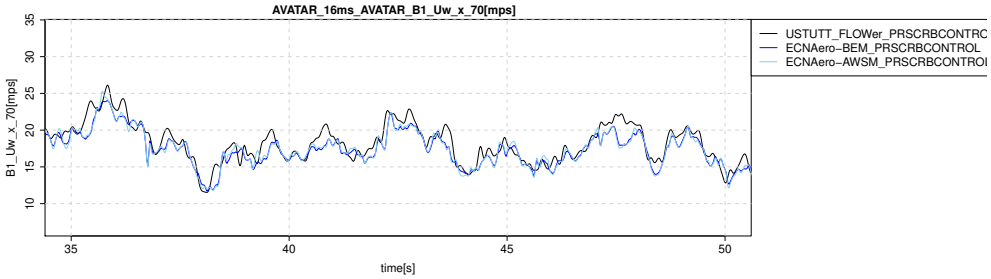

(c) Wind probe axial velocity at 70%R

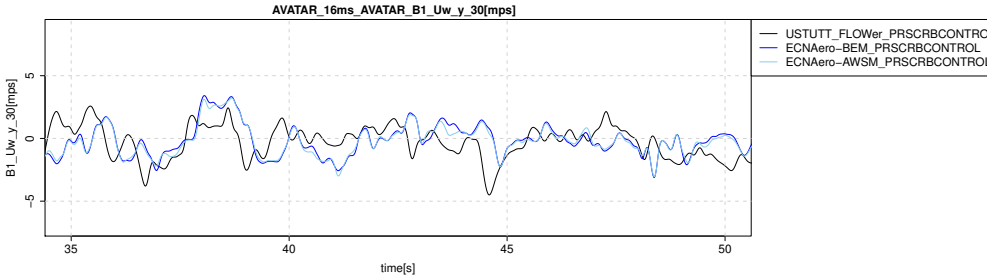

(d) Wind probe lateral velocity at 30%R

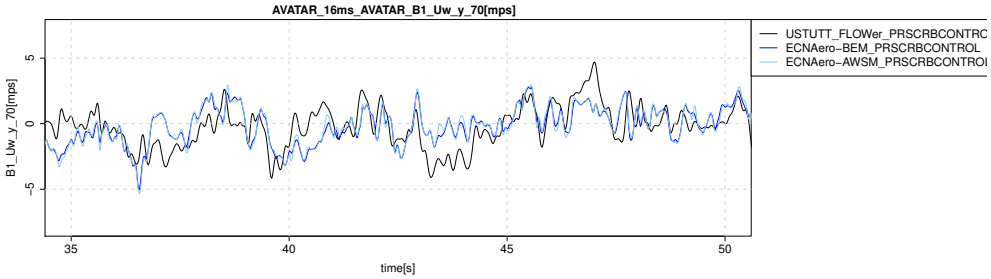

(e) Wind probe lateral velocity at 70%R

Figure B.46: Wind speed alignment check

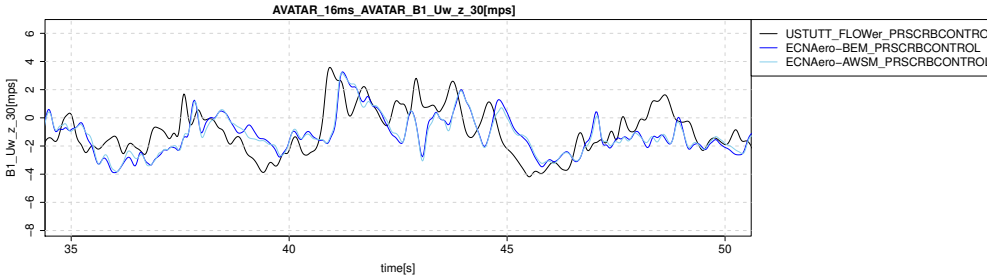

(a) Wind probe vertical velocity at 30%R

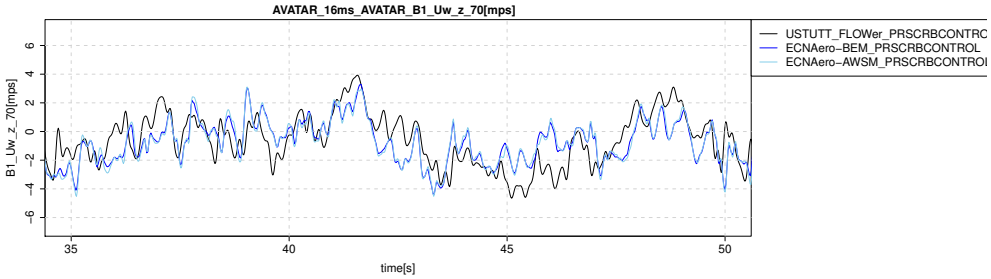

(b) Wind probe vertical velocity at 70%R

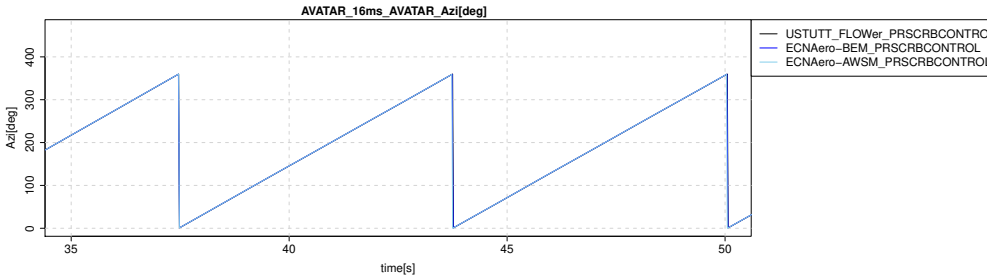

(c) Rotor azimuth angle

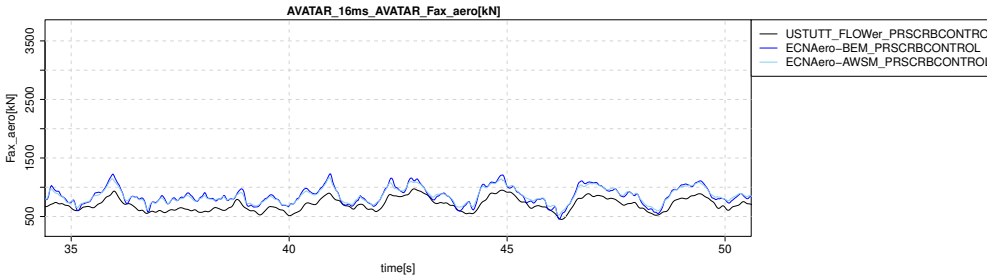

(d) Rotor axial force

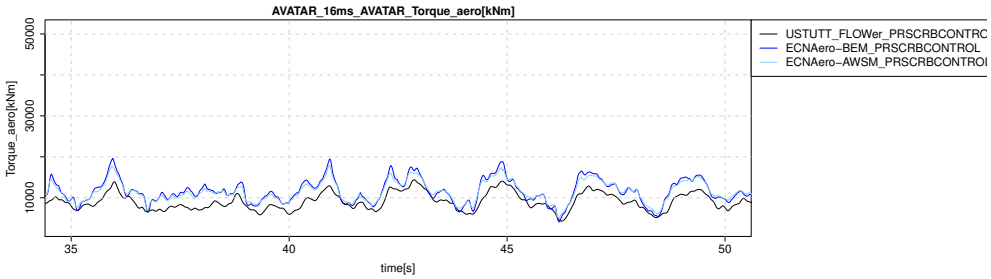

(e) Rotor torque

Figure B.47: Alignment check

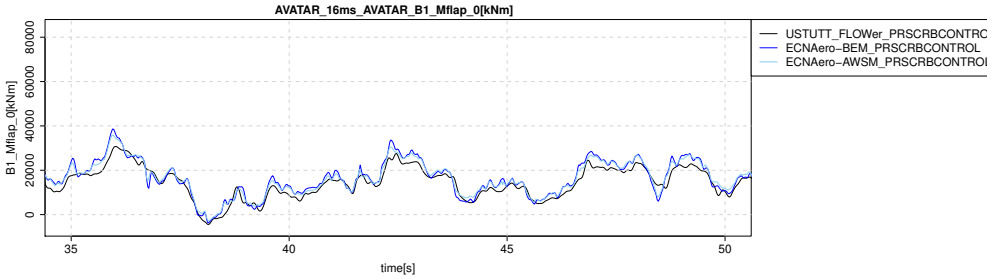

(a) Flapwise blade root moment

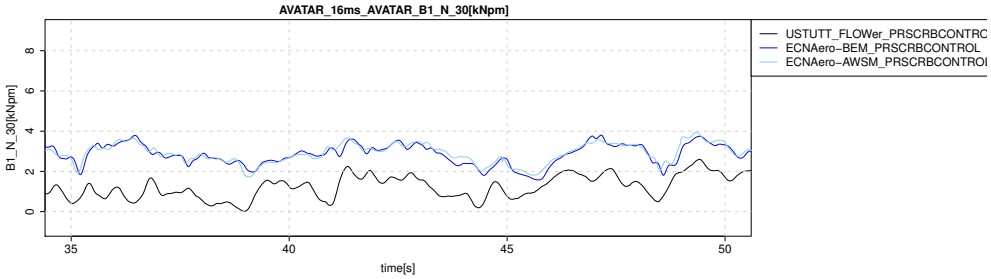

(b) Chord normal force at 30%R

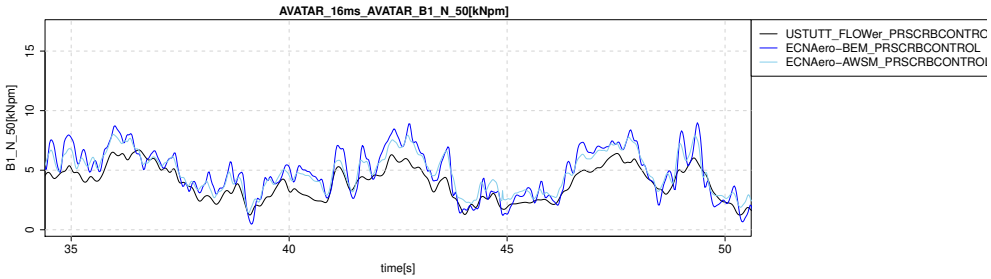

(c) Chord normal force at 50%R

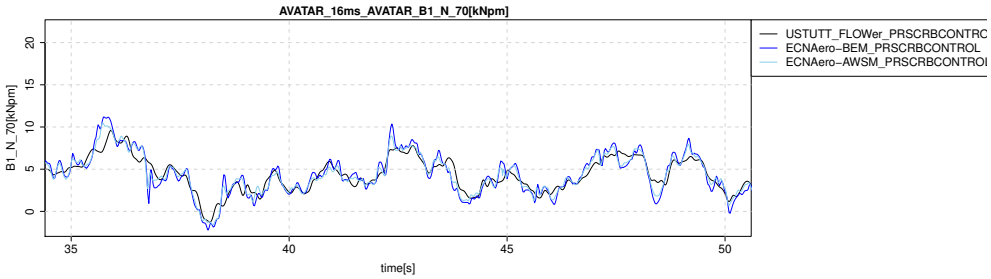

(d) Chord normal force at 70%R

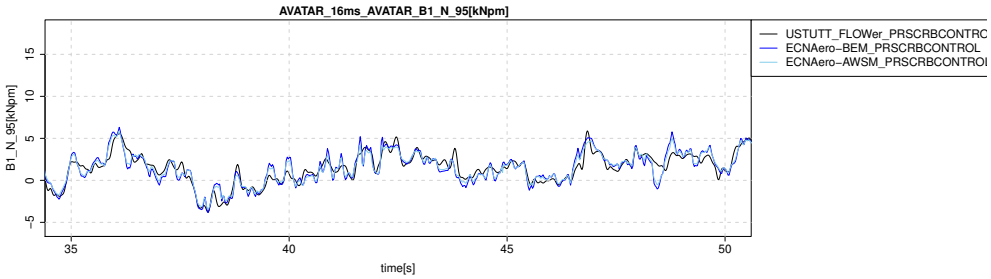

(e) Chord normal force at 95%R

Figure B.48: Flapwise moment and normal force

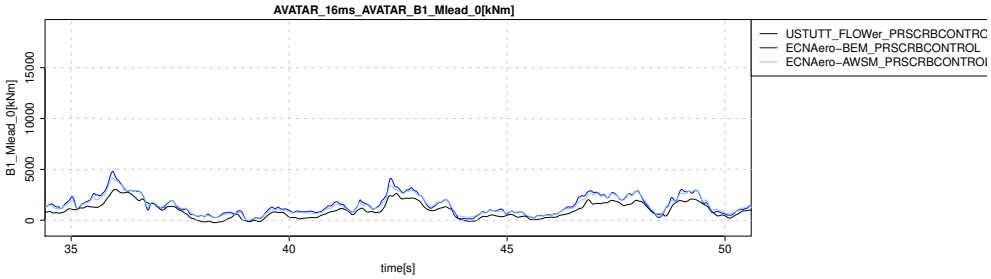

(a) Leadwise blade root moment

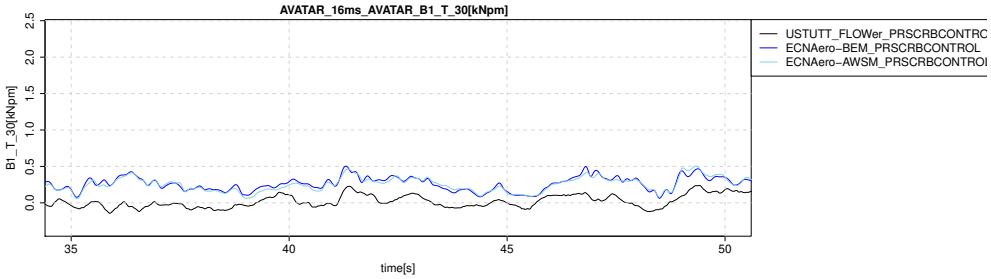

(b) Chord tangential force at 30%R

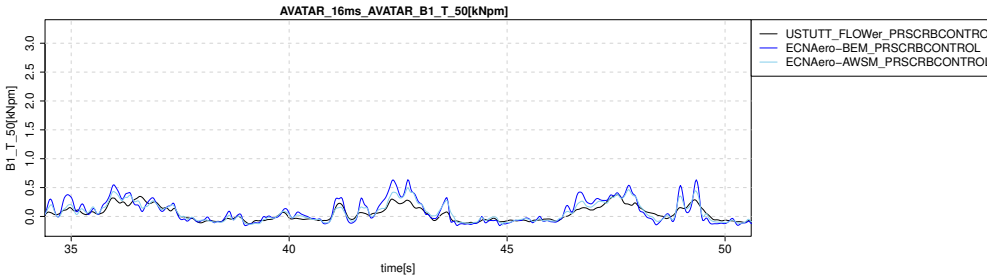

(c) Chord tangential force at 50%R

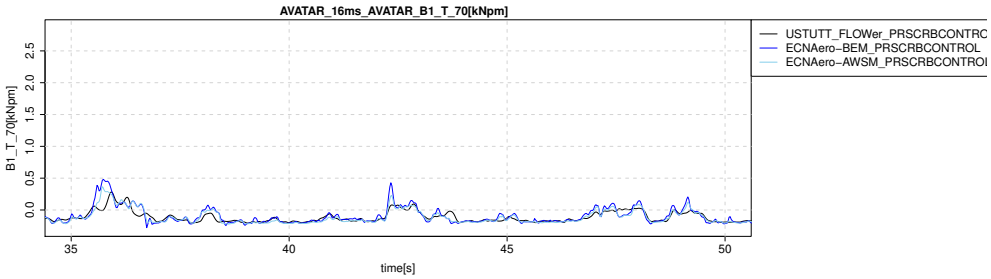

(d) Chord tangential force at 70%R

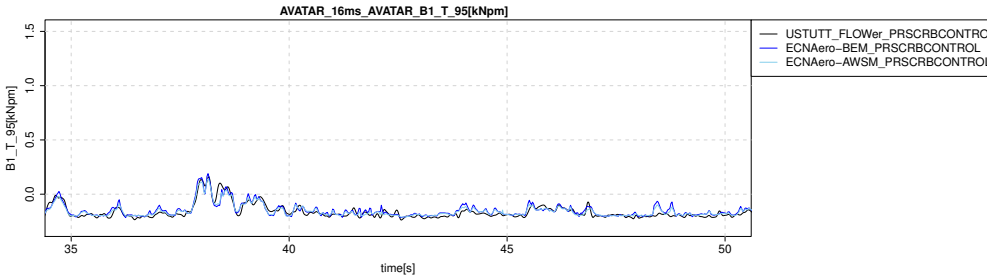

(e) Chord tangential force at 95%R

Figure B.49: Leadwise moment and tangential force

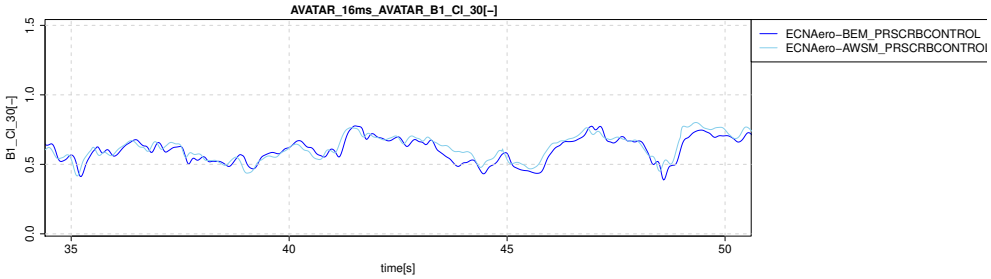

(a) Lift coefficient at 30%R

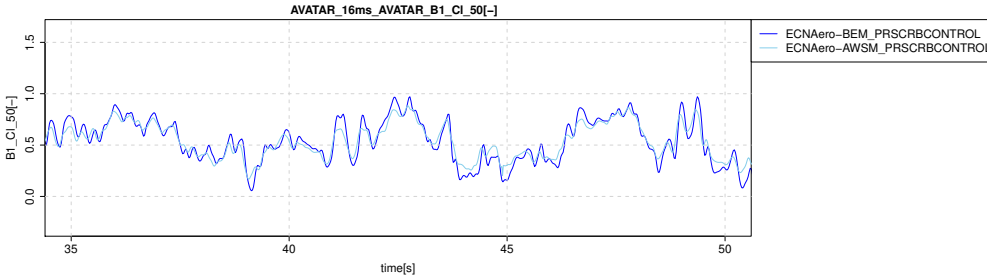

(b) Lift coefficient at 50%R

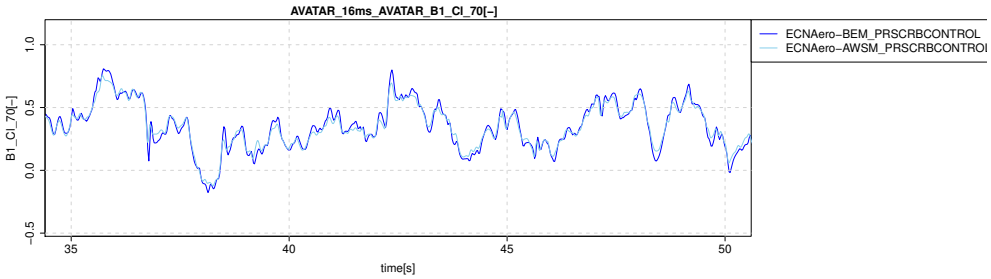

(c) Lift coefficient at 70%R

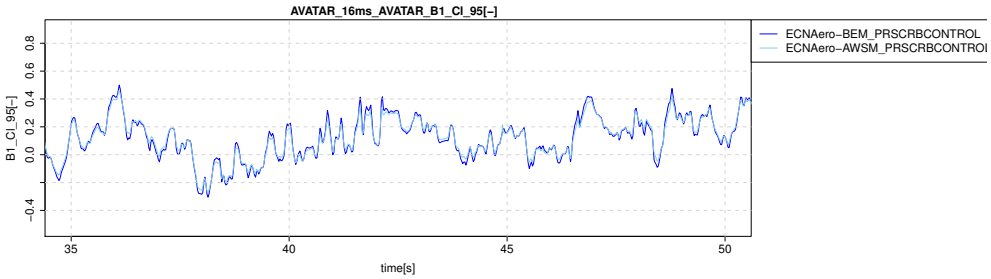

(d) Lift coefficient at 95%R

Figure B.50: Lift coefficients

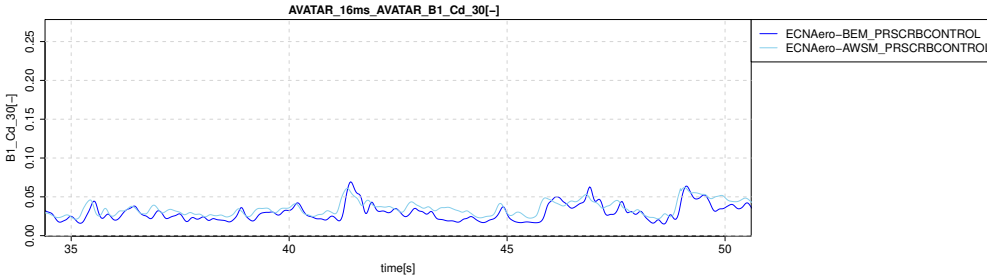

(a) Drag coefficient at 30%R

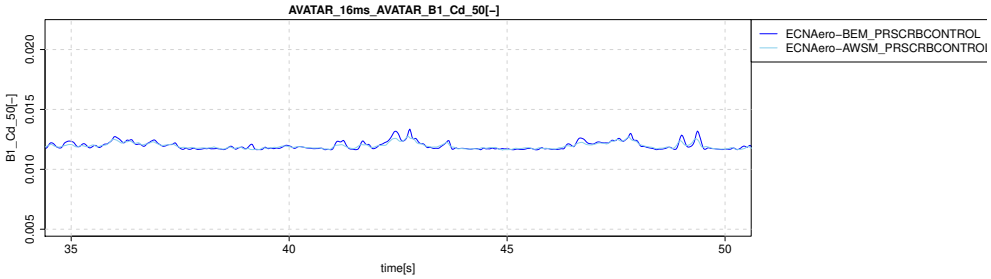

(b) Drag coefficient at 50%R

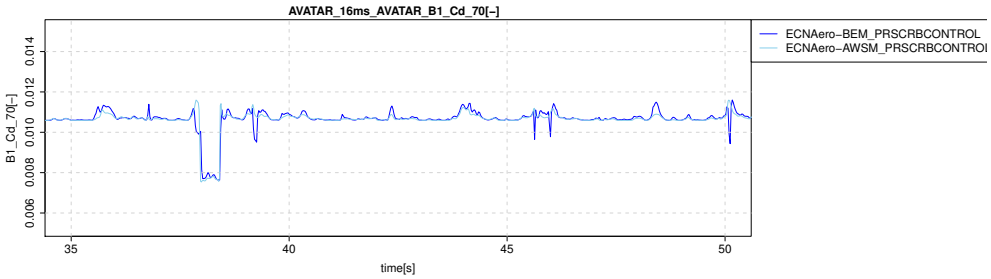

(c) Drag coefficient at 70%R

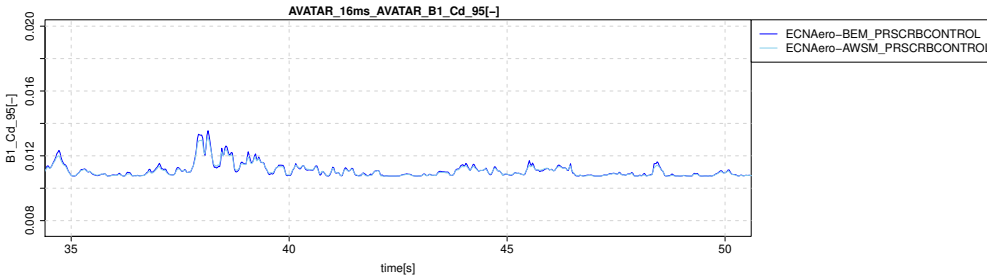

(d) Drag coefficient at 95%R

Figure B.51: Drag coefficients

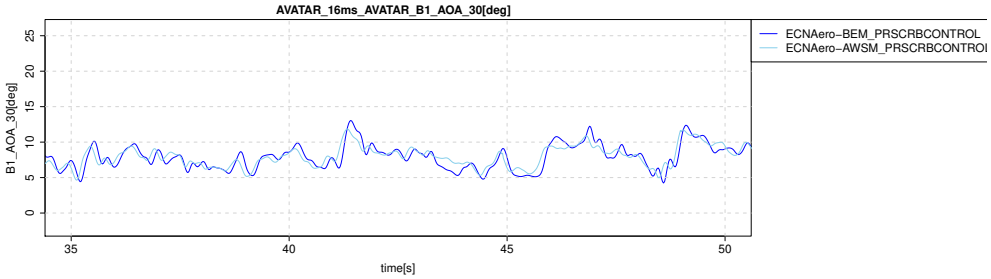

(a) Angle of attack at 30%R

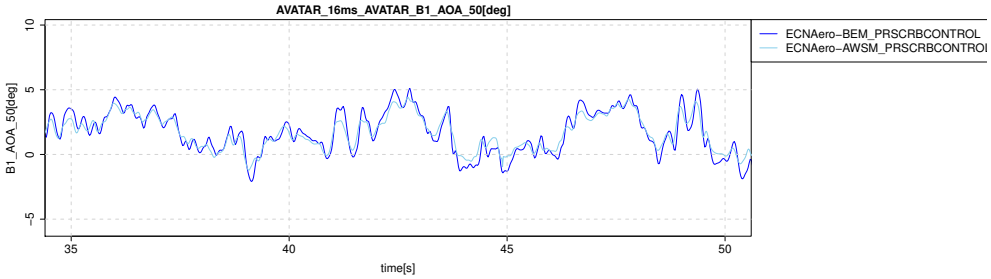

(b) Angle of attack at 50%R

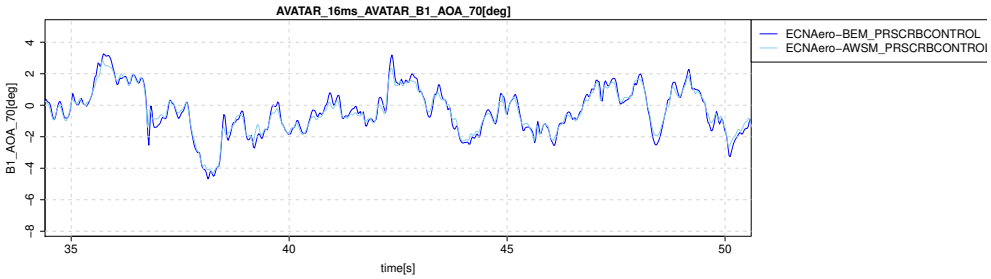

(c) Angle of attack at 70%R

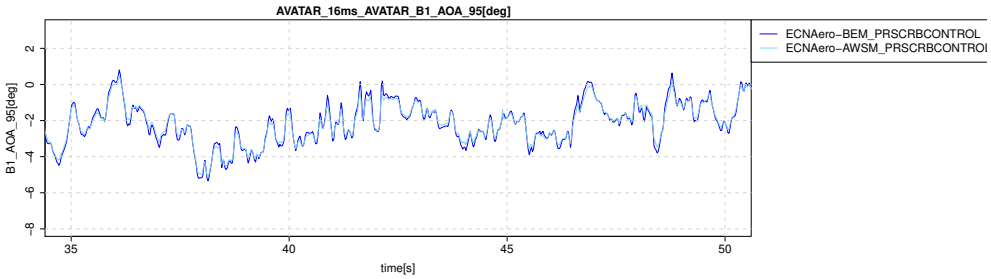

(d) Angle of attack at 95%R

Figure B.52: Angles of attack

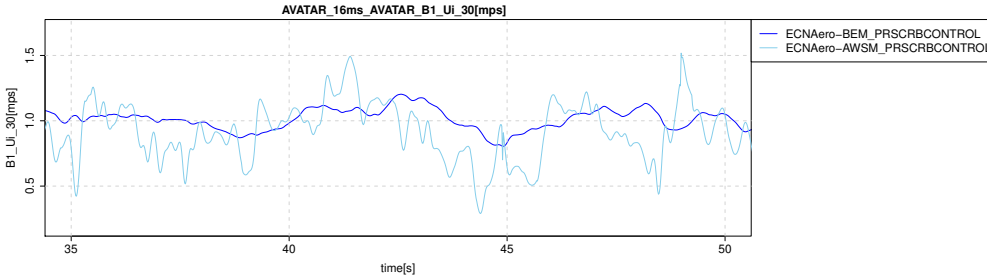

(a) Axial induced velocity at 30%R

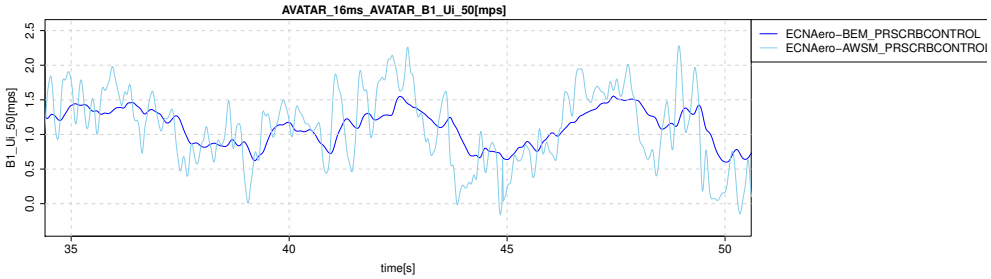

(b) Axial induced velocity at 50%R

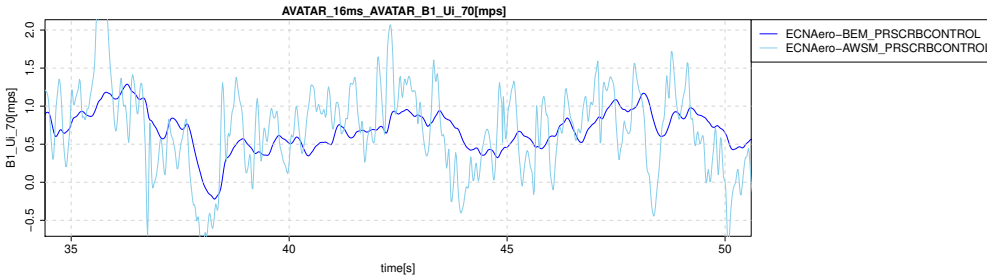

(c) Axial induced velocity at 70%R

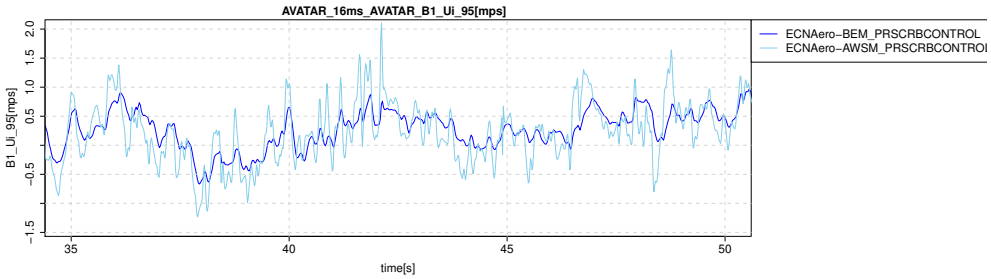

(d) Axial induced velocity at 95%R

Figure B.53: Axial induced velocities

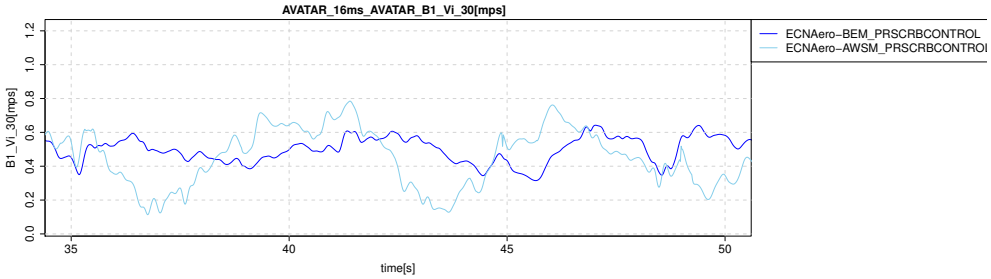

(a) Tangential induced velocity at 30%R

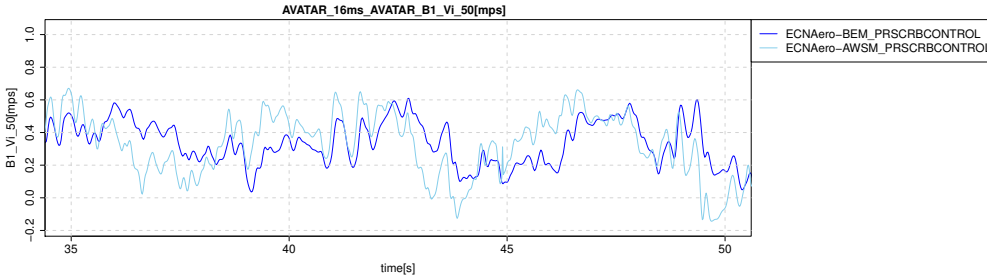

(b) Tangential induced velocity at 50%R

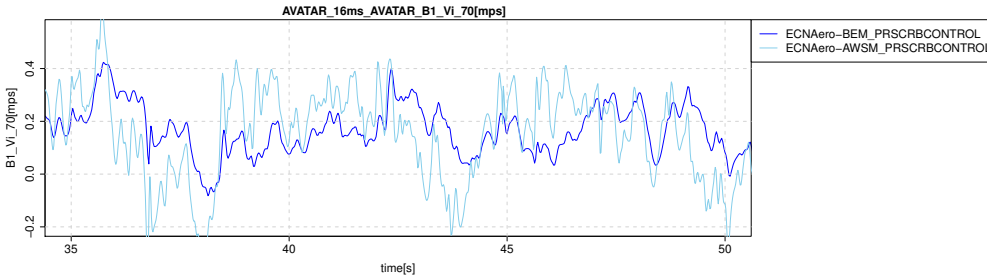

(c) Tangential induced velocity at 70%R

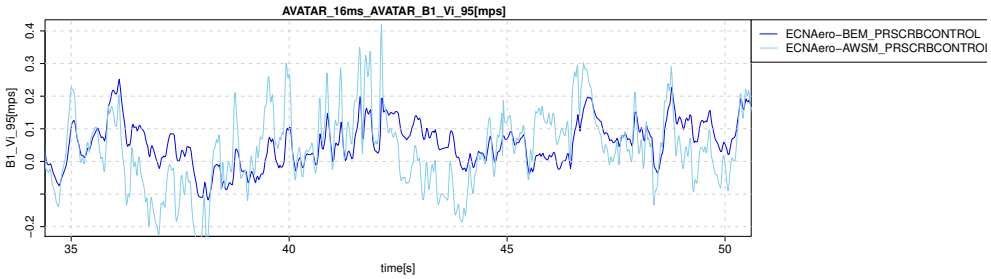

(d) Tangential induced velocity at 95%R

Figure B.54: Tangential induced velocities

B.3.2 Time

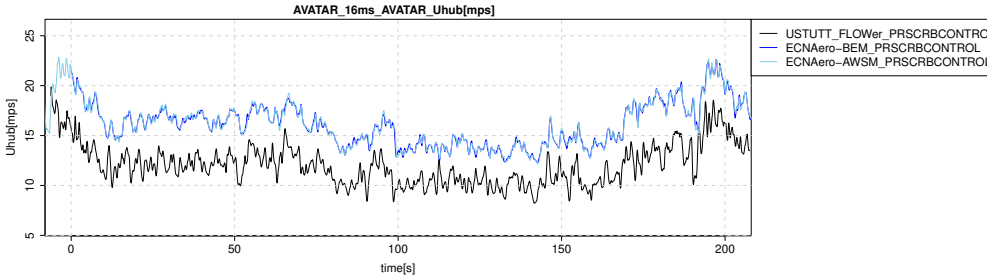

(a) Hub height wind speed

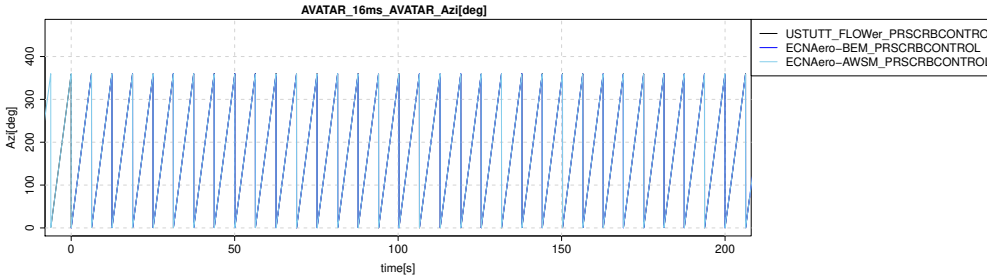

(b) Rotor azimuth

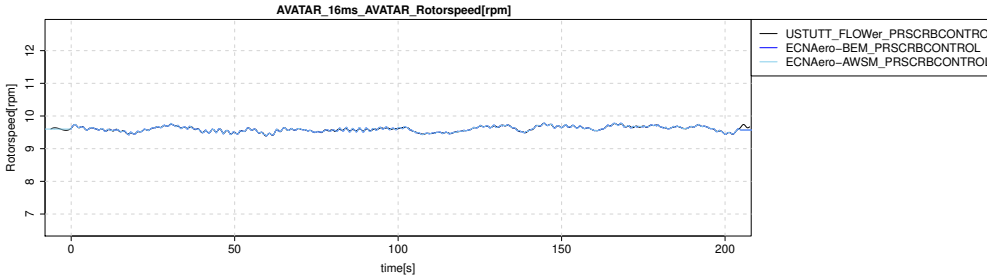

(c) Rotor speed

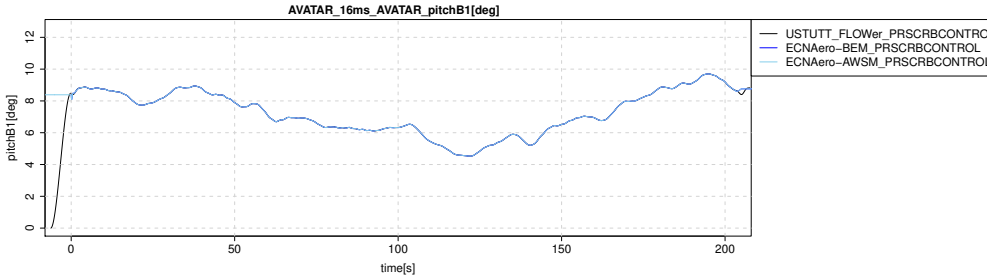

(d) Pitch angle

Figure B.55: Wind and control parameters

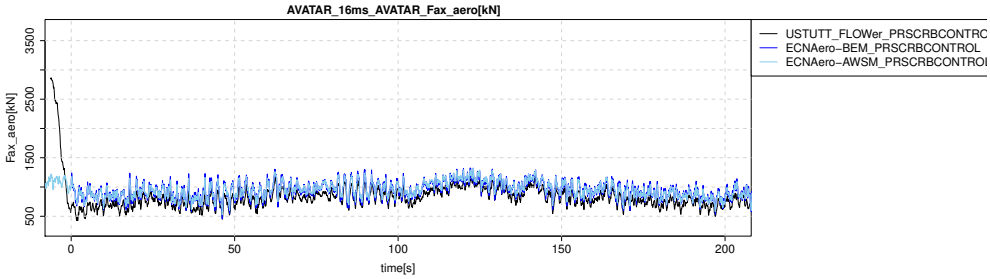

(a) Rotor axial force

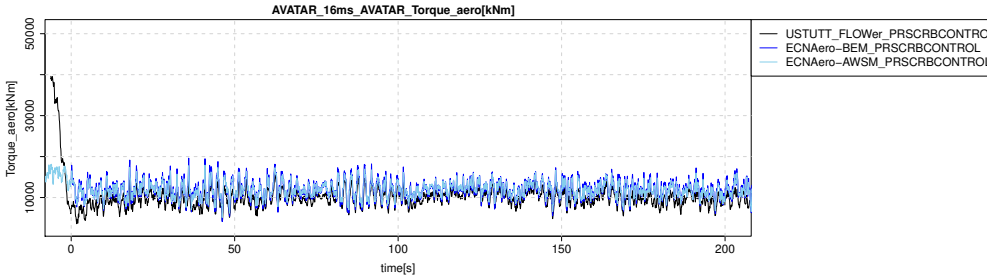

(b) Rotor torque

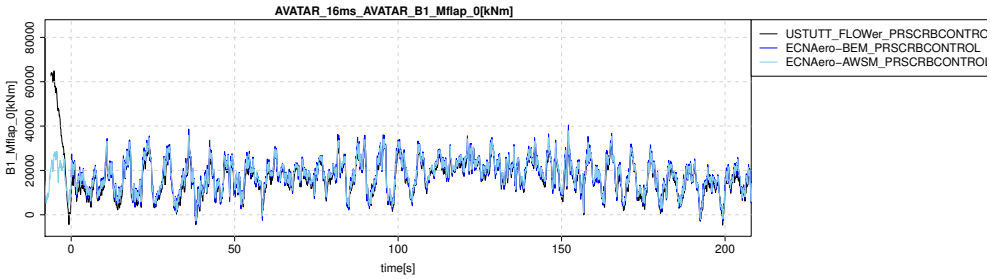

(c) Flapwise blade root moment

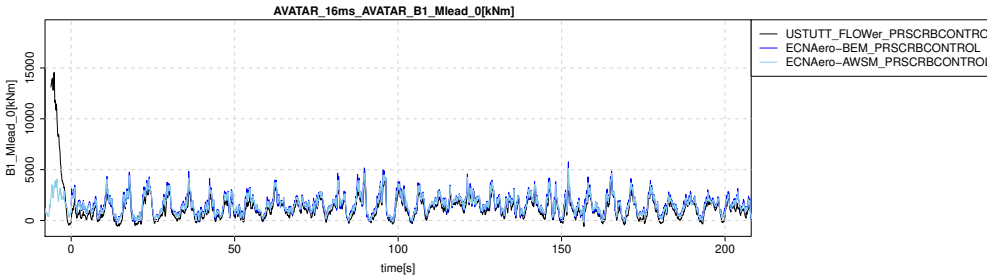

(d) Leadwise blade root moment

Figure B.56: Rotor and blade forces and moments

B.3.3 Statistics

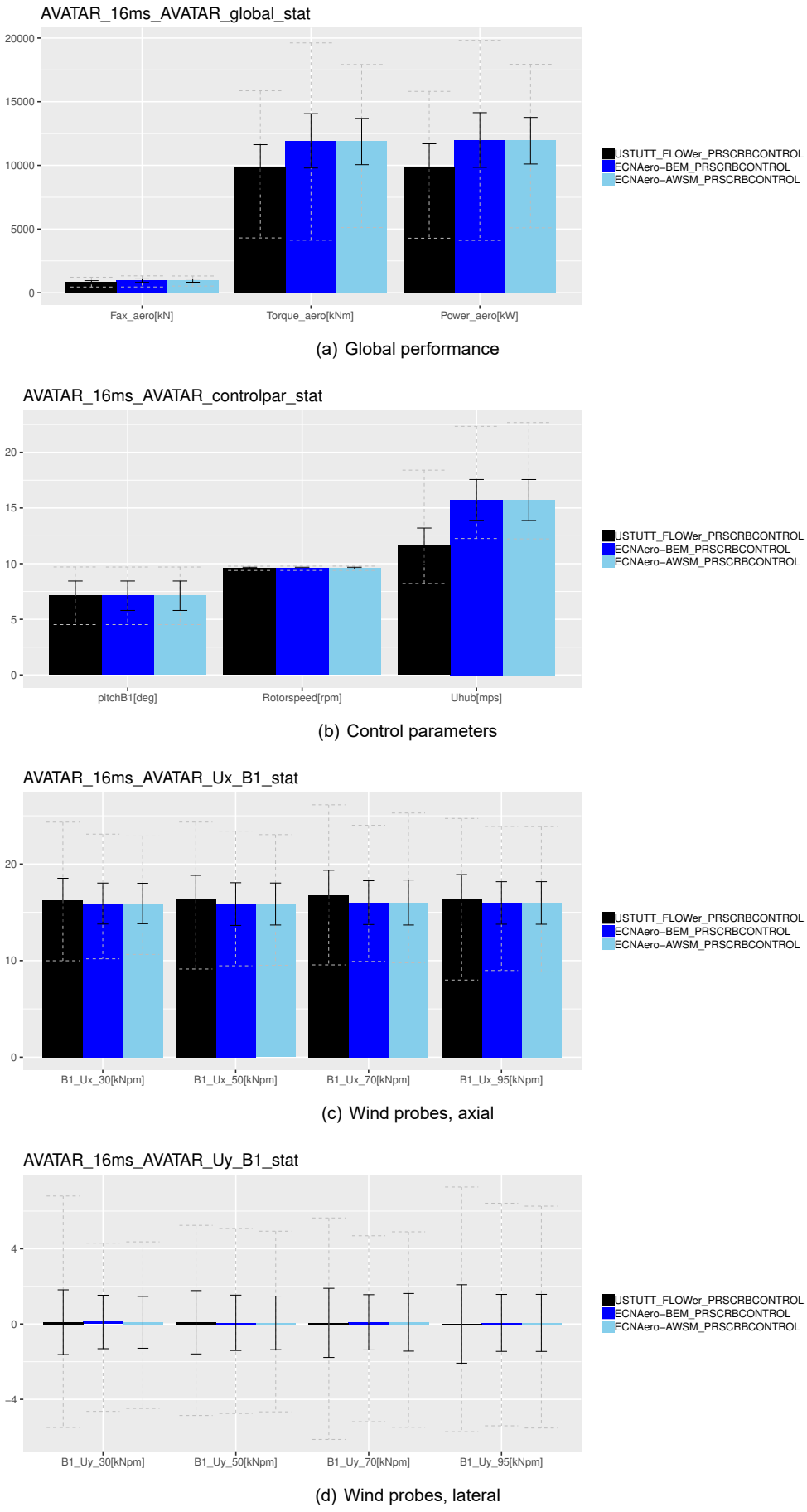

Figure B.57: Global performance, wind and control parameters

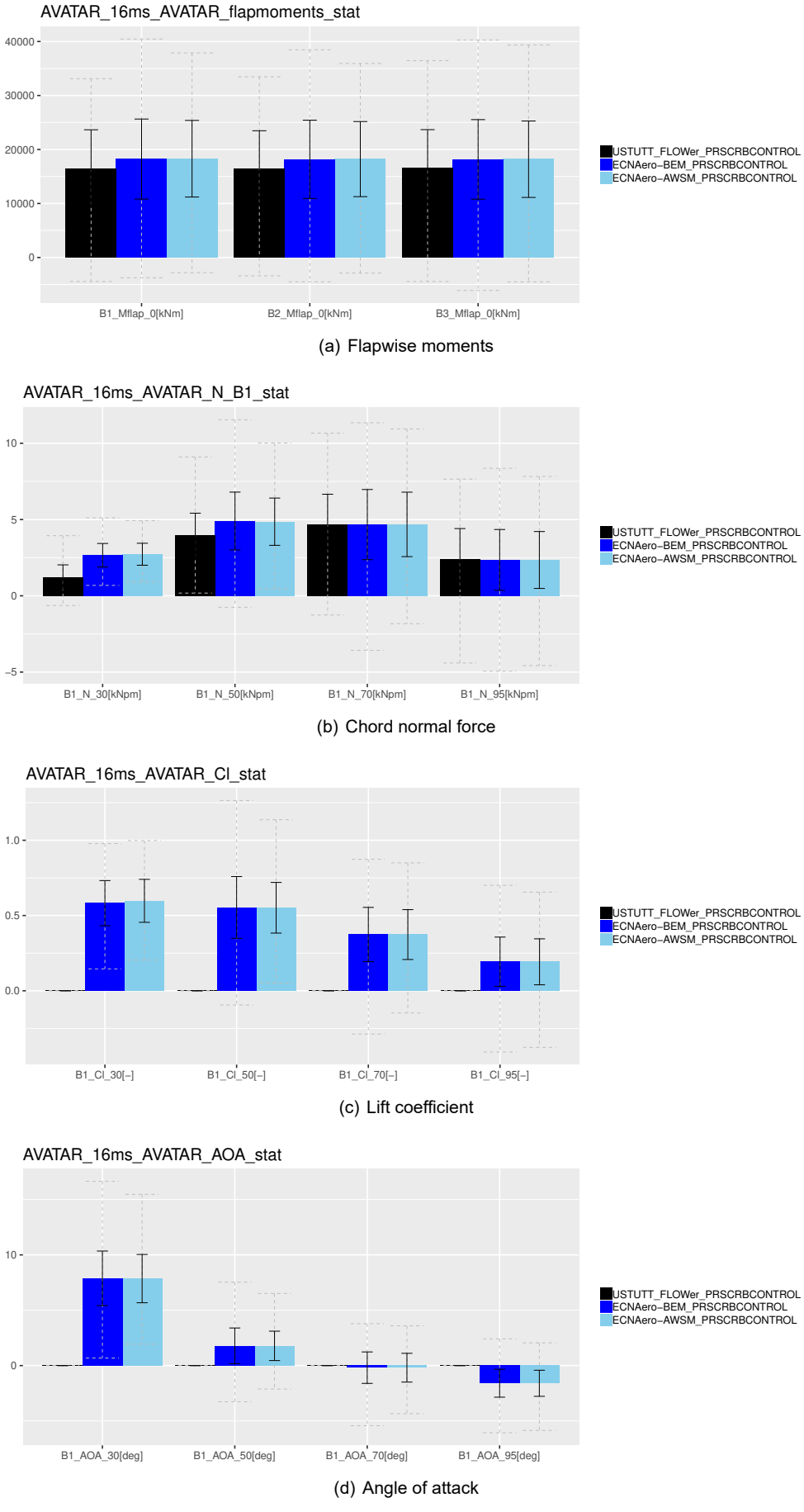

Figure B.58: Force decompostion in axial direction

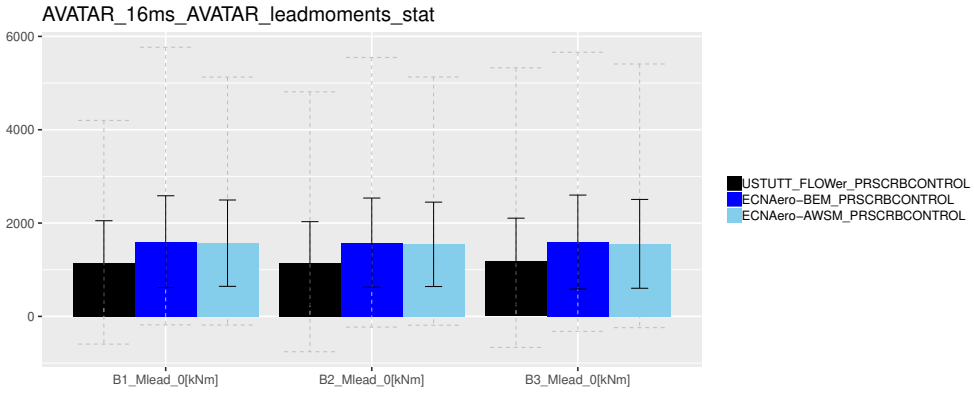

(a) Leadwise moments

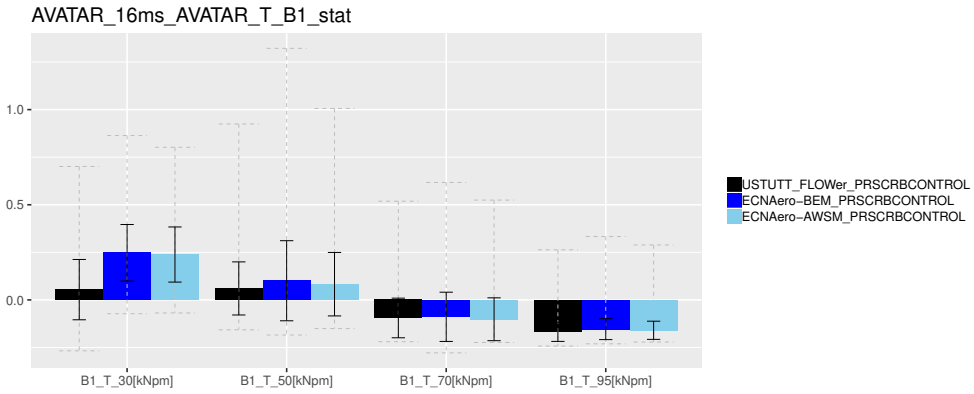

(b) Chord tangential force

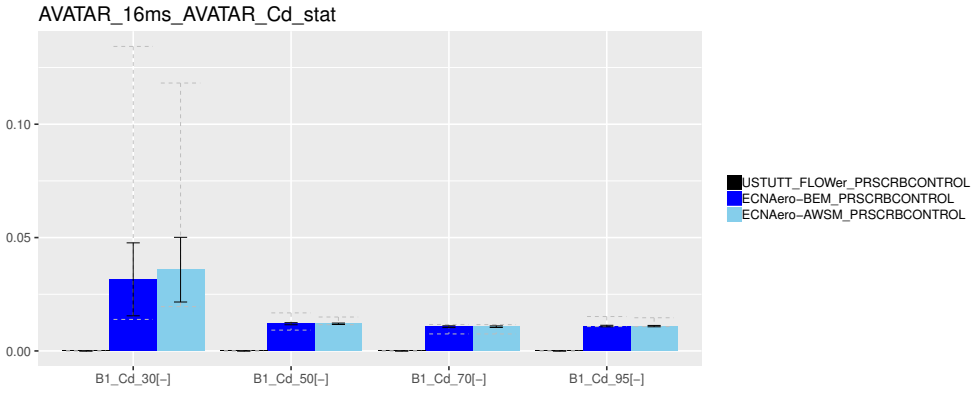

(c) Drag coefficient

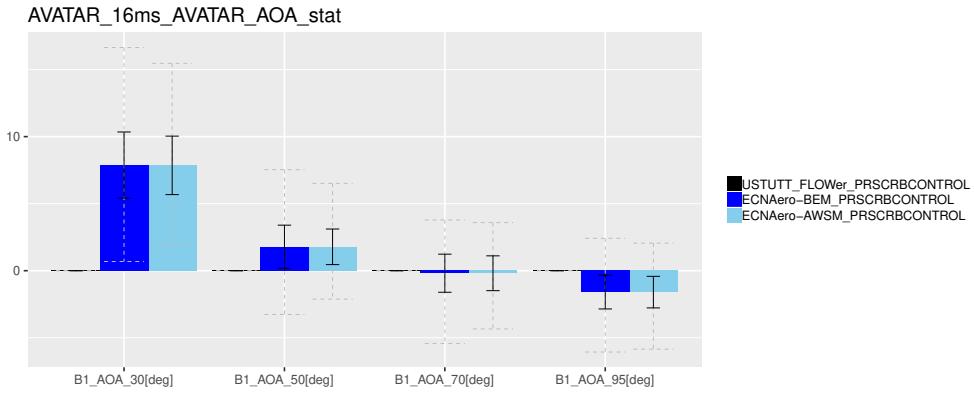

(d) Angle of attack

Figure B.59: Force decompostion in tangential direction

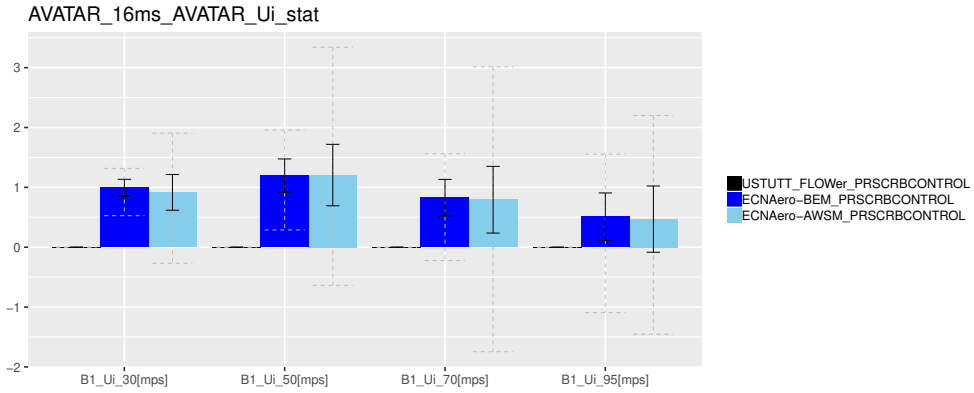

(a) Axial induced velocity

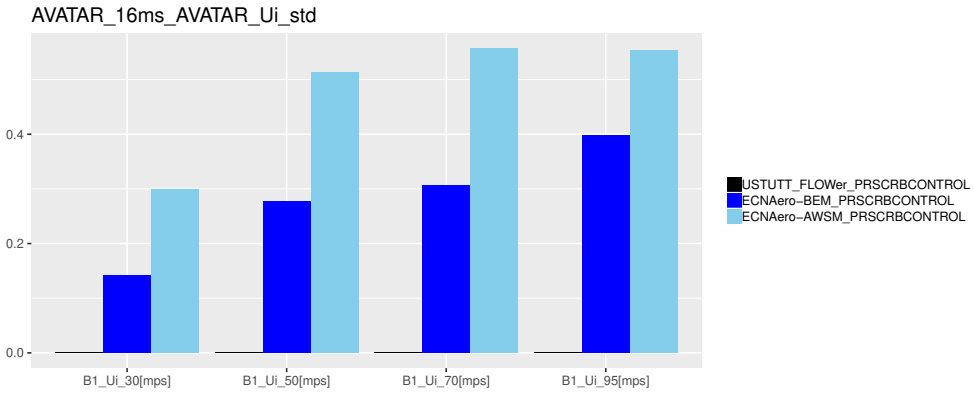

(b) Axial induced velocity (standard deviation)

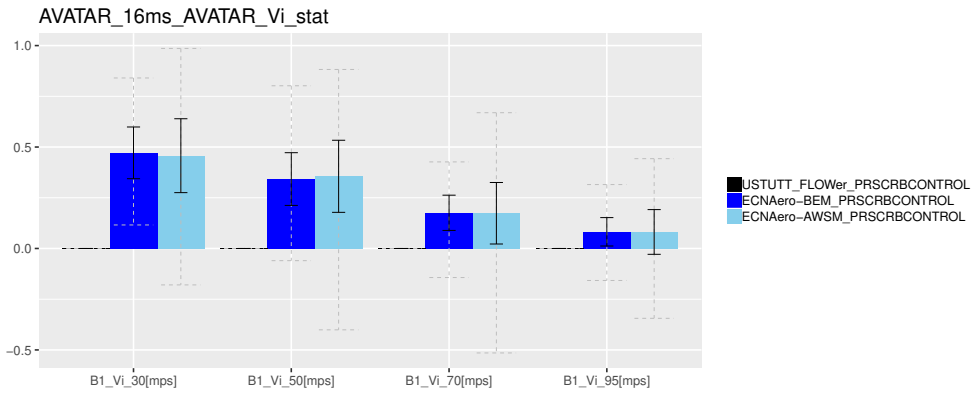

(c) Tangential induced velocity

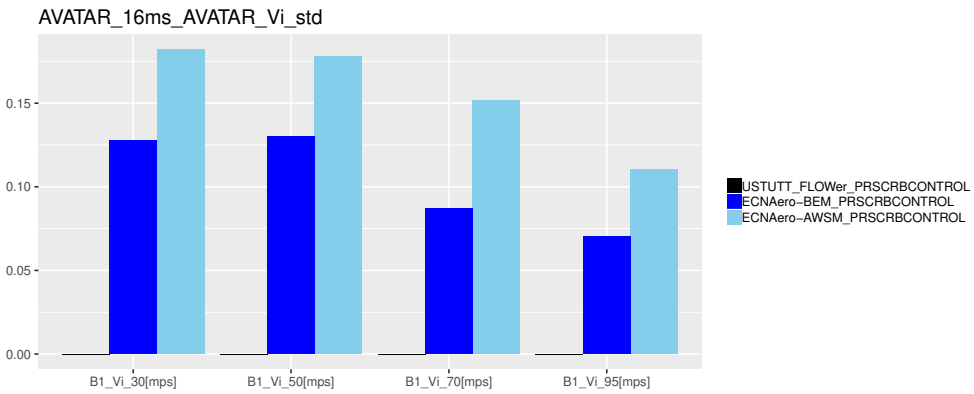

(d) Tangential induced velocity (standard deviation)

Figure B.60: Induced velocities

B.3.4 Equivalent load levels

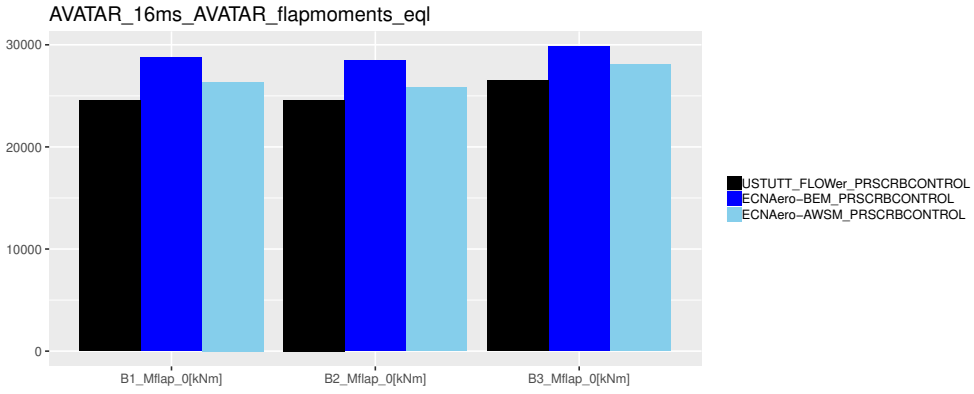

(a) Flapwise moments

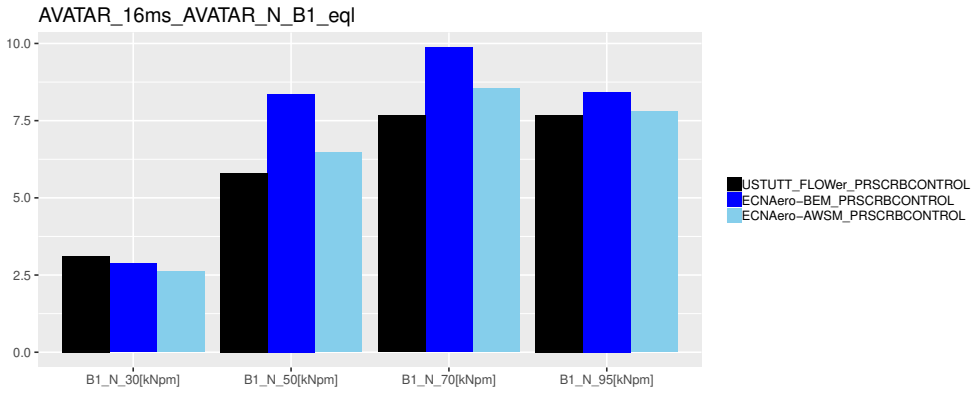

(b) Normal force

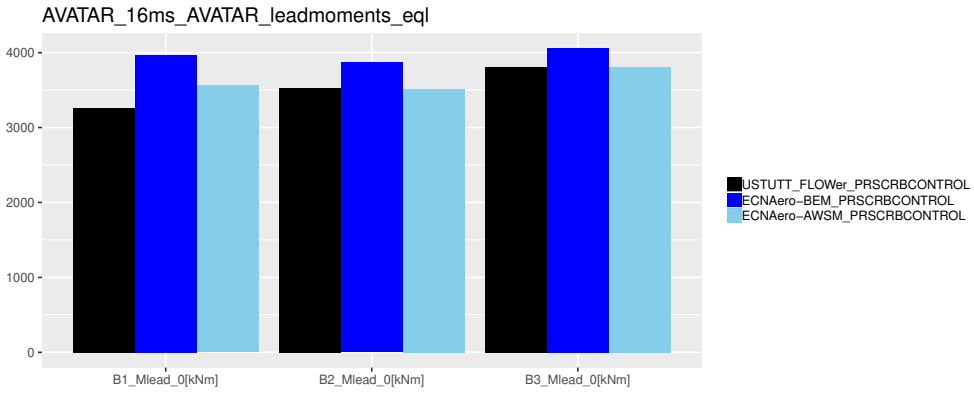

(c) Leadwise moments

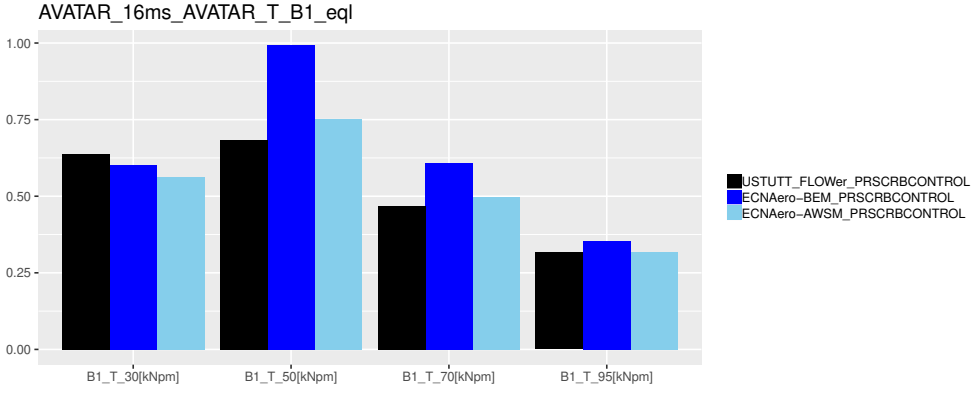

(d) Tangential force

Figure B.61: Forces and moments

B.3.5 Staircase plots

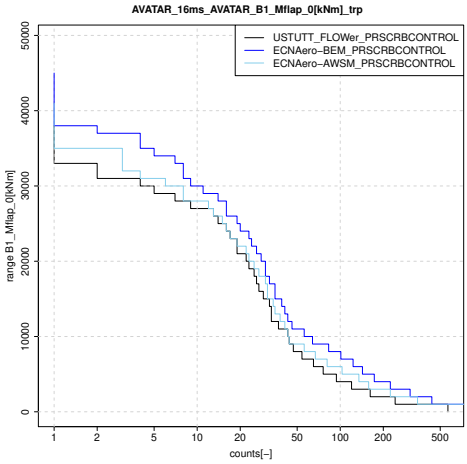

(a) Flapwise blade root moment

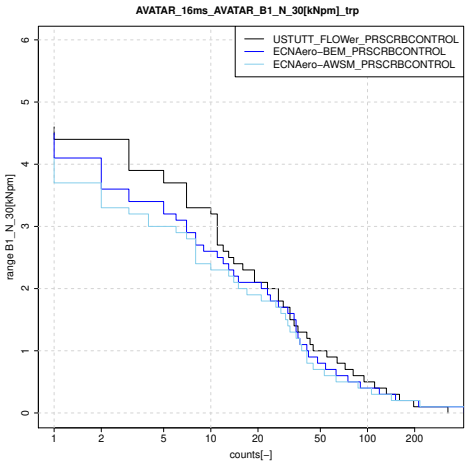

(b) Normal force, 30%R

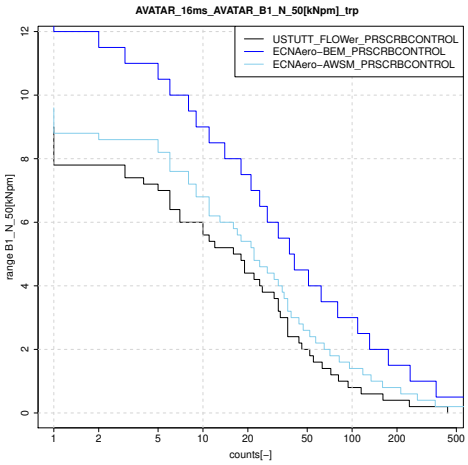

(c) Normal force, 50%R

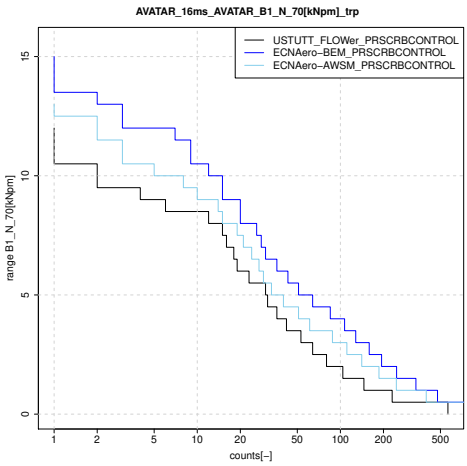

(d) Normal force, 70%R

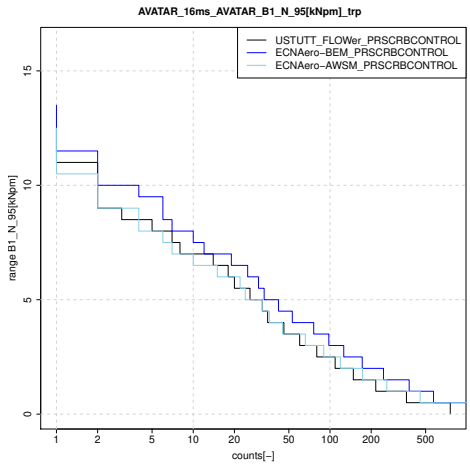

(e) Normal force, 95%R

Figure B.62: Flapwise moment and normal forces

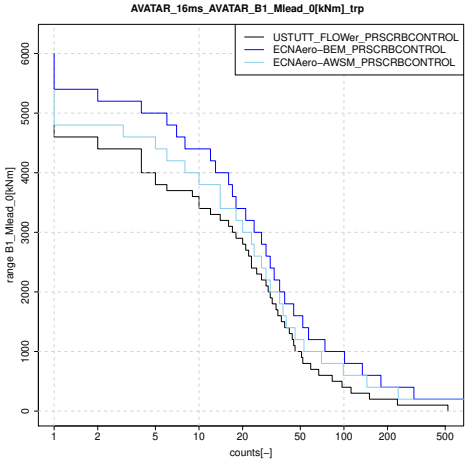

(a) Leadwise blade root moment

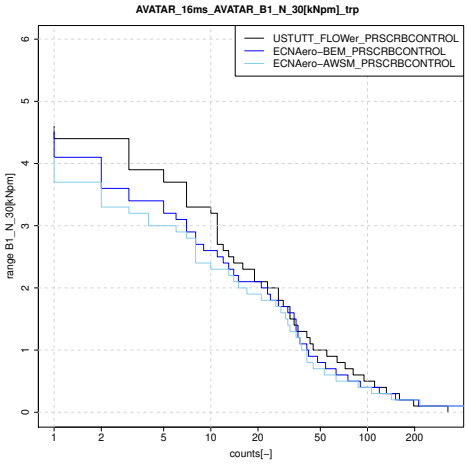

(b) Tangential force, 30%R

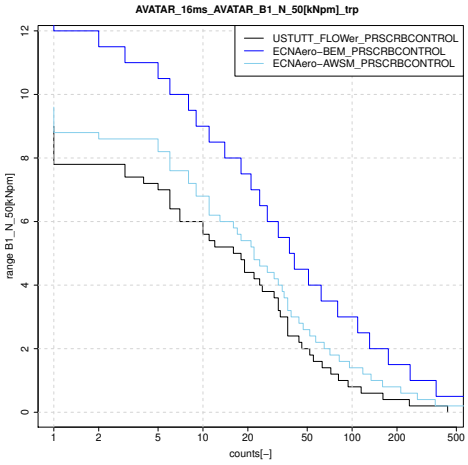

(c) Tangential force, 50%R

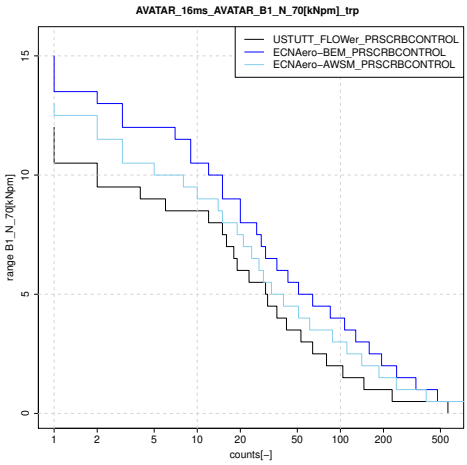

(d) Tangential force, 70%R

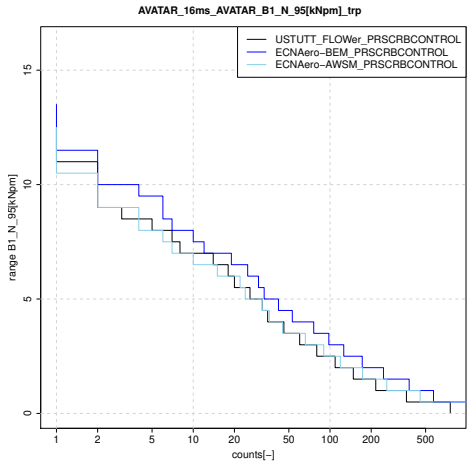

(e) Tangential force, 95%R

Figure B.63: Leadwise moment and tangential forces

B.3.6 PSD

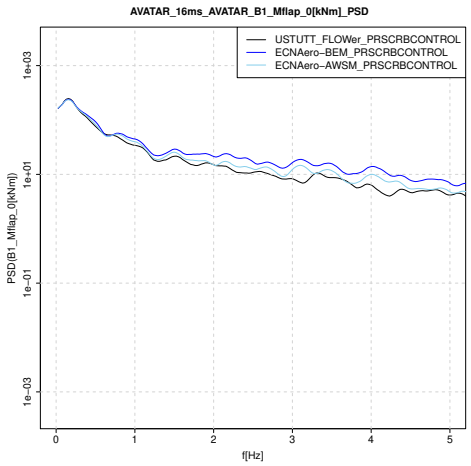

(a) Flapwise blade root moment

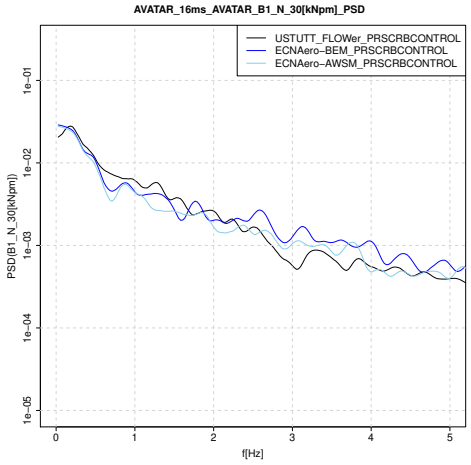

(b) Normal force, 30%R

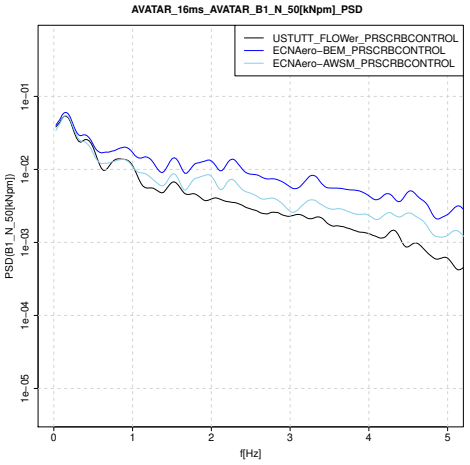

(c) Normal force, 50%R

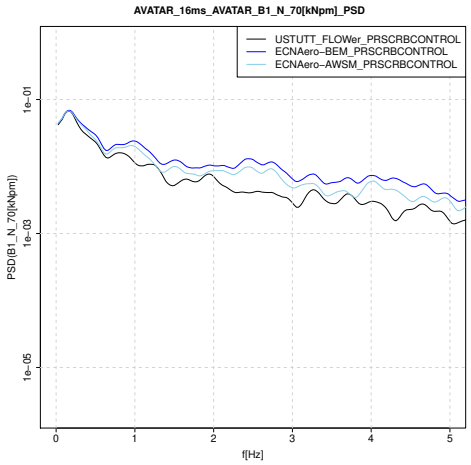

(d) Normal force, 70%R

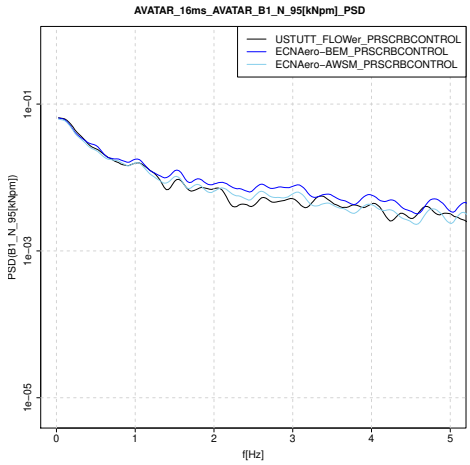

(e) Normal force, 95%R

Figure B.64: Flapwise moment and normal forces

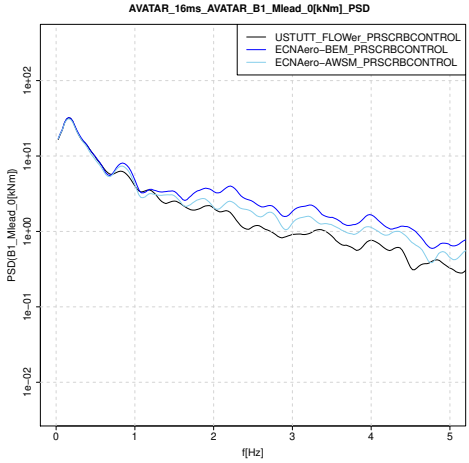

(a) Leadwise blade root moment

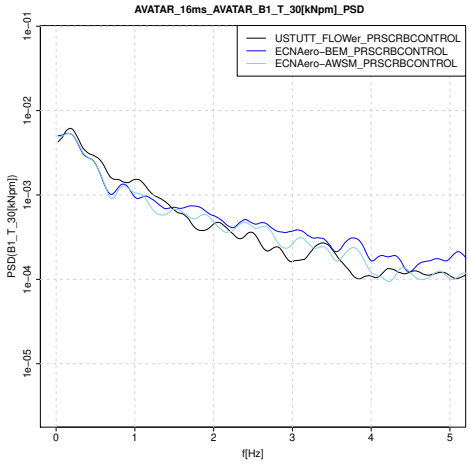

(b) Tangential force, 30%R

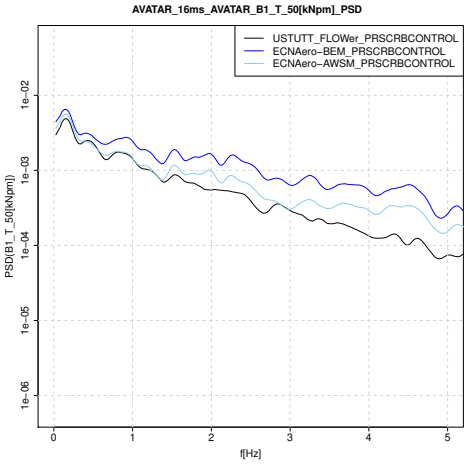

(c) Tangential force, 50%R

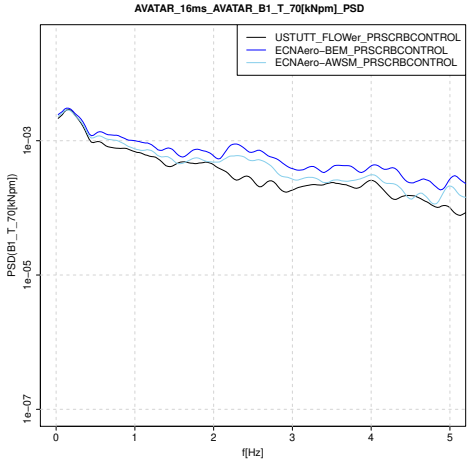

(d) Tangential force, 70%R

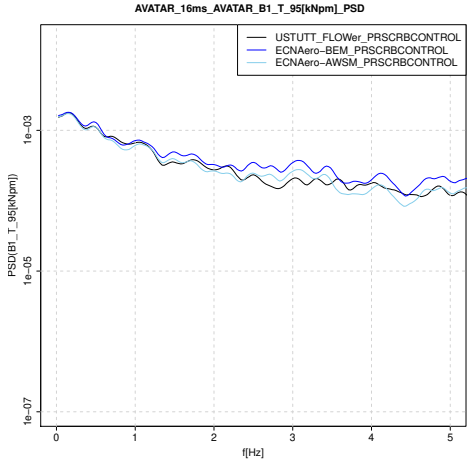

(e) Tangential force, 95%R

Figure B.65: Leadwise moment and tangential forces

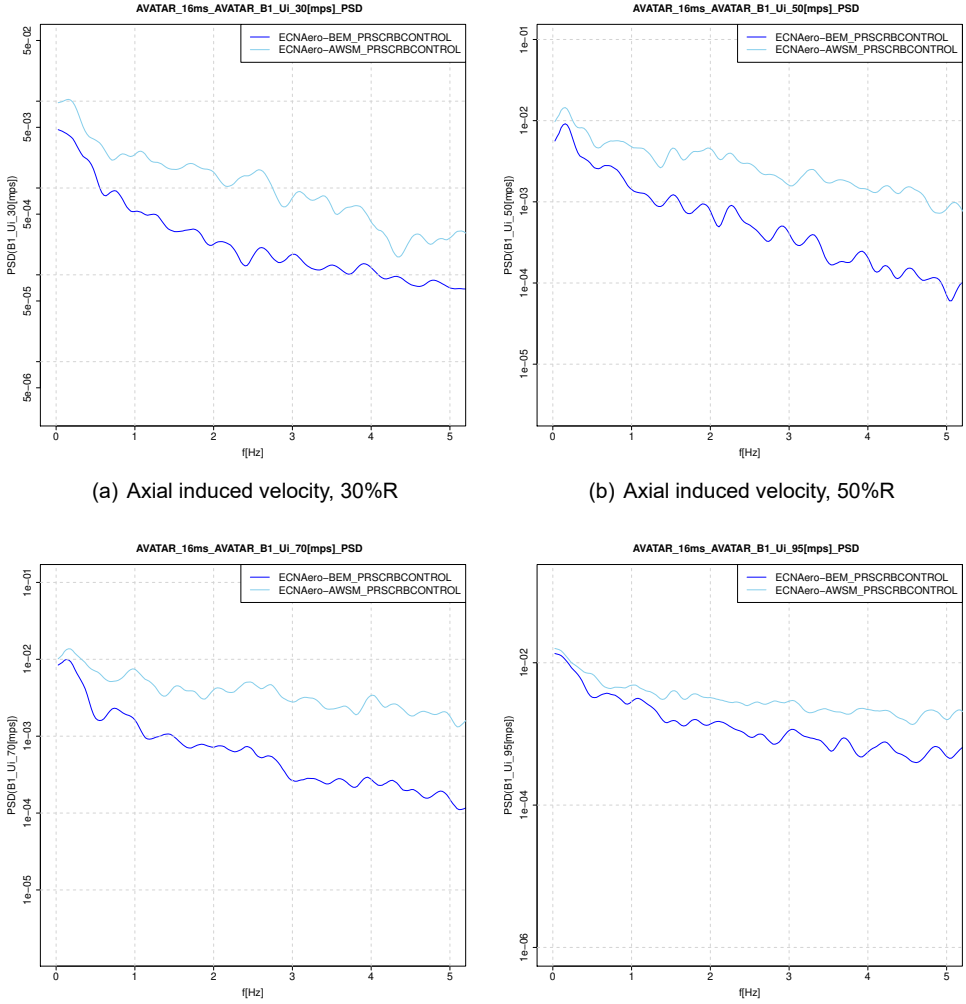

(a) Axial induced velocity, 30%R

(b) Axial induced velocity, 50%R

(c) Axial induced velocity, 70%R

(d) Axial induced velocity, 95%R

Figure B.66: Axial induced velocities

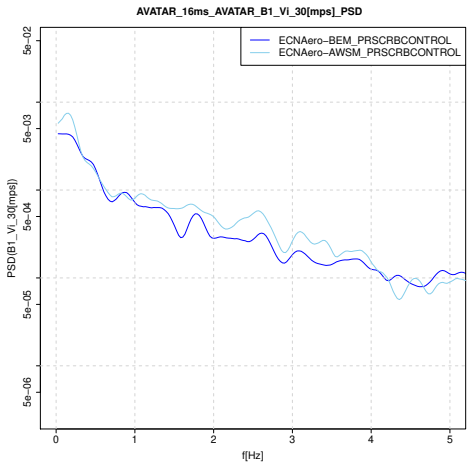

(a) Tangential induced velocity, 30%R

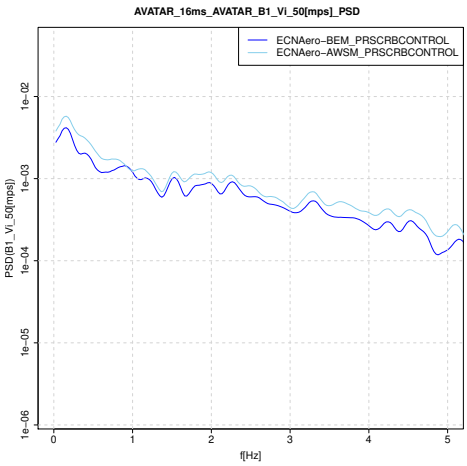

(b) Tangential induced velocity, 50%R

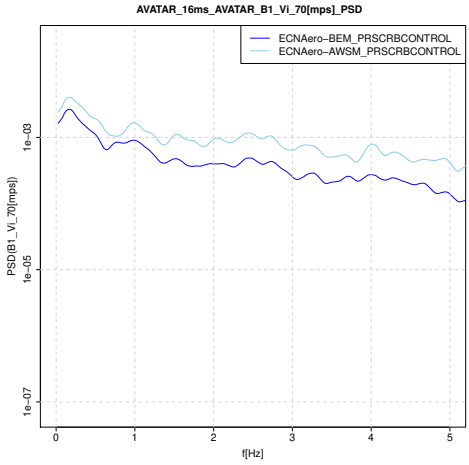

(c) Tangential induced velocity, 70%R

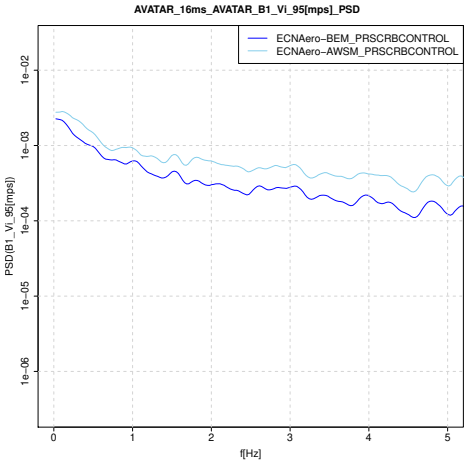

(d) Tangential induced velocity, 95%R

Figure B.67: Tangential induced velocities

B.4 8 m/s, TI=10% case

B.4.1 Time (zoomed)

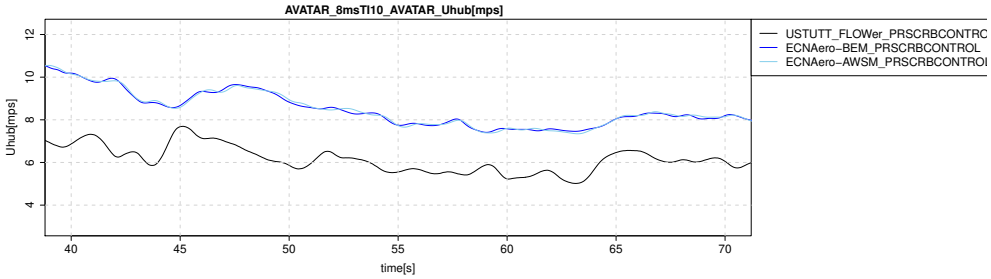

(a) Hub height wind speed

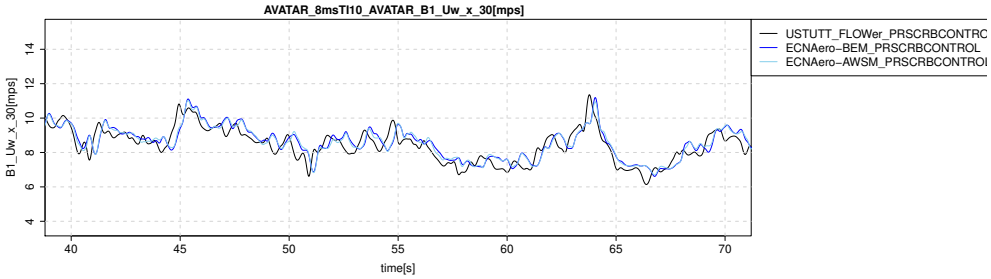

(b) Wind probe axial velocity at 30%R

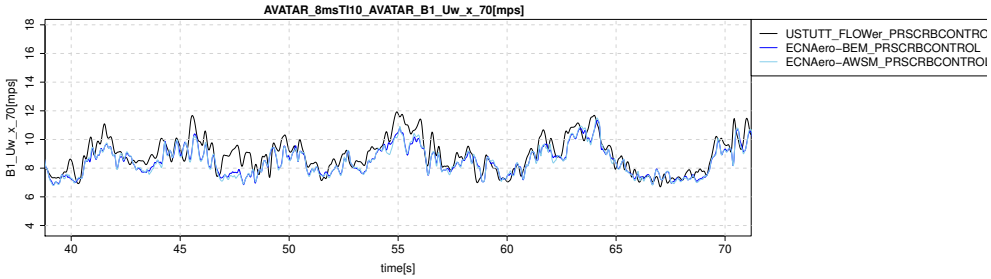

(c) Wind probe axial velocity at 70%R

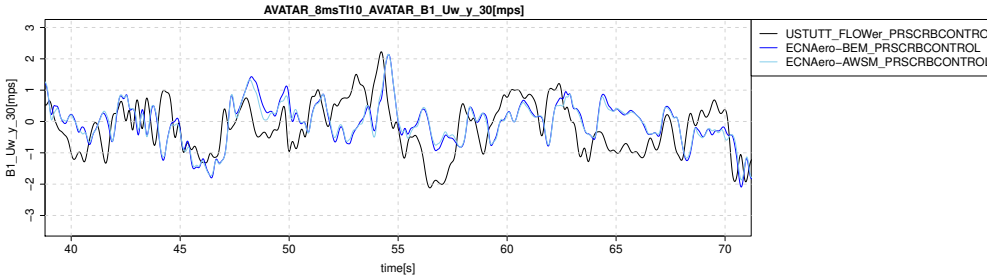

(d) Wind probe lateral velocity at 30%R

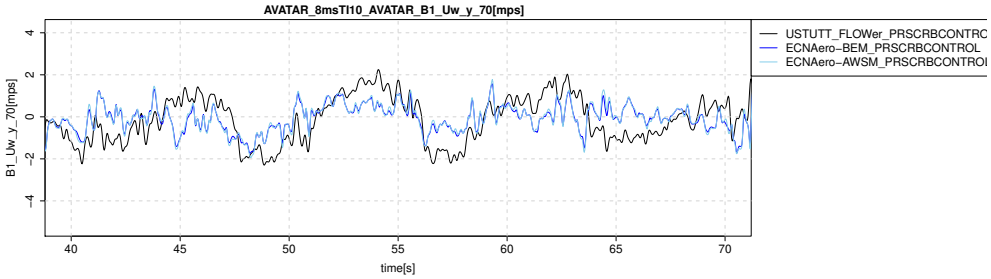

(e) Wind probe lateral velocity at 70%R

Figure B.68: Wind speed alignment check

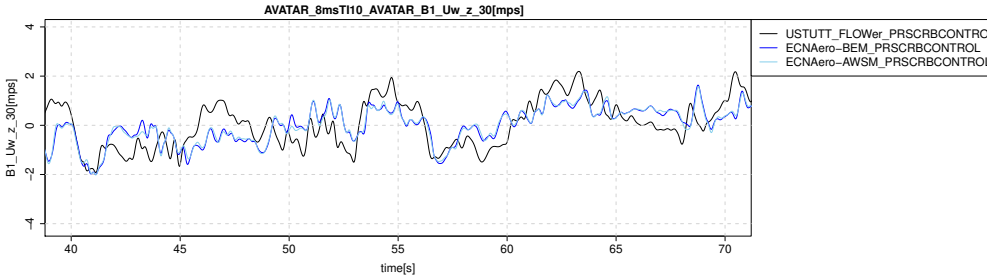

(a) Wind probe vertical velocity at 30%R

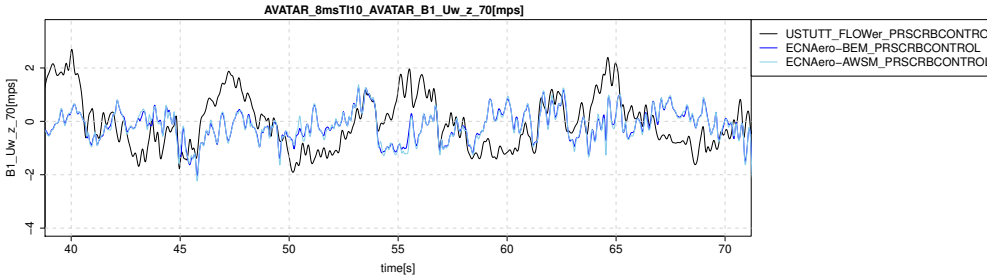

(b) Wind probe vertical velocity at 70%R

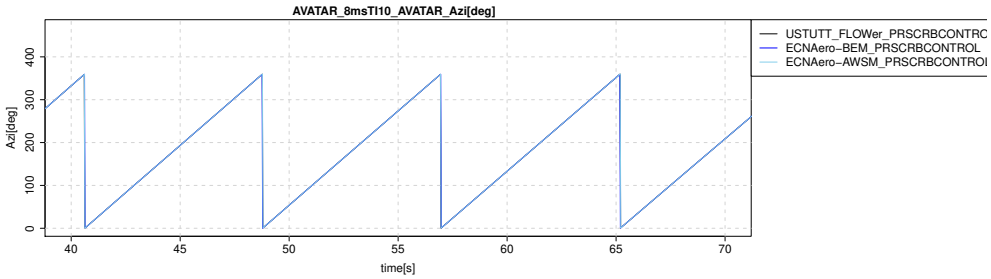

(c) Rotor azimuth angle

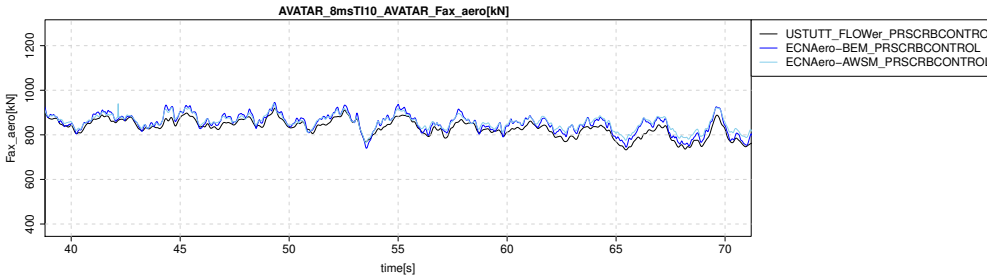

(d) Rotor axial force

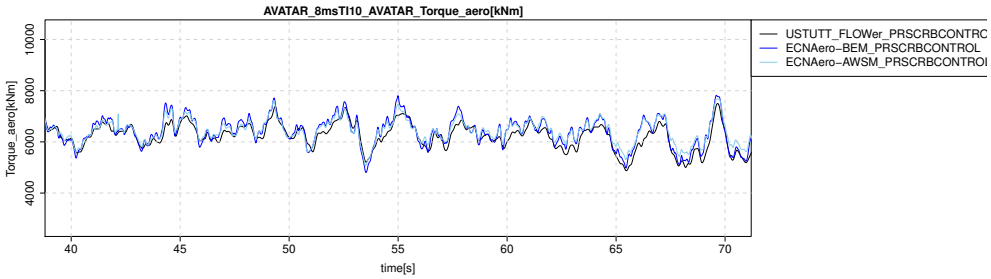

(e) Rotor torque

Figure B.69: Alignment check

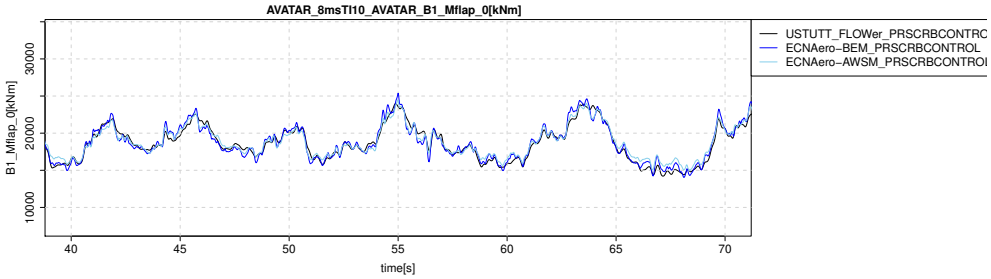

(a) Flapwise blade root moment

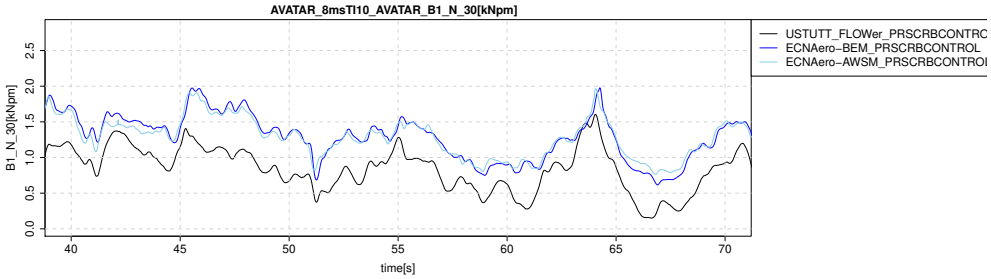

(b) Chord normal force at 30%R

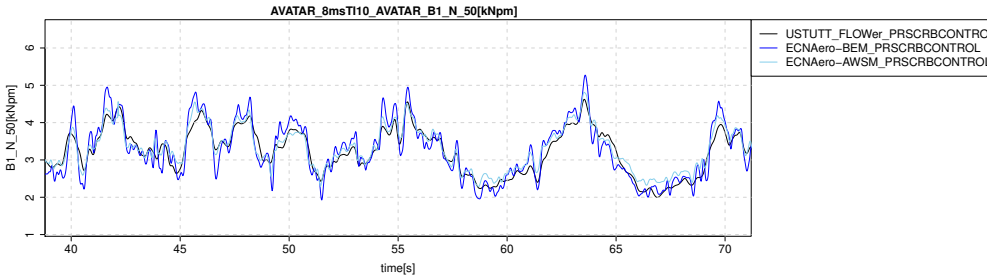

(c) Chord normal force at 50%R

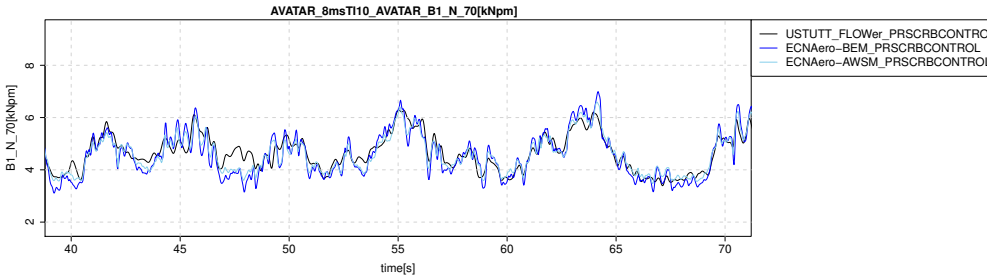

(d) Chord normal force at 70%R

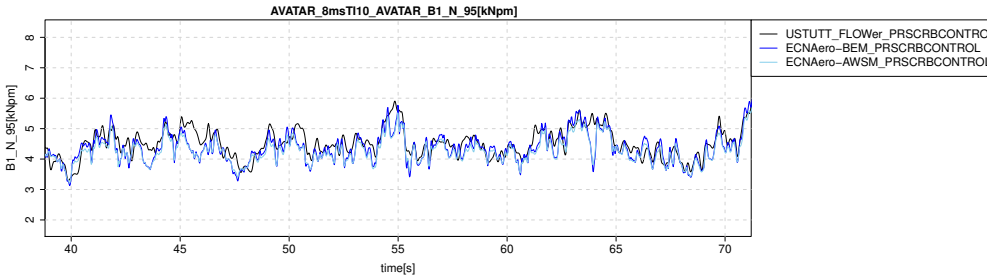

(e) Chord normal force at 95%R

Figure B.70: Flapwise moment and normal force

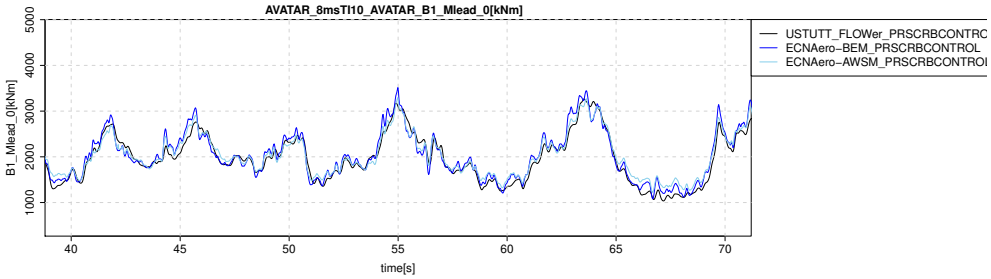

(a) Leadwise blade root moment

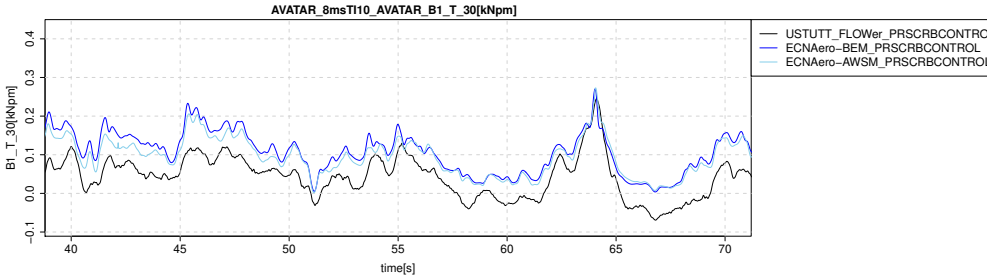

(b) Chord tangential force at 30%R

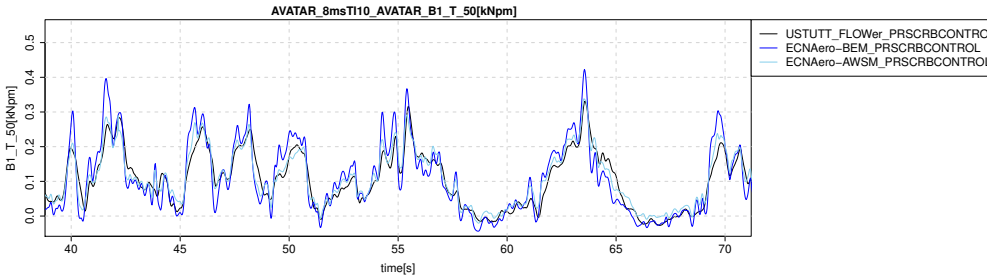

(c) Chord tangential force at 50%R

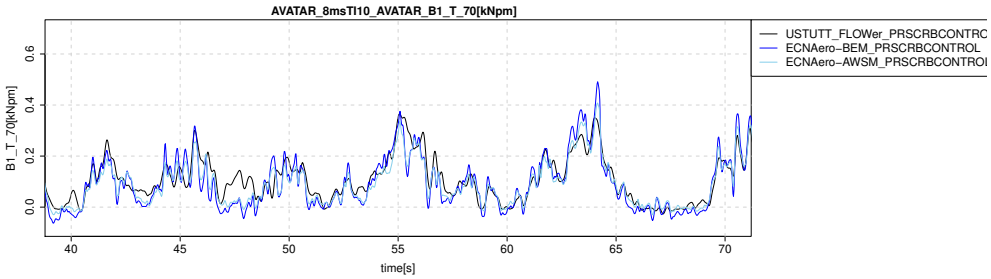

(d) Chord tangential force at 70%R

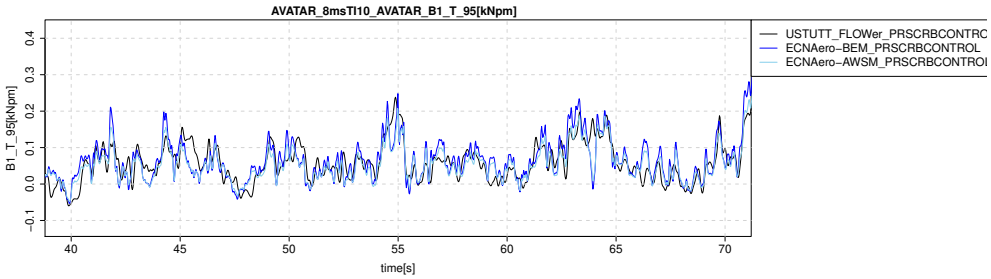

(e) Chord tangential force at 95%R

Figure B.71: Leadwise moment and tangential force

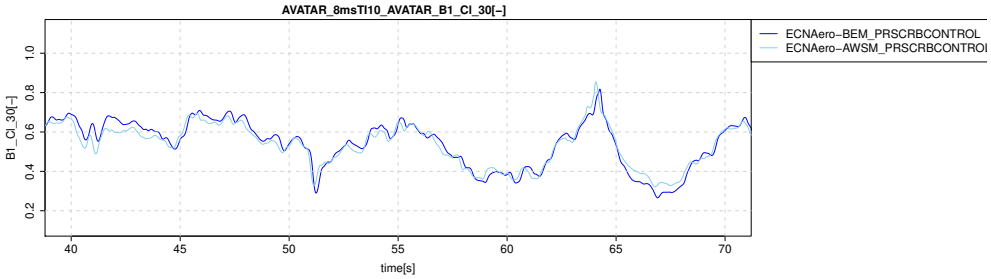

(a) Lift coefficient at 30%R

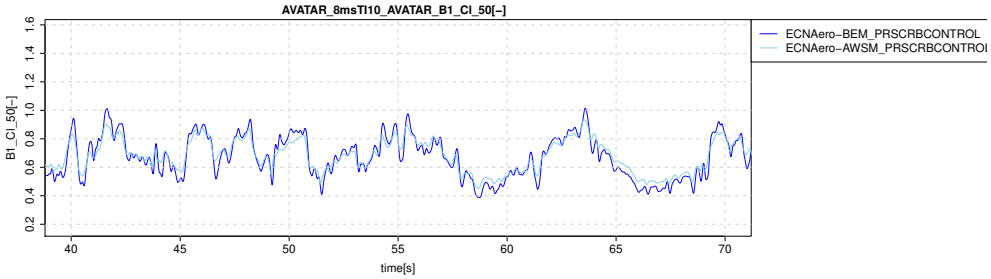

(b) Lift coefficient at 50%R

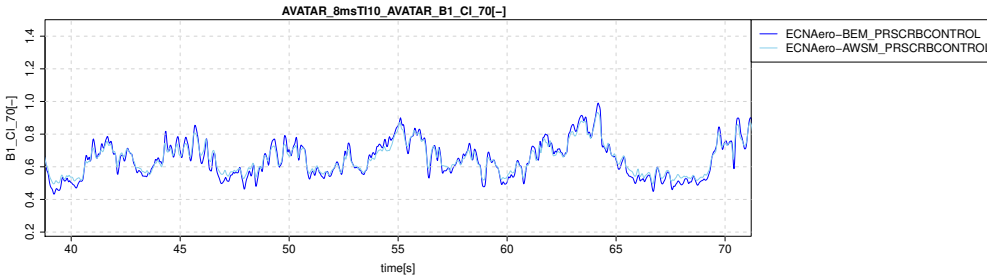

(c) Lift coefficient at 70%R

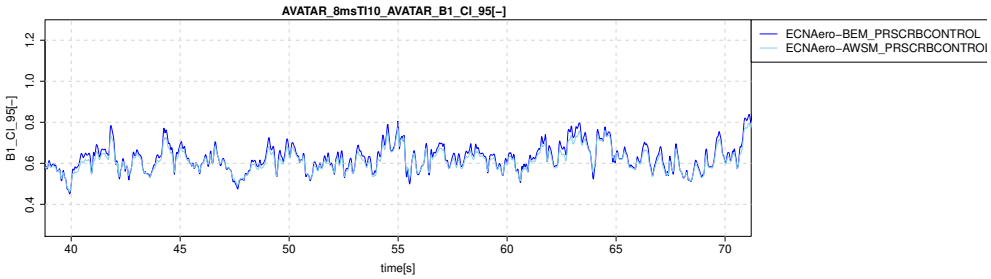

(d) Lift coefficient at 95%R

Figure B.72: Lift coefficients

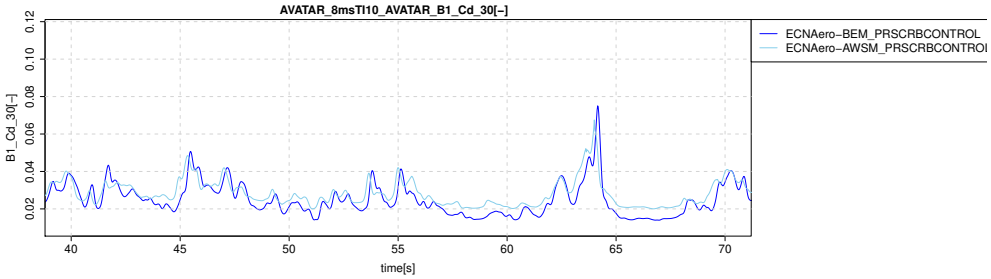

(a) Drag coefficient at 30%R

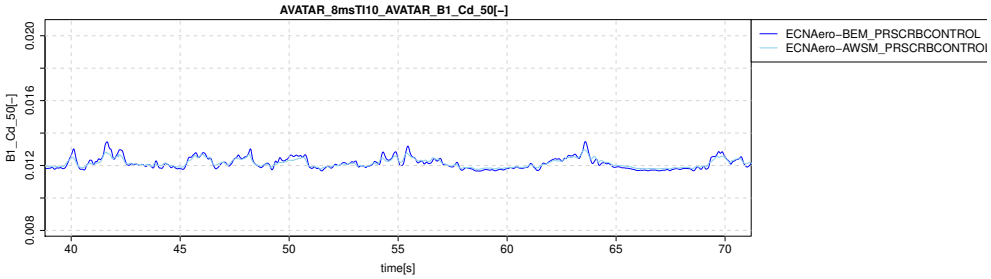

(b) Drag coefficient at 50%R

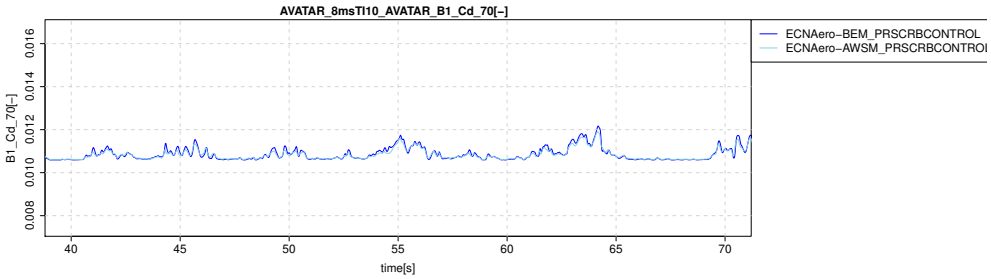

(c) Drag coefficient at 70%R

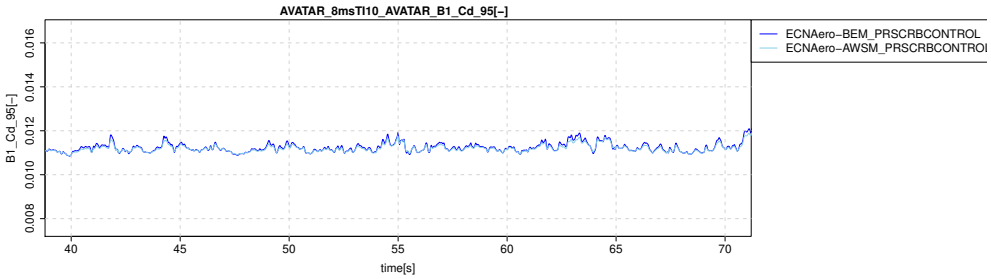

(d) Drag coefficient at 95%R

Figure B.73: Drag coefficients

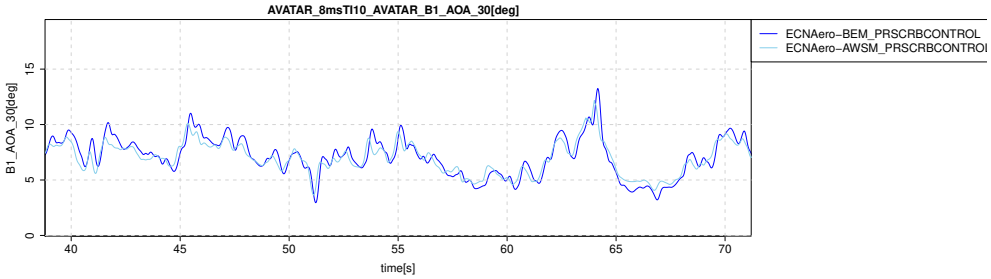

(a) Angle of attack at 30%R

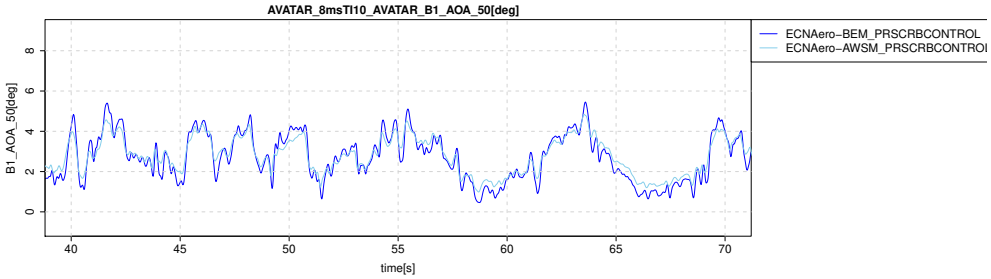

(b) Angle of attack at 50%R

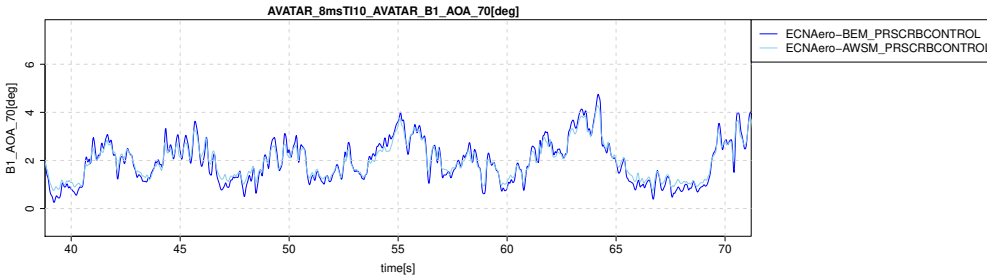

(c) Angle of attack at 70%R

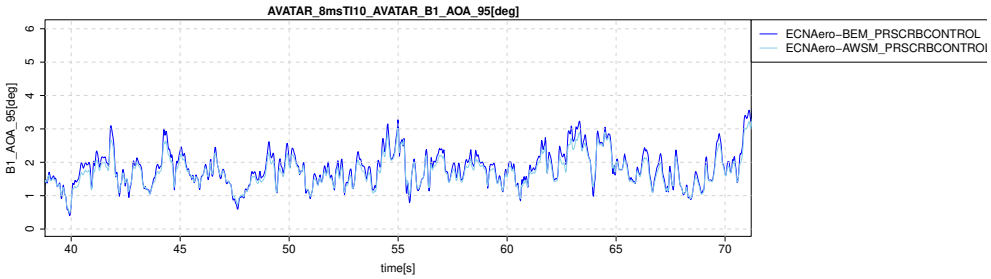

(d) Angle of attack at 95%R

Figure B.74: Angles of attack

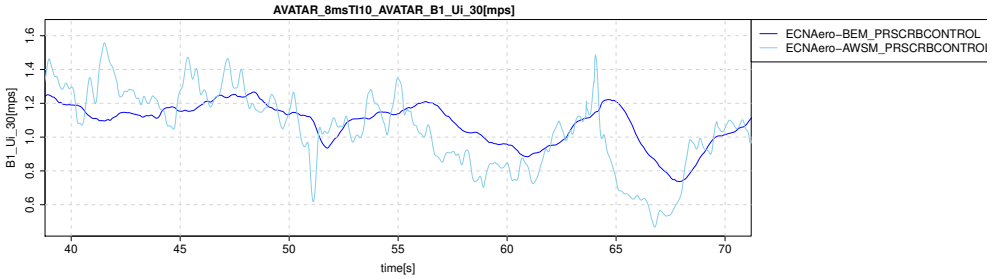

(a) Axial induced velocity at 30%R

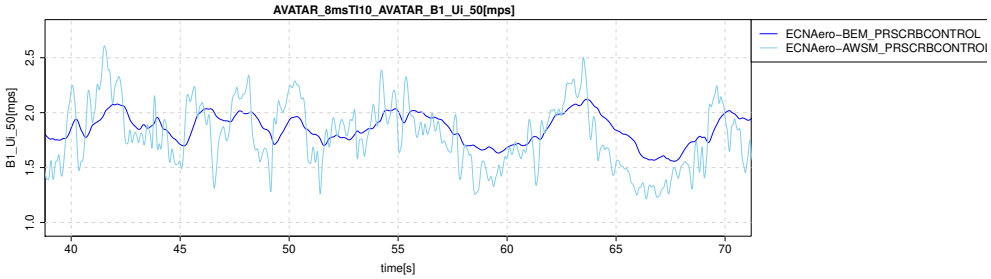

(b) Axial induced velocity at 50%R

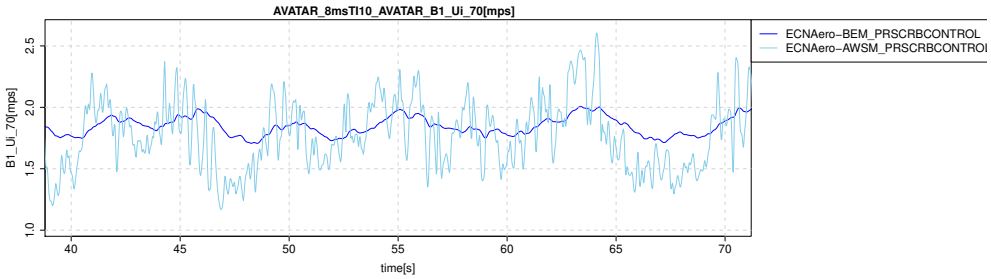

(c) Axial induced velocity at 70%R

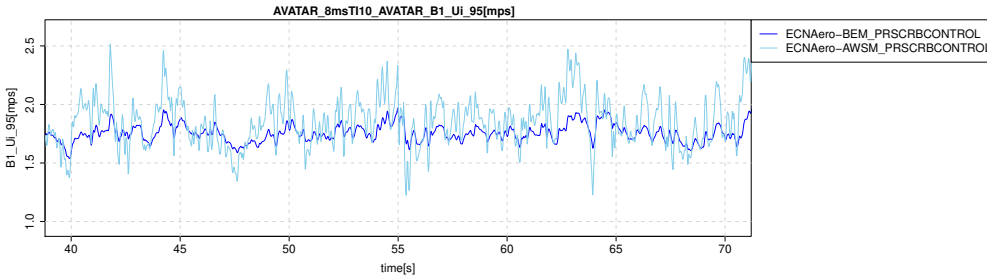

(d) Axial induced velocity at 95%R

Figure B.75: Axial induced velocities

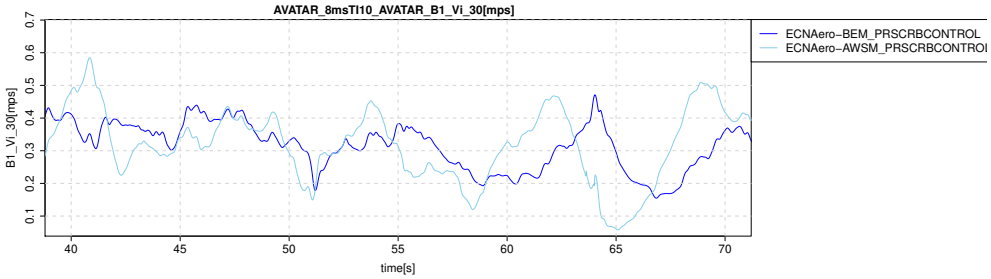

(a) Tangential induced velocity at 30%R

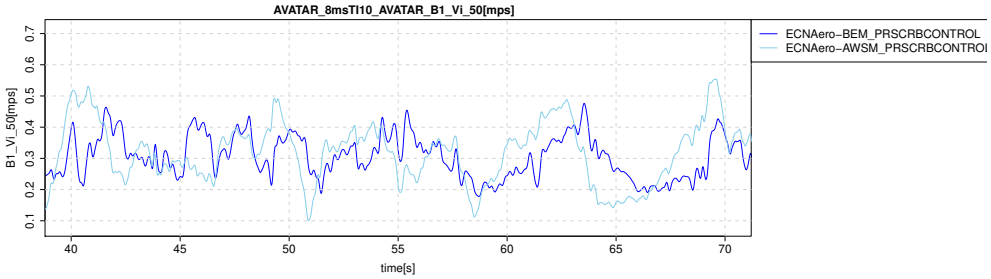

(b) Tangential induced velocity at 50%R

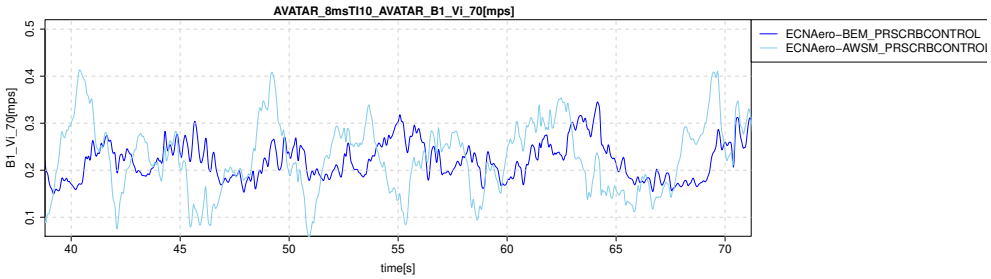

(c) Tangential induced velocity at 70%R

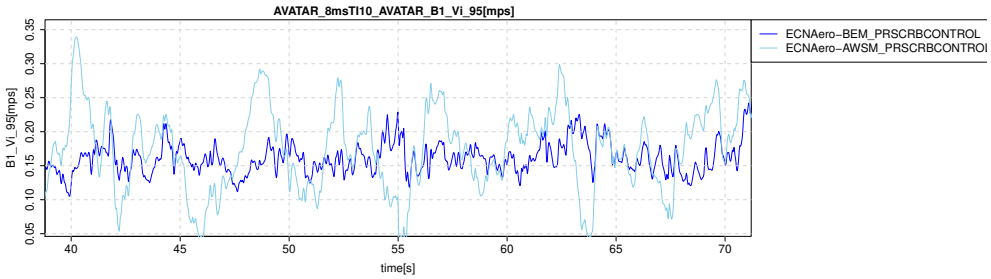

(d) Tangential induced velocity at 95%R

Figure B.76: Tangential induced velocities

B.4.2 Time

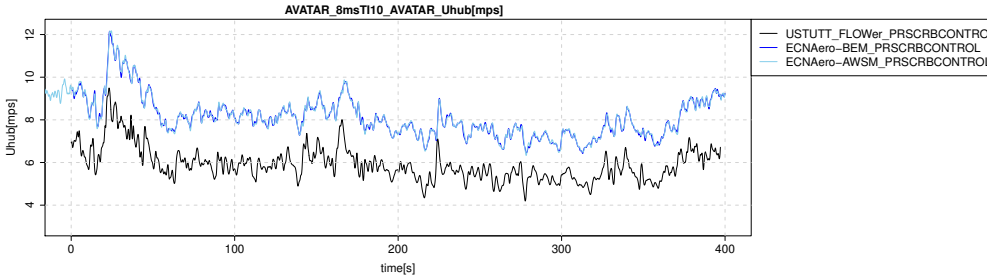

(a) Hub height wind speed

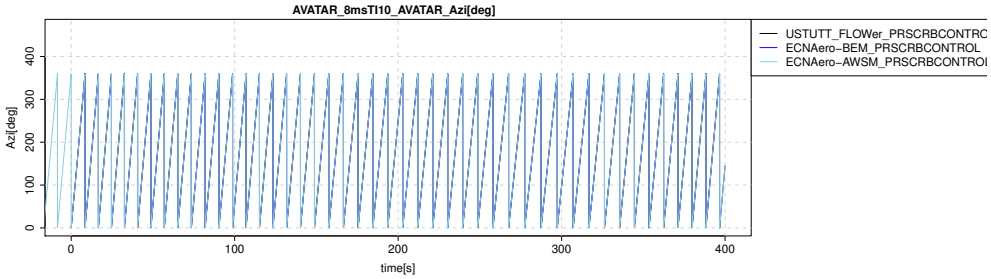

(b) Rotor azimuth

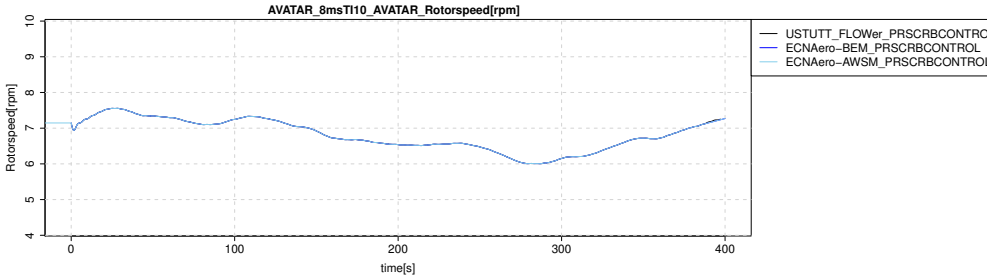

(c) Rotor speed

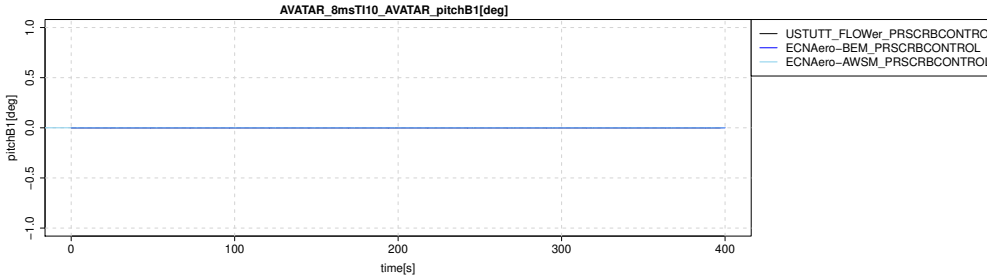

(d) Pitch angle

Figure B.77: Wind and control parameters

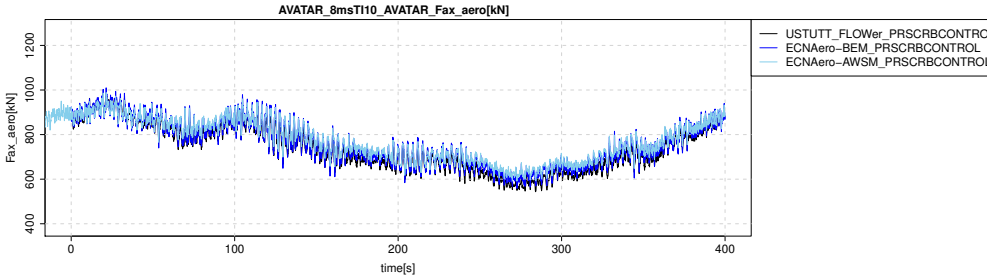

(a) Rotor axial force

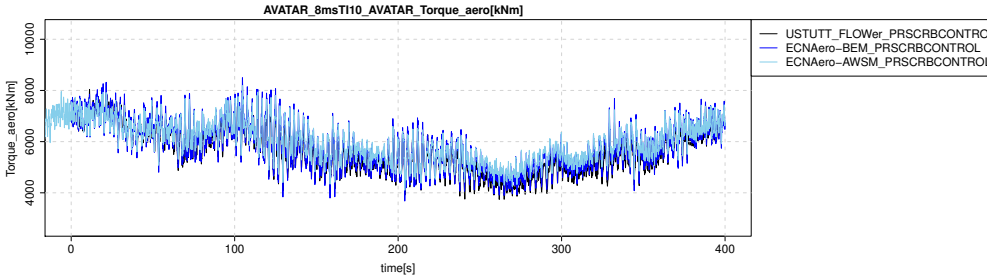

(b) Rotor torque

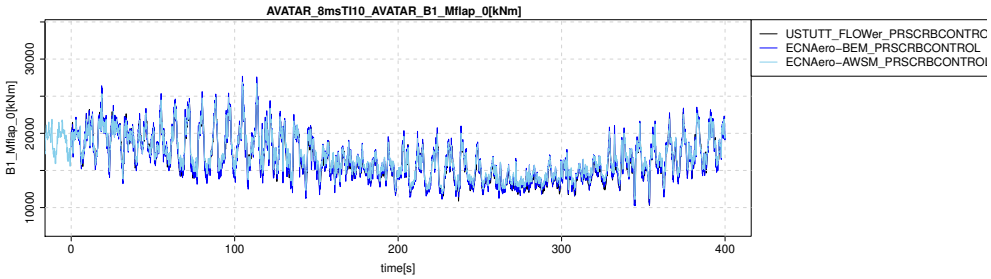

(c) Flapwise blade root moment

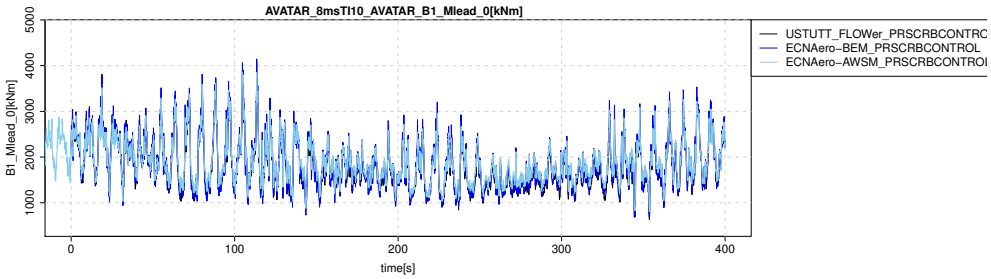

(d) Leadwise blade root moment

Figure B.78: Rotor and blade forces and moments

B.4.3 Statistics

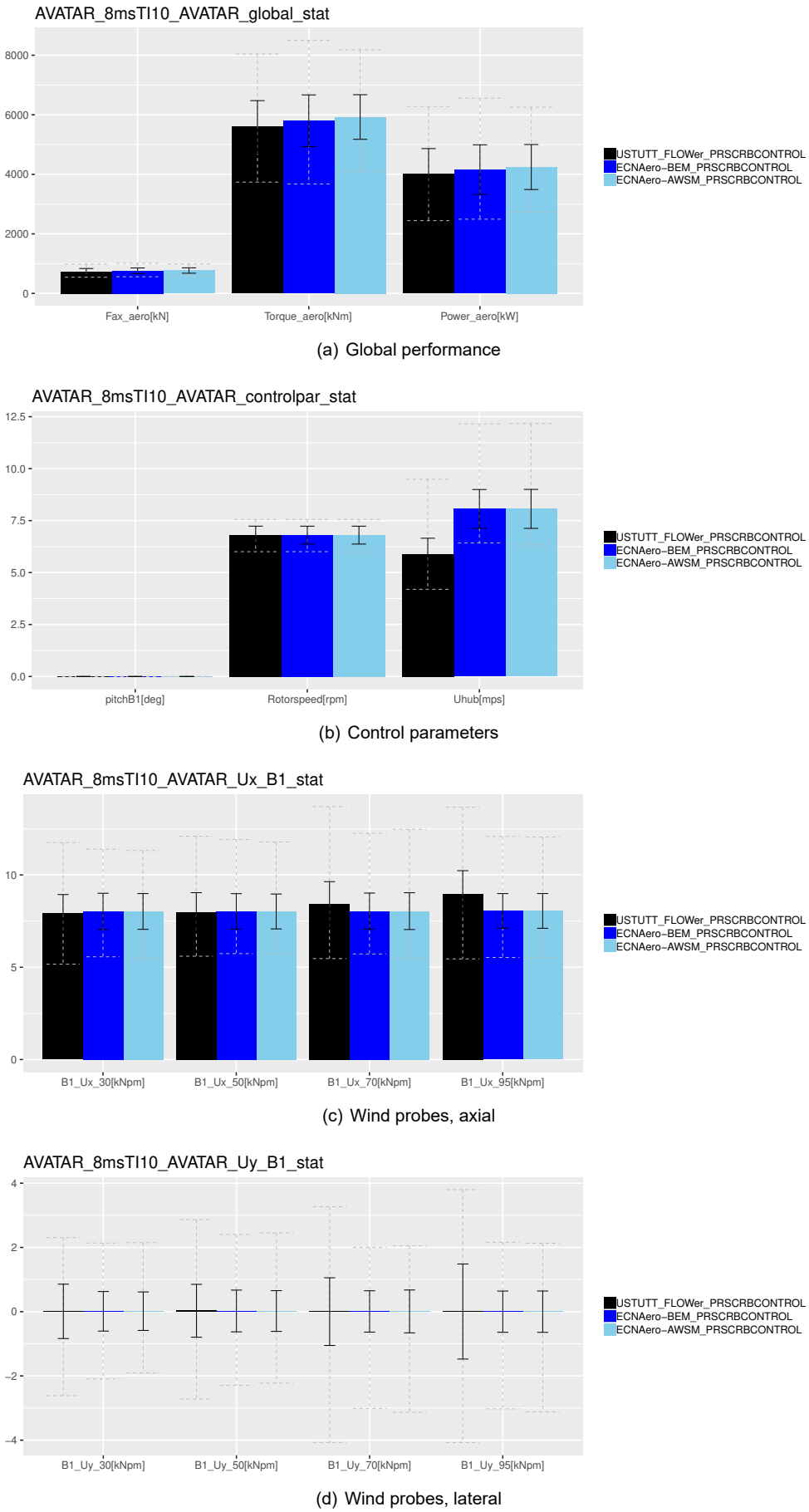

Figure B.79: Global performance, wind and control parameters

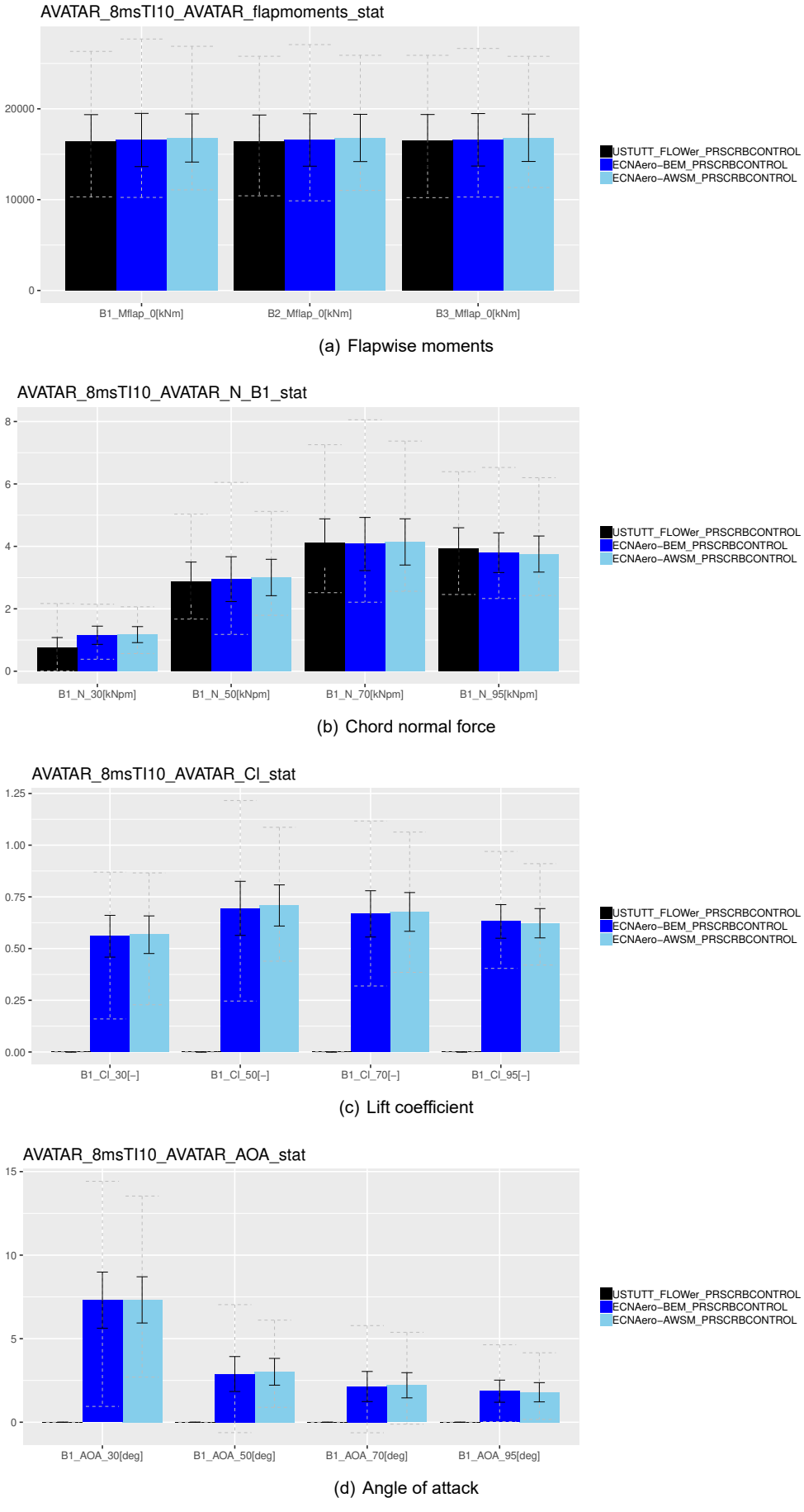

Figure B.80: Force decompostion in axial direction

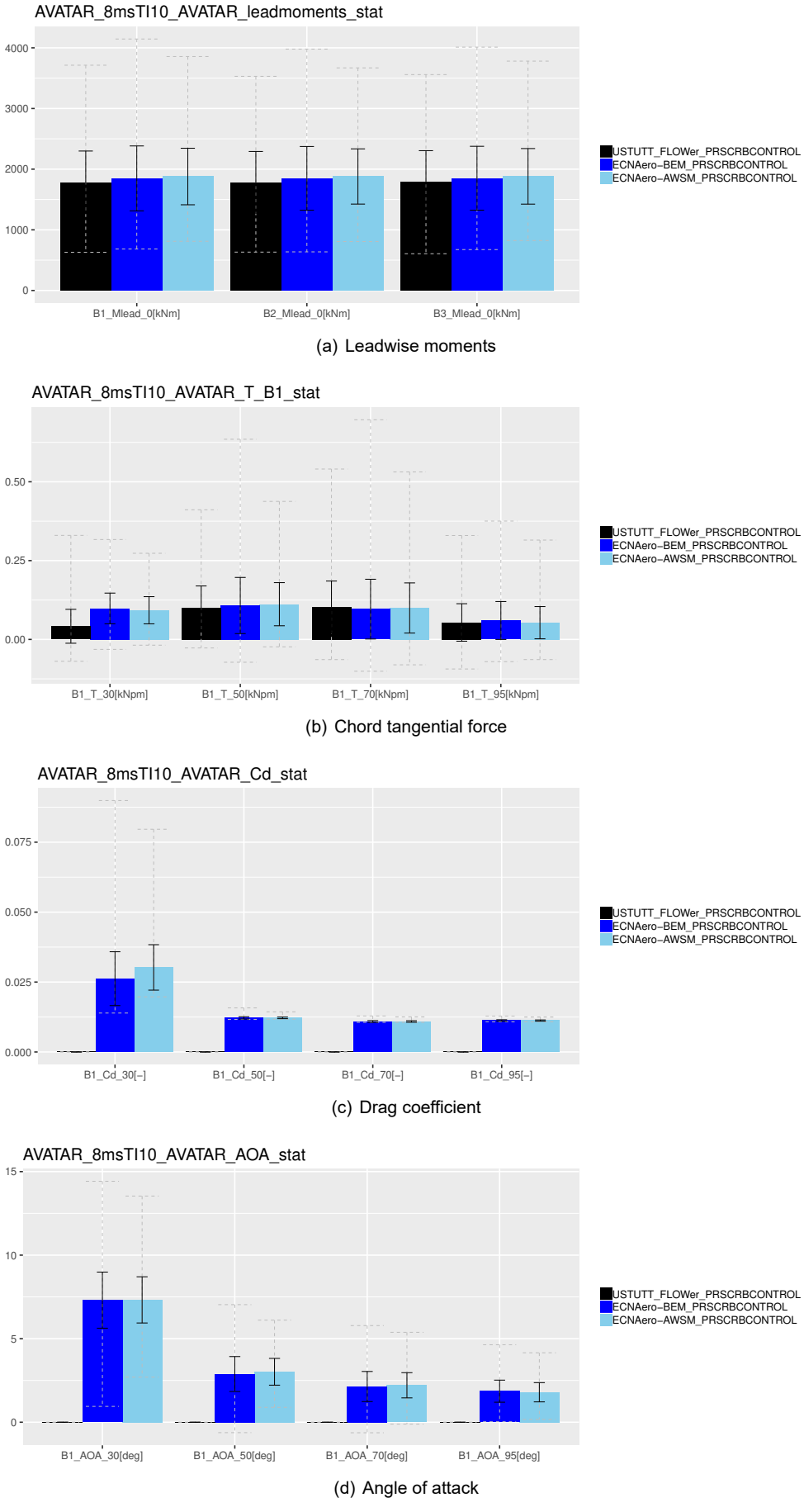

Figure B.81: Force decompostion in tangential direction

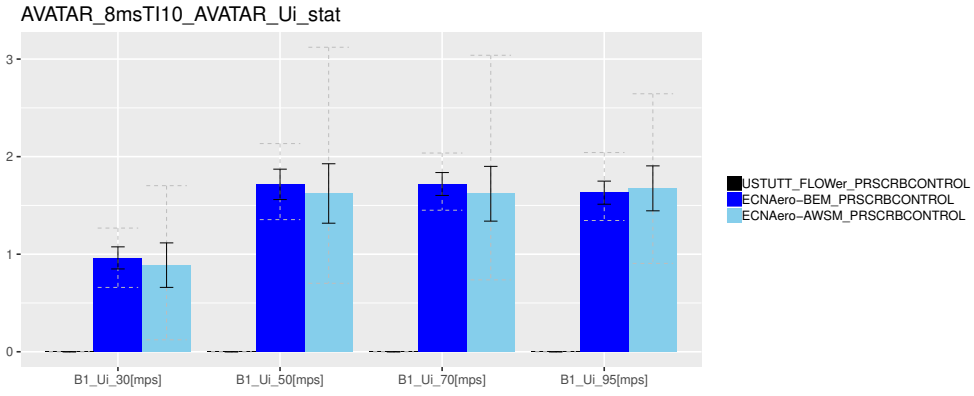

(a) Axial induced velocity

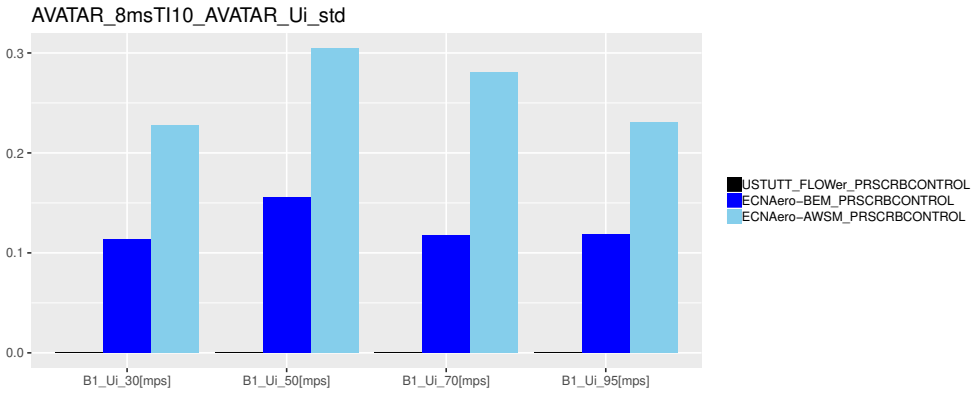

(b) Axial induced velocity (standard deviation)

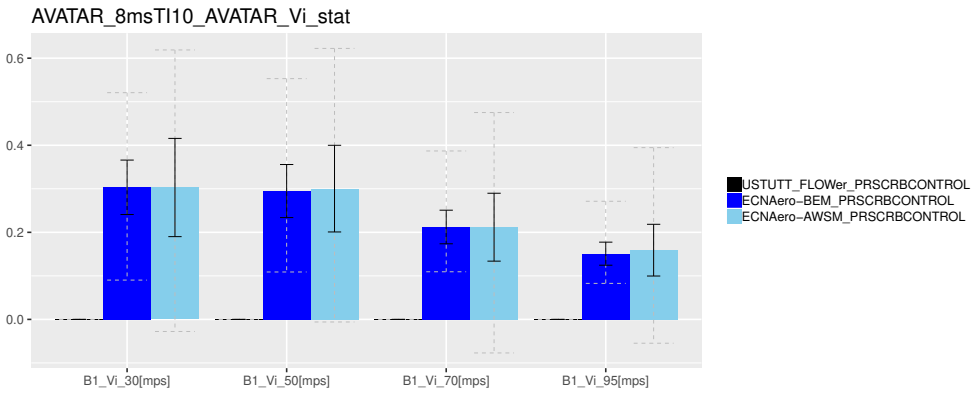

(c) Tangential induced velocity

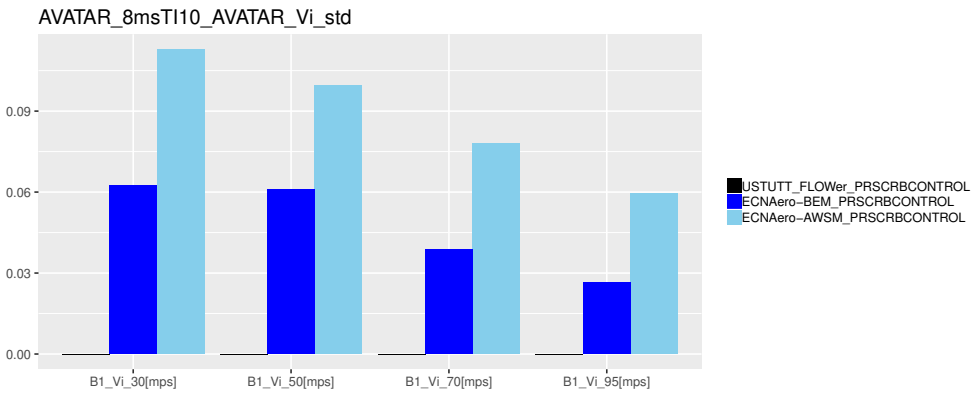

(d) Tangential induced velocity (standard deviation)

Figure B.82: Induced velocities

B.4.4 Equivalent load levels

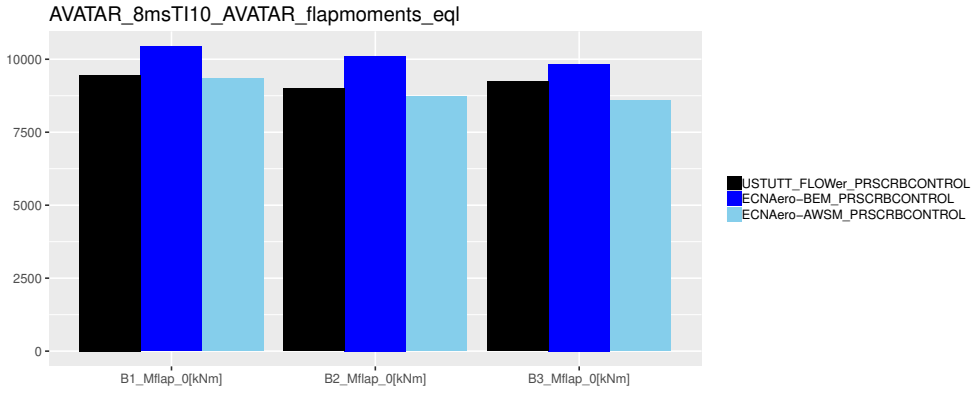

(a) Flapwise moments

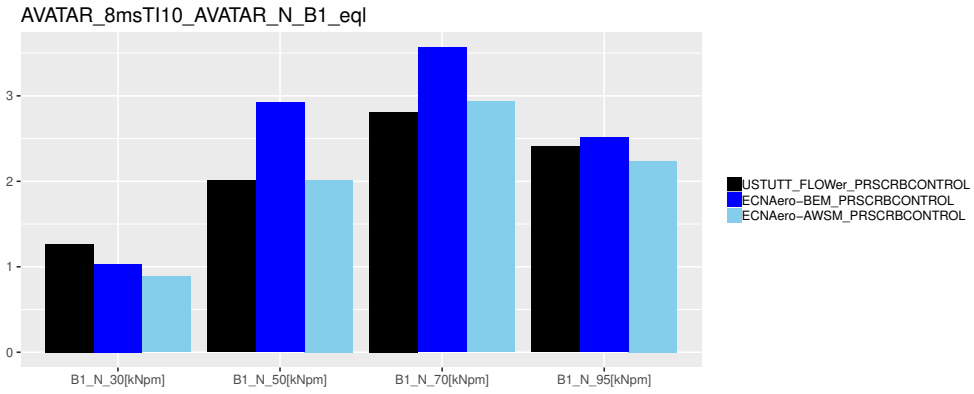

(b) Normal force

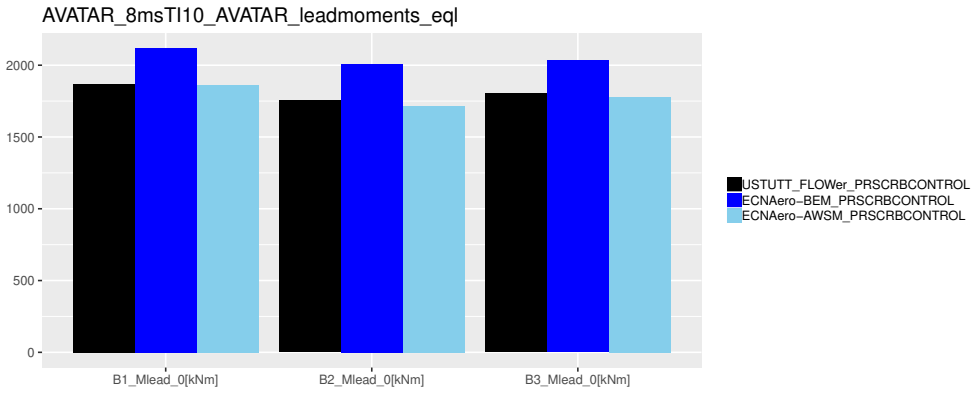

(c) Leadwise moments

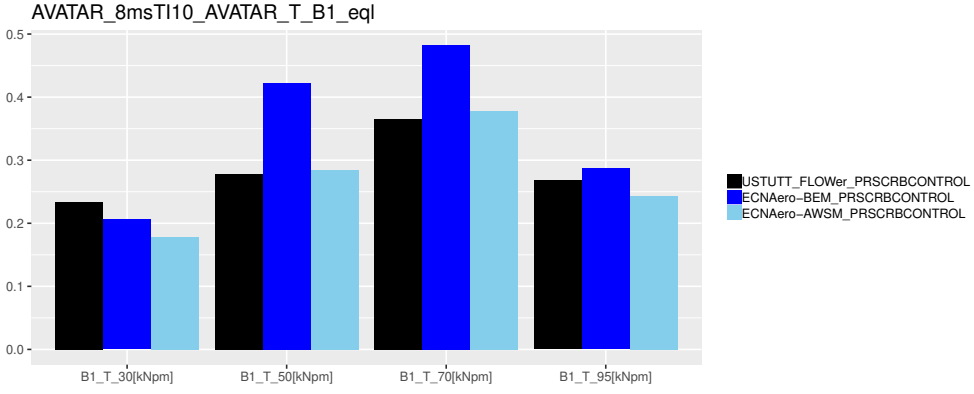

(d) Tangential force

Figure B.83: Forces and moments

B.4.5 Staircase plots

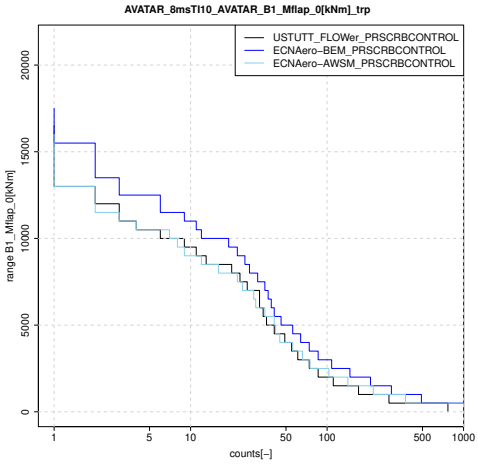

(a) Flapwise blade root moment

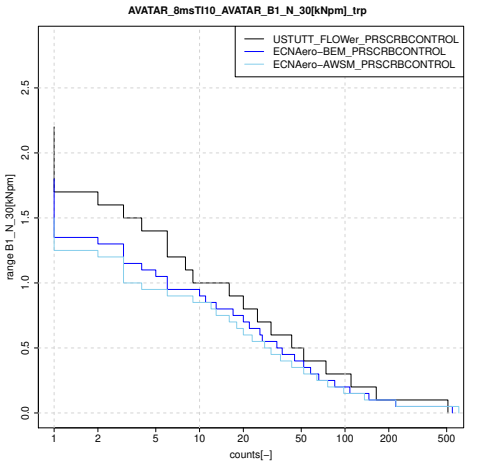

(b) Normal force, 30%R

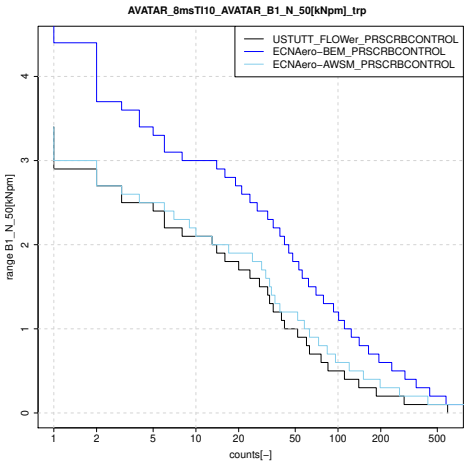

(c) Normal force, 50%R

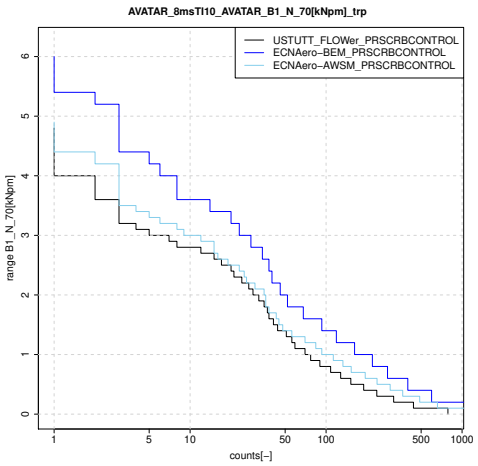

(d) Normal force, 70%R

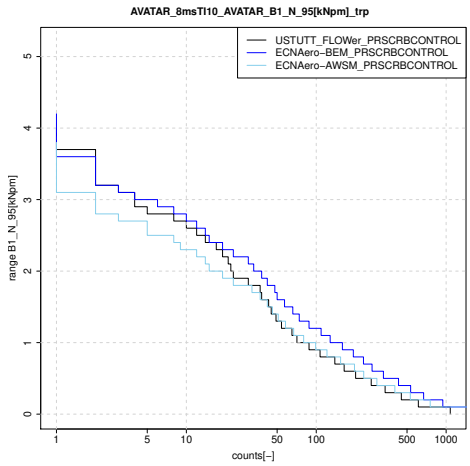

(e) Normal force, 95%R

Figure B.84: Flapwise moment and normal forces

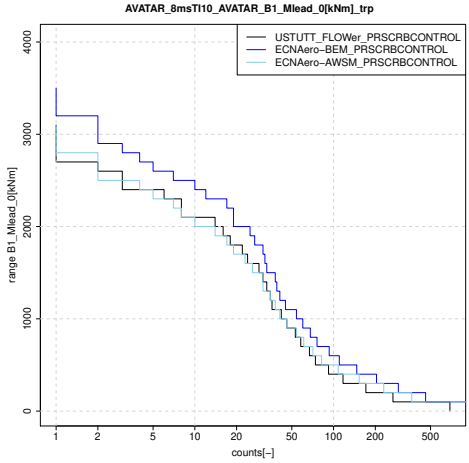

(a) Leadwise blade root moment

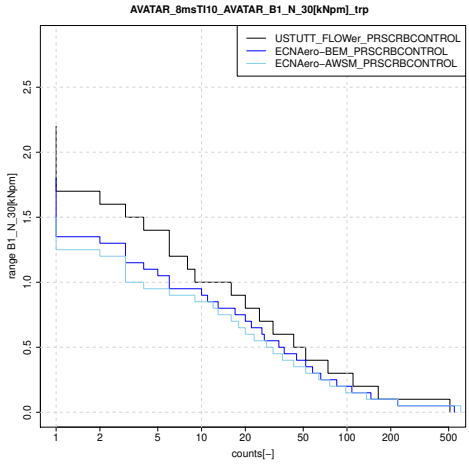

(b) Tangential force, 30%R

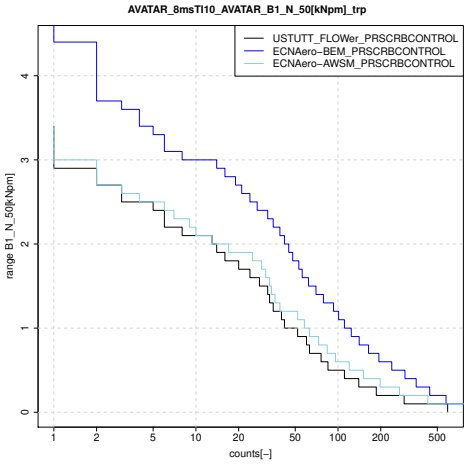

(c) Tangential force, 50%R

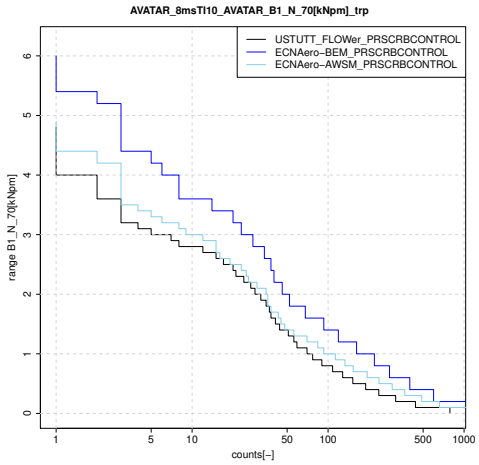

(d) Tangential force, 70%R

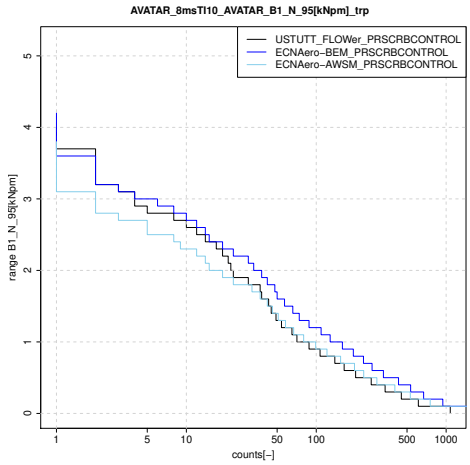

(e) Tangential force, 95%R

Figure B.85: Leadwise moment and tangential forces

B.4.6 PSD

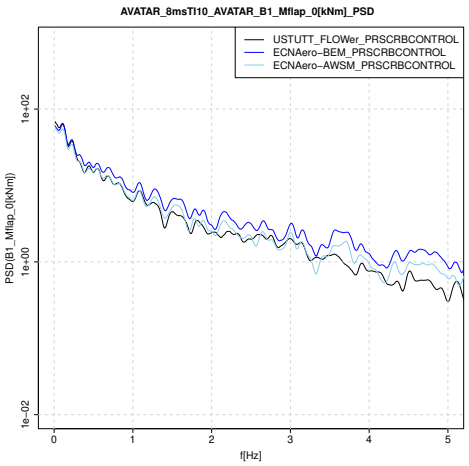

(a) Flapwise blade root moment

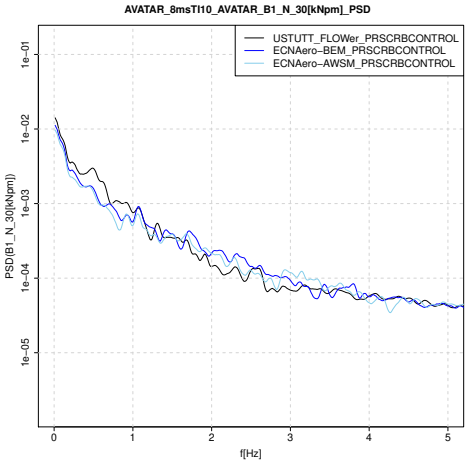

(b) Normal force, 30%R

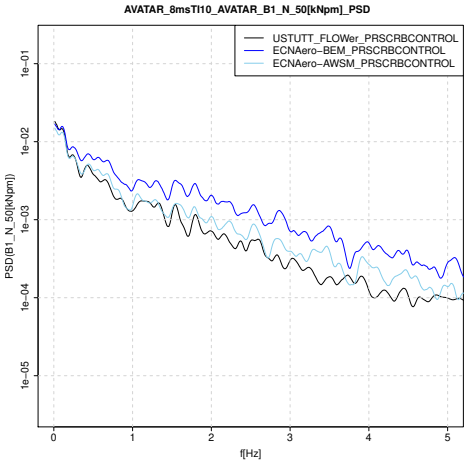

(c) Normal force, 50%R

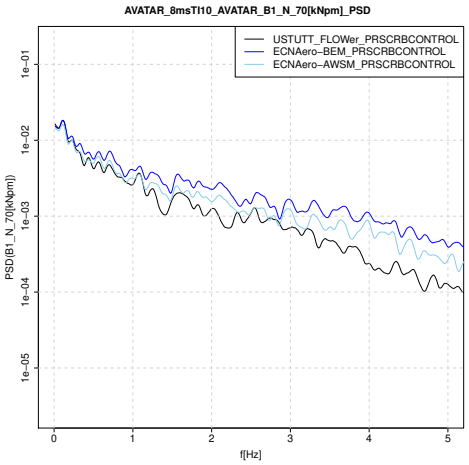

(d) Normal force, 70%R

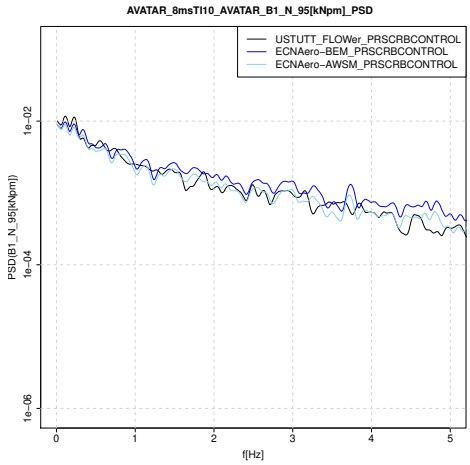

(e) Normal force, 95%R

Figure B.86: Flapwise moment and normal forces

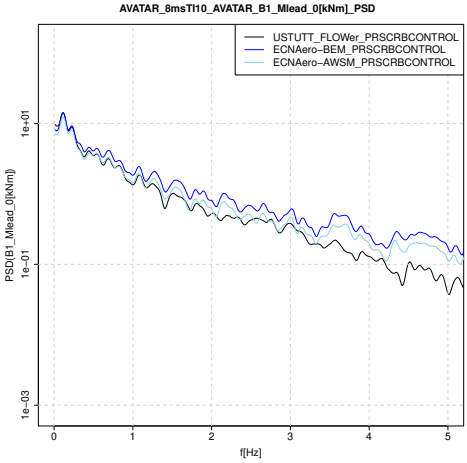

(a) Leadwise blade root moment

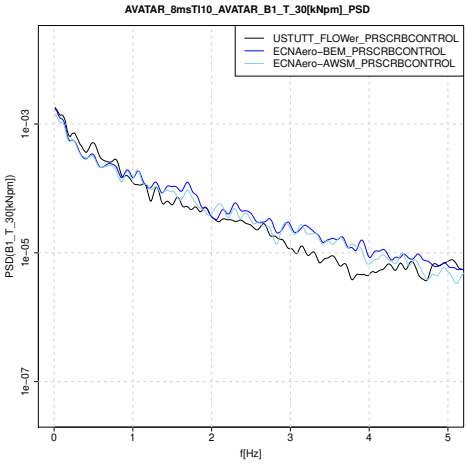

(b) Tangential force, 30%R

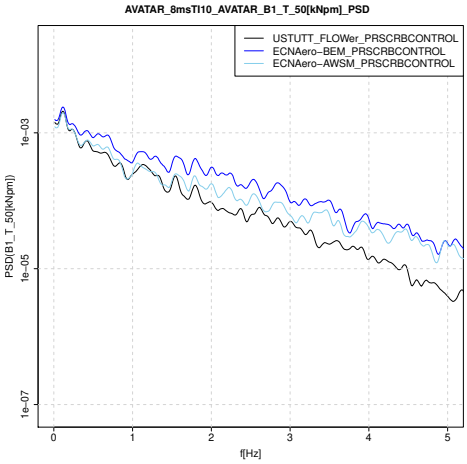

(c) Tangential force, 50%R

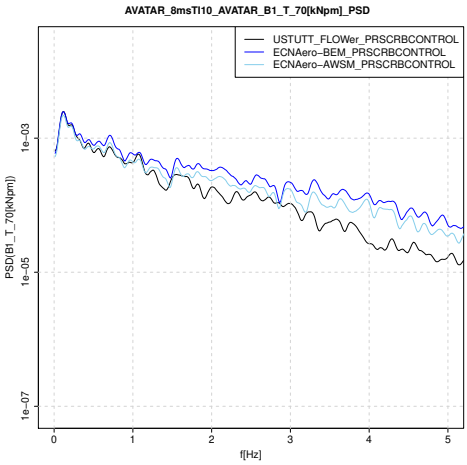

(d) Tangential force, 70%R

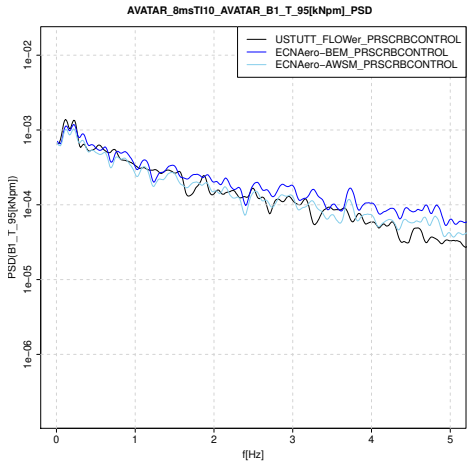

(e) Tangential force, 95%R

Figure B.87: Leadwise moment and tangential forces

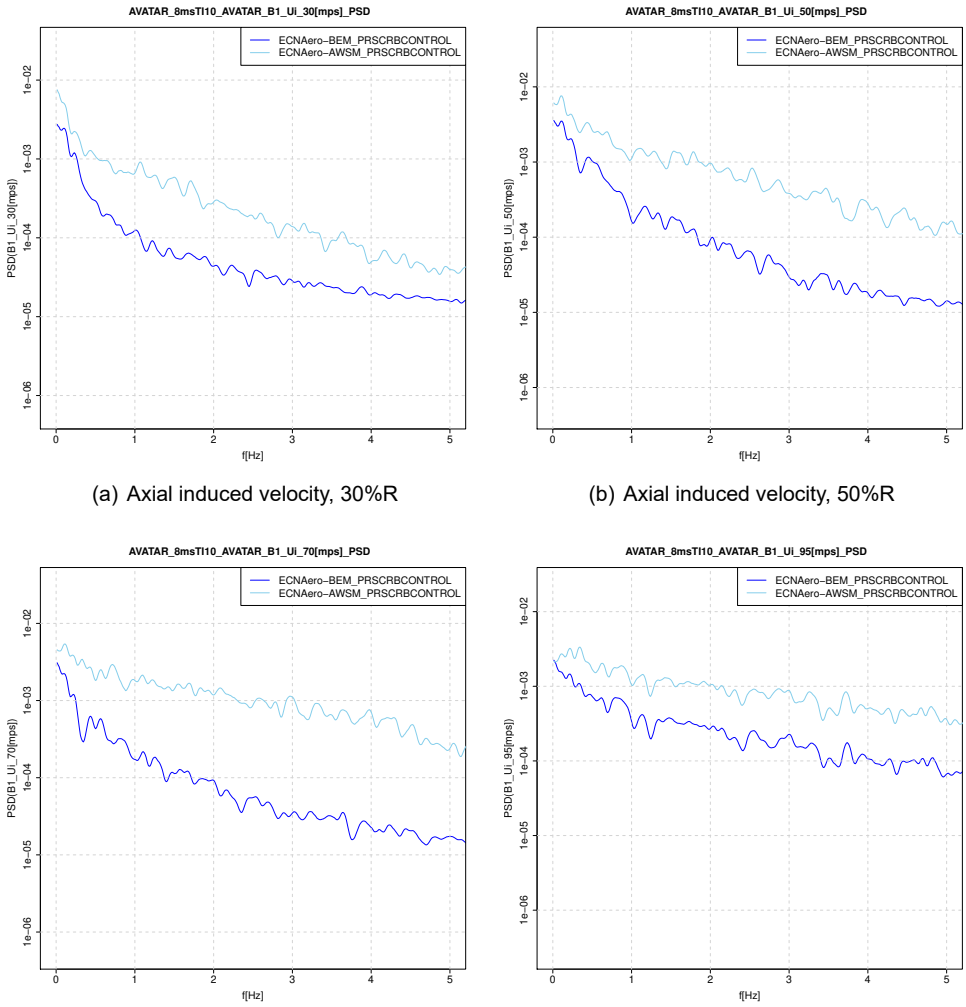

(a) Axial induced velocity, 30%R

(b) Axial induced velocity, 50%R

(c) Axial induced velocity, 70%R

(d) Axial induced velocity, 95%R

Figure B.88: Axial induced velocities

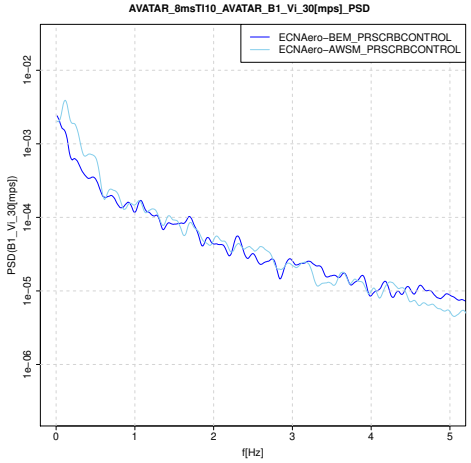

(a) Tangential induced velocity, 30%R

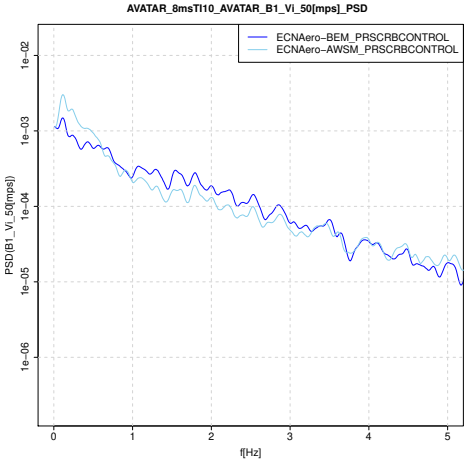

(b) Tangential induced velocity, 50%R

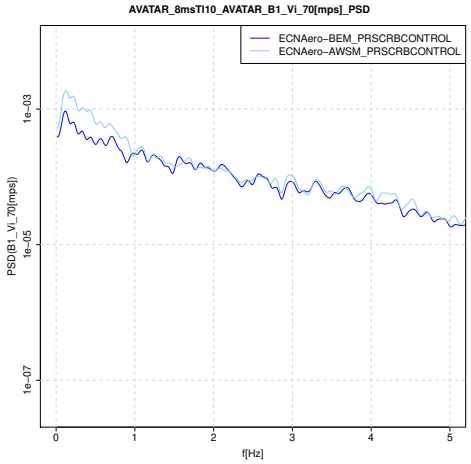

(c) Tangential induced velocity, 70%R

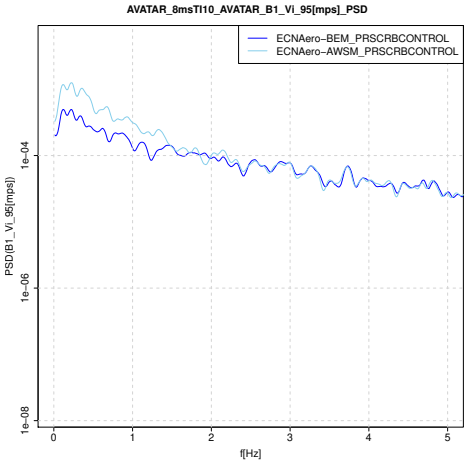

(d) Tangential induced velocity, 95%R

Figure B.89: Tangential induced velocities

B.5 8 m/s, high Ct case

B.5.1 Time (zoomed)

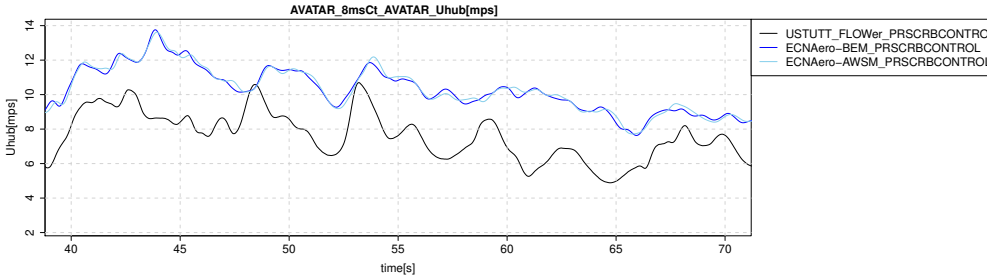

(a) Hub height wind speed

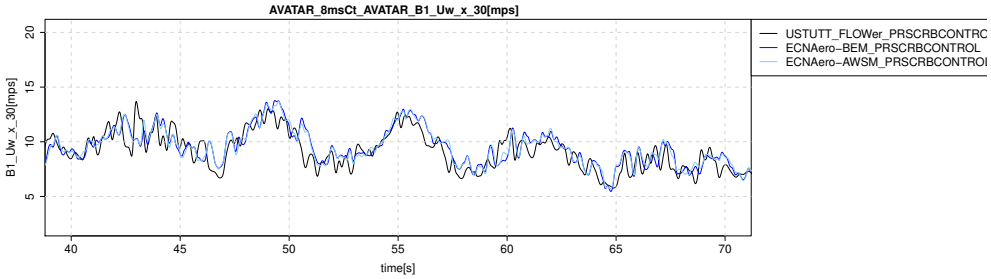

(b) Wind probe axial velocity at 30%R

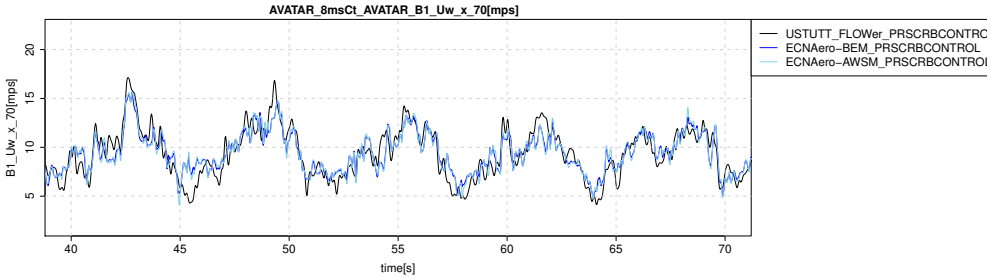

(c) Wind probe axial velocity at 70%R

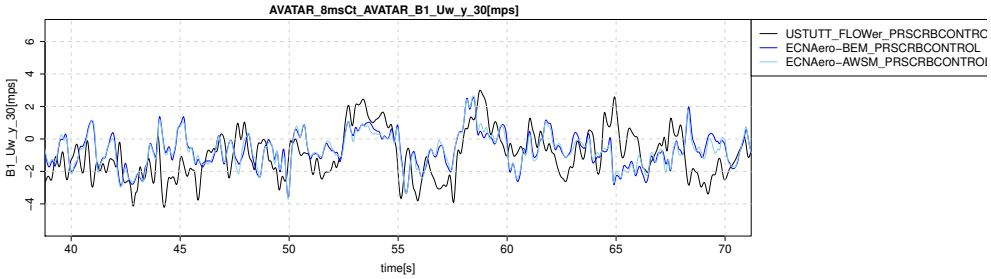

(d) Wind probe lateral velocity at 30%R

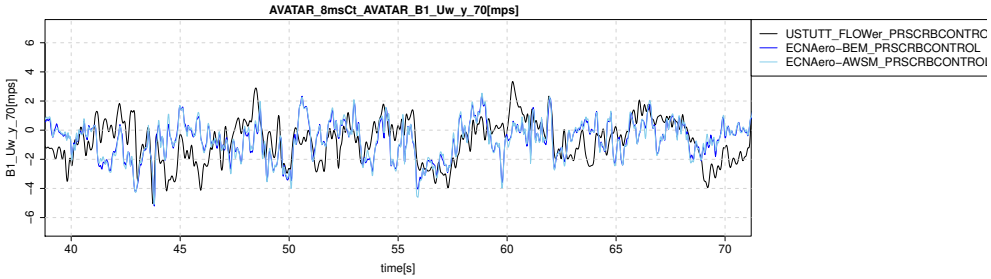

(e) Wind probe lateral velocity at 70%R

Figure B.90: Wind speed alignment check

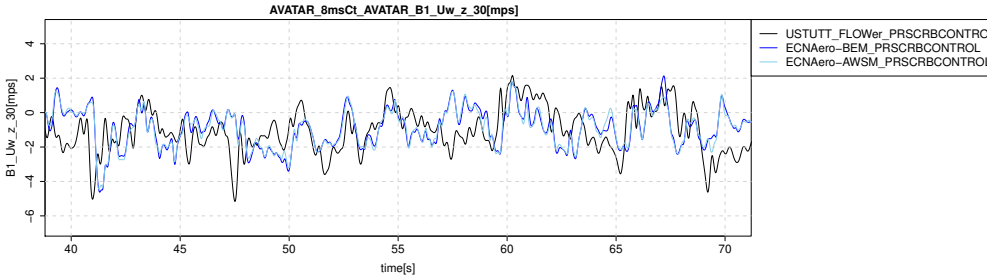

(a) Wind probe vertical velocity at 30%R

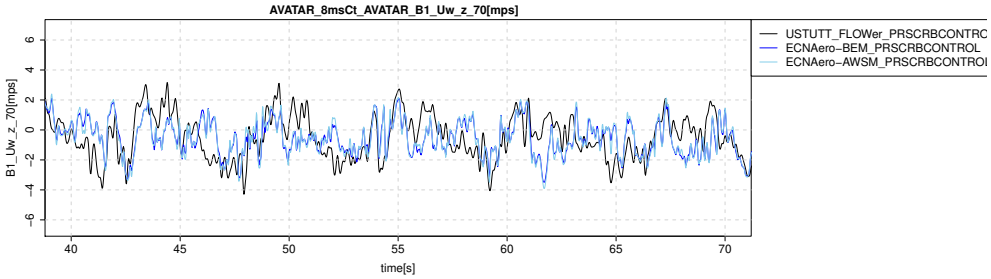

(b) Wind probe vertical velocity at 70%R

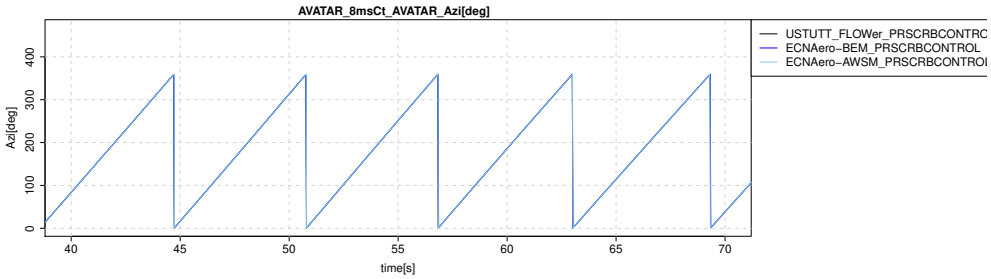

(c) Rotor azimuth angle

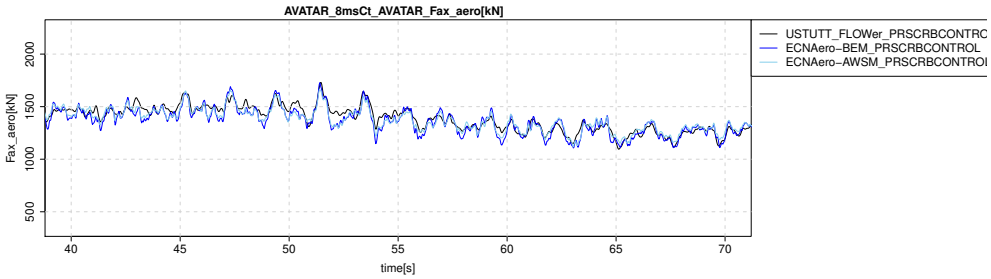

(d) Rotor axial force

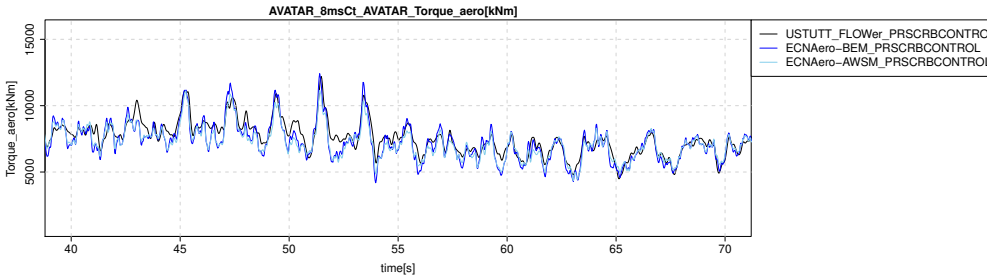

(e) Rotor torque

Figure B.91: Alignment check

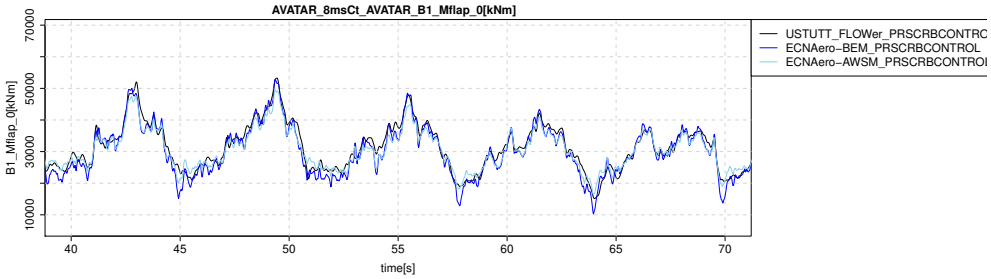

(a) Flapwise blade root moment

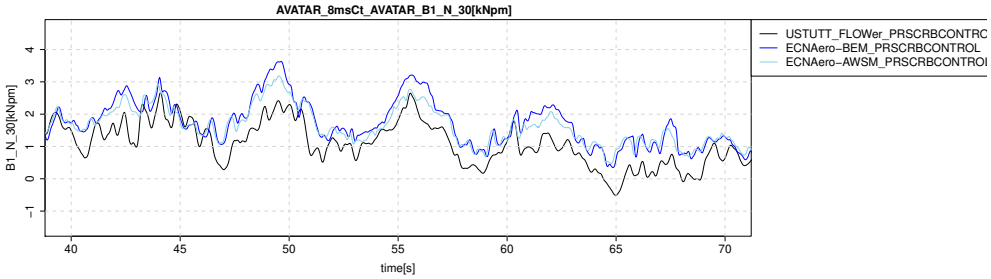

(b) Chord normal force at 30%R

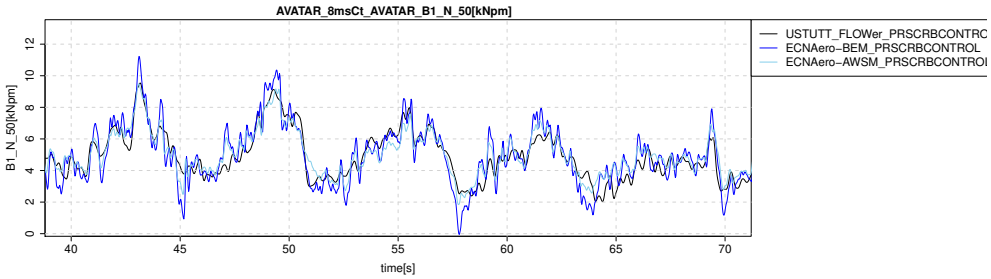

(c) Chord normal force at 50%R

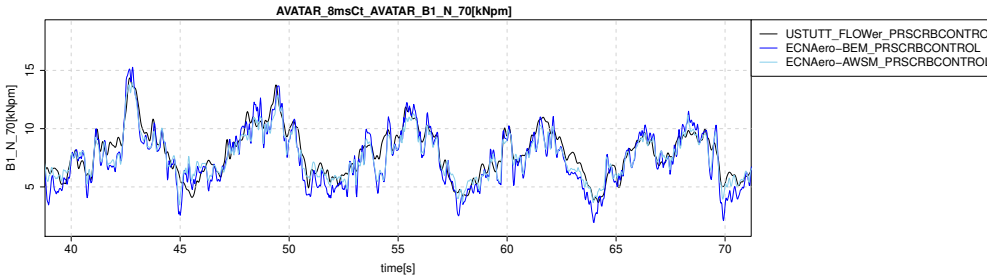

(d) Chord normal force at 70%R

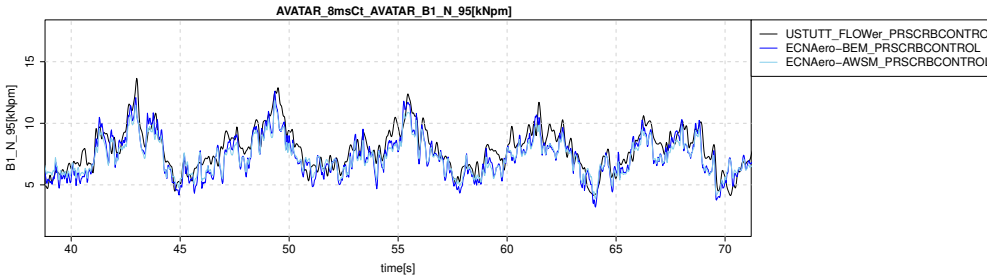

(e) Chord normal force at 95%R

Figure B.92: Flapwise moment and normal force

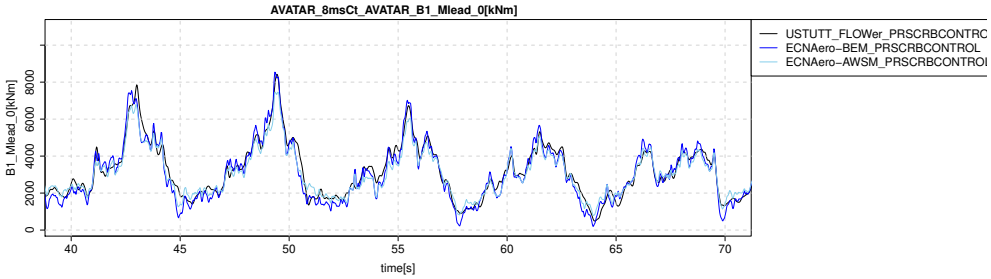

(a) Leadwise blade root moment

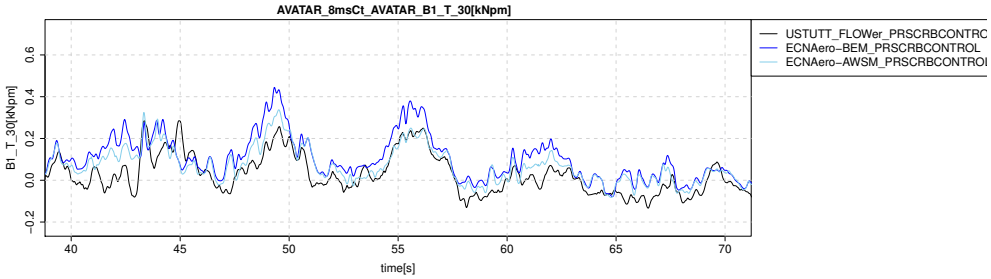

(b) Chord tangential force at 30%R

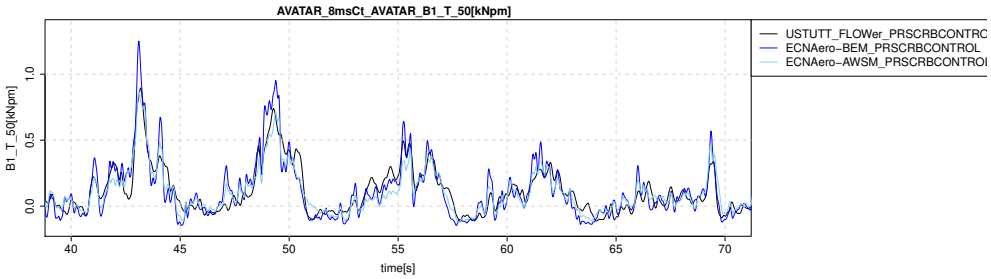

(c) Chord tangential force at 50%R

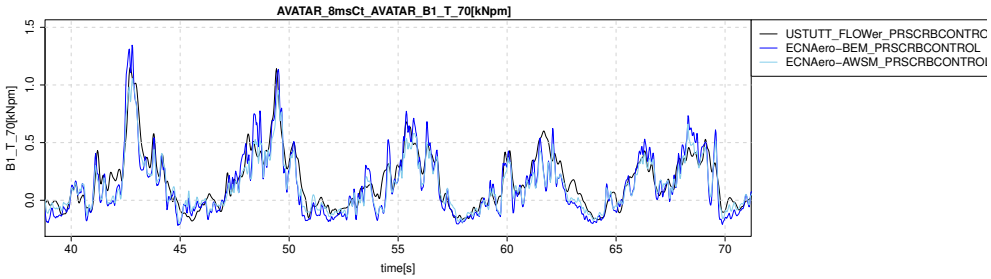

(d) Chord tangential force at 70%R

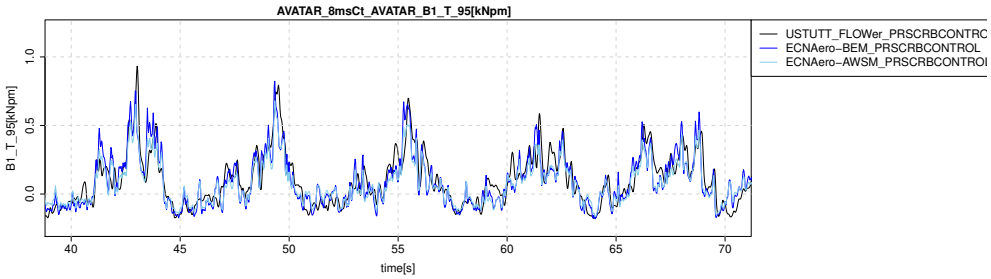

(e) Chord tangential force at 95%R

Figure B.93: Leadwise moment and tangential force

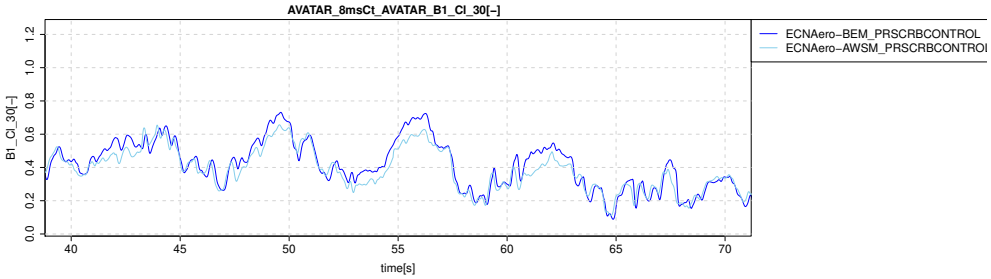

(a) Lift coefficient at 30%R

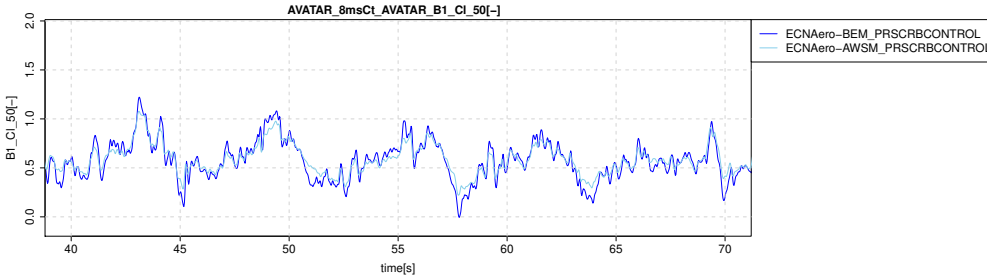

(b) Lift coefficient at 50%R

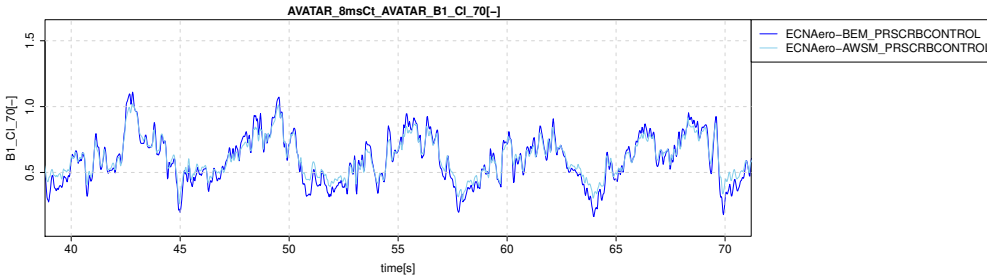

(c) Lift coefficient at 70%R

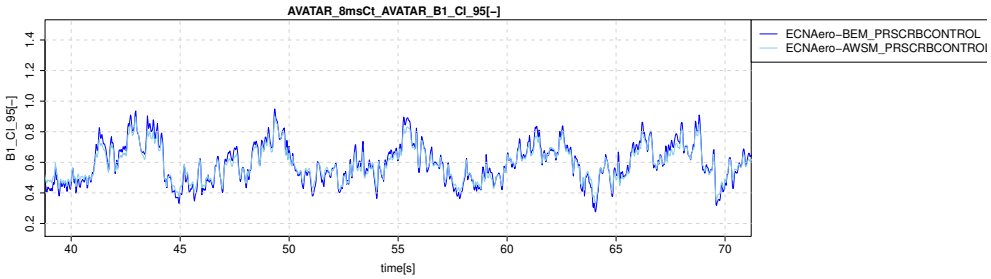

(d) Lift coefficient at 95%R

Figure B.94: Lift coefficients

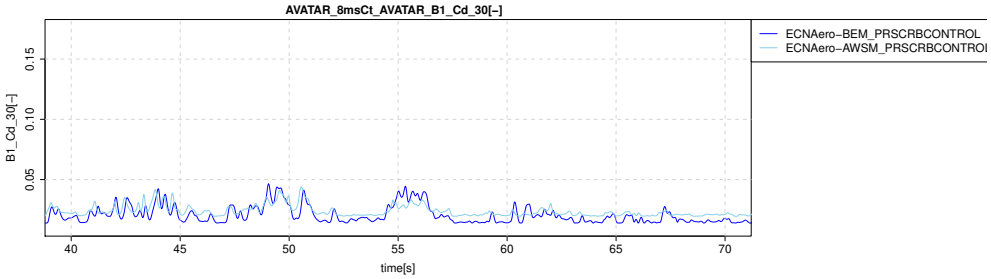

(a) Drag coefficient at 30%R

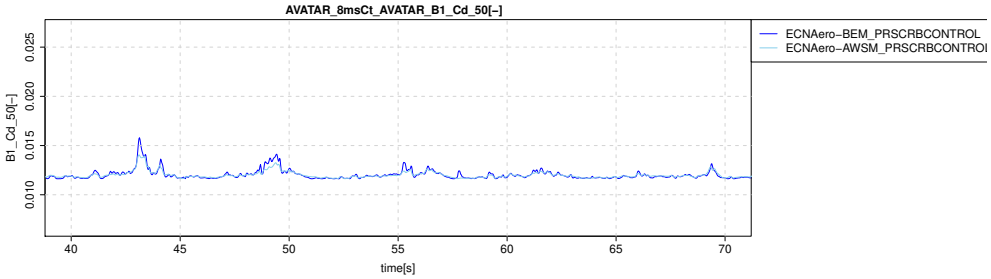

(b) Drag coefficient at 50%R

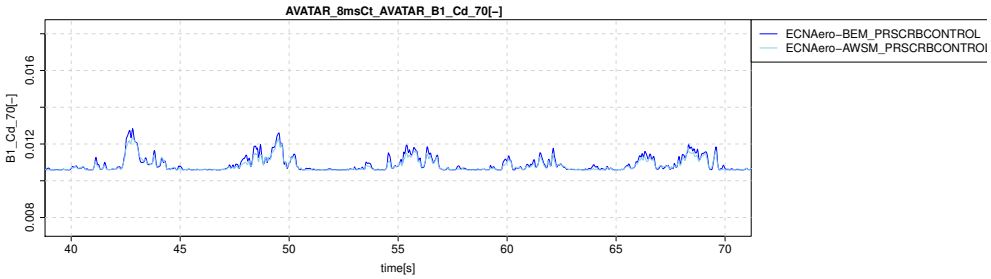

(c) Drag coefficient at 70%R

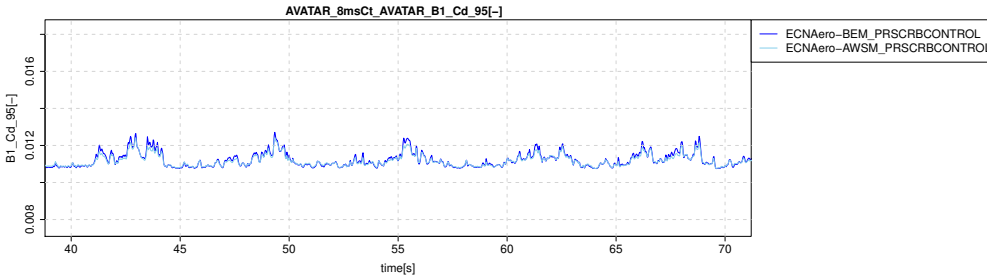

(d) Drag coefficient at 95%R

Figure B.95: Drag coefficients

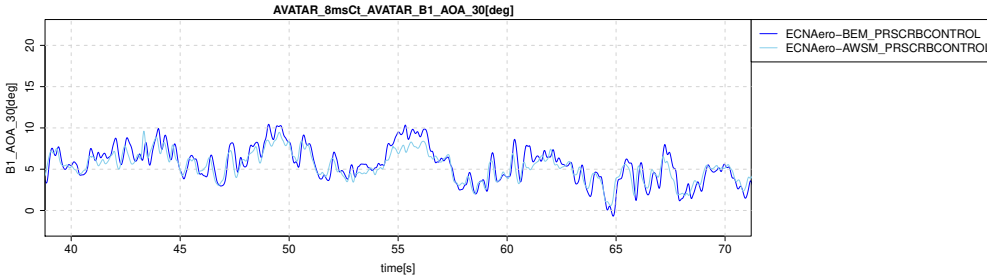

(a) Angle of attack at 30%R

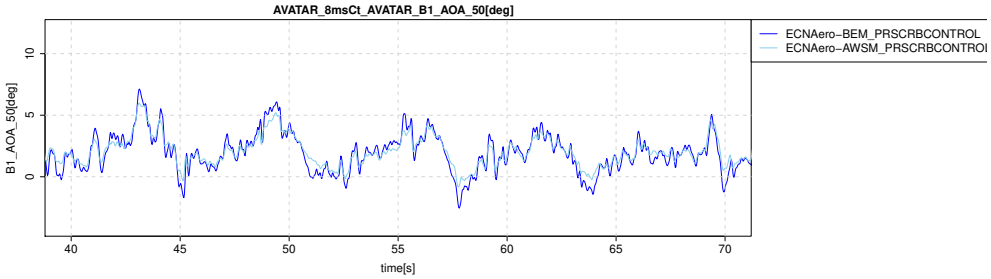

(b) Angle of attack at 50%R

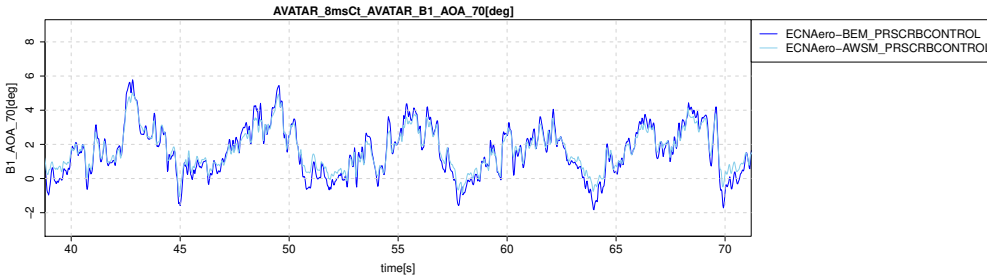

(c) Angle of attack at 70%R

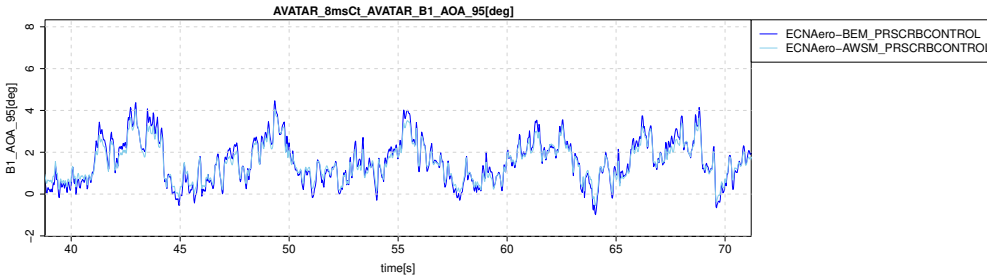

(d) Angle of attack at 95%R

Figure B.96: Angles of attack

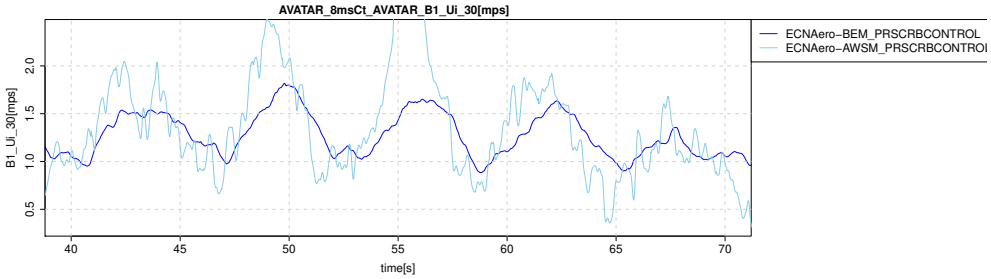

(a) Axial induced velocity at 30%R

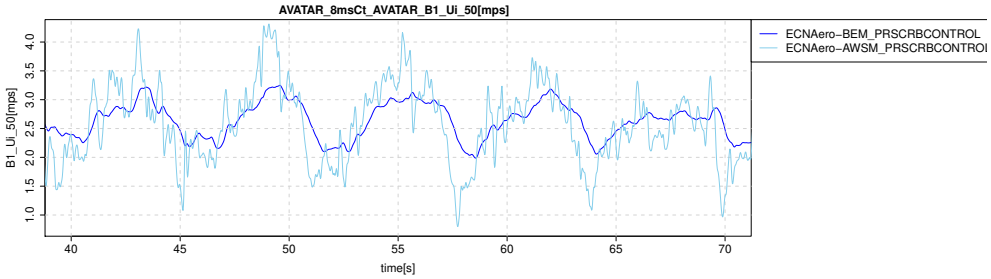

(b) Axial induced velocity at 50%R

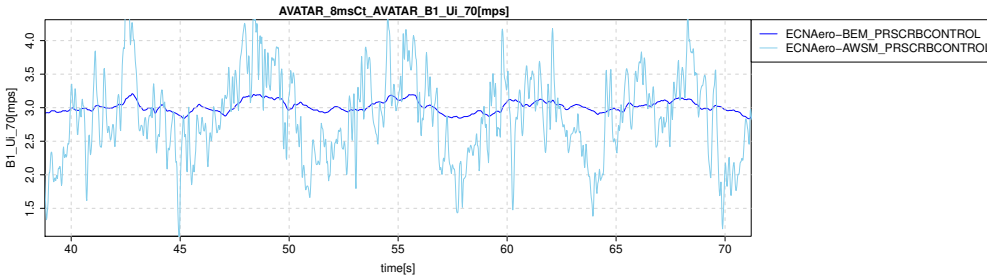

(c) Axial induced velocity at 70%R

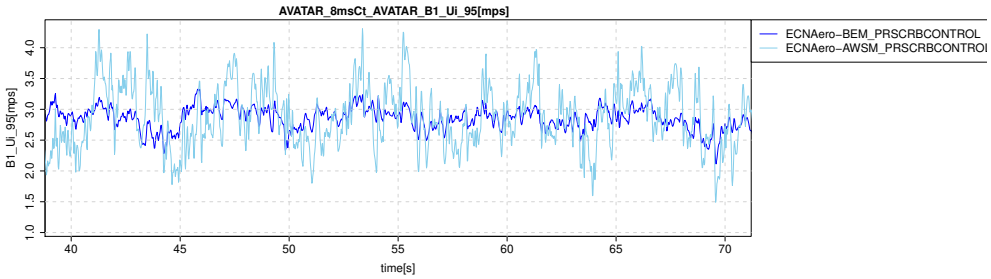

(d) Axial induced velocity at 95%R

Figure B.97: Axial induced velocities

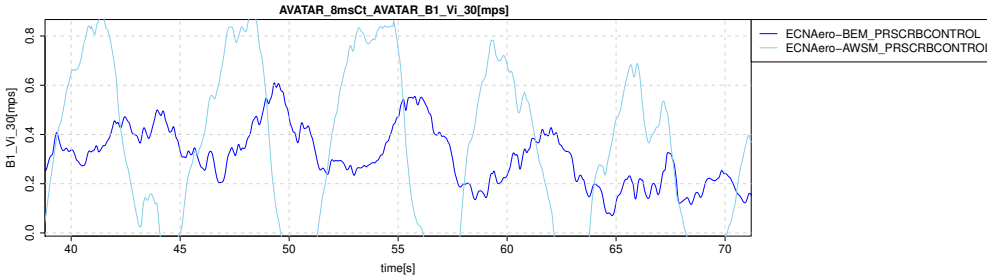

(a) Tangential induced velocity at 30%R

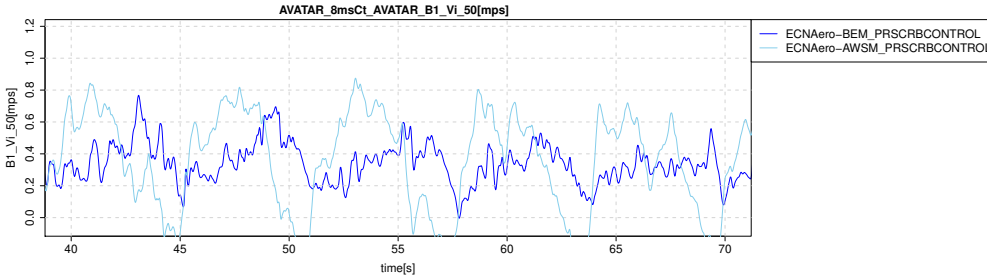

(b) Tangential induced velocity at 50%R

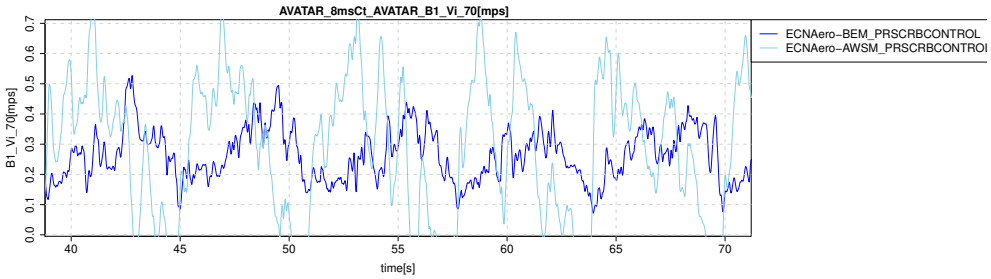

(c) Tangential induced velocity at 70%R

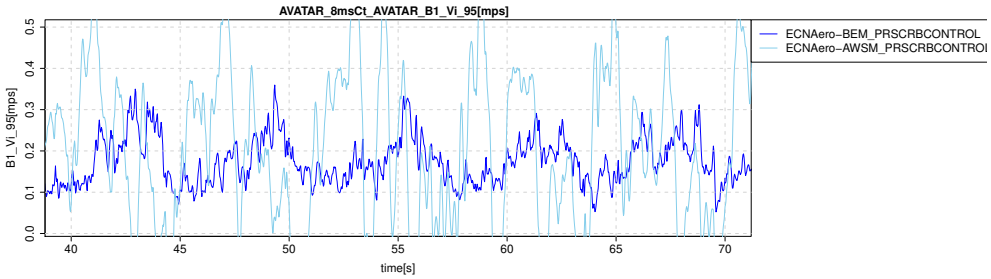

(d) Tangential induced velocity at 95%R

Figure B.98: Tangential induced velocities

B.5.2 Time

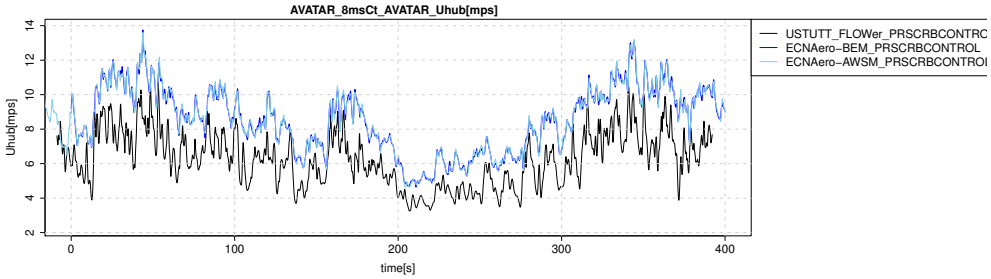

(a) Hub height wind speed

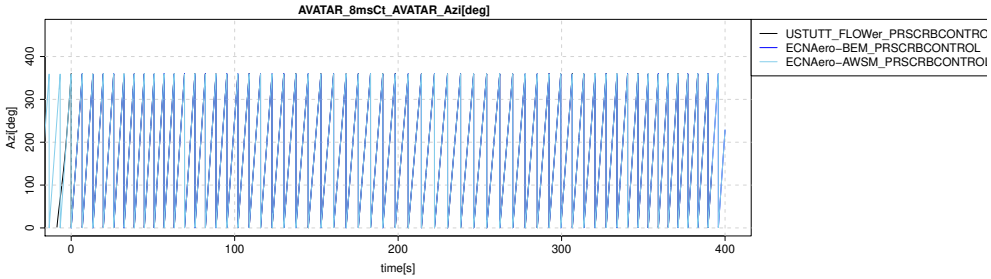

(b) Rotor azimuth

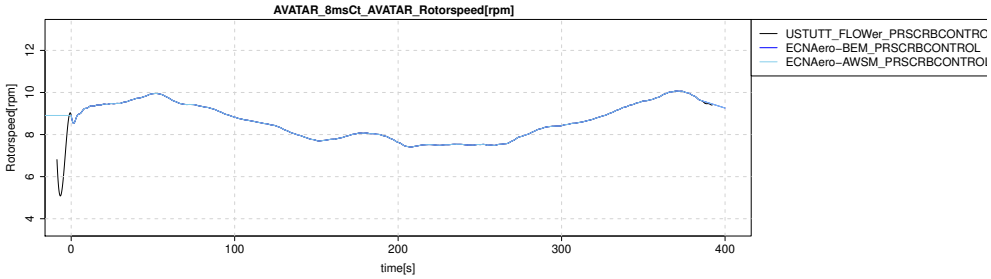

(c) Rotor speed

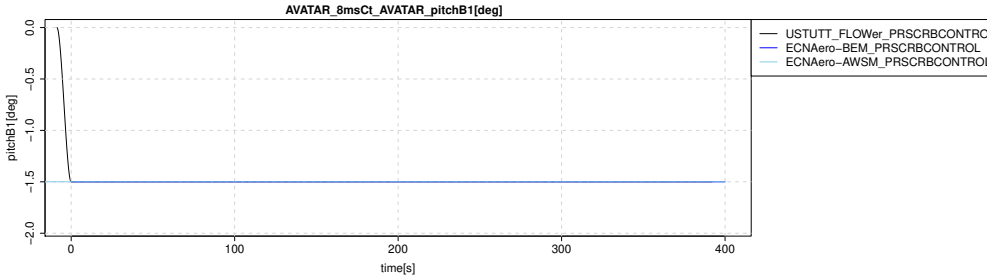

(d) Pitch angle

Figure B.99: Wind and control parameters

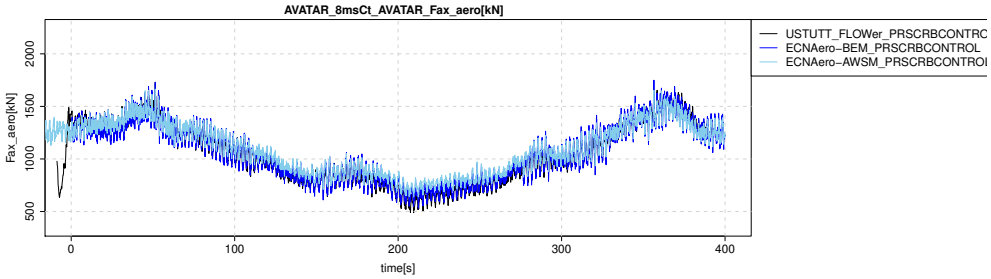

(a) Rotor axial force

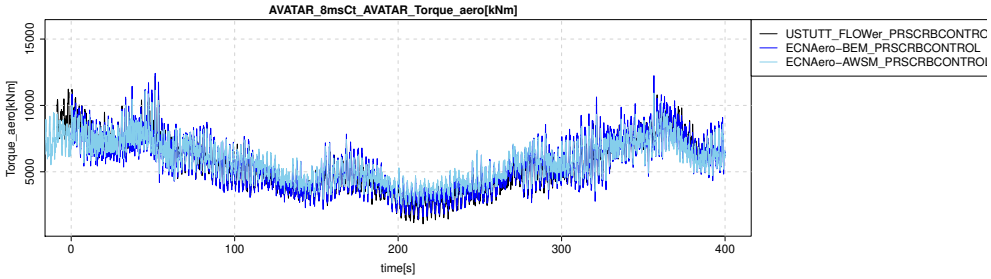

(b) Rotor torque

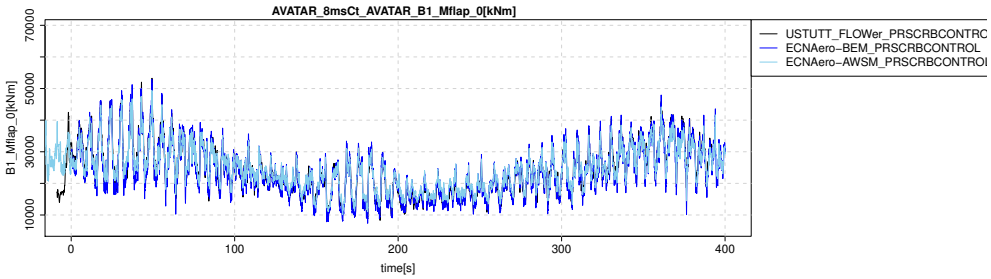

(c) Flapwise blade root moment

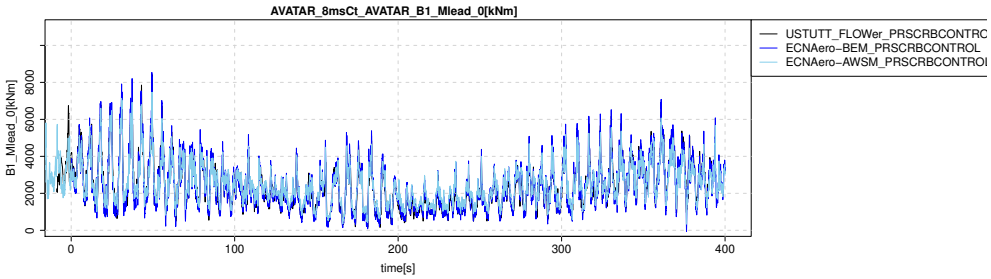

(d) Leadwise blade root moment

Figure B.100: Rotor and blade forces and moments

B.5.3 Statistics

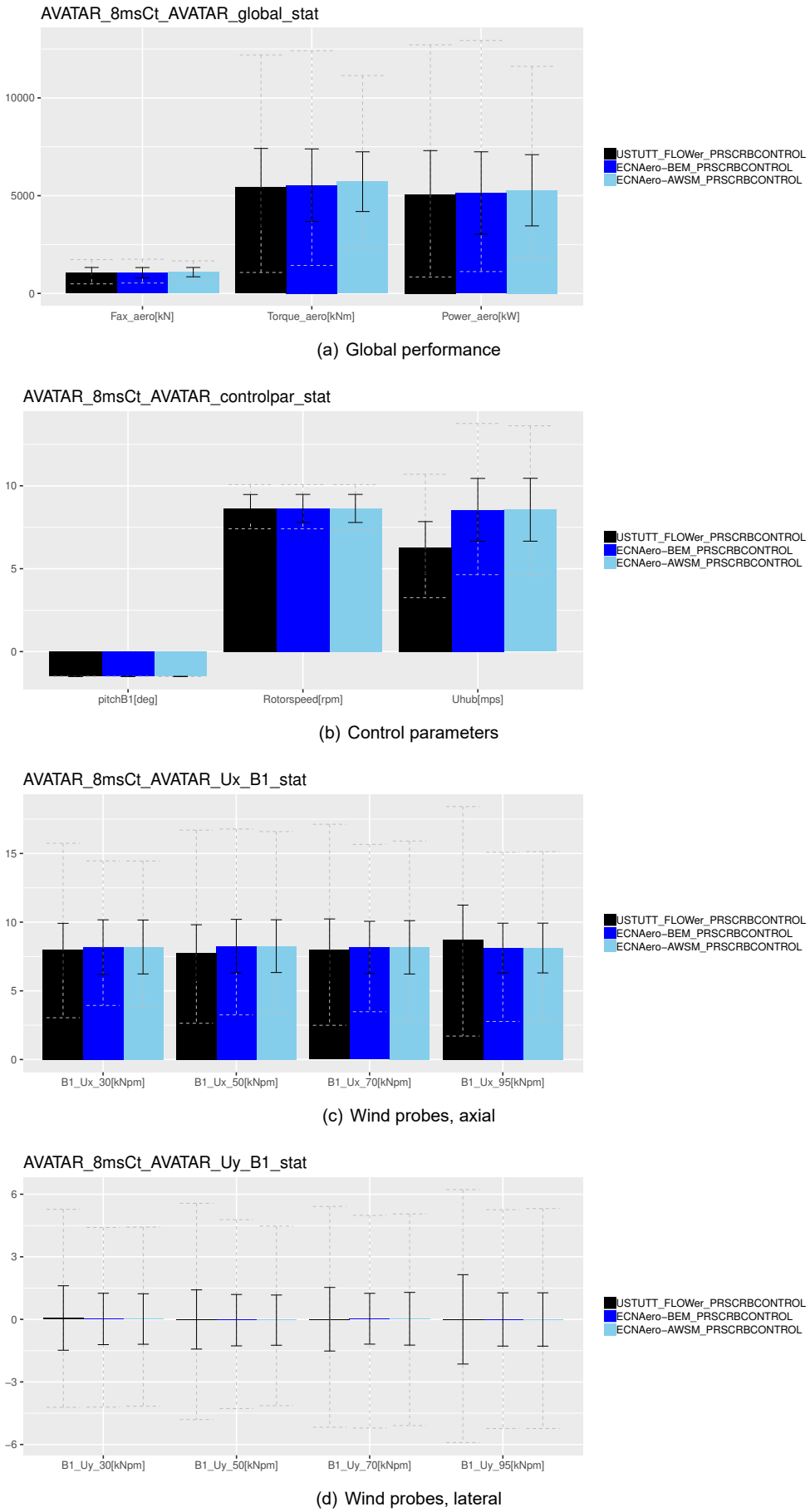

Figure B.101: Global performance, wind and control parameters

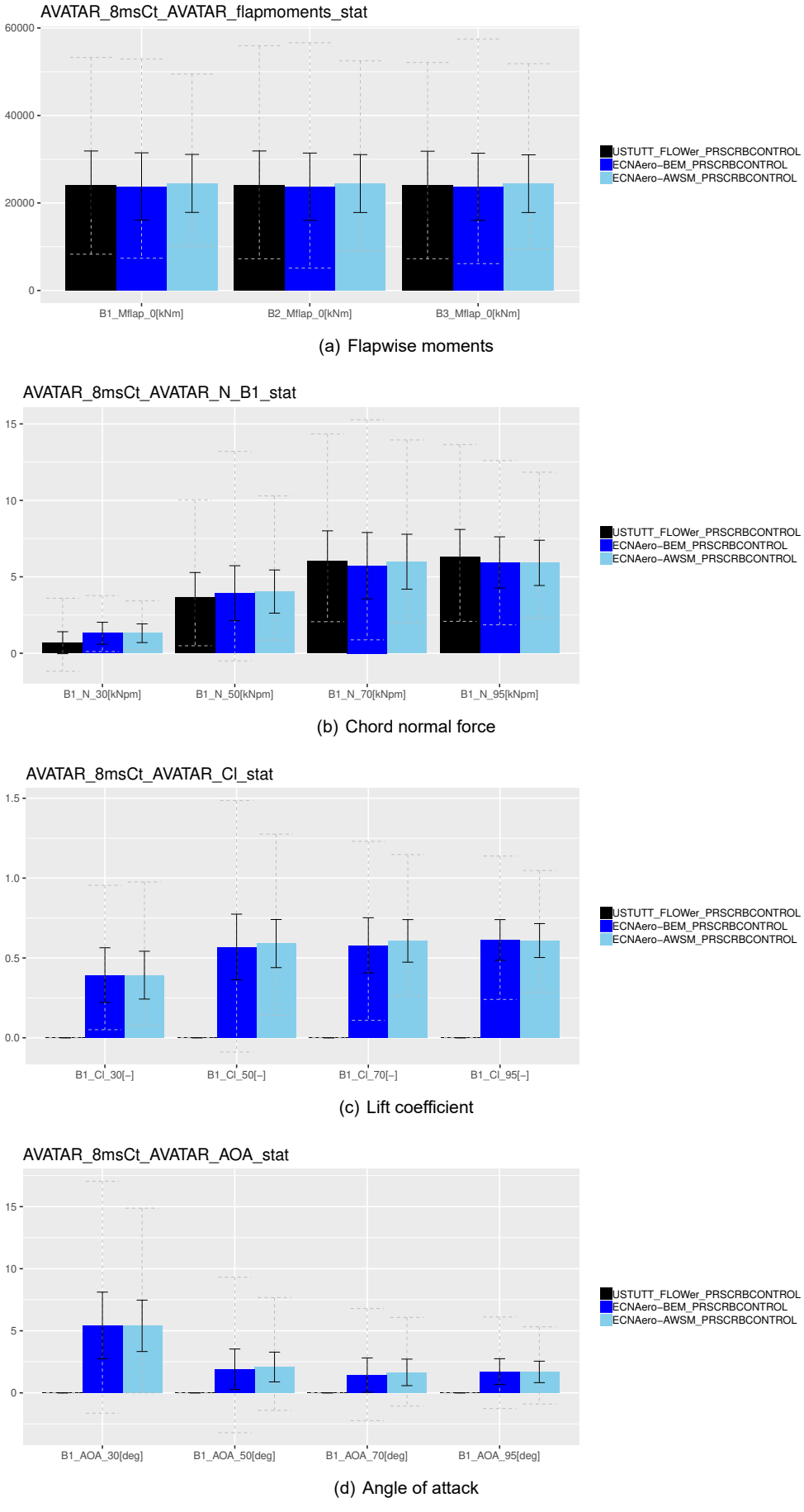

Figure B.102: Force decompostion in axial direction

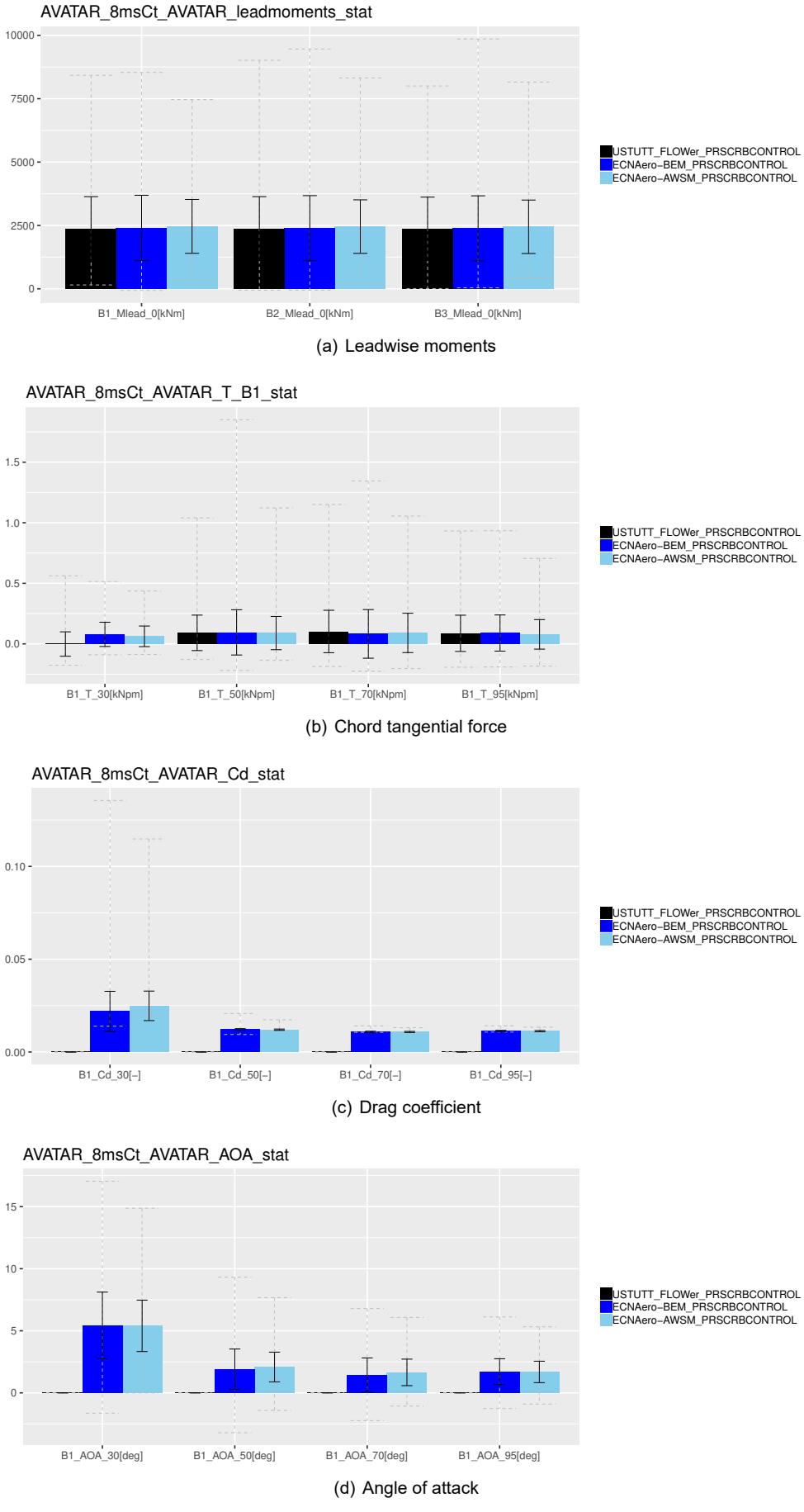

Figure B.103: Force decompostion in tangential direction

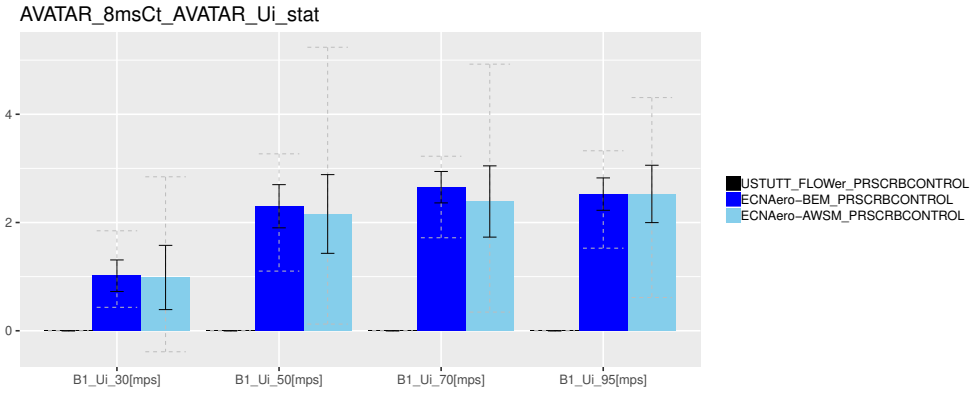

(a) Axial induced velocity

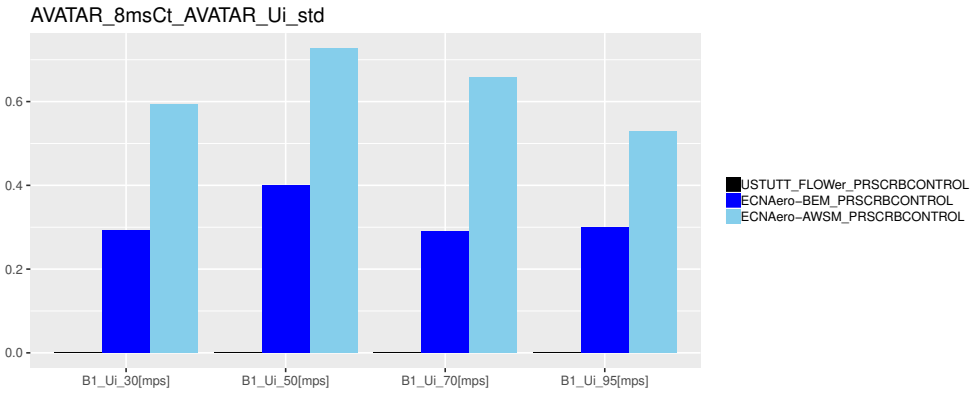

(b) Axial induced velocity (standard deviation)

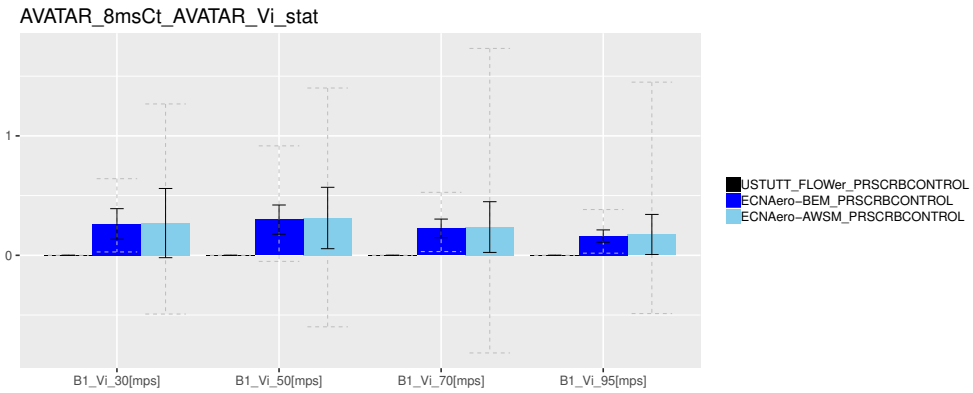

(c) Tangential induced velocity

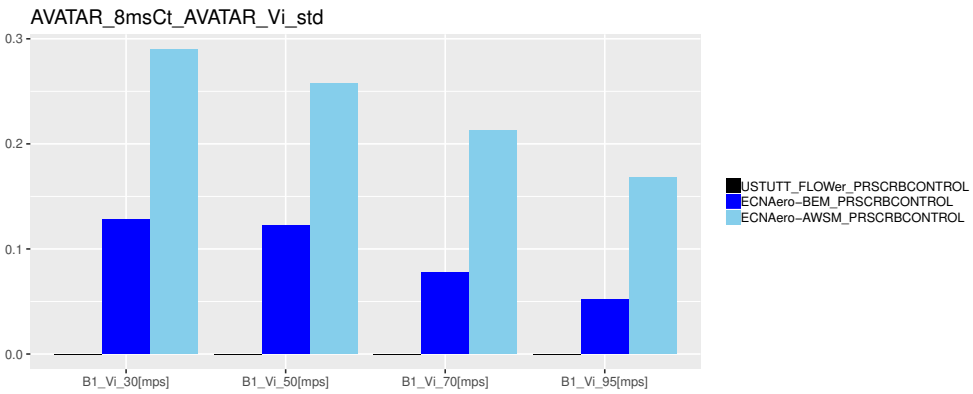

(d) Tangential induced velocity (standard deviation)

Figure B.104: Induced velocities

B.5.4 Equivalent load levels

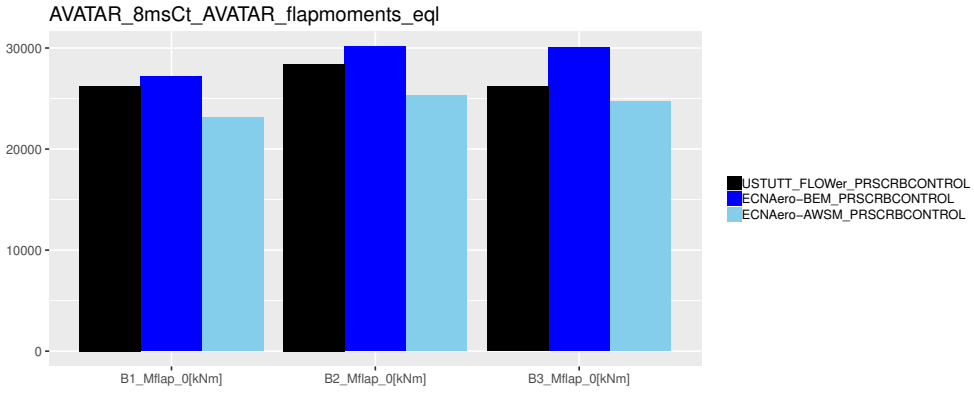

(a) Flapwise moments

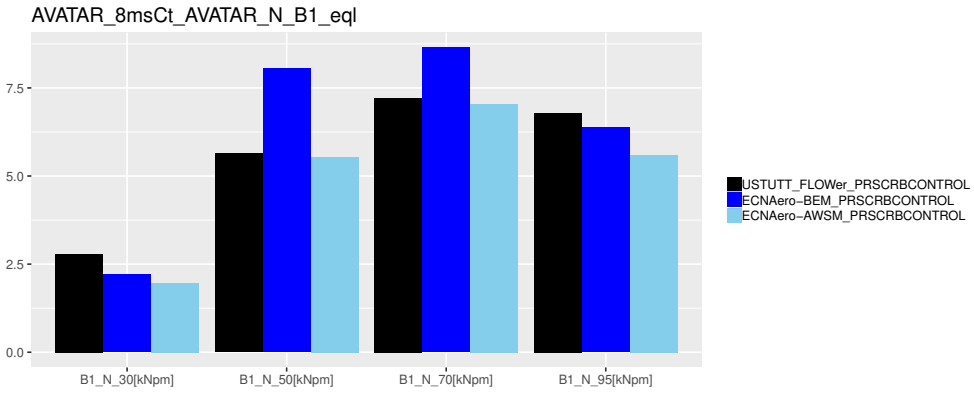

(b) Normal force

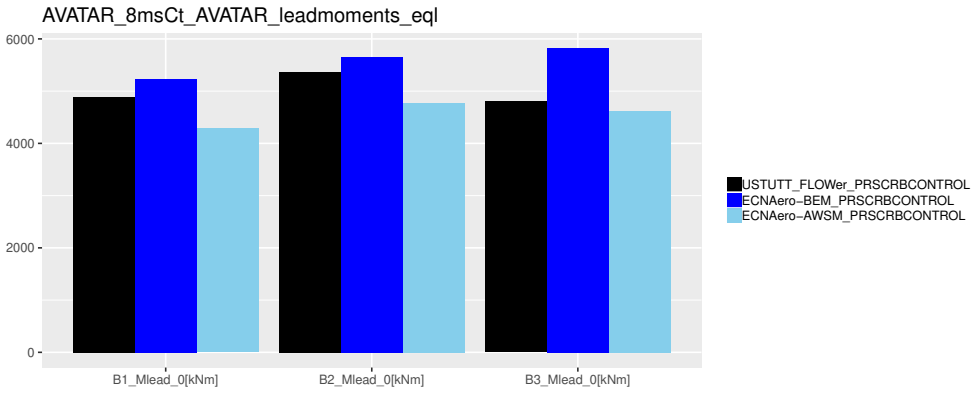

(c) Leadwise moments

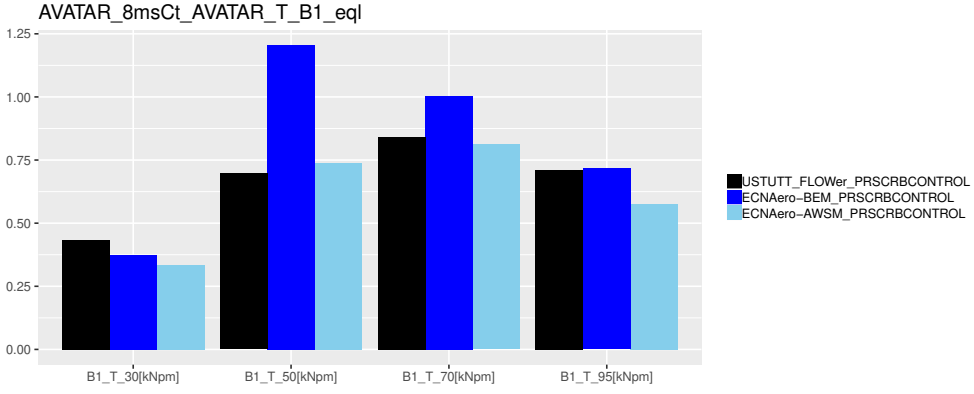

(d) Tangential force

Figure B.105: Forces and moments

B.5.5 Staircase plots

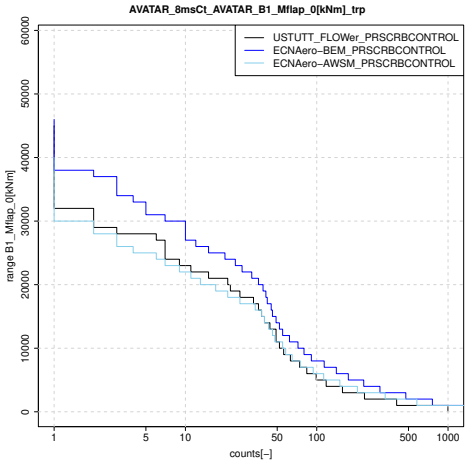

(a) Flapwise blade root moment

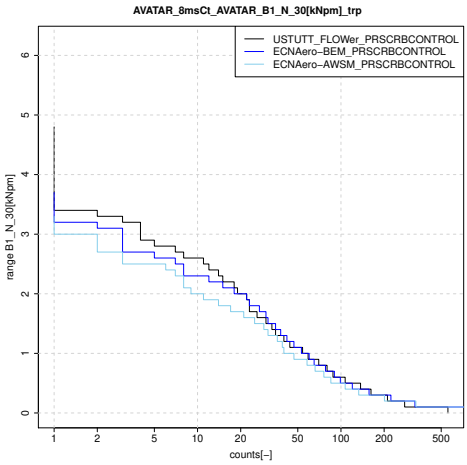

(b) Normal force, 30%R

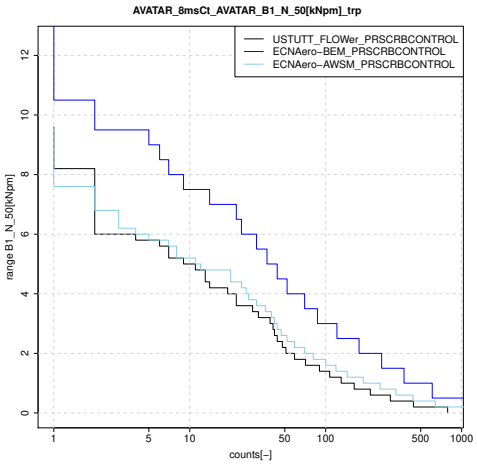

(c) Normal force, 50%R

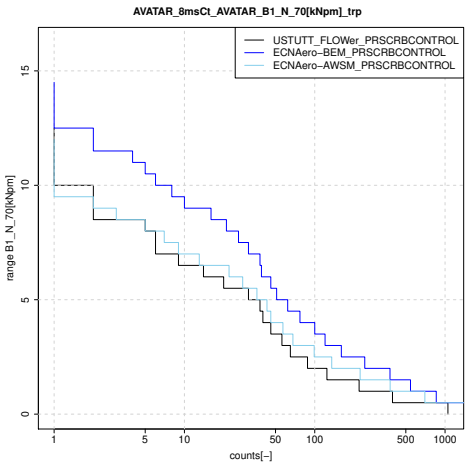

(d) Normal force, 70%R

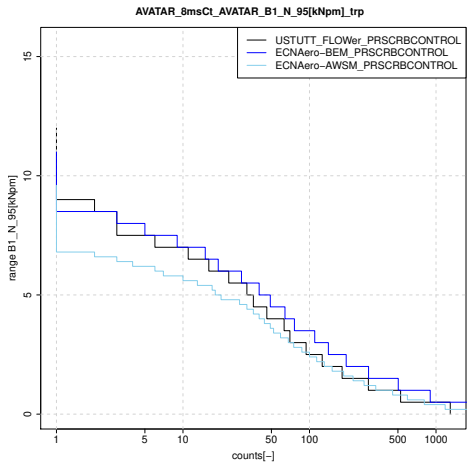

(e) Normal force, 95%R

Figure B.106: Flapwise moment and normal forces

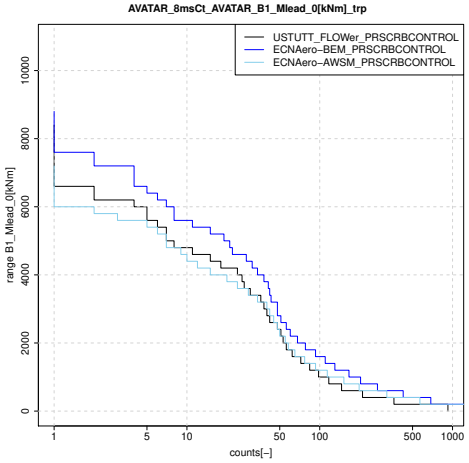

(a) Leadwise blade root moment

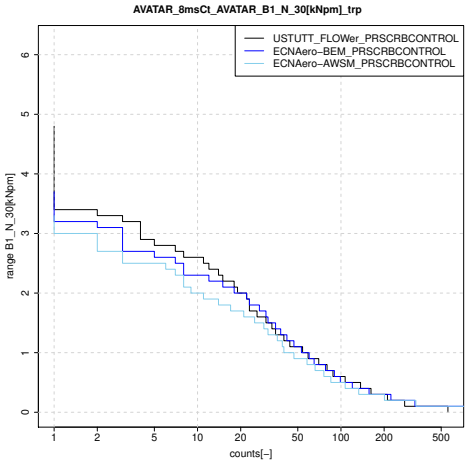

(b) Tangential force, 30%R

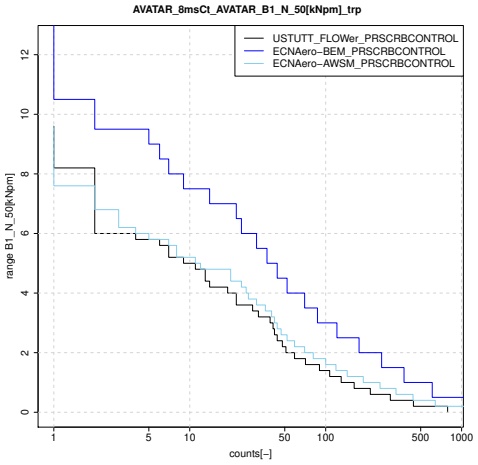

(c) Tangential force, 50%R

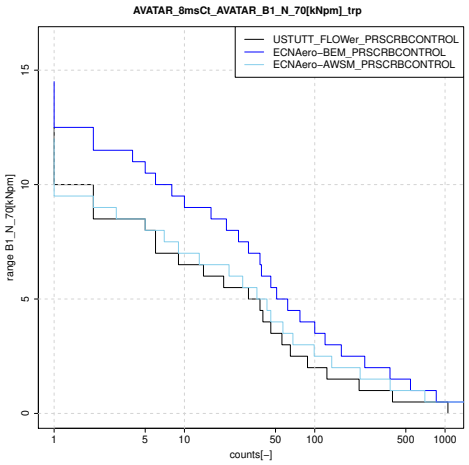

(d) Tangential force, 70%R

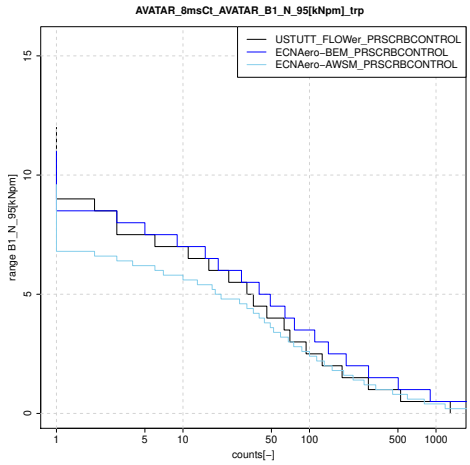

(e) Tangential force, 95%R

Figure B.107: Leadwise moment and tangential forces

B.5.6 PSD

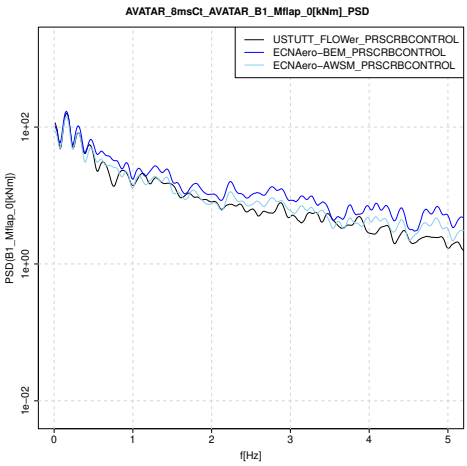

(a) Flapwise blade root moment

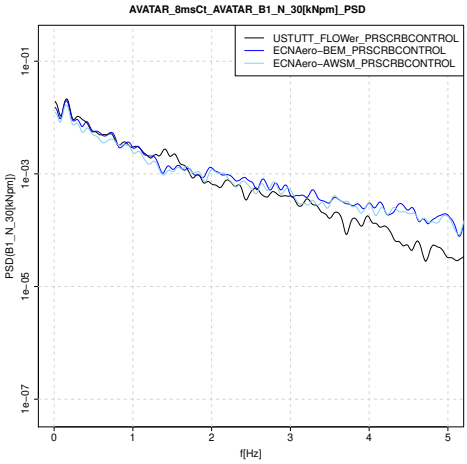

(b) Normal force, 30%R

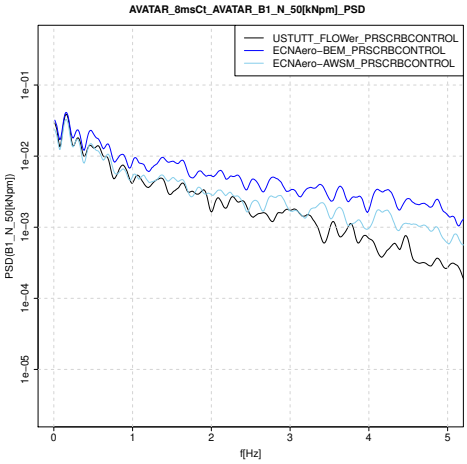

(c) Normal force, 50%R

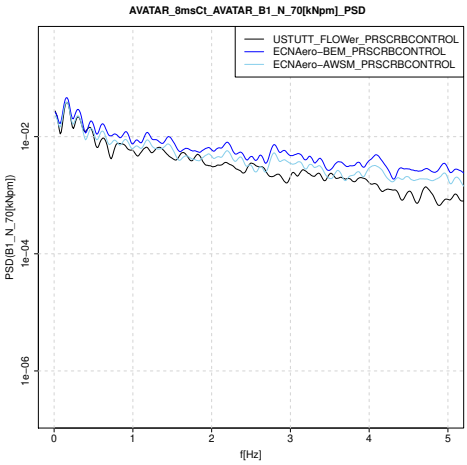

(d) Normal force, 70%R

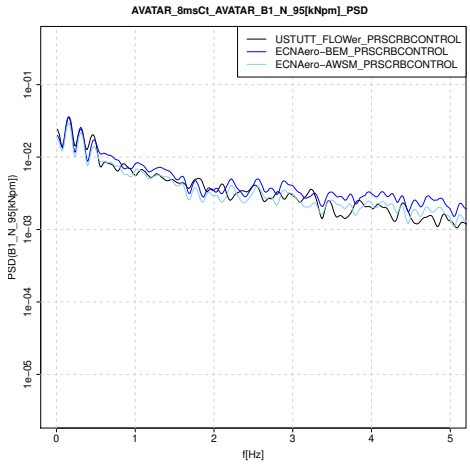

(e) Normal force, 95%R

Figure B.108: Flapwise moment and normal forces

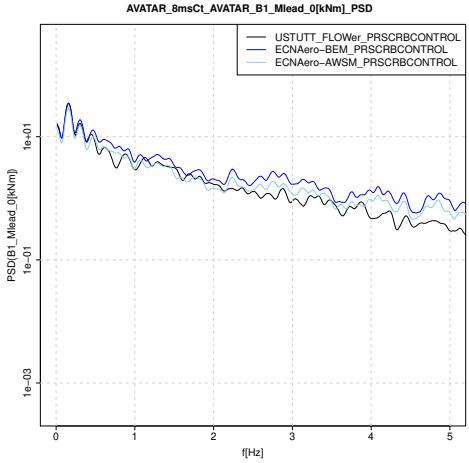

(a) Leadwise blade root moment

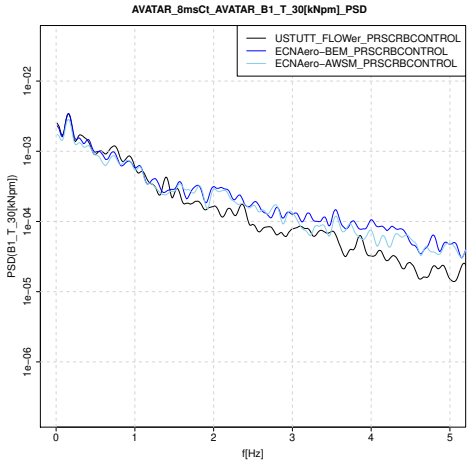

(b) Tangential force, 30%R

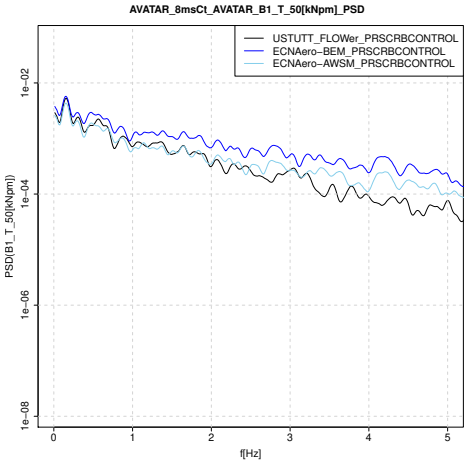

(c) Tangential force, 50%R

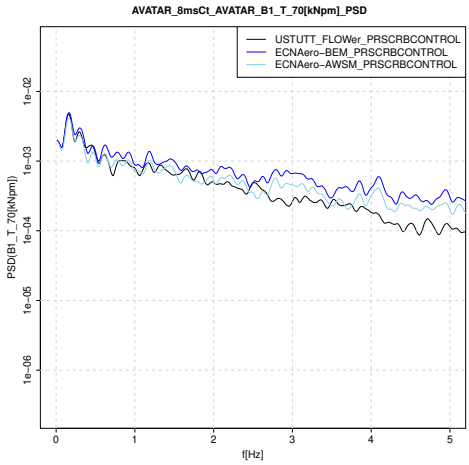

(d) Tangential force, 70%R

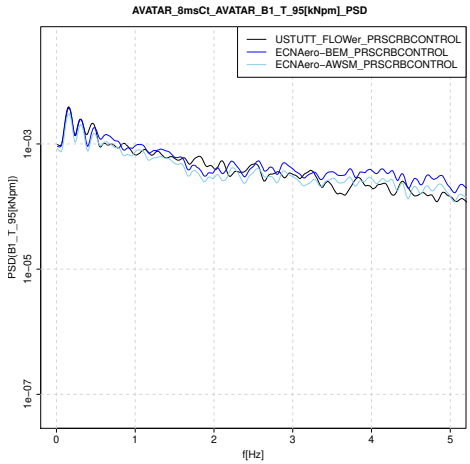

(e) Tangential force, 95%R

Figure B.109: Leadwise moment and tangential forces

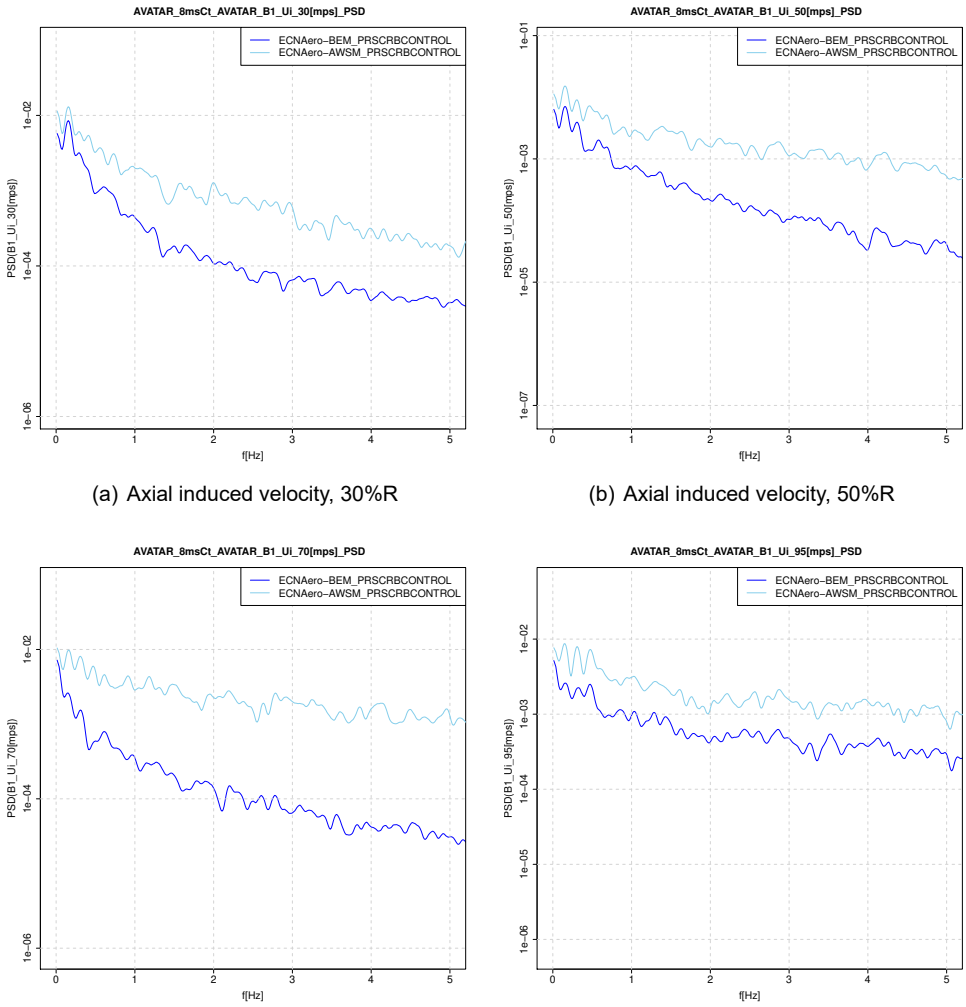

(a) Axial induced velocity, 30%R

(b) Axial induced velocity, 50%R

(c) Axial induced velocity, 70%R

(d) Axial induced velocity, 95%R

Figure B.110: Axial induced velocities

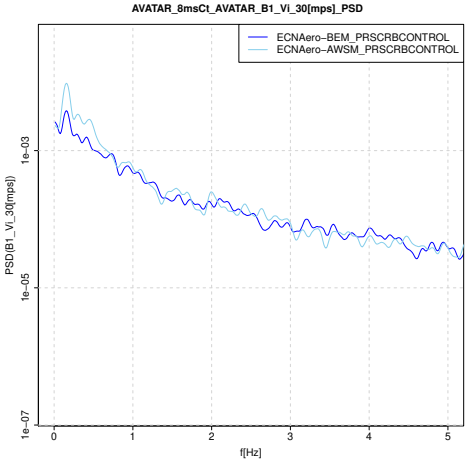

(a) Tangential induced velocity, 30%R

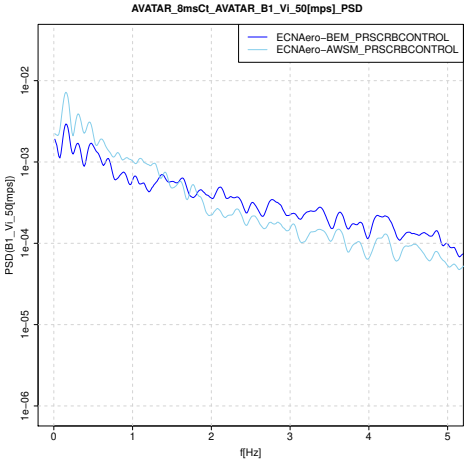

(b) Tangential induced velocity, 50%R

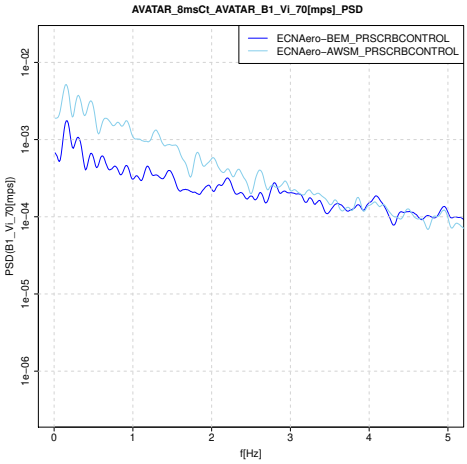

(c) Tangential induced velocity, 70%R

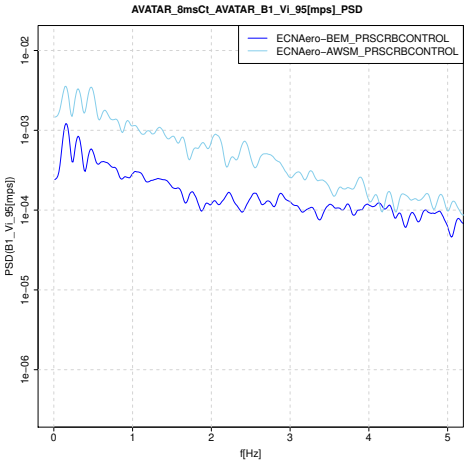

(d) Tangential induced velocity, 95%R

Figure B.111: Tangential induced velocities

B.6 8 m/s, high L case

B.6.1 Time (zoomed)

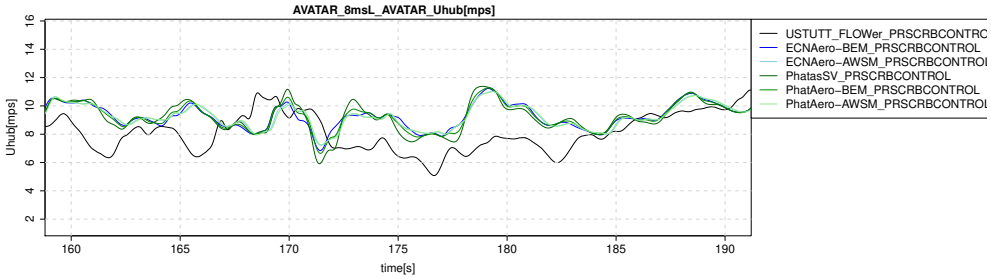

(a) Hub height wind speed

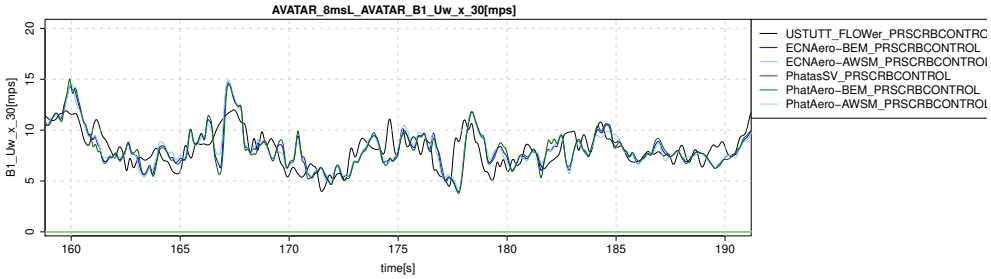

(b) Wind probe axial velocity at 30%R

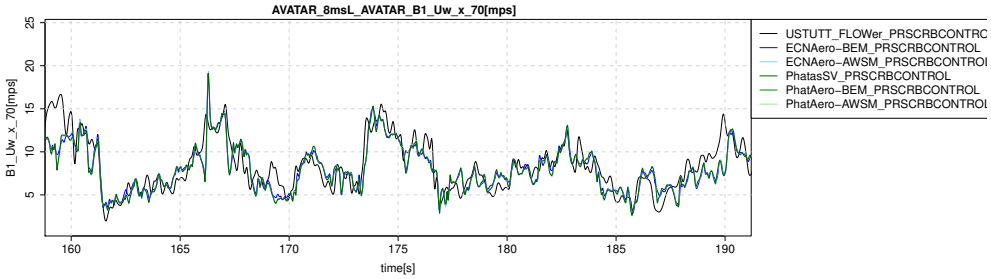

(c) Wind probe axial velocity at 70%R

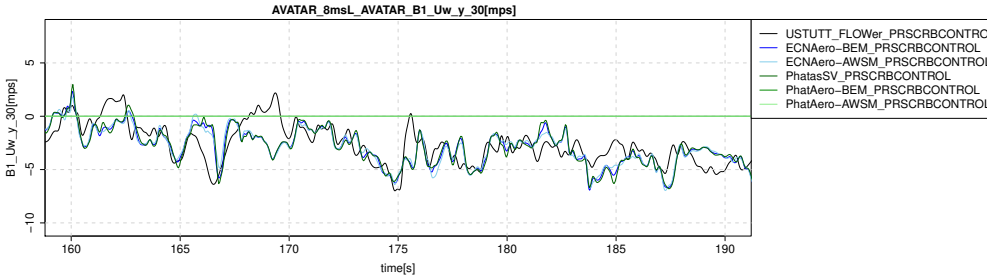

(d) Wind probe lateral velocity at 30%R

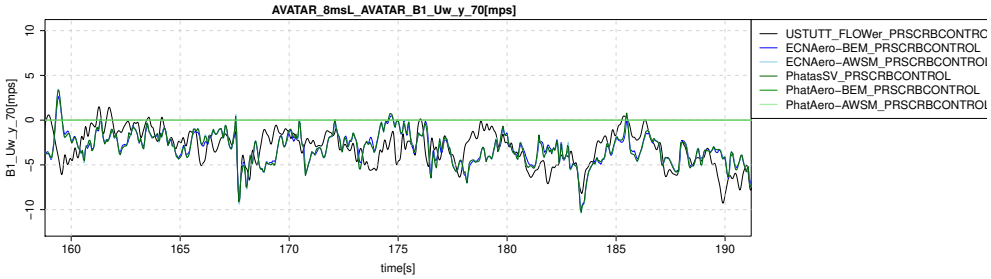

(e) Wind probe lateral velocity at 70%R

Figure B.112: Wind speed alignment check

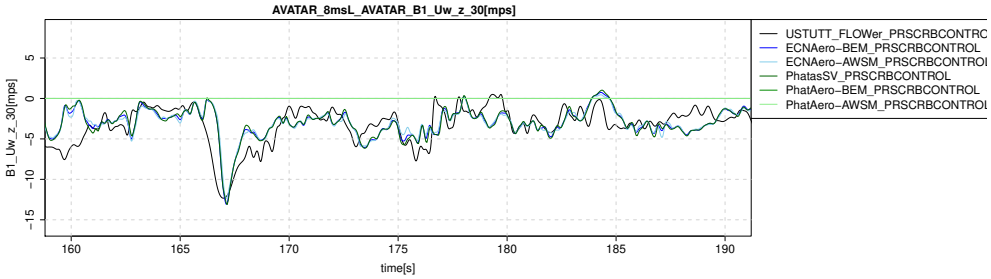

(a) Wind probe vertical velocity at 30%R

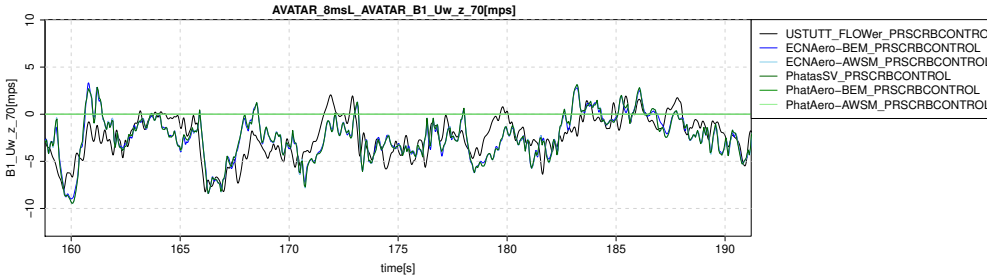

(b) Wind probe vertical velocity at 70%R

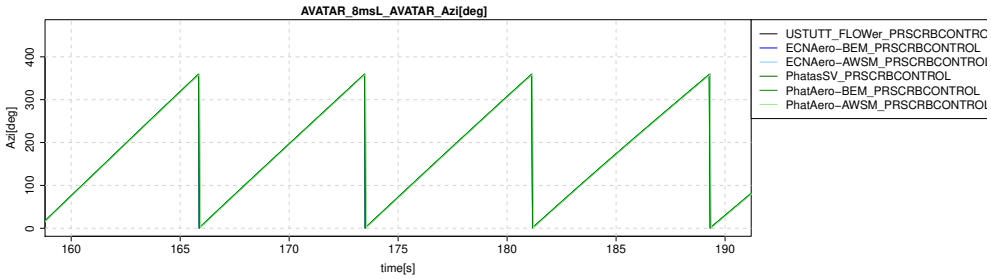

(c) Rotor azimuth angle

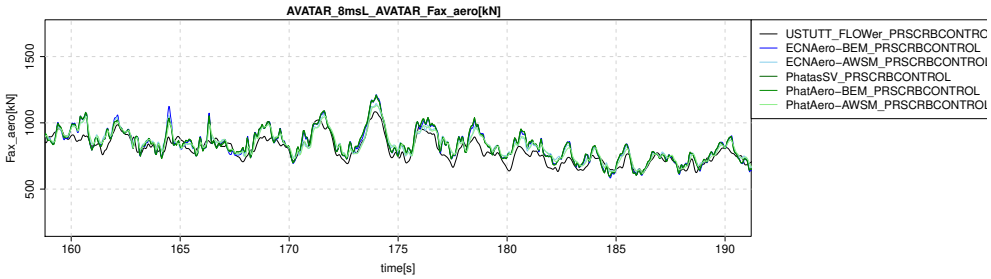

(d) Rotor axial force

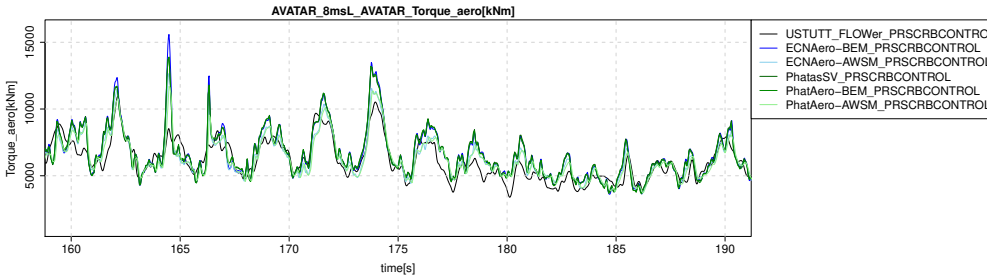

(e) Rotor torque

Figure B.113: Alignment check

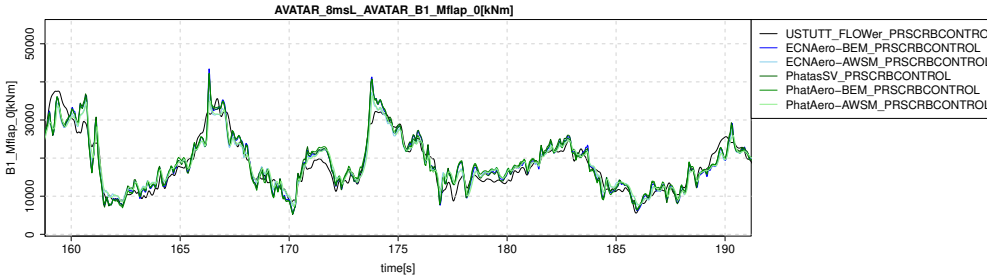

(a) Flapwise blade root moment

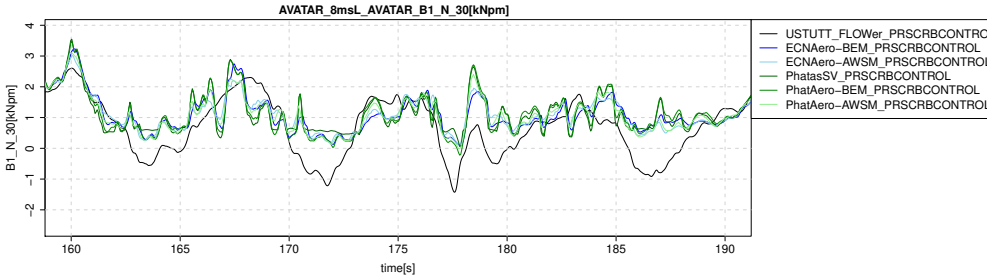

(b) Chord normal force at 30%R

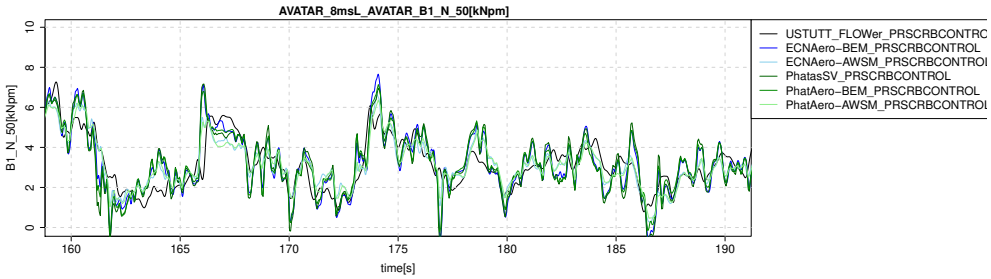

(c) Chord normal force at 50%R

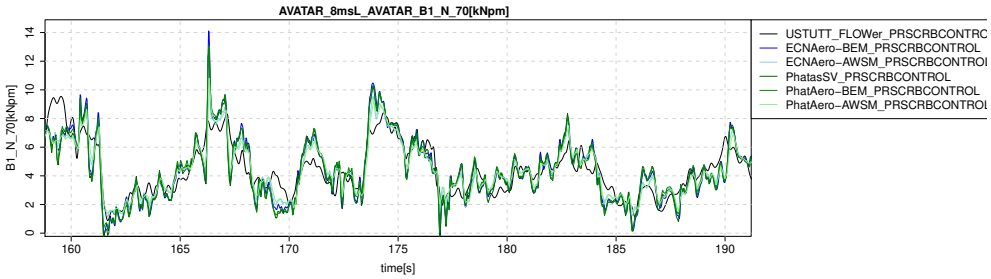

(d) Chord normal force at 70%R

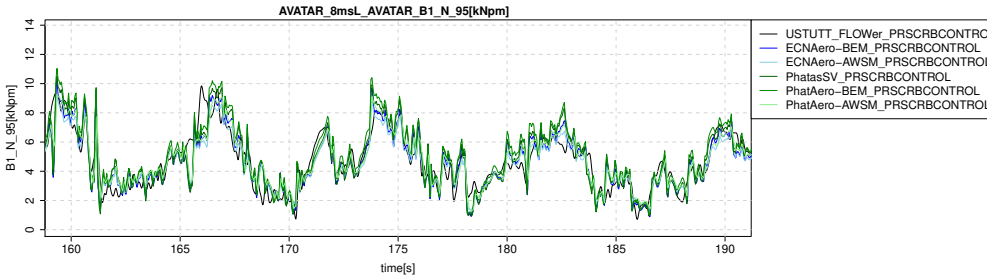

(e) Chord normal force at 95%R

Figure B.114: Flapwise moment and normal force

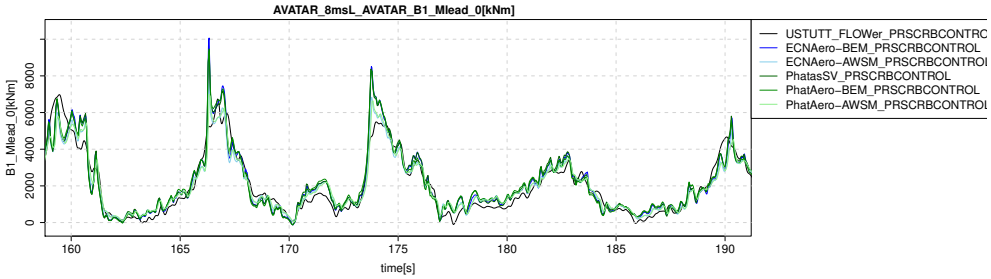

(a) Leadwise blade root moment

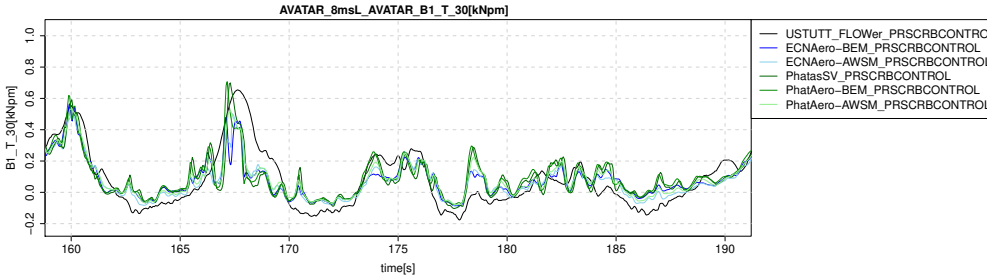

(b) Chord tangential force at 30%R

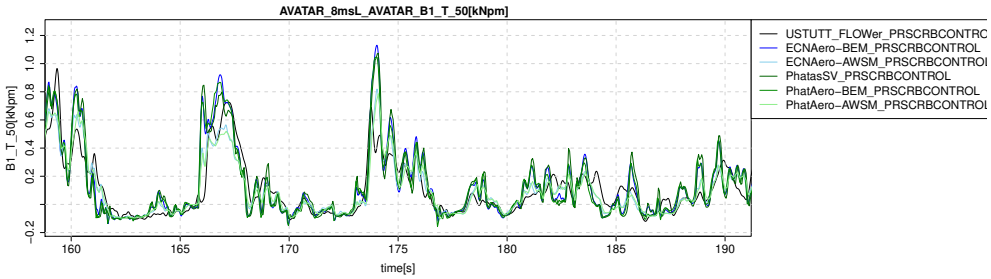

(c) Chord tangential force at 50%R

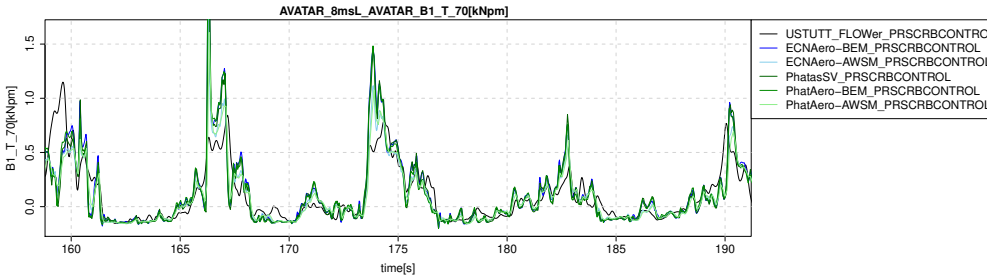

(d) Chord tangential force at 70%R

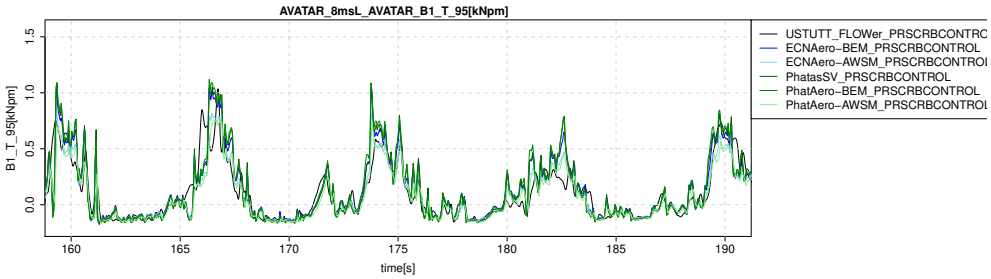

(e) Chord tangential force at 95%R

Figure B.115: Leadwise moment and tangential force

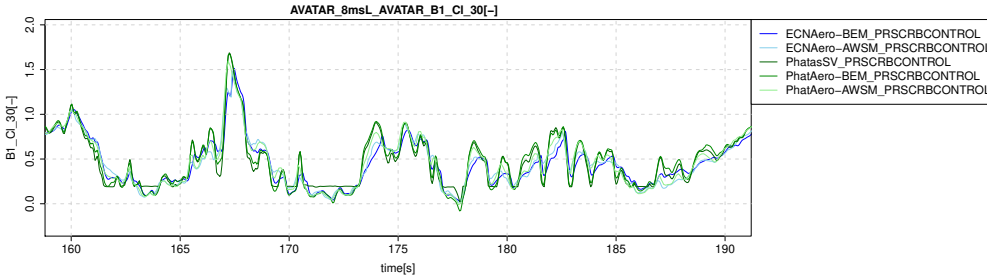

(a) Lift coefficient at 30%R

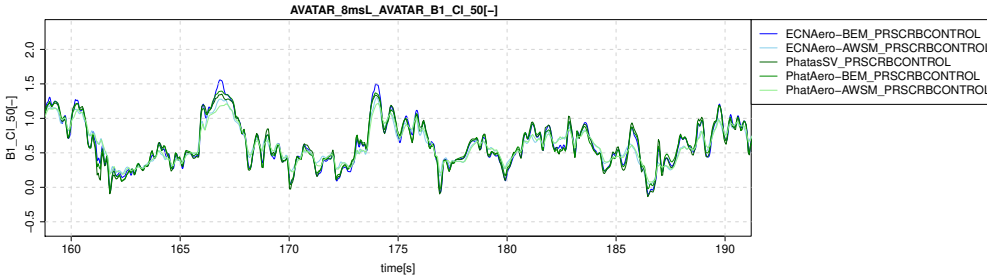

(b) Lift coefficient at 50%R

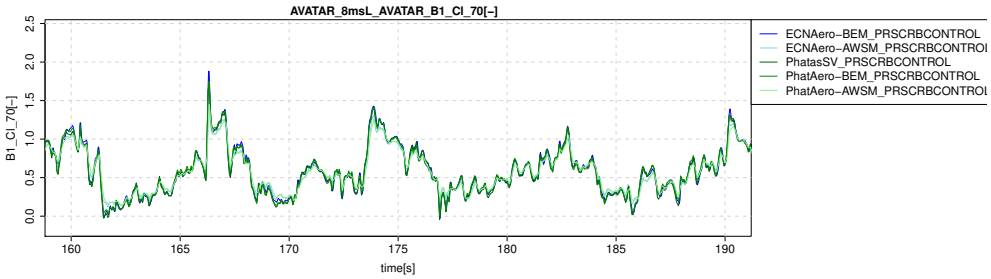

(c) Lift coefficient at 70%R

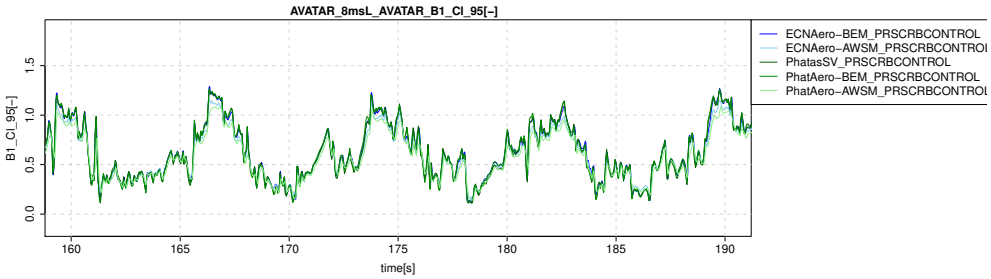

(d) Lift coefficient at 95%R

Figure B.116: Lift coefficients

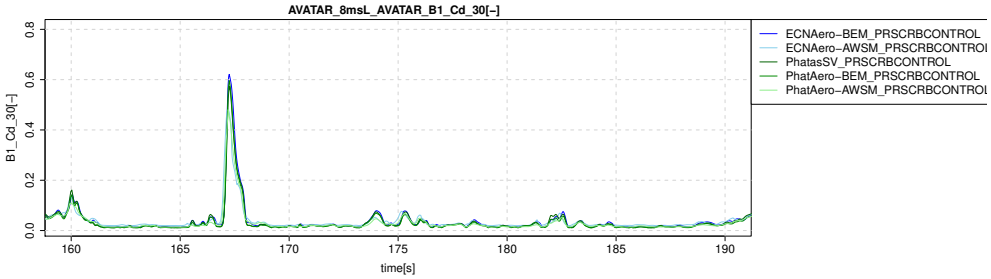

(a) Drag coefficient at 30%R

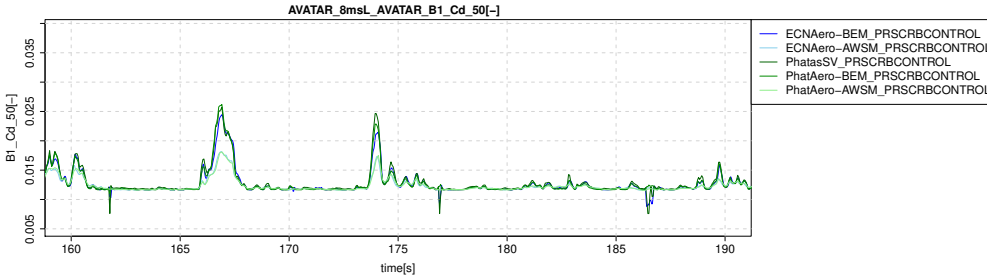

(b) Drag coefficient at 50%R

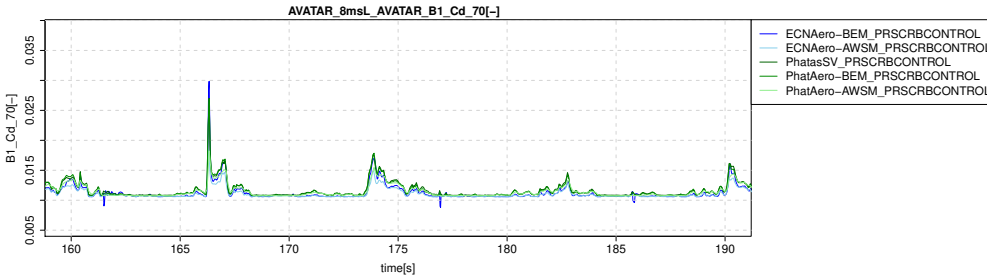

(c) Drag coefficient at 70%R

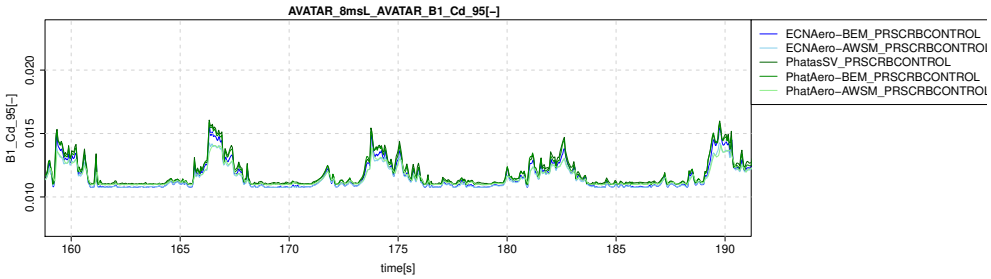

(d) Drag coefficient at 95%R

Figure B.117: Drag coefficients

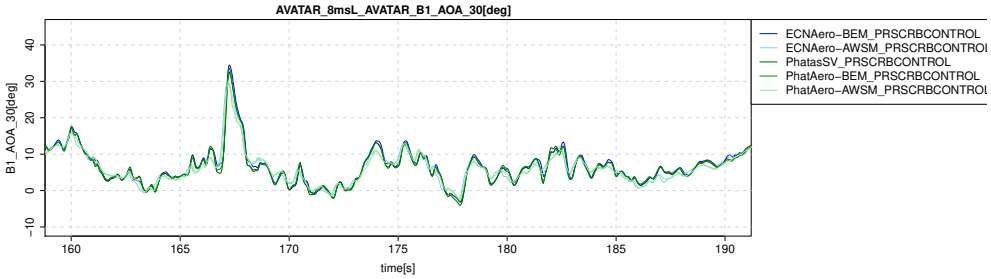

(a) Angle of attack at 30%R

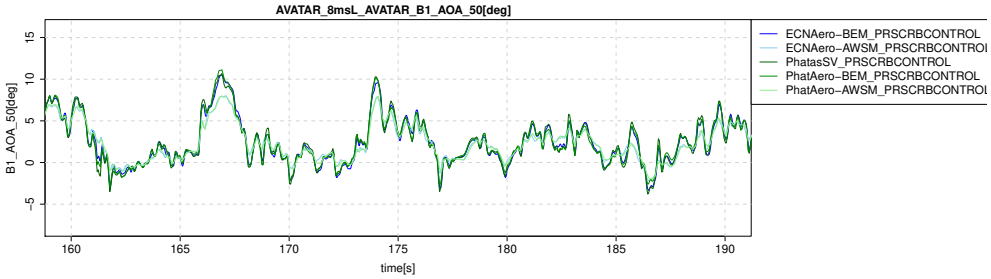

(b) Angle of attack at 50%R

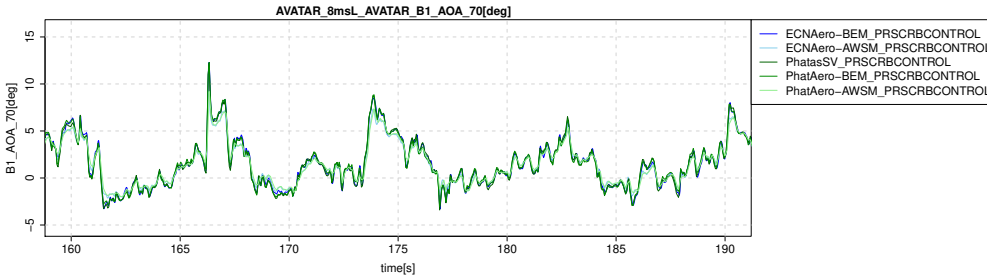

(c) Angle of attack at 70%R

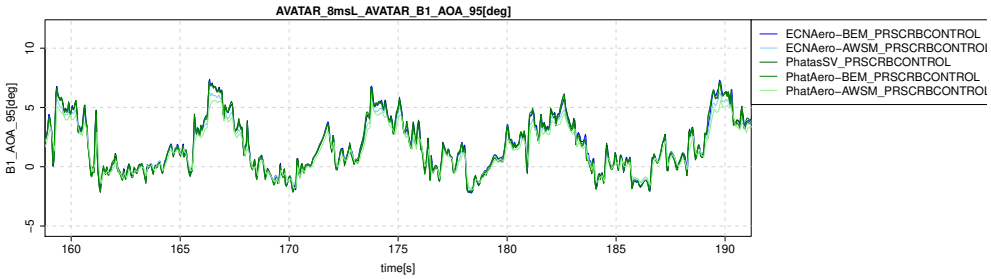

(d) Angle of attack at 95%R

Figure B.118: Angles of attack

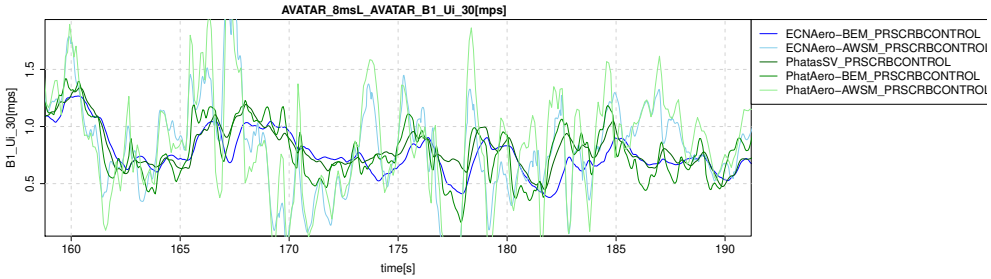

(a) Axial induced velocity at 30%R

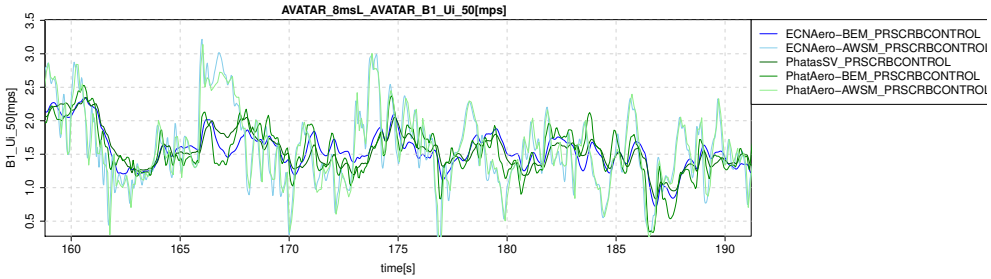

(b) Axial induced velocity at 50%R

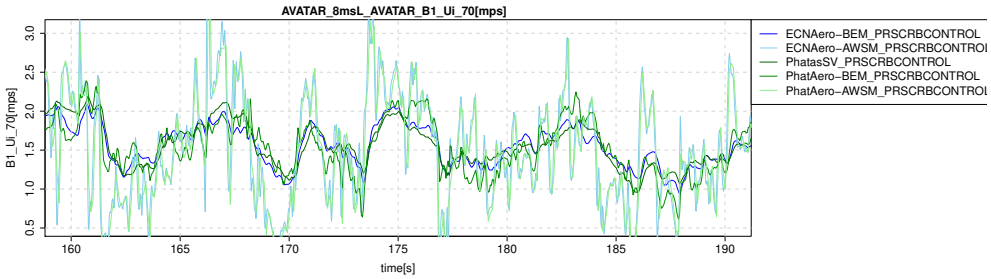

(c) Axial induced velocity at 70%R

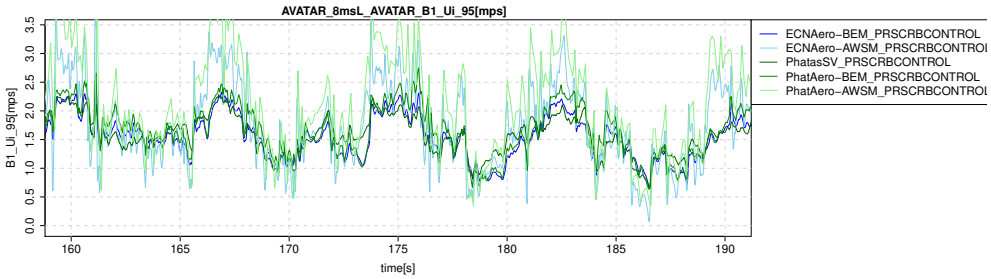

(d) Axial induced velocity at 95%R

Figure B.119: Axial induced velocities

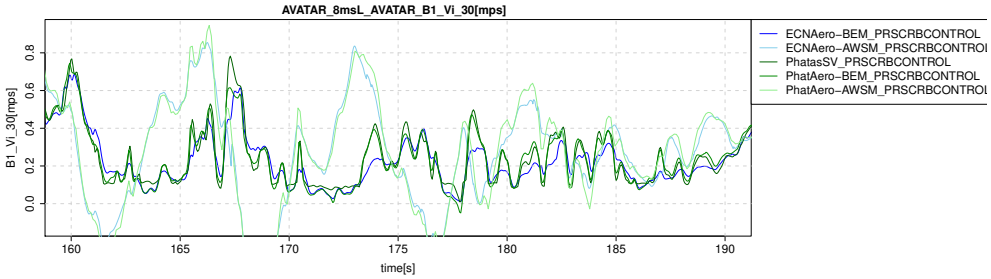

(a) Tangential induced velocity at 30%R

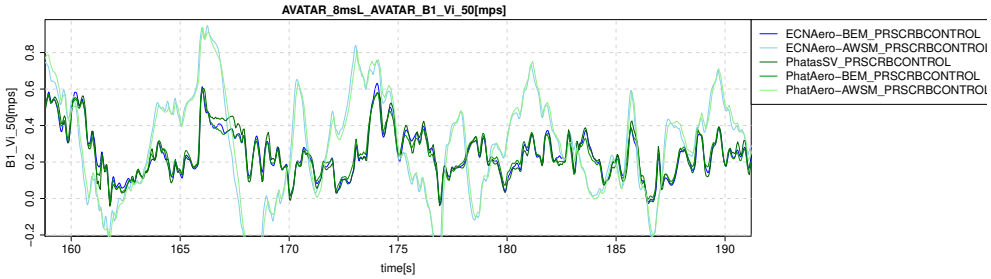

(b) Tangential induced velocity at 50%R

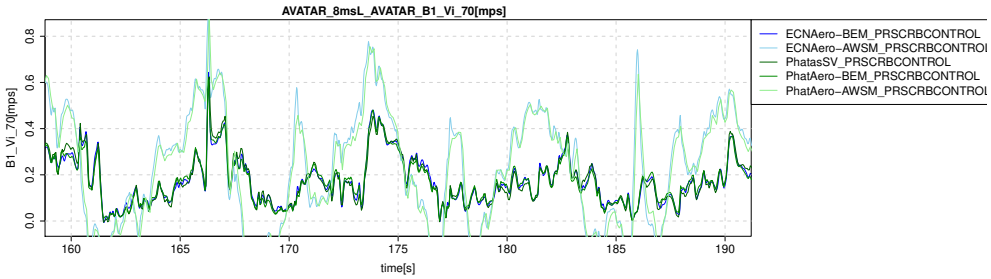

(c) Tangential induced velocity at 70%R

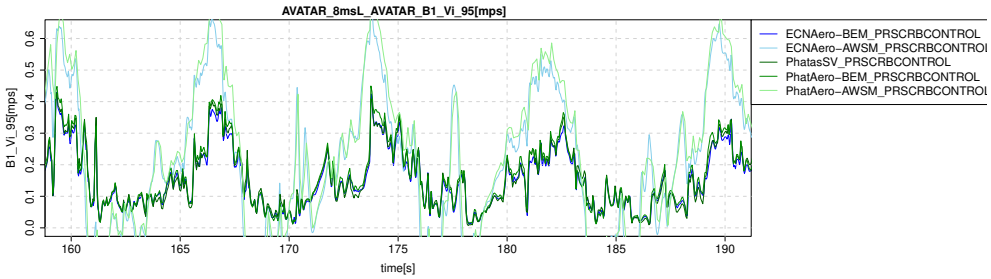

(d) Tangential induced velocity at 95%R

Figure B.120: Tangential induced velocities

B.6.2 Time

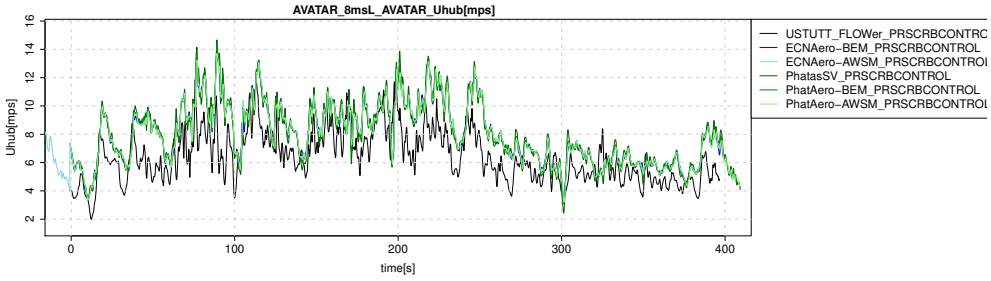

(a) Hub height wind speed

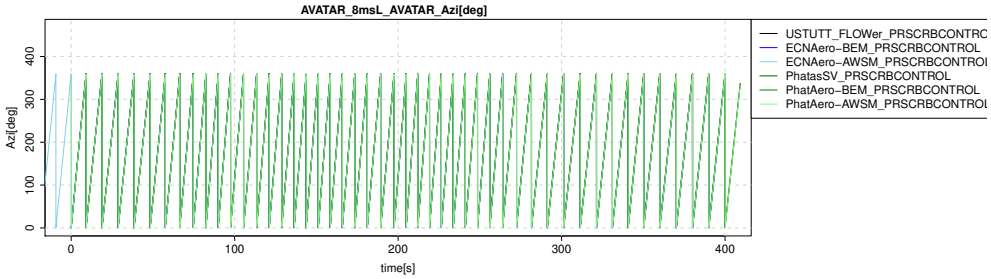

(b) Rotor azimuth

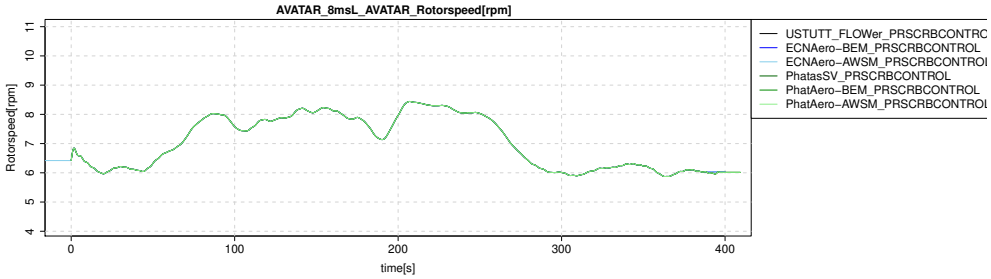

(c) Rotor speed

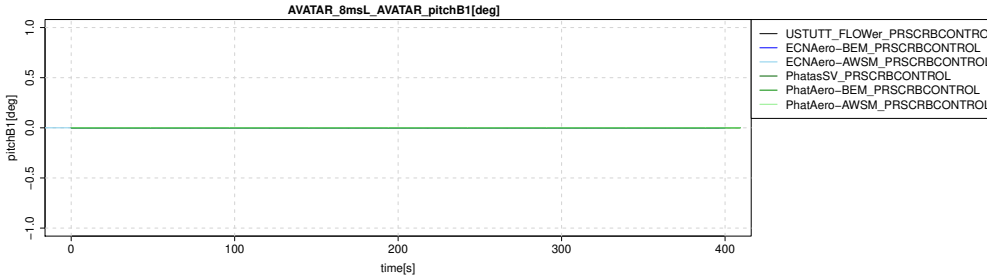

(d) Pitch angle

Figure B.121: Wind and control parameters

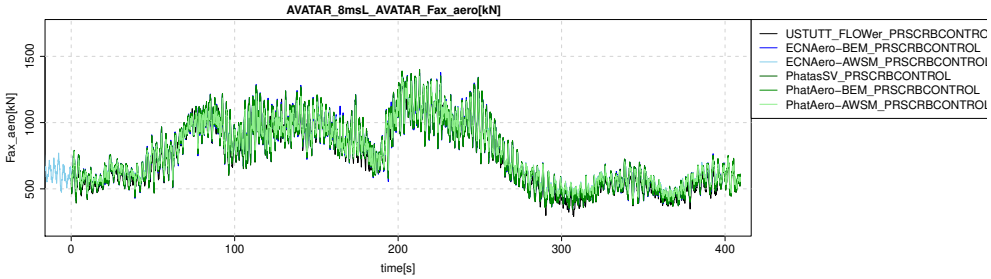

(a) Rotor axial force

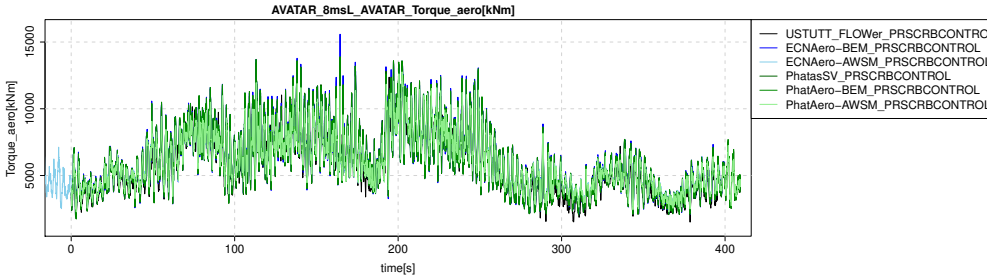

(b) Rotor torque

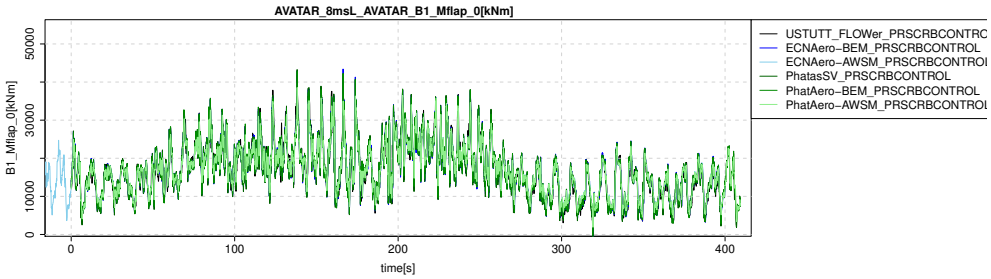

(c) Flapwise blade root moment

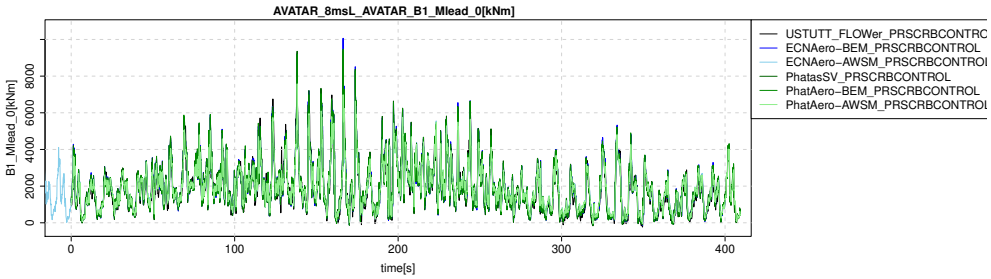

(d) Leadwise blade root moment

Figure B.122: Rotor and blade forces and moments

B.6.3 Statistics

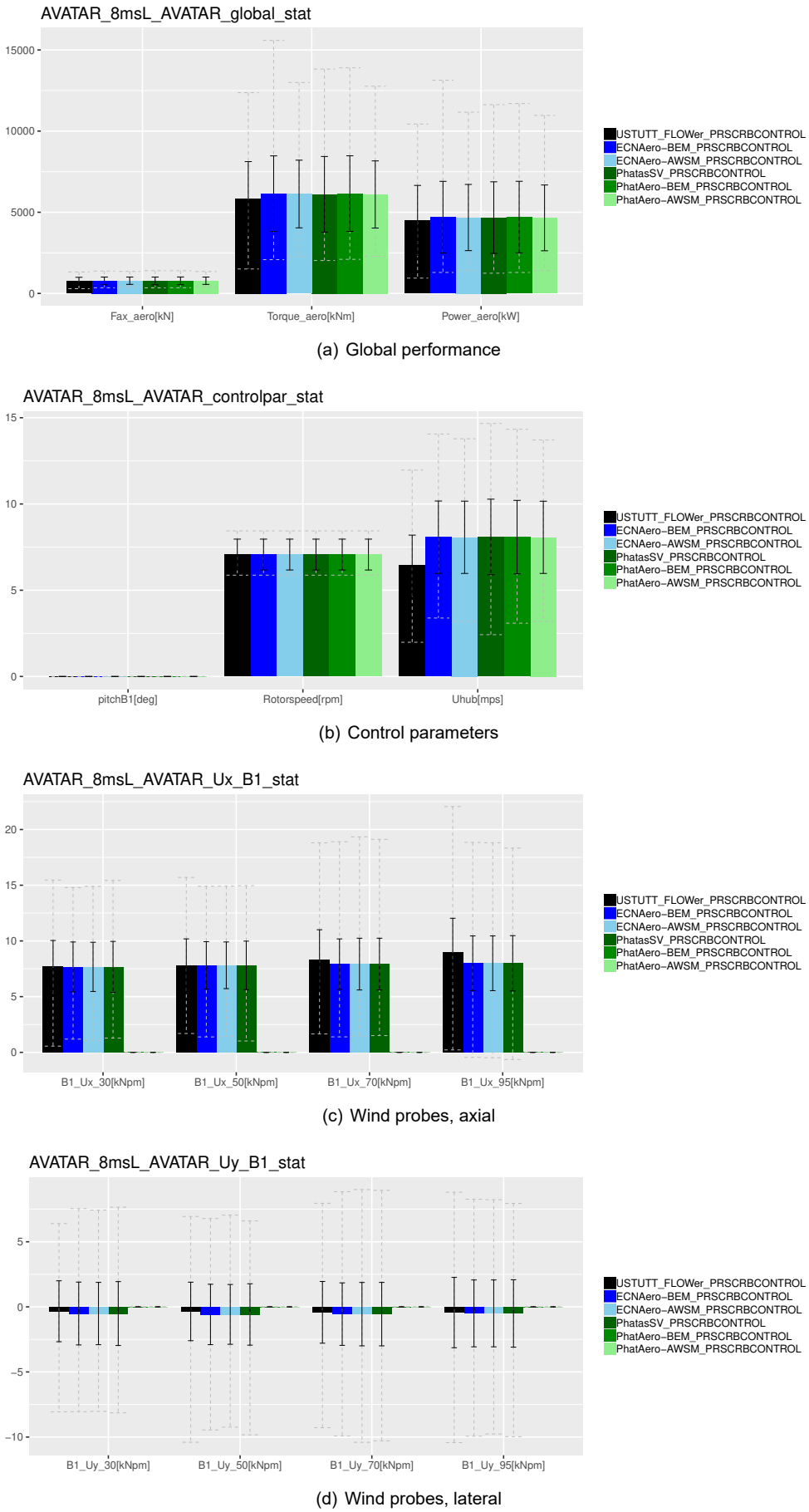

Figure B.123: Global performance, wind and control parameters

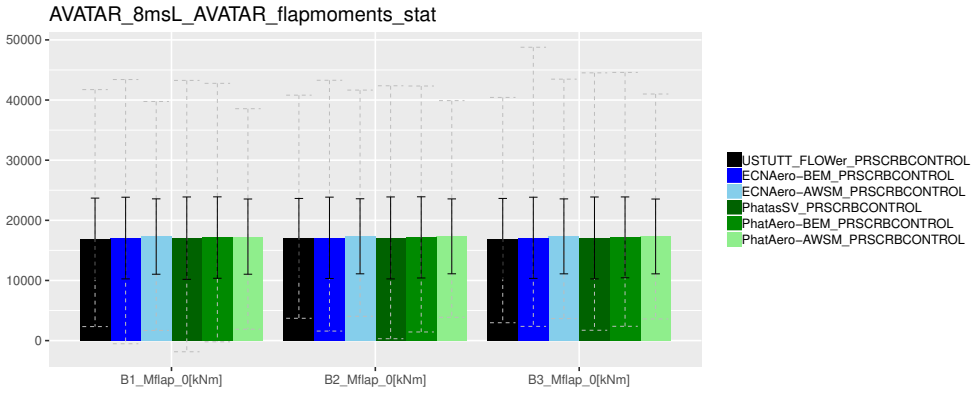

(a) Flapwise moments

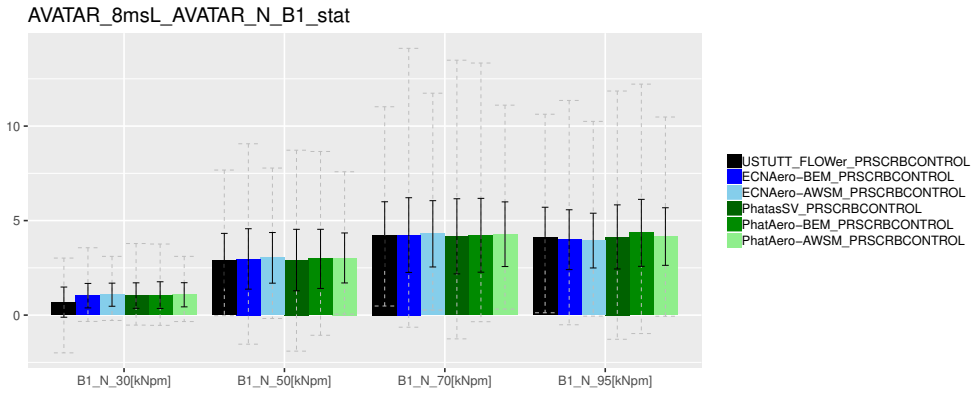

(b) Chord normal force

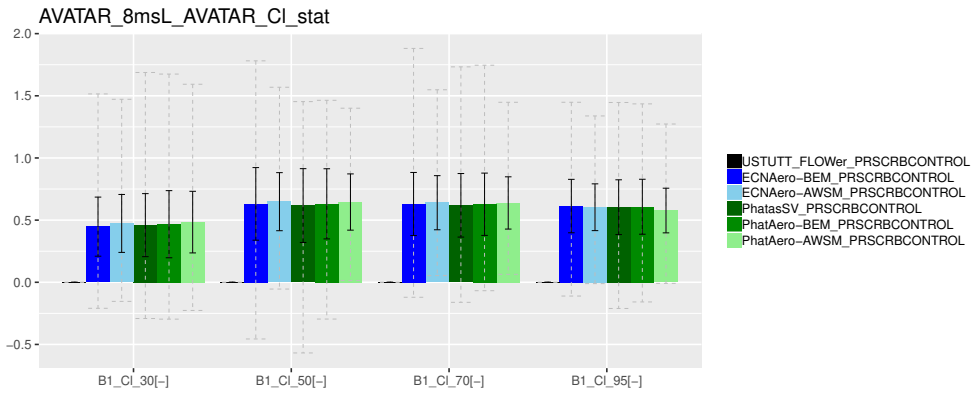

(c) Lift coefficient

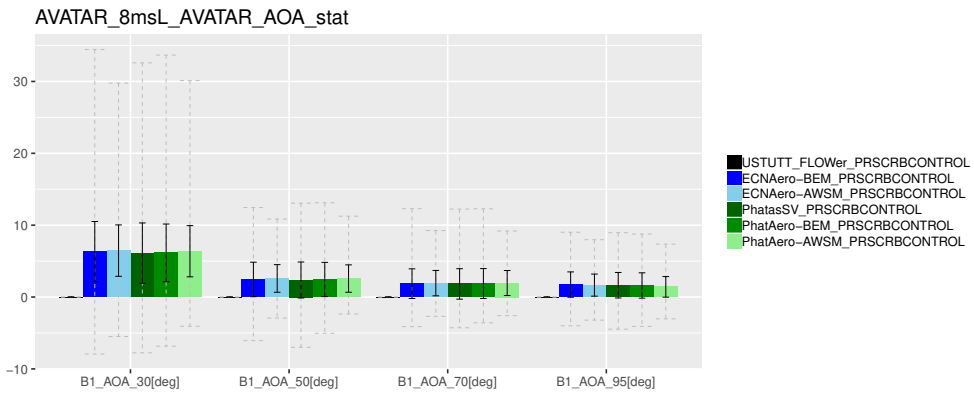

(d) Angle of attack

Figure B.124: Force decompostion in axial direction

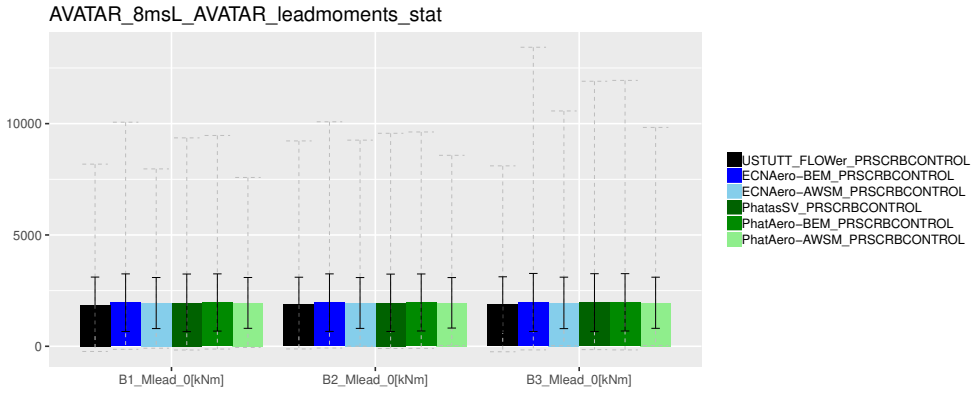

(a) Leadwise moments

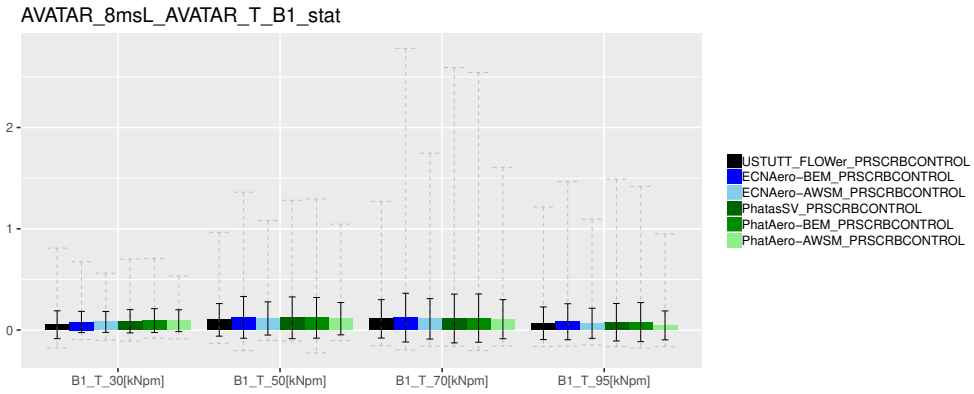

(b) Chord tangential force

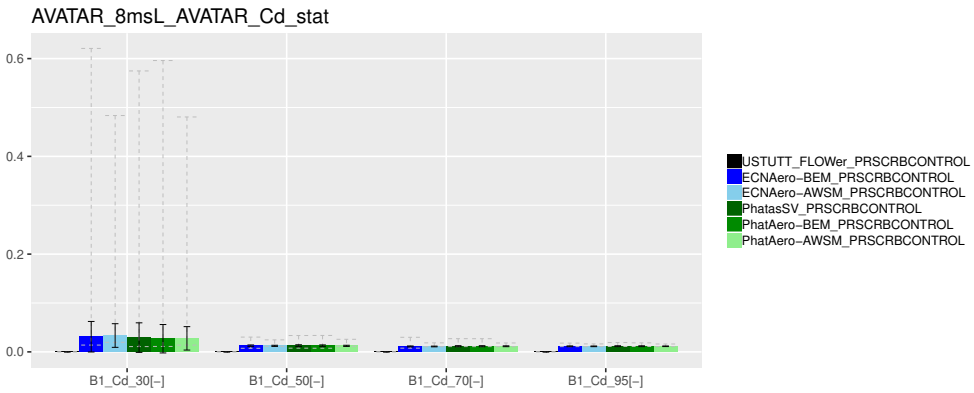

(c) Drag coefficient

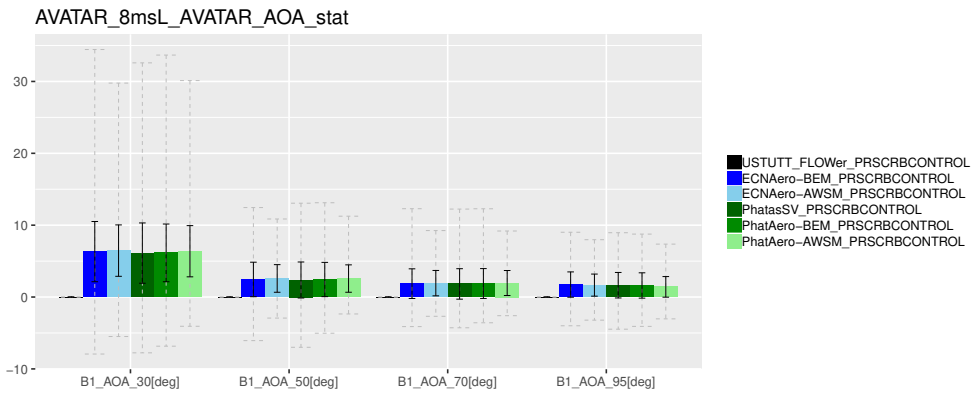

(d) Angle of attack

Figure B.125: Force decompostion in tangential direction

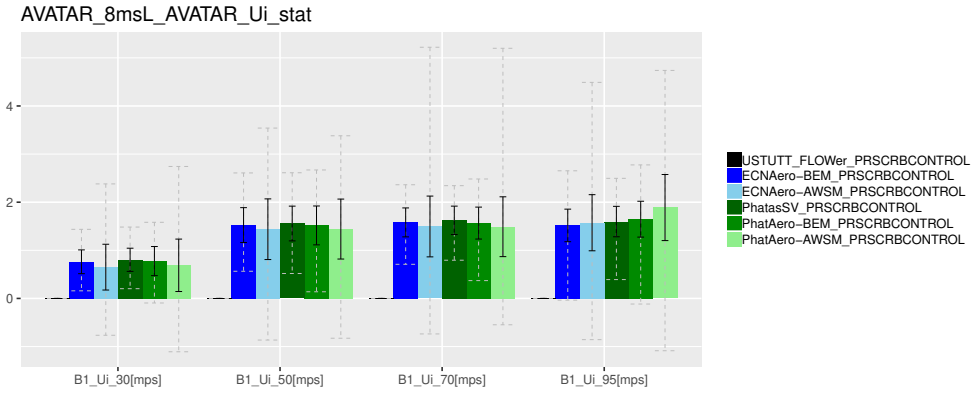

(a) Axial induced velocity

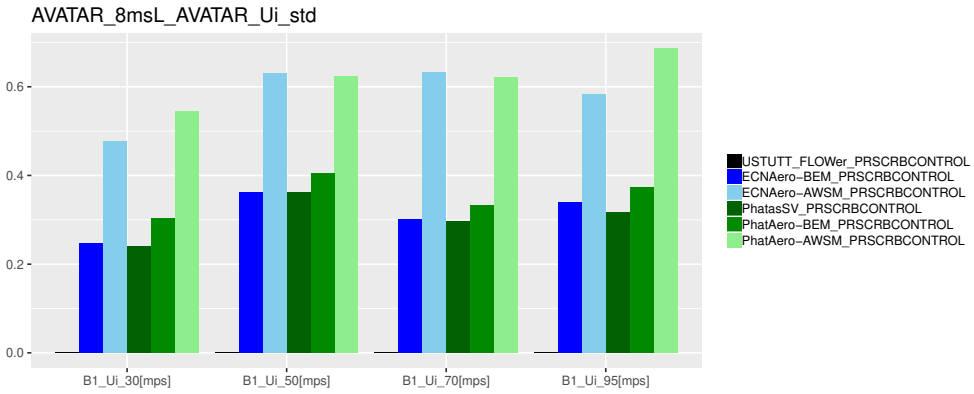

(b) Axial induced velocity (standard deviation)

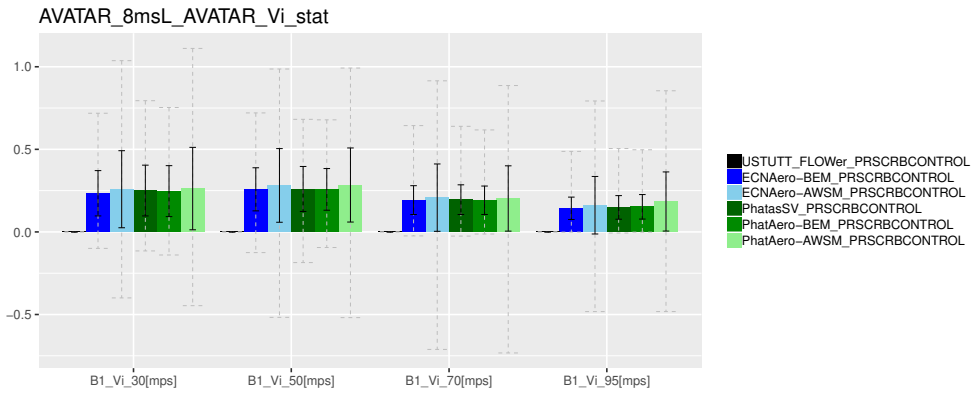

(c) Tangential induced velocity

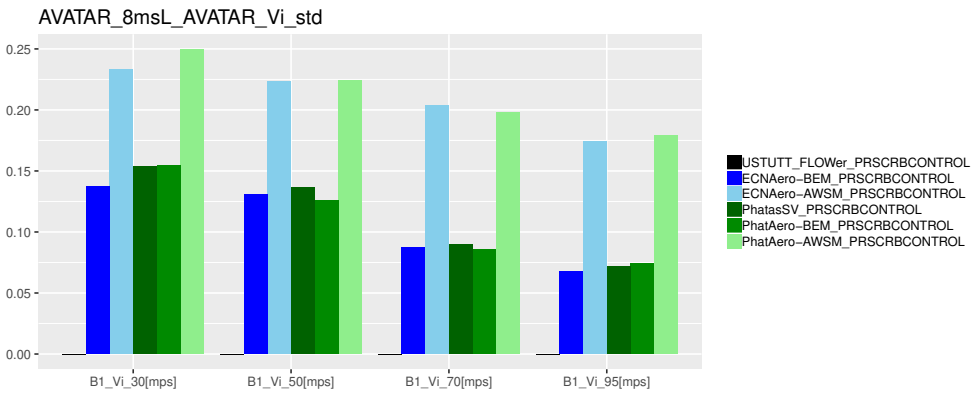

(d) Tangential induced velocity (standard deviation)

Figure B.126: Induced velocities

B.6.4 Equivalent load levels

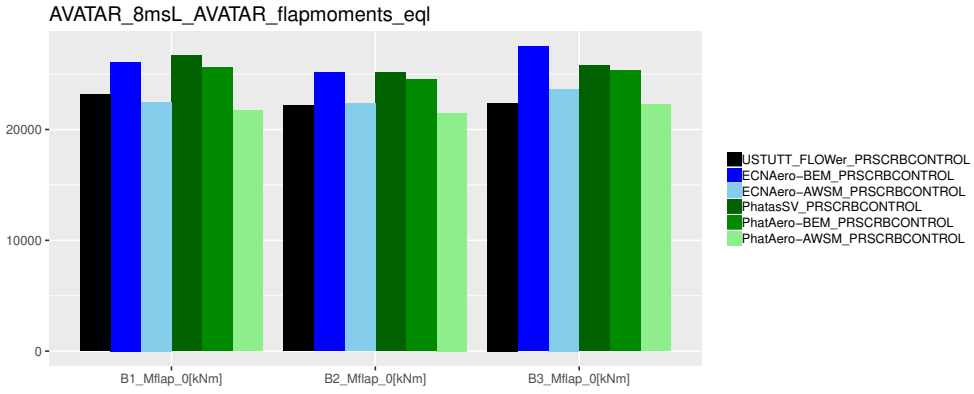

(a) Flapwise moments

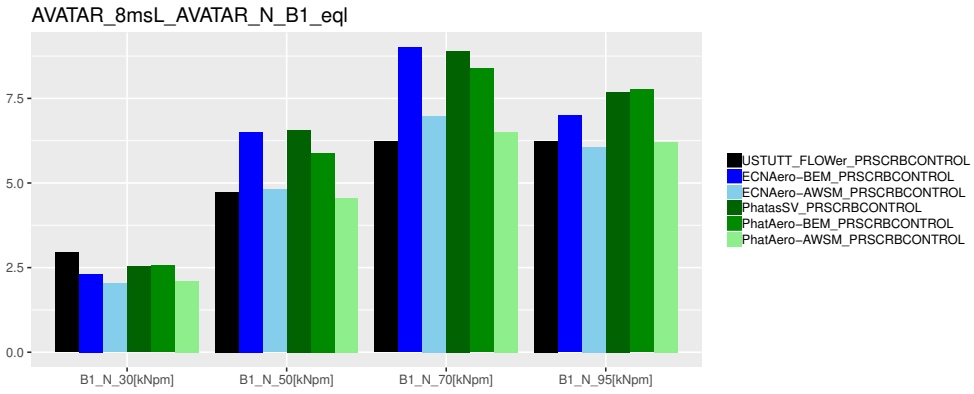

(b) Normal force

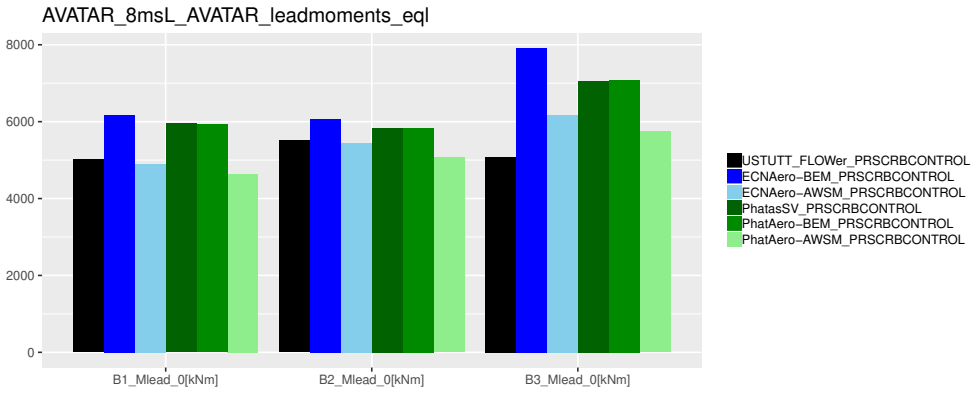

(c) Leadwise moments

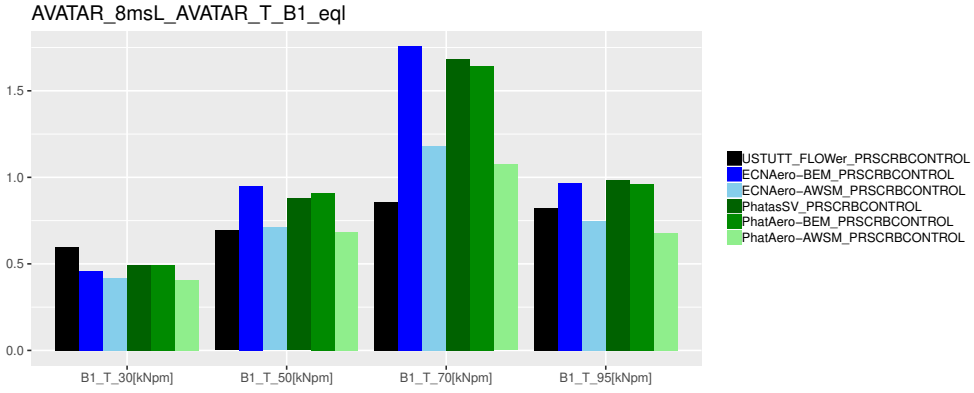

(d) Tangential force

Figure B.127: Forces and moments

B.6.5 Staircase plots

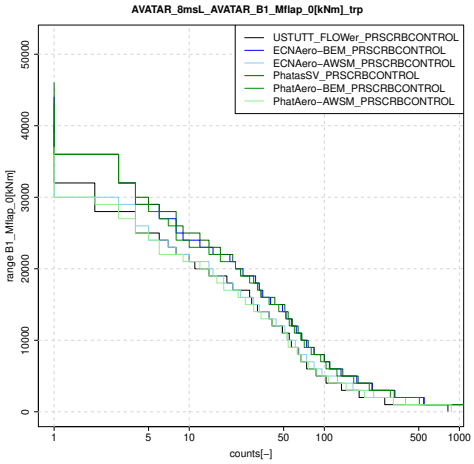

(a) Flapwise blade root moment

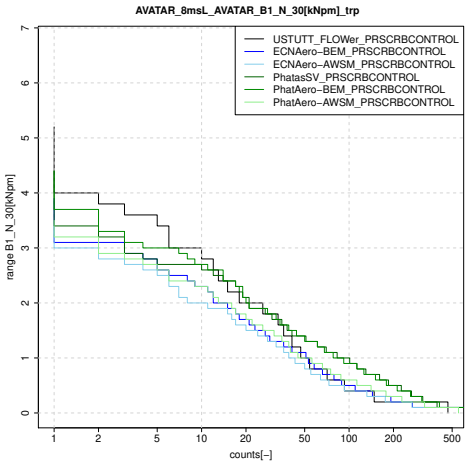

(b) Normal force, 30%R

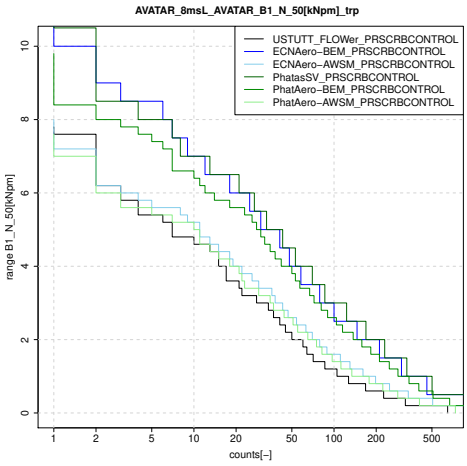

(c) Normal force, 50%R

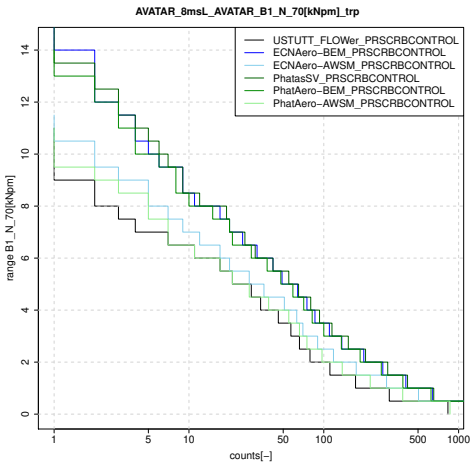

(d) Normal force, 70%R

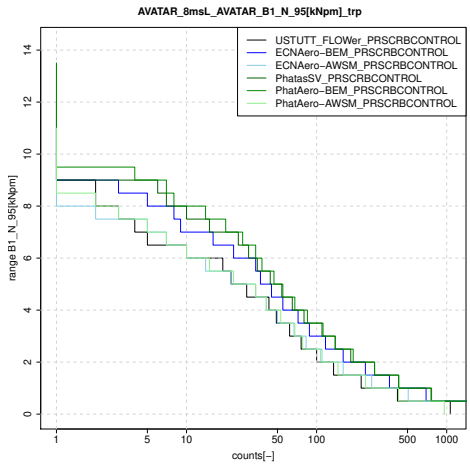

(e) Normal force, 95%R

Figure B.128: Flapwise moment and normal forces

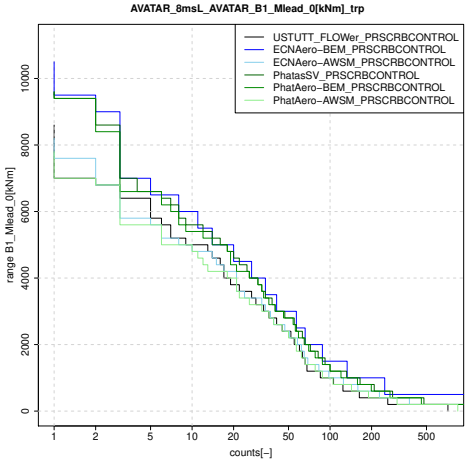

(a) Leadwise blade root moment

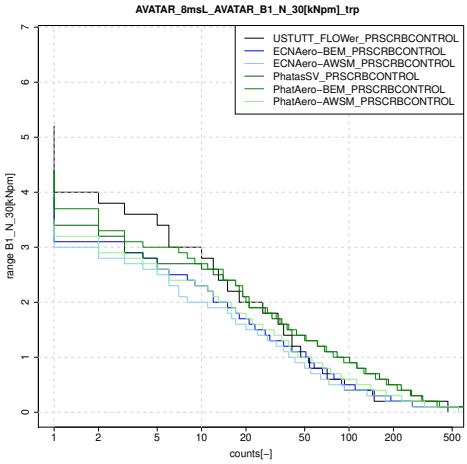

(b) Tangential force, 30%R

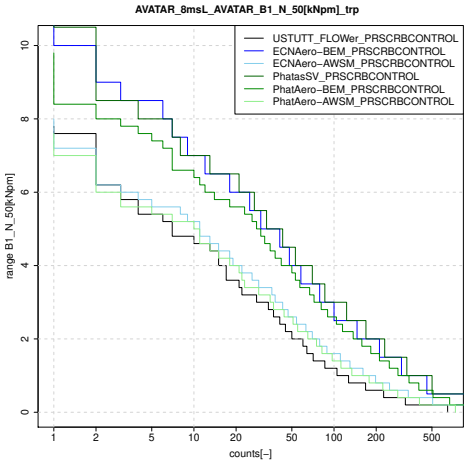

(c) Tangential force, 50%R

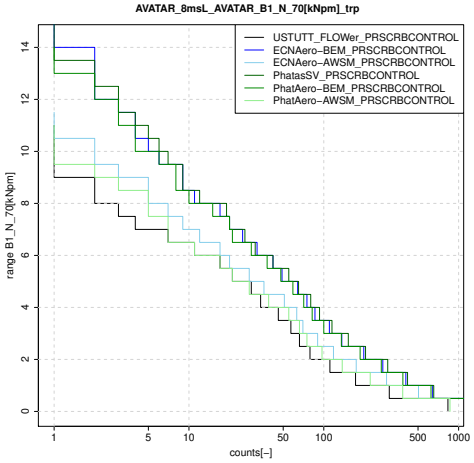

(d) Tangential force, 70%R

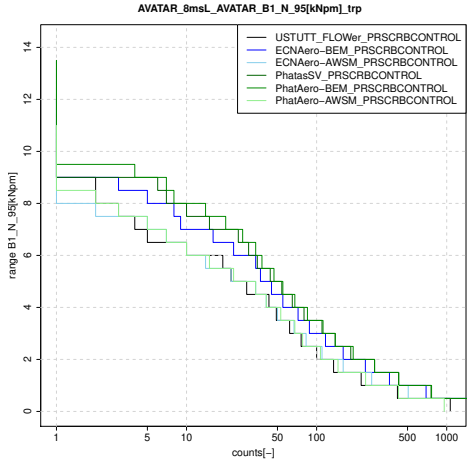

(e) Tangential force, 95%R

Figure B.129: Leadwise moment and tangential forces

B.6.6 PSD

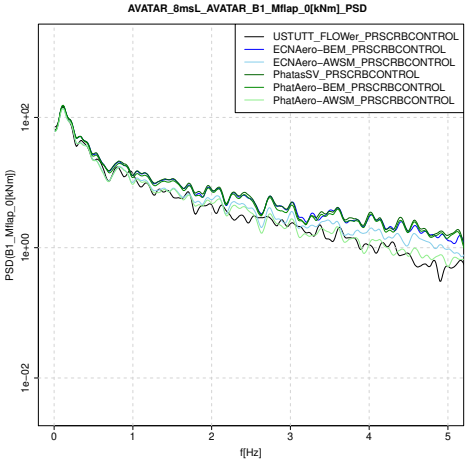

(a) Flapwise blade root moment

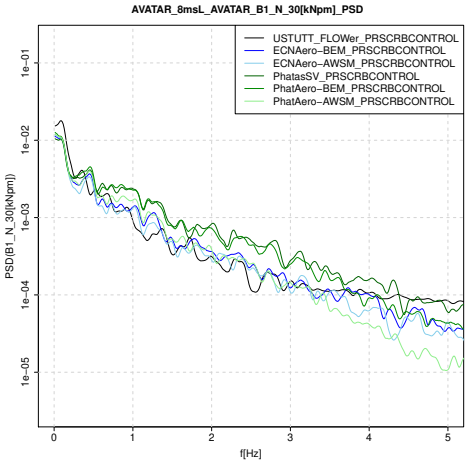

(b) Normal force, 30%R

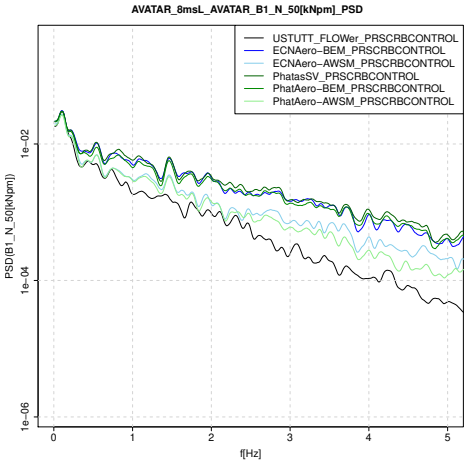

(c) Normal force, 50%R

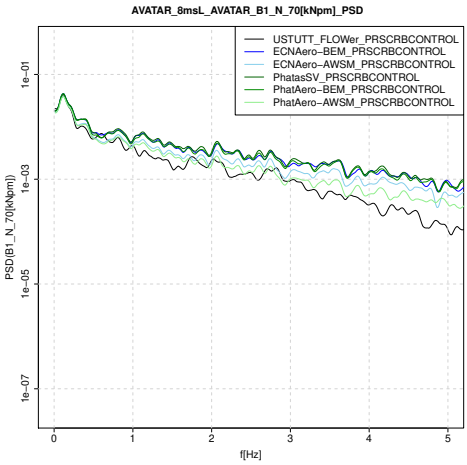

(d) Normal force, 70%R

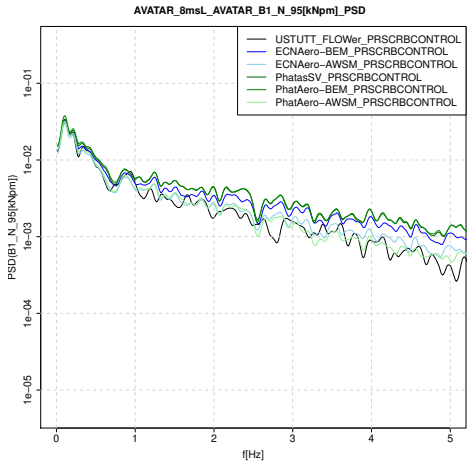

(e) Normal force, 95%R

Figure B.130: Flapwise moment and normal forces

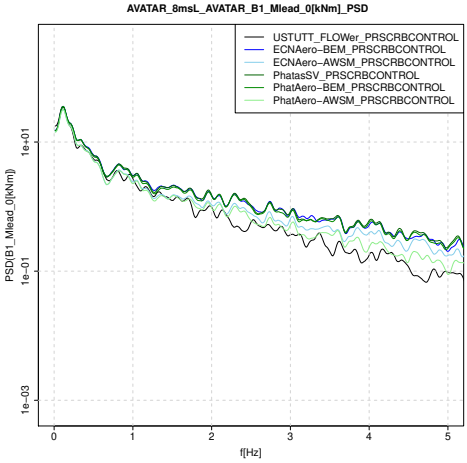

(a) Leadwise blade root moment

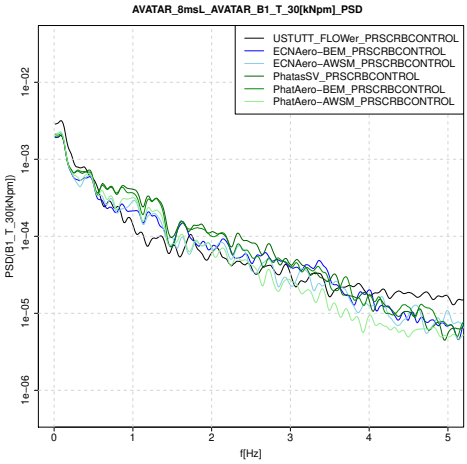

(b) Tangential force, 30%R

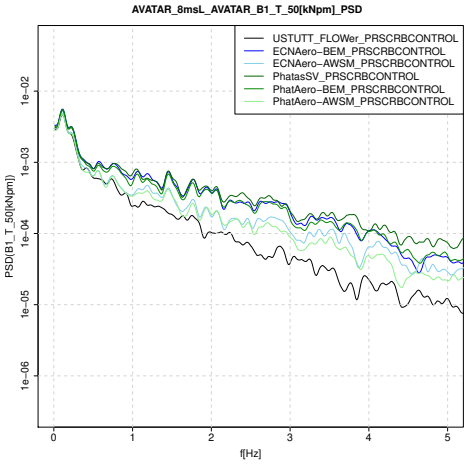

(c) Tangential force, 50%R

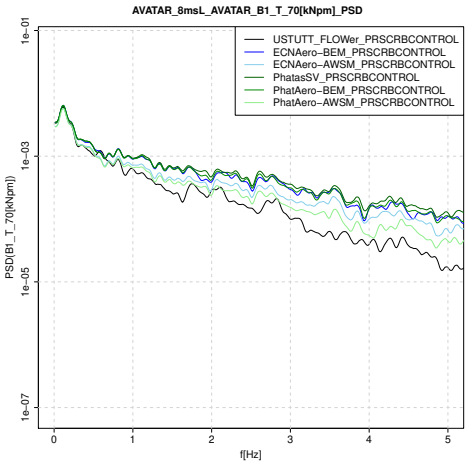

(d) Tangential force, 70%R

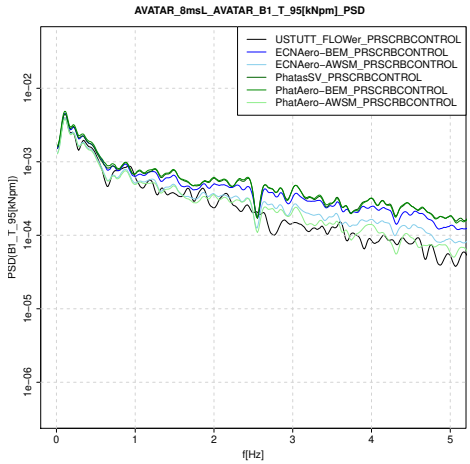

(e) Tangential force, 95%R

Figure B.131: Leadwise moment and tangential forces

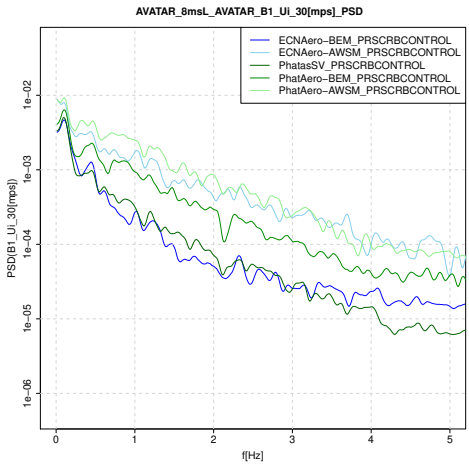

(a) Axial induced velocity, 30%R

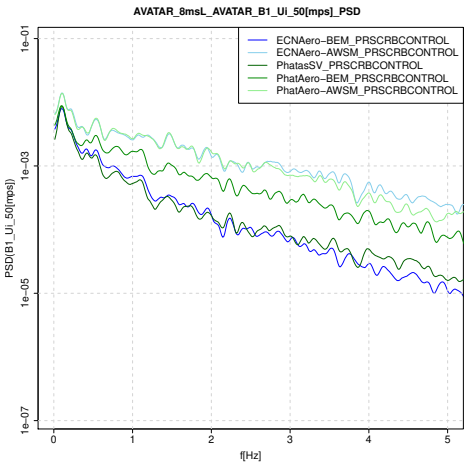

(b) Axial induced velocity, 50%R

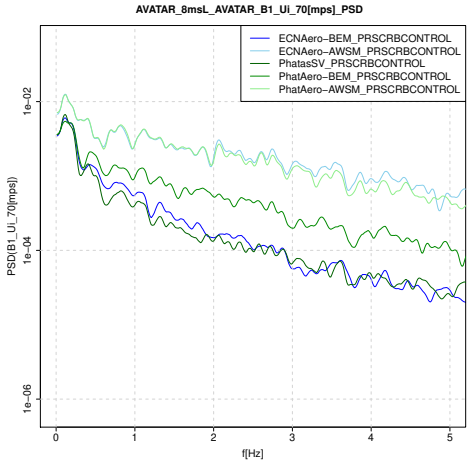

(c) Axial induced velocity, 70%R

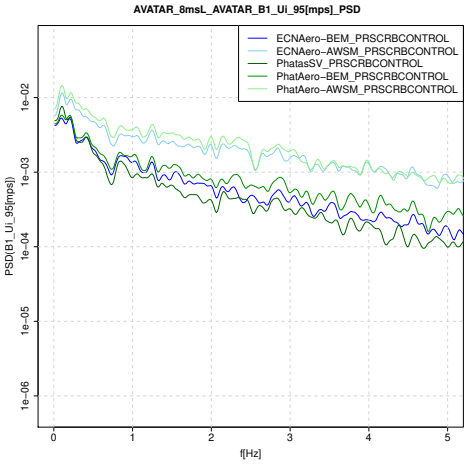

(d) Axial induced velocity, 95%R

Figure B.132: Axial induced velocities

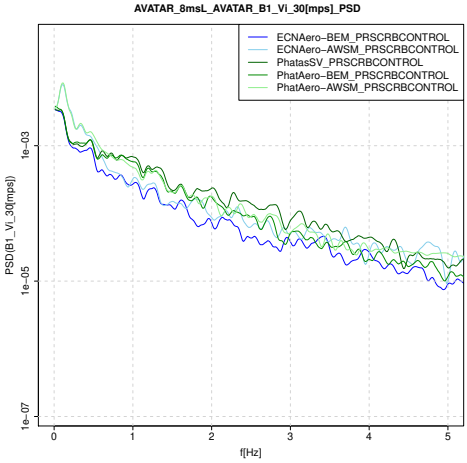

(a) Tangential induced velocity, 30%R

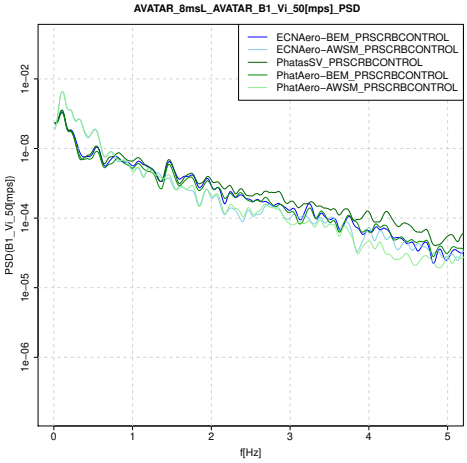

(b) Tangential induced velocity, 50%R

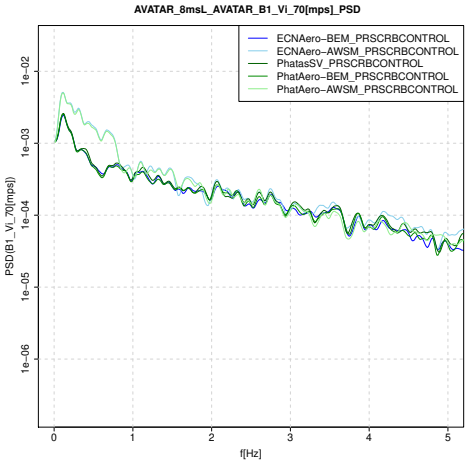

(c) Tangential induced velocity, 70%R

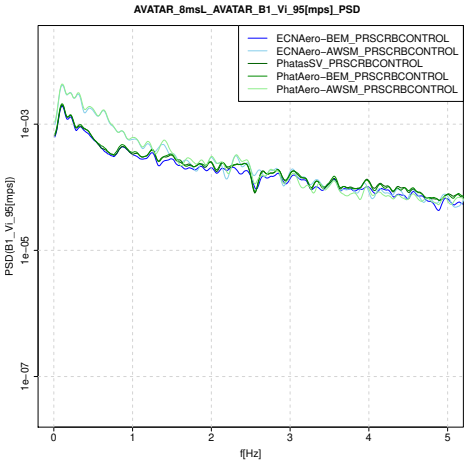

(d) Tangential induced velocity, 95%R

Figure B.133: Tangential induced velocities

C Shed vorticity modeling (8 m/s fixed case)

C.0.1 Time (zoomed)

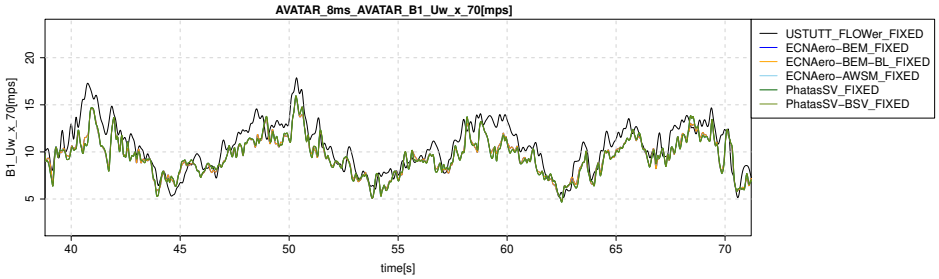

(a) Wind probe axial velocity at 70%R

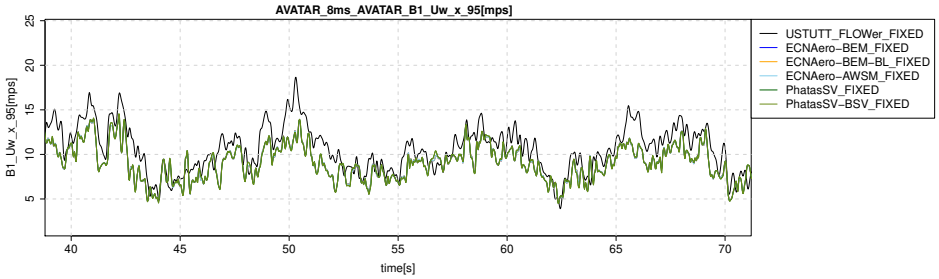

(b) Wind probe axial velocity at 95%R

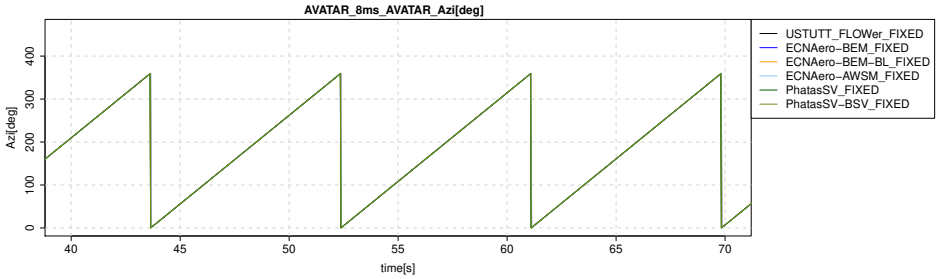

(c) Rotor azimuth angle

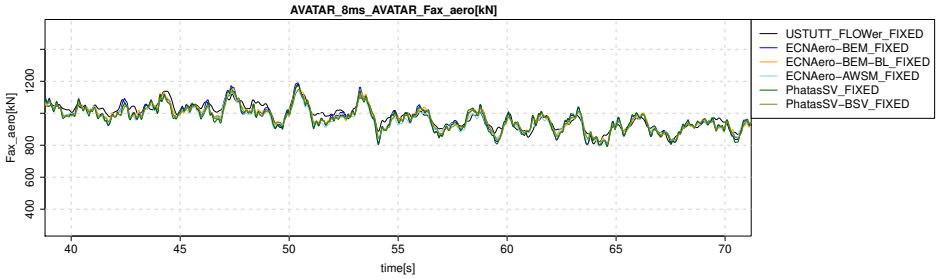

(d) Rotor axial force

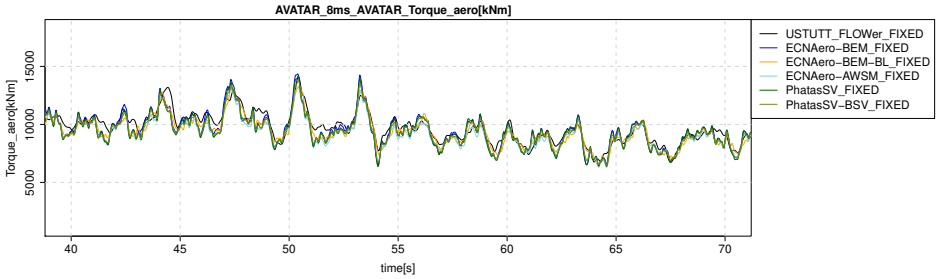

(e) Rotor torque

Figure C.1: Alignment check

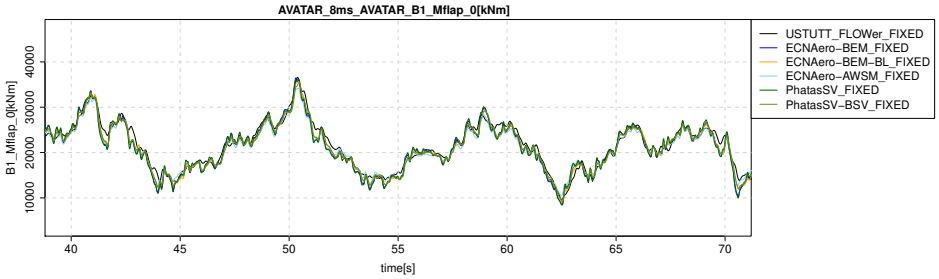

(a) Flapwise blade root moment

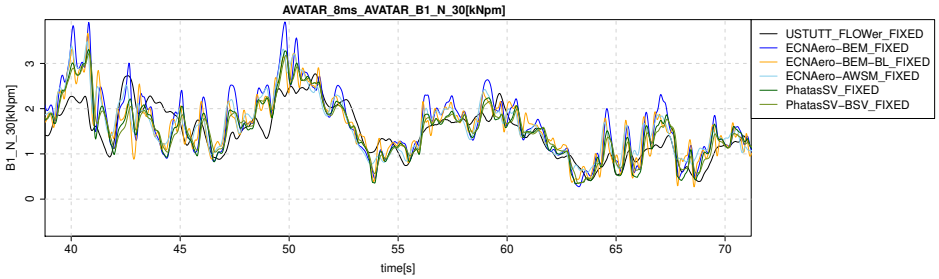

(b) Chord normal force at 30%R

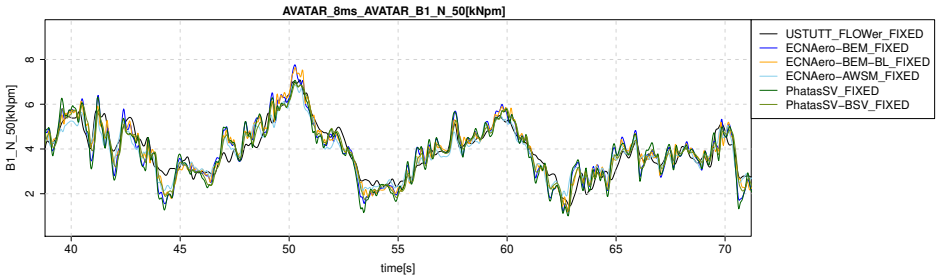

(c) Chord normal force at 50%R

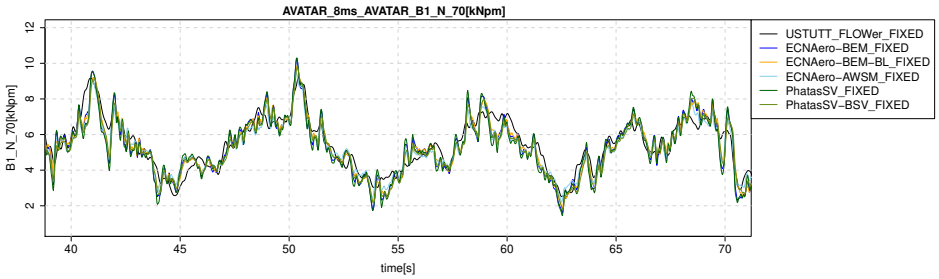

(d) Chord normal force at 70%R

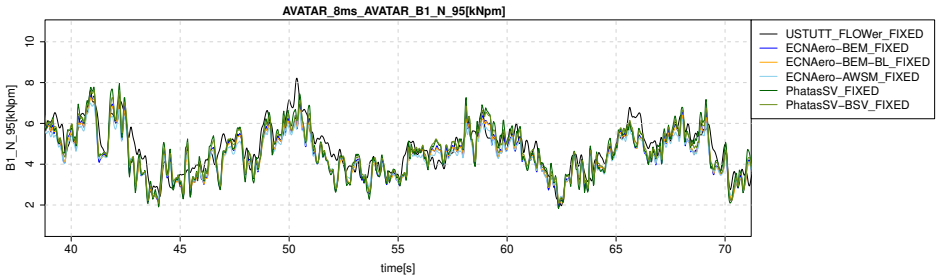

(e) Chord normal force at 95%R

Figure C.2: Flapwise moment and normal force

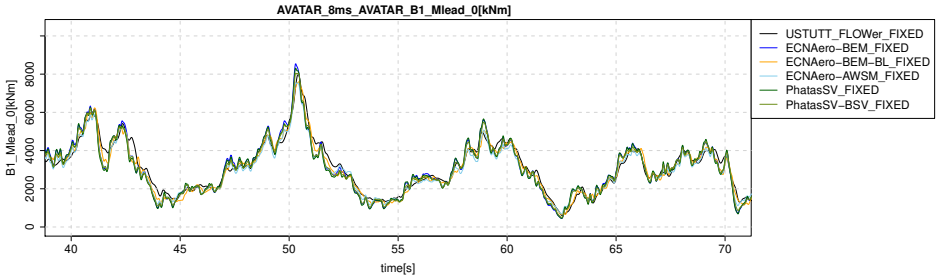

(a) Leadwise blade root moment

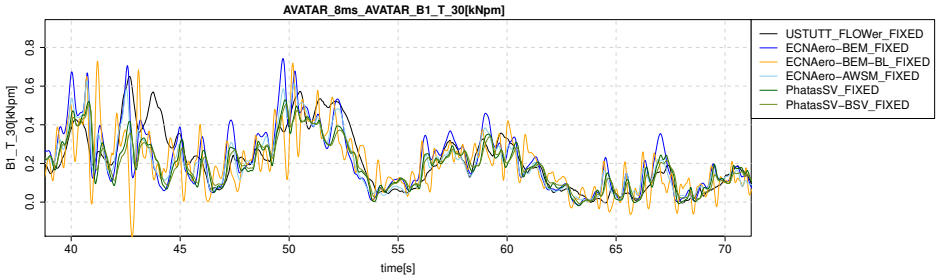

(b) Chord tangential force at 30%R

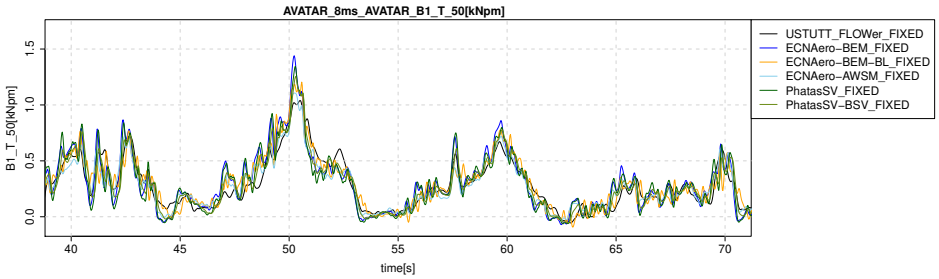

(c) Chord tangential force at 50%R

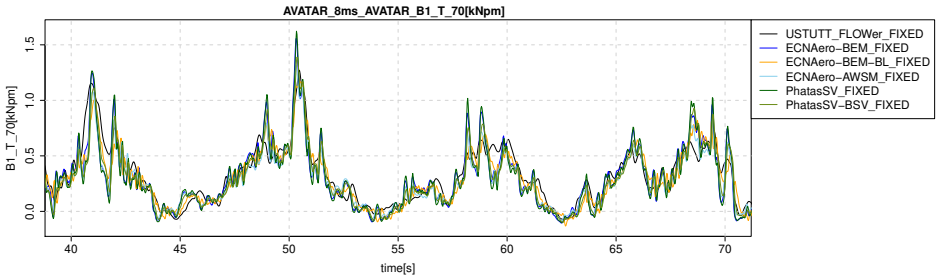

(d) Chord tangential force at 70%R

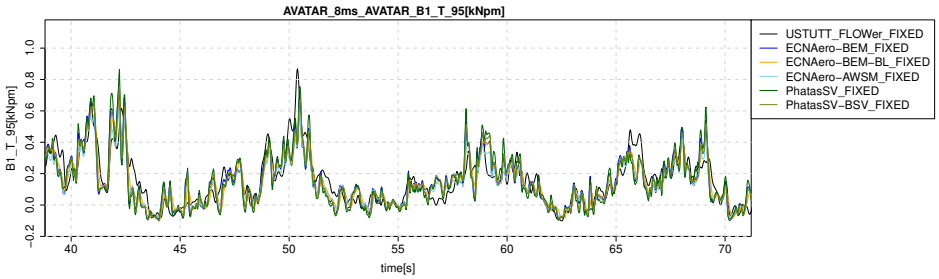

(e) Chord tangential force at 95%R

Figure C.3: Leadwise moment and tangential force

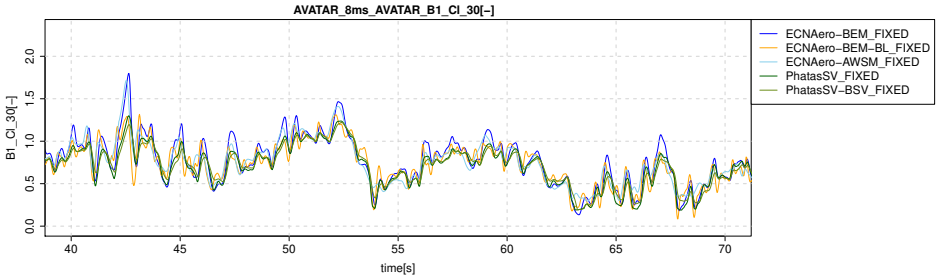

(a) Lift coefficient at 30%R

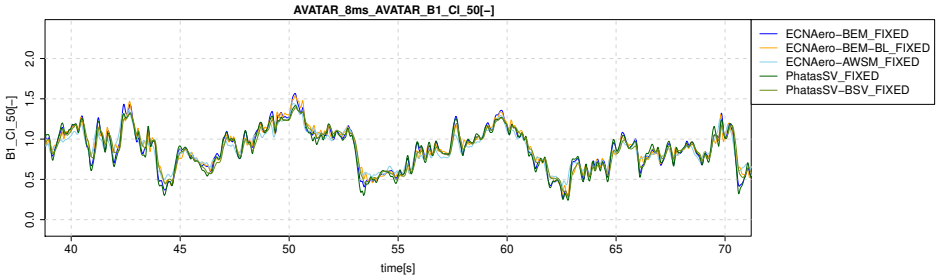

(b) Lift coefficient at 50%R

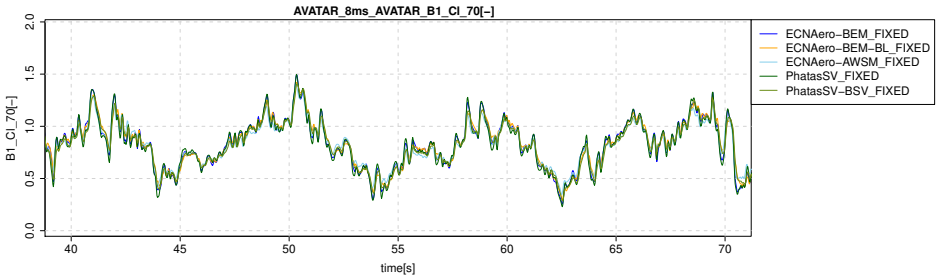

(c) Lift coefficient at 70%R

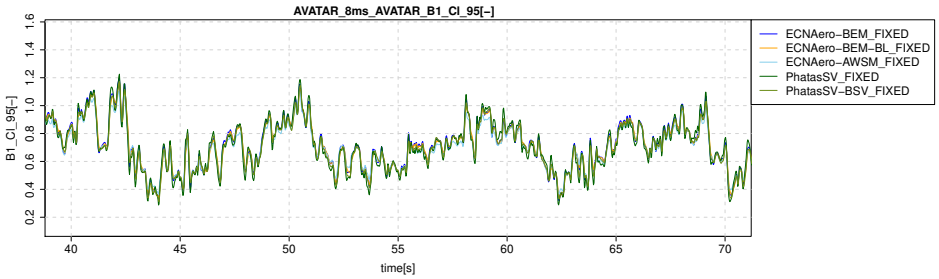

(d) Lift coefficient at 95%R

Figure C.4: Lift coefficients

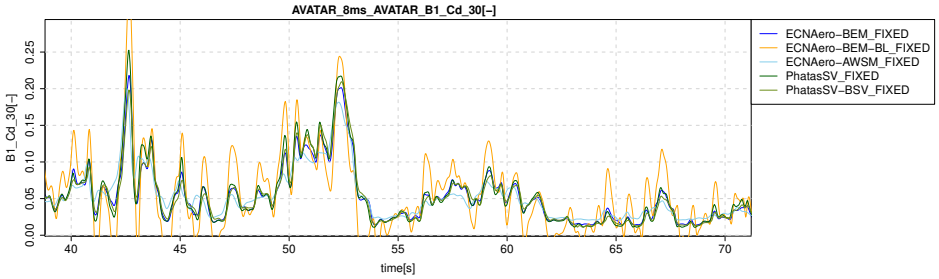

(a) Drag coefficient at 30%R

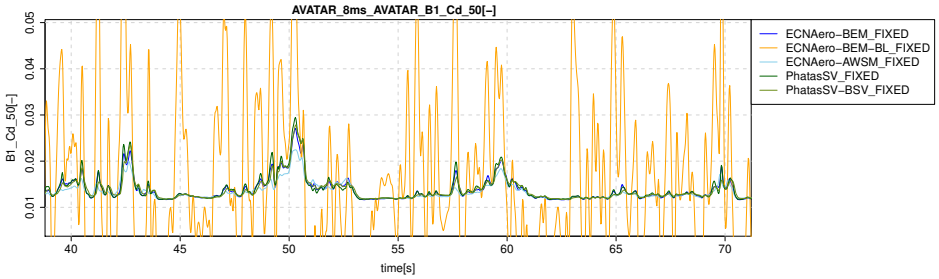

(b) Drag coefficient at 50%R

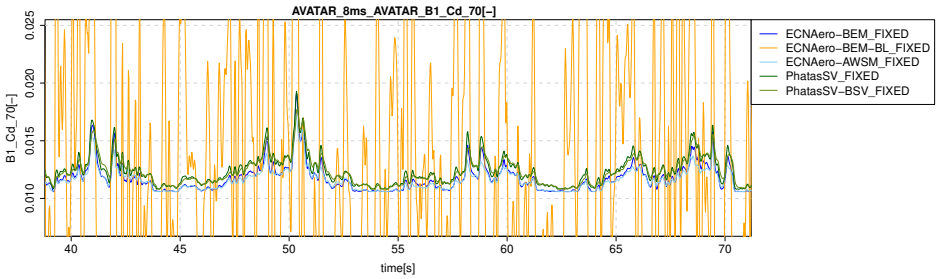

(c) Drag coefficient at 70%R

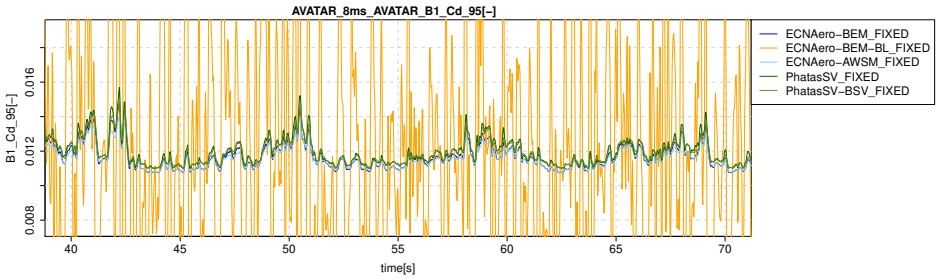

(d) Drag coefficient at 95%R

Figure C.5: Drag coefficients

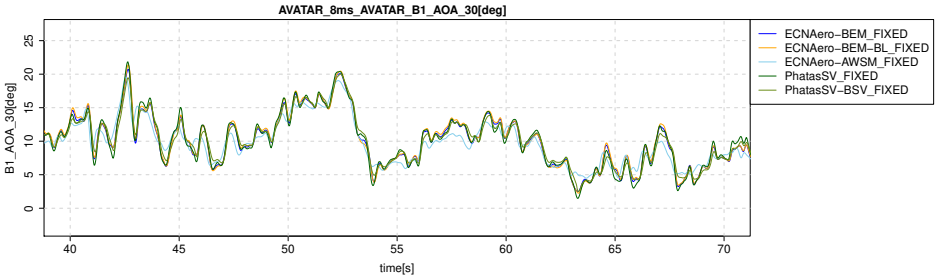

(a) Angle of attack at 30%R

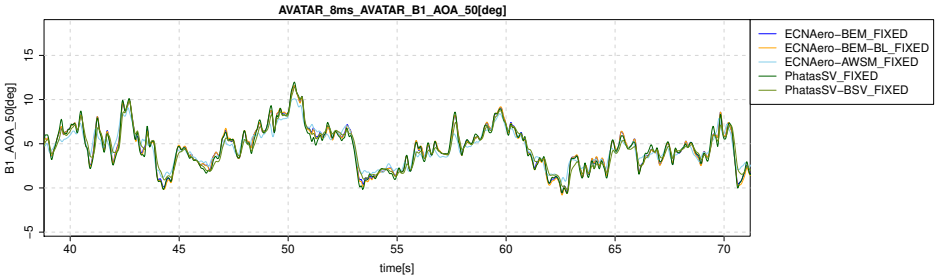

(b) Angle of attack at 50%R

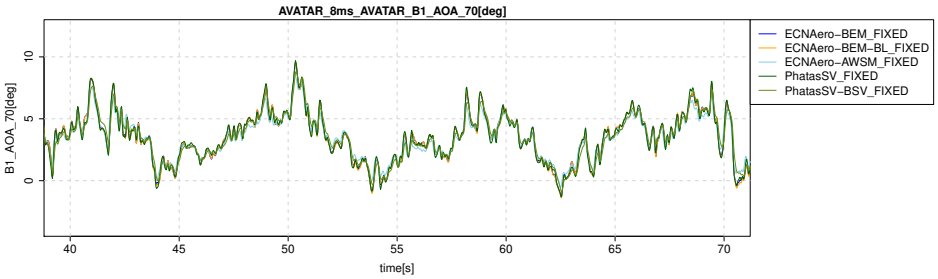

(c) Angle of attack at 70%R

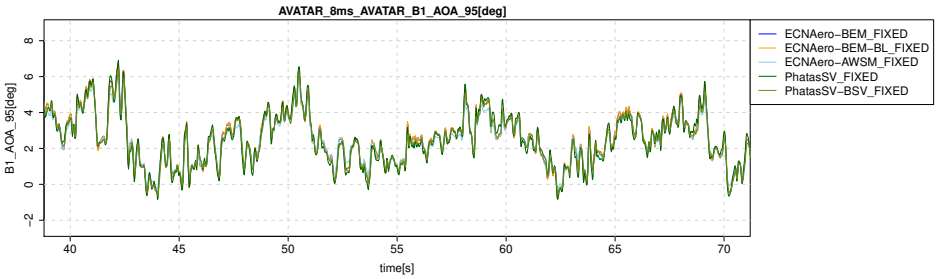

(d) Angle of attack at 95%R

Figure C.6: Angles of attack

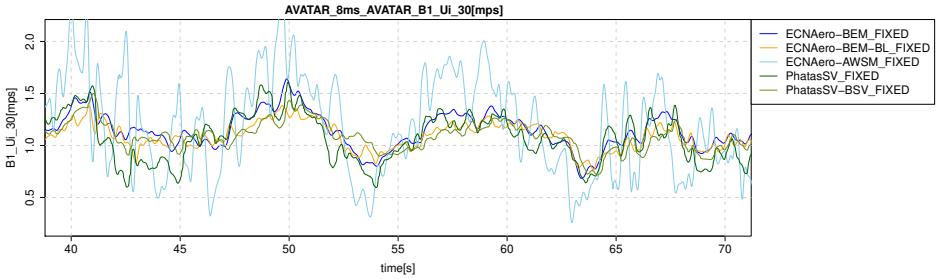

(a) Axial induced velocity at 30%R

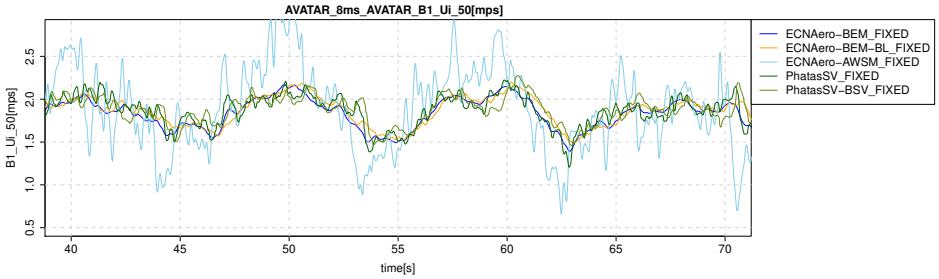

(b) Axial induced velocity at 50%R

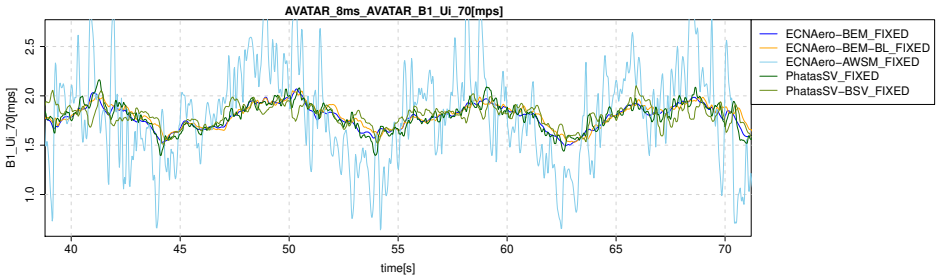

(c) Axial induced velocity at 70%R

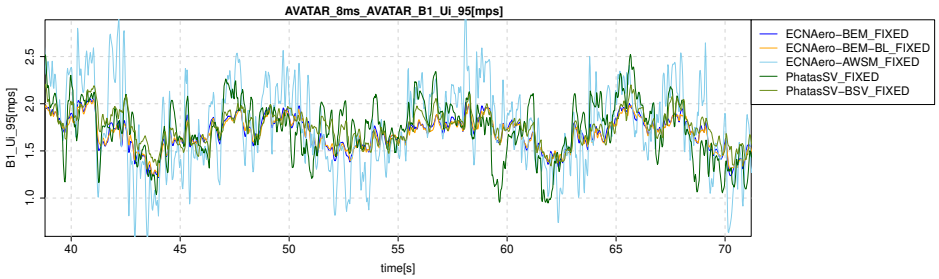

(d) Axial induced velocity at 95%R

Figure C.7: Axial induced velocities

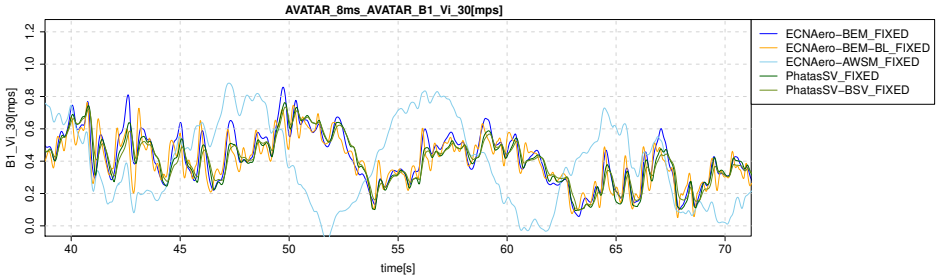

(a) Tangential induced velocity at 30%R

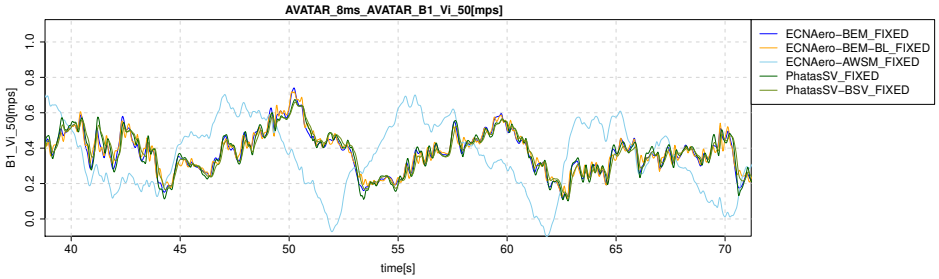

(b) Tangential induced velocity at 50%R

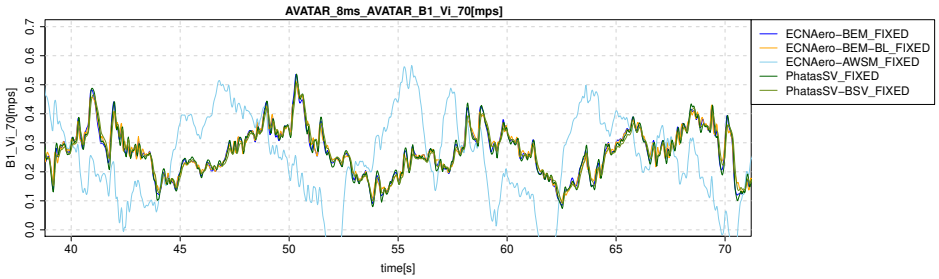

(c) Tangential induced velocity at 70%R

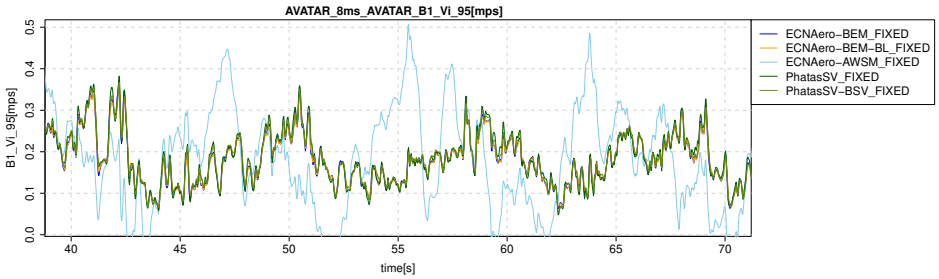

(d) Tangential induced velocity at 95%R

Figure C.8: Tangential induced velocities

C.0.2 Time

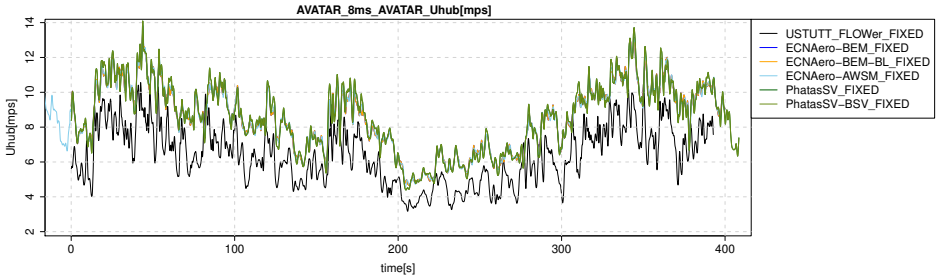

(a) Hub height wind speed

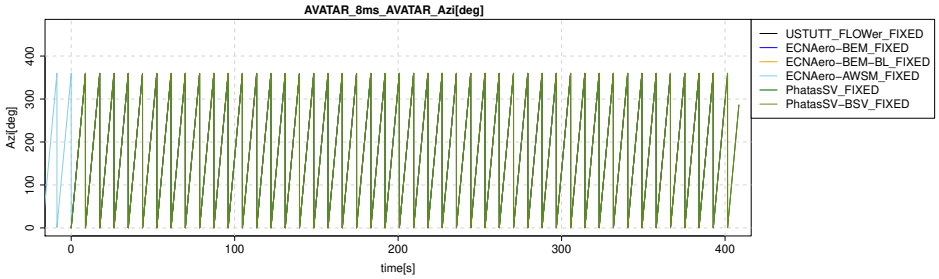

(b) Rotor azimuth

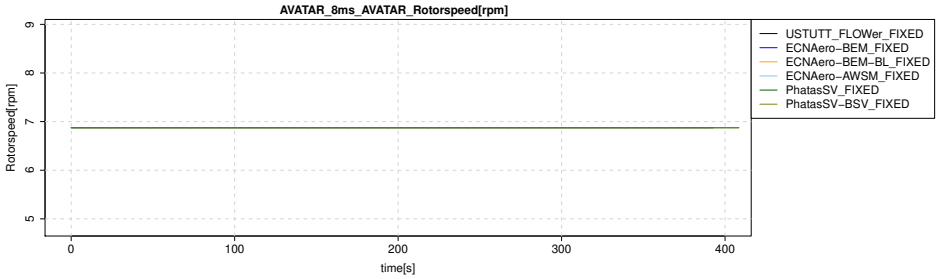

(c) Rotor speed

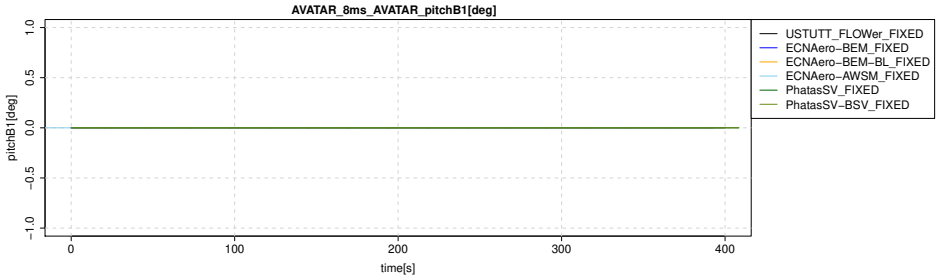

(d) Pitch angle

Figure C.9: Wind and control parameters

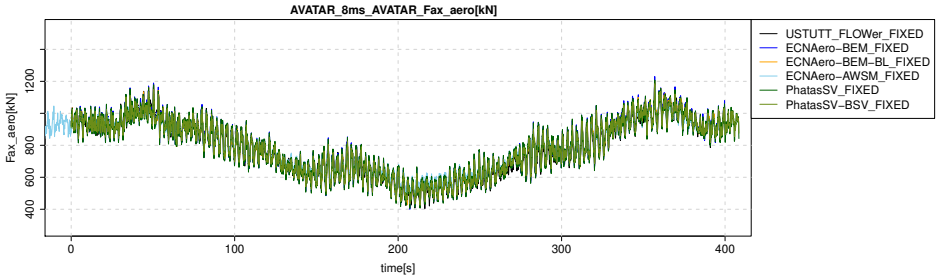

(a) Rotor axial force

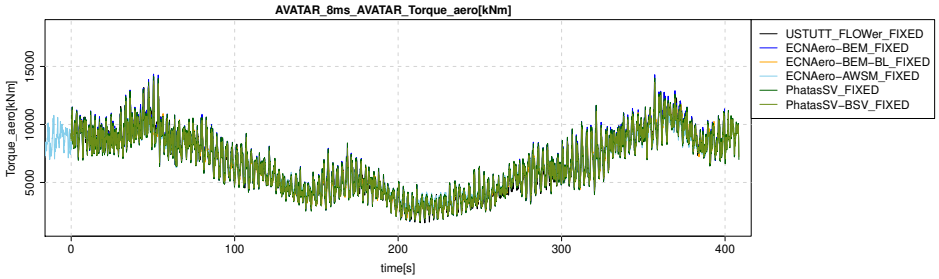

(b) Rotor torque

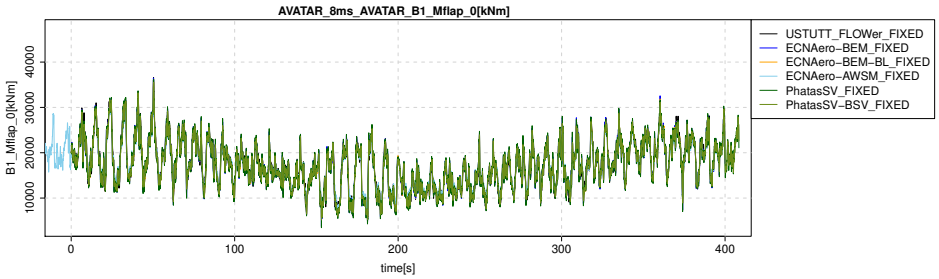

(c) Flapwise blade root moment

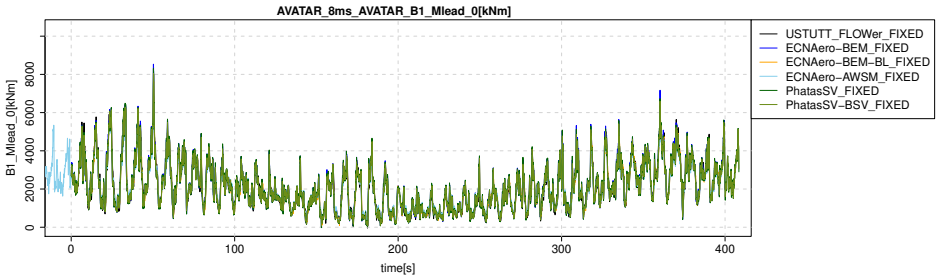

(d) Leadwise blade root moment

Figure C.10: Rotor and blade forces and moments

C.0.3 Statistics

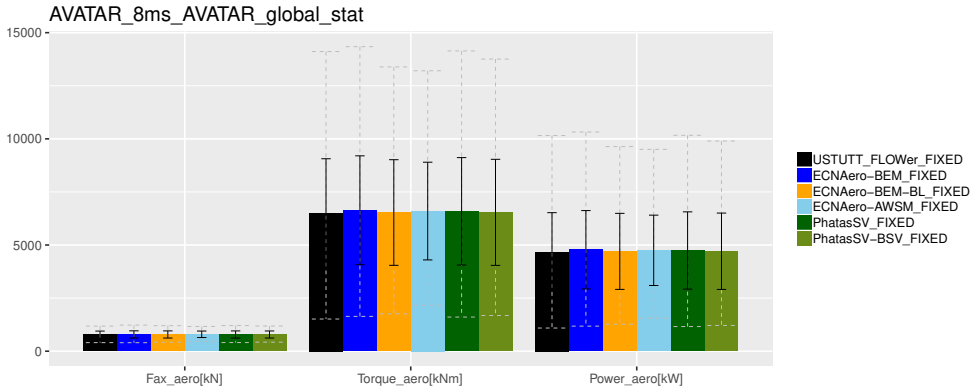

(a) Global performance

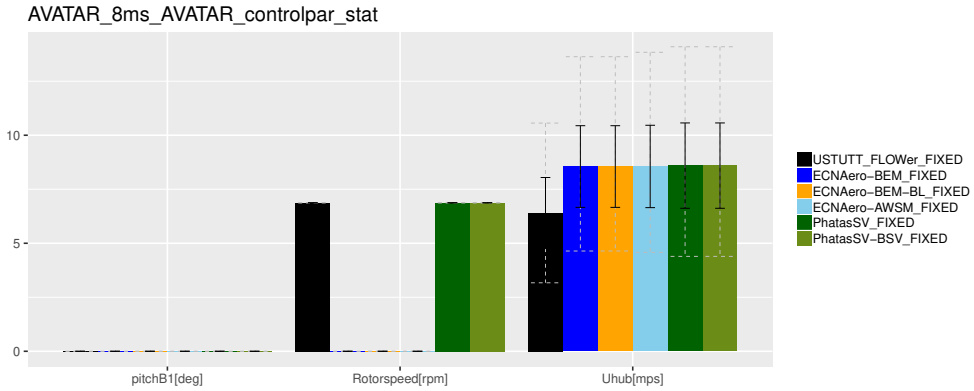

(b) Control parameters

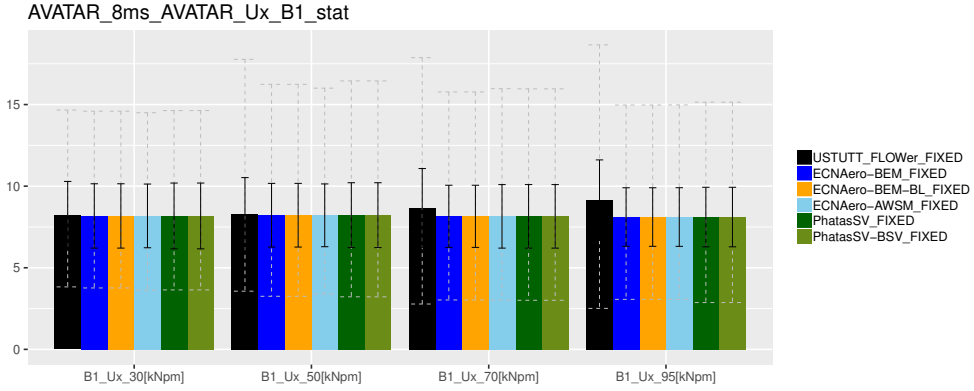

(c) Wind probes, axial

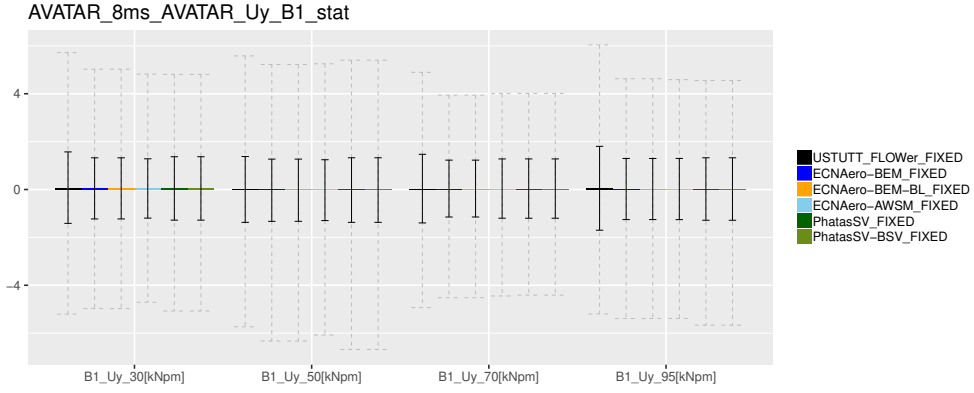

(d) Wind probes, lateral

Figure C.11: Global performance, wind and control parameters

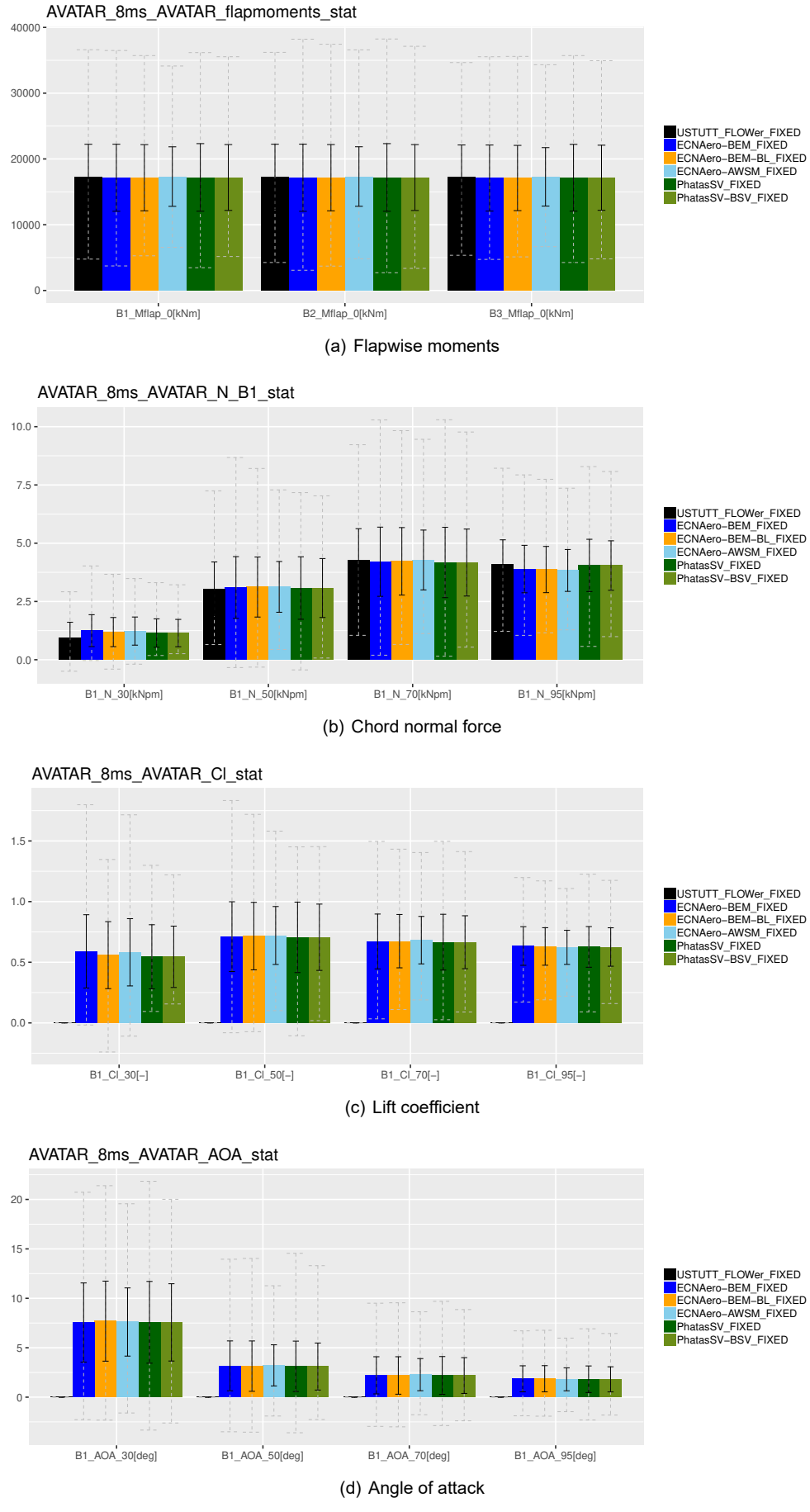

Figure C.12: Force decompostion in axial direction

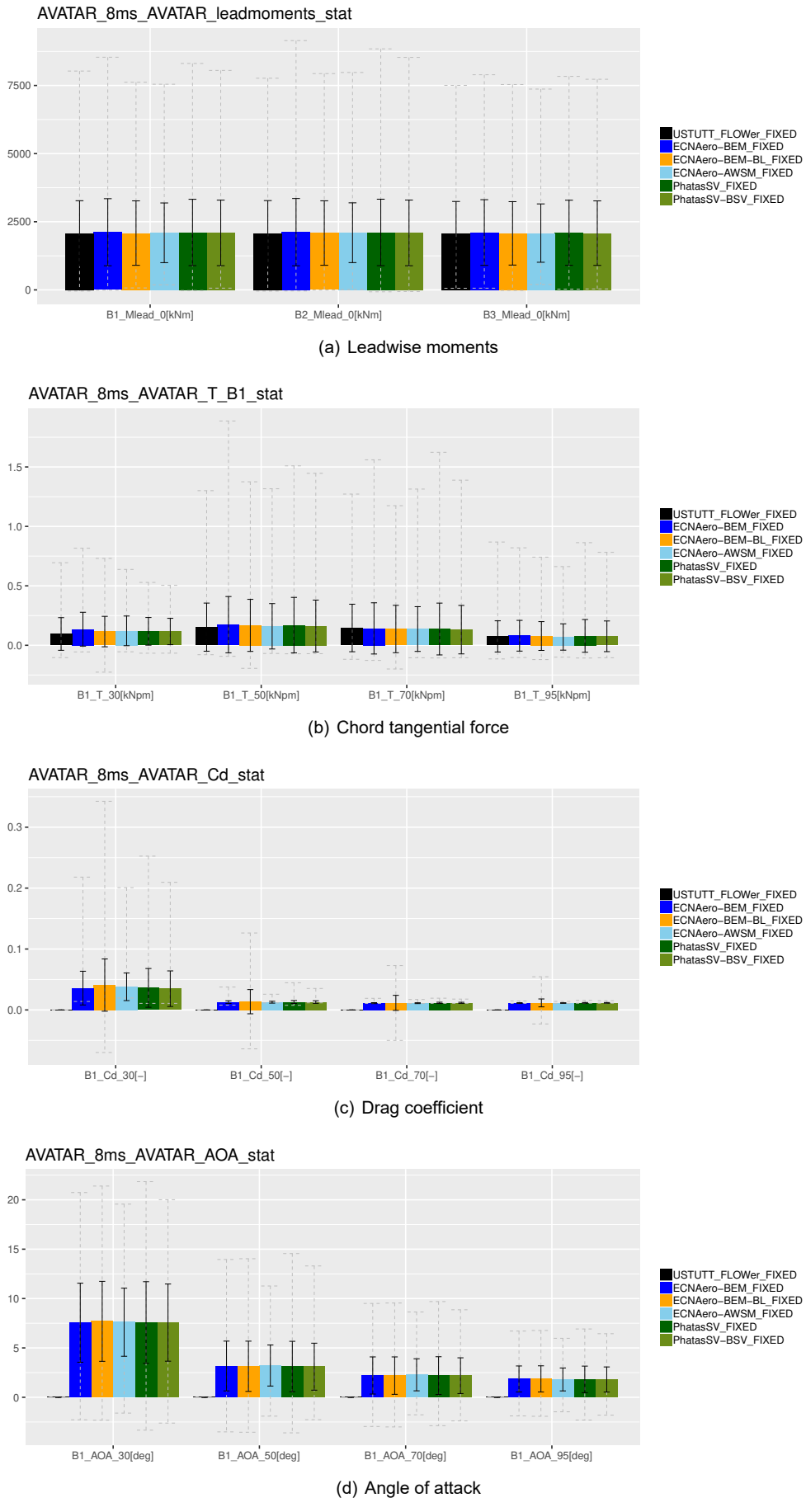

Figure C.13: Force decompostion in tangential direction

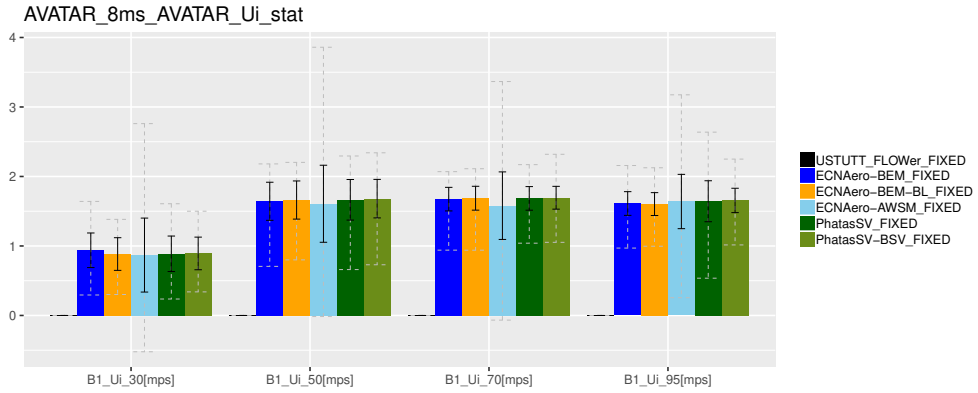

(a) Axial induced velocity

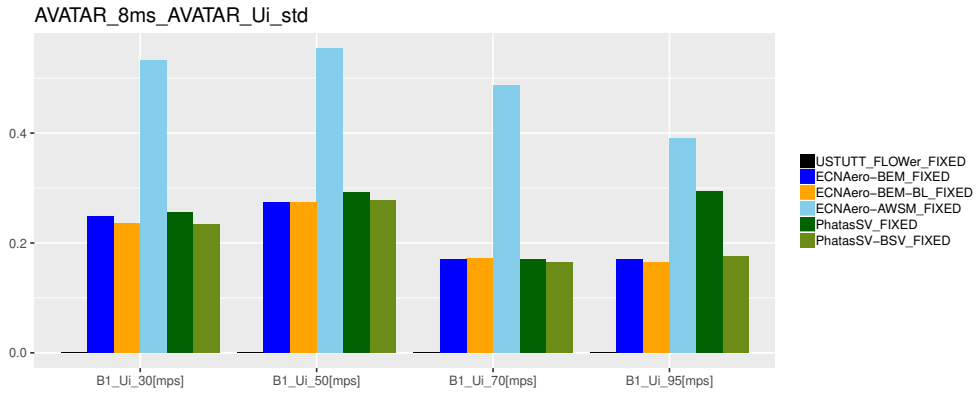

(b) Axial induced velocity (standard deviation)

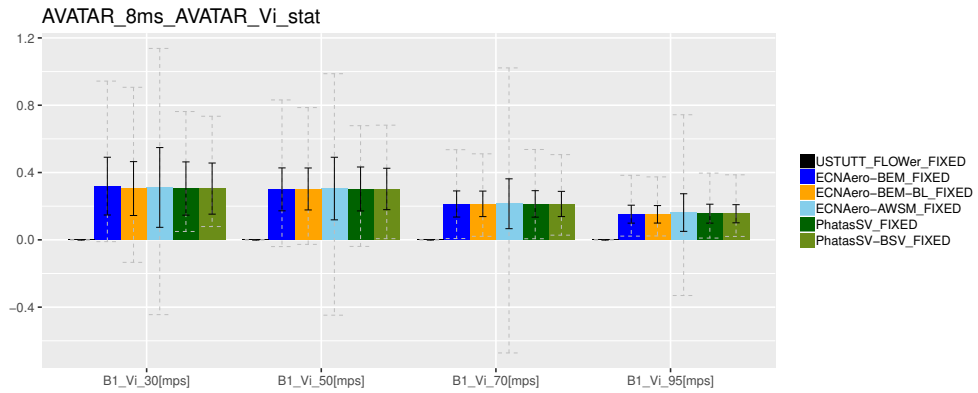

(c) Tangential induced velocity

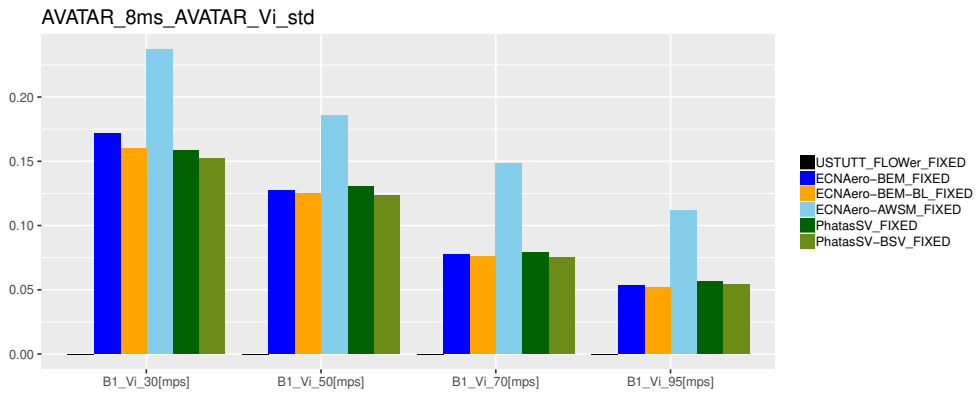

(d) Tangential induced velocity (standard deviation)

Figure C.14: Induced velocities

C.0.4 Equivalent load levels

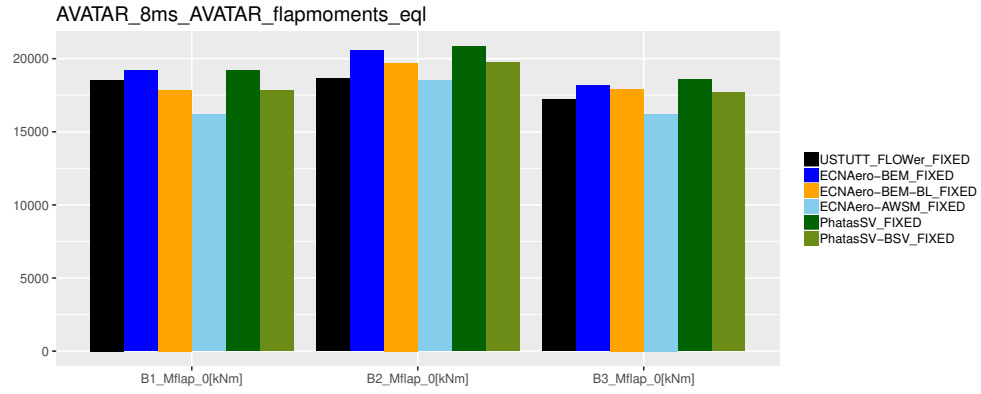

(a) Flapwise moments

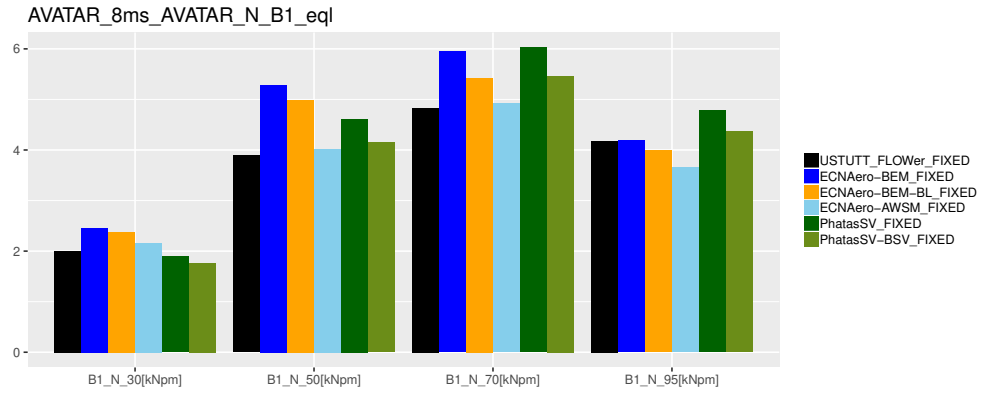

(b) Normal force

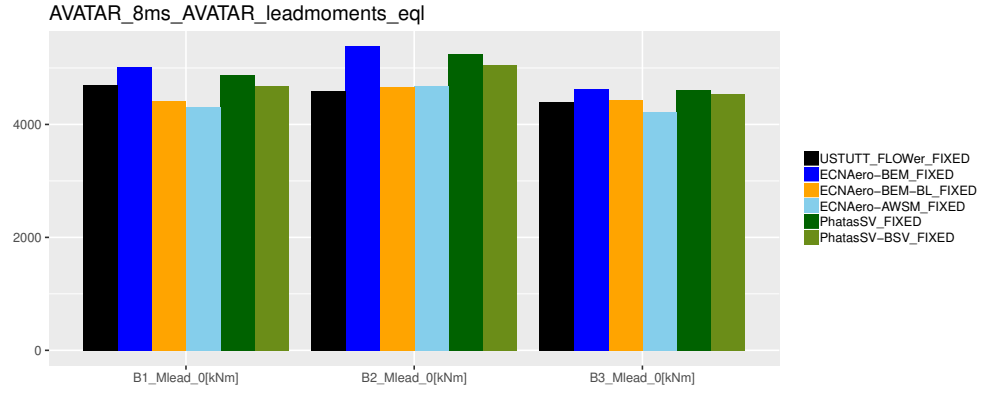

(c) Leadwise moments

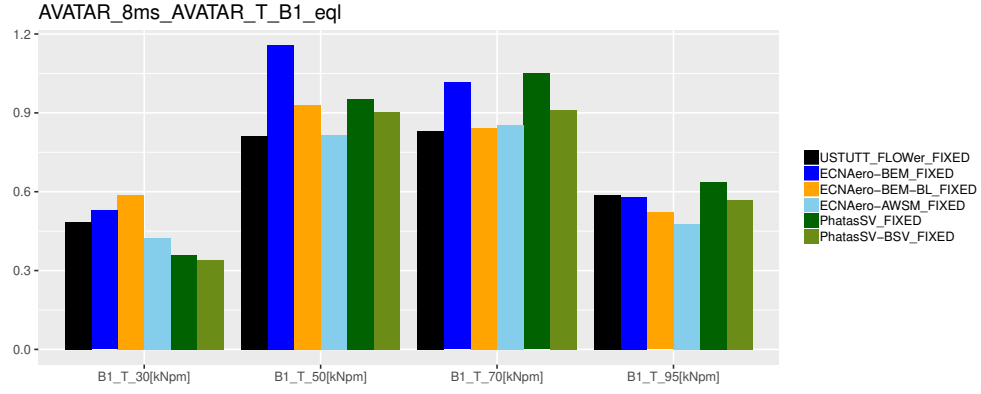

(d) Tangential force

Figure C.15: Forces and moments

C.0.5 Staircase plots

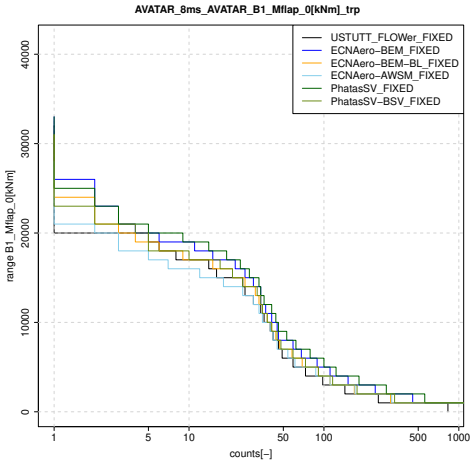

(a) Flapwise blade root moment

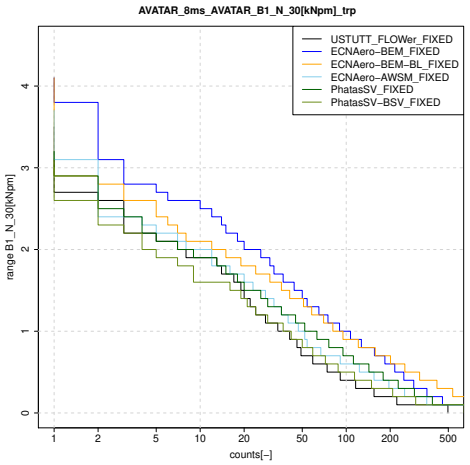

(b) Normal force, 30%R

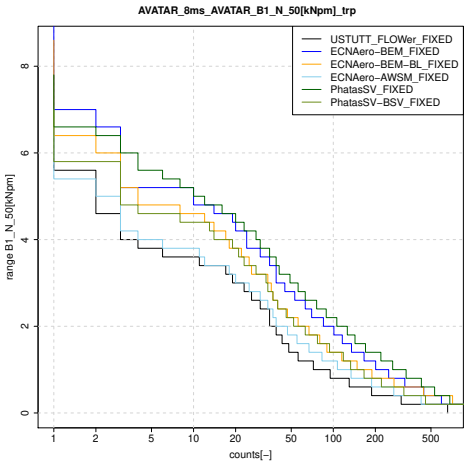

(c) Normal force, 50%R

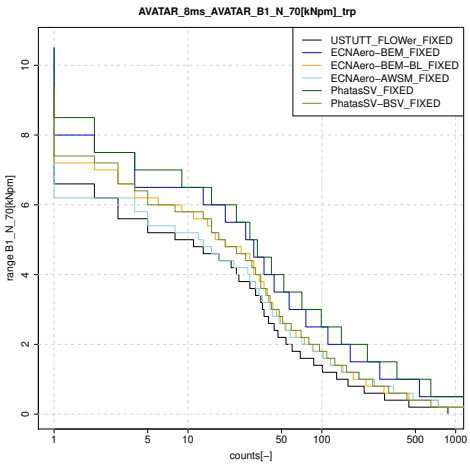

(d) Normal force, 70%R

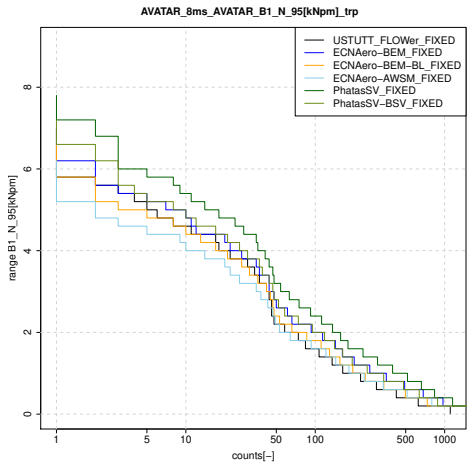

(e) Normal force, 95%R

Figure C.16: Flapwise moment and normal forces

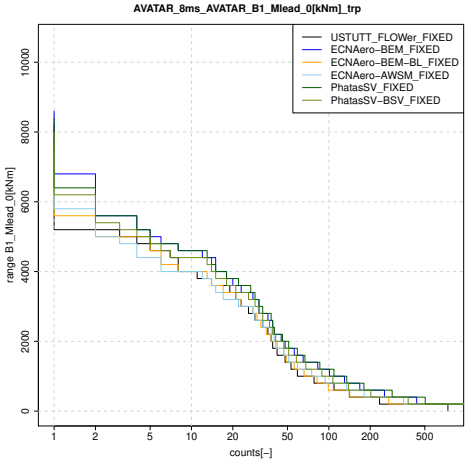

(a) Leadwise blade root moment

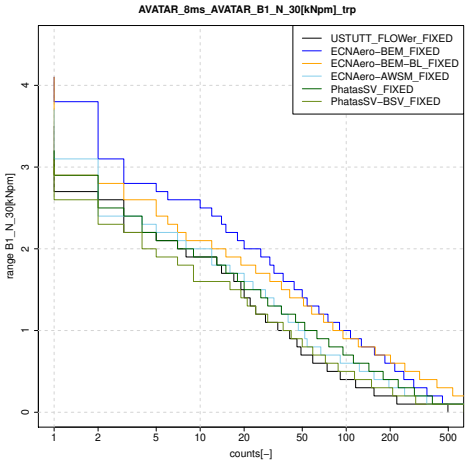

(b) Tangential force, 30%R

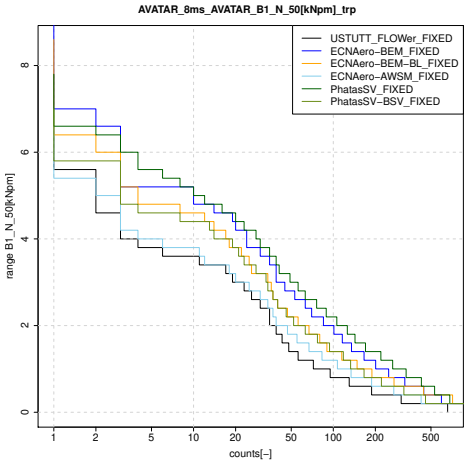

(c) Tangential force, 50%R

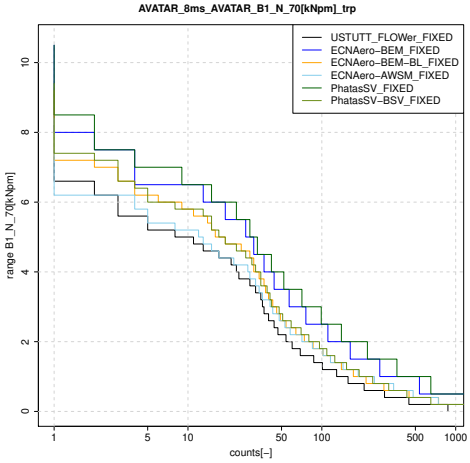

(d) Tangential force, 70%R

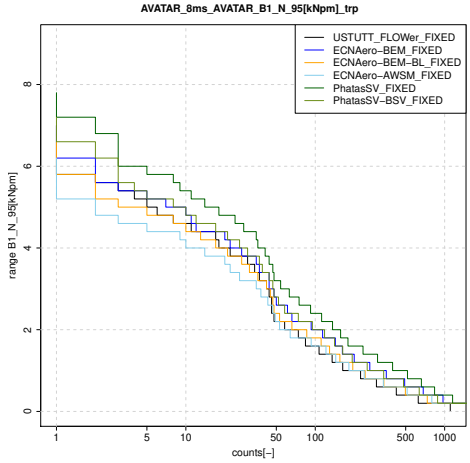

(e) Tangential force, 95%R

Figure C.17: Leadwise moment and tangential forces

C.0.6 PSD

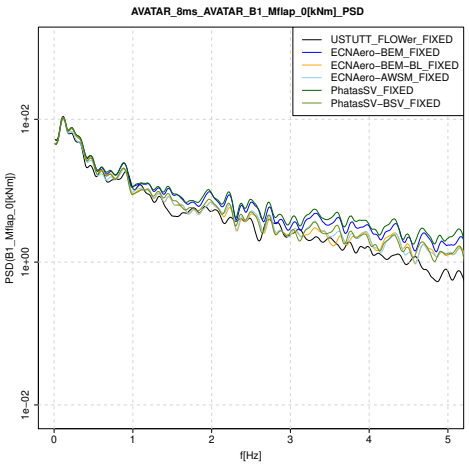

(a) Flapwise blade root moment

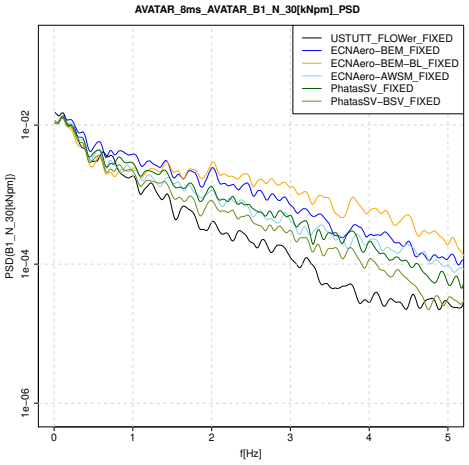

(b) Normal force, 30%R

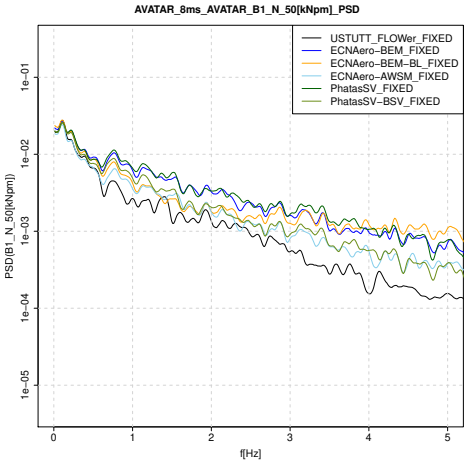

(c) Normal force, 50%R

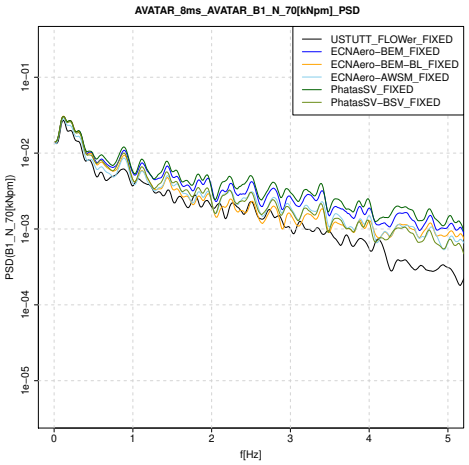

(d) Normal force, 70%R

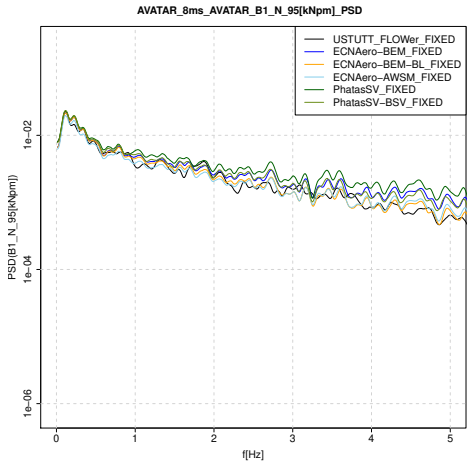

(e) Normal force, 95%R

Figure C.18: Flapwise moment and normal forces

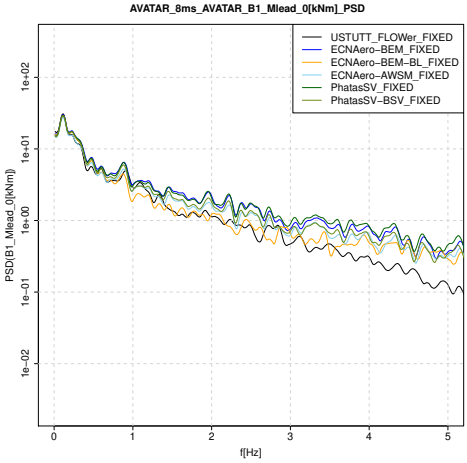

(a) Leadwise blade root moment

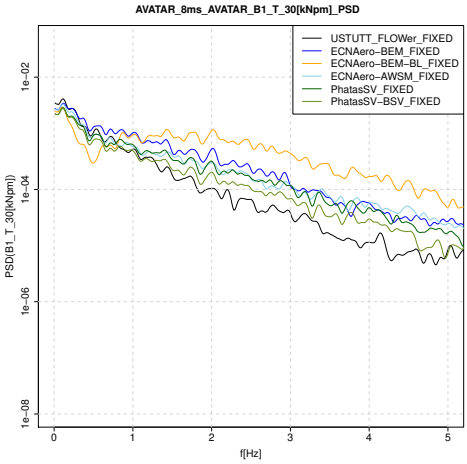

(b) Tangential force, 30%R

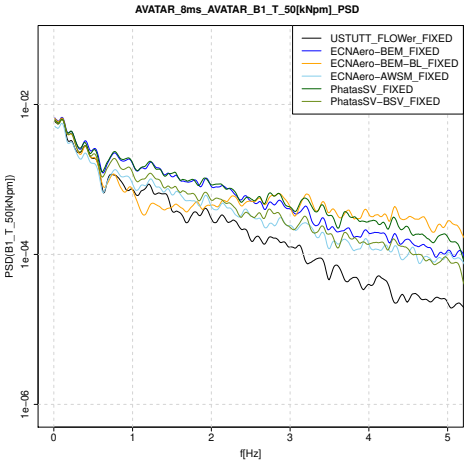

(c) Tangential force, 50%R

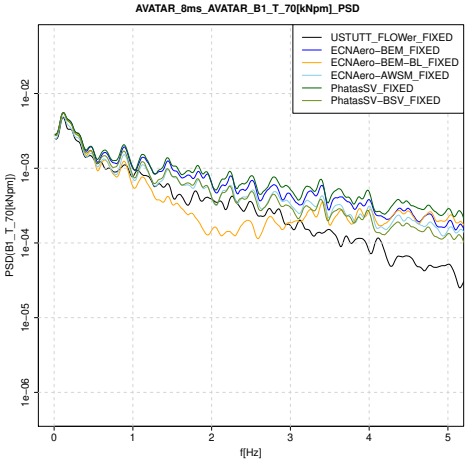

(d) Tangential force, 70%R

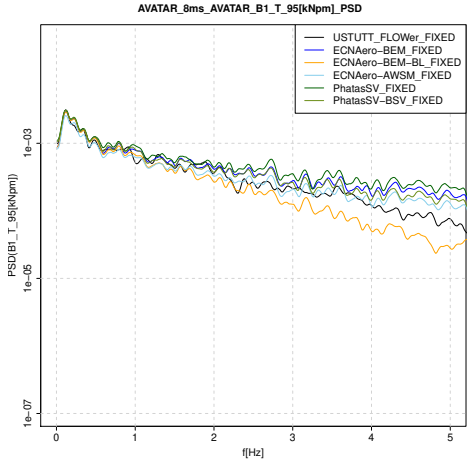

(e) Tangential force, 95%R

Figure C.19: Leadwise moment and tangential forces

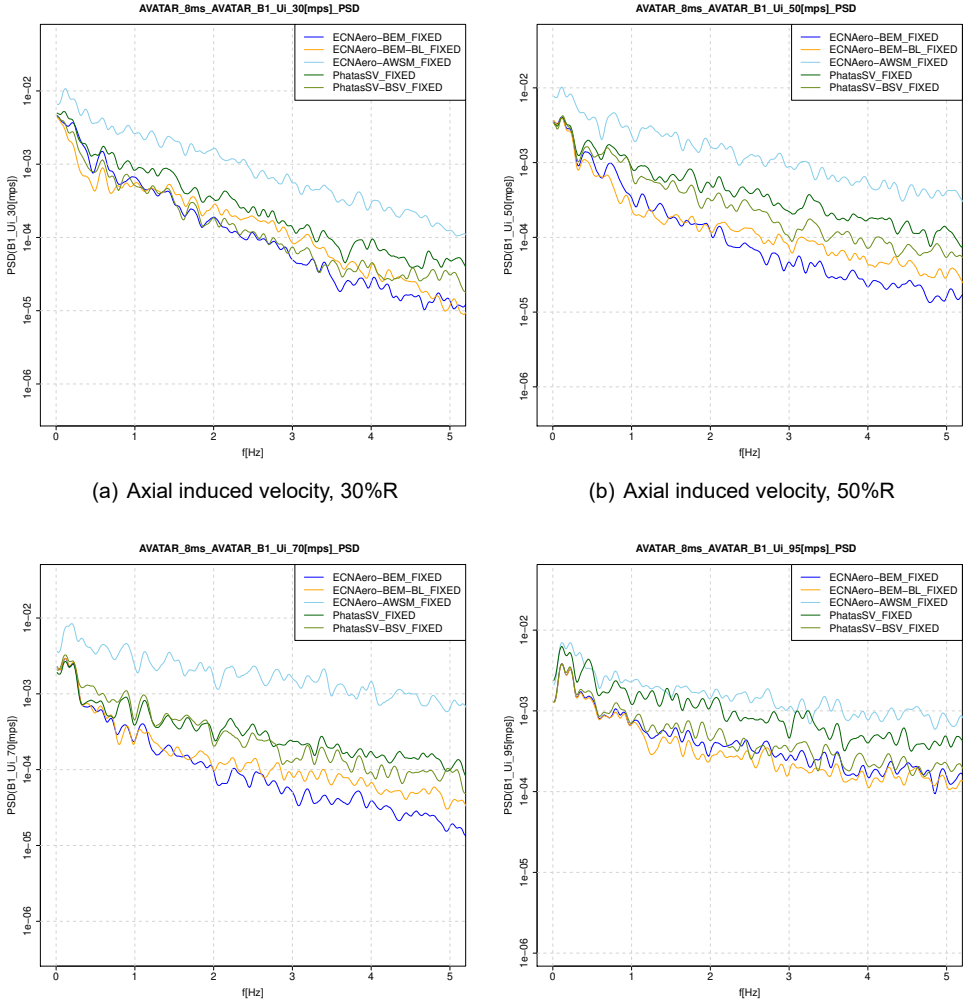

(a) Axial induced velocity, 30%R

(b) Axial induced velocity, 50%R

(c) Axial induced velocity, 70%R

(d) Axial induced velocity, 95%R

Figure C.20: Axial induced velocities

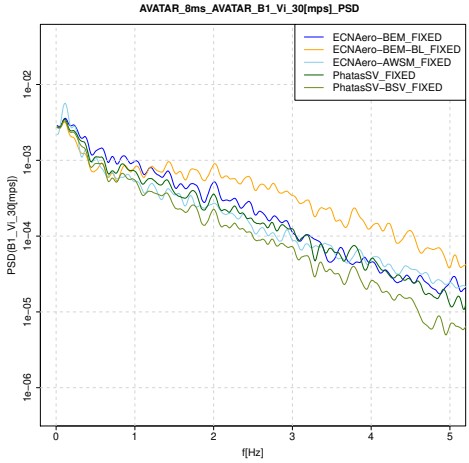

(a) Tangential induced velocity, 30%R

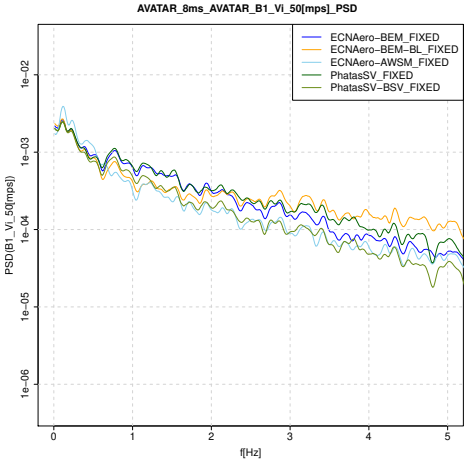

(b) Tangential induced velocity, 50%R

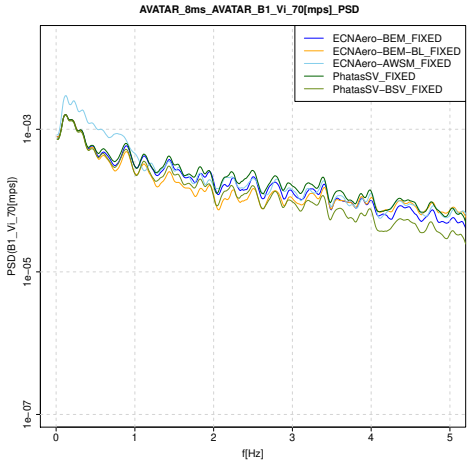

(c) Tangential induced velocity, 70%R

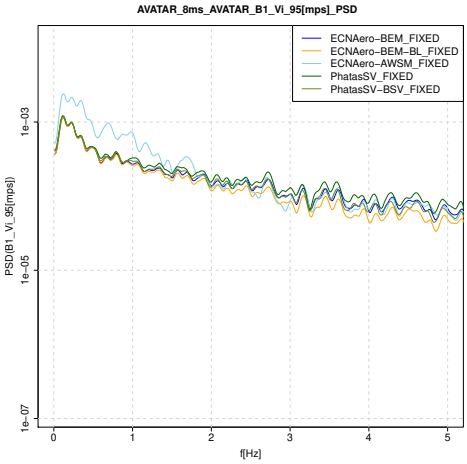

(d) Tangential induced velocity, 95%R

Figure C.21: Tangential induced velocities